Title

Engineered Barrier System Research Activities at LBNL: FY20 Progress Report

Authors

Zheng, LianGe
Lammers, Laura
Fox, Patricia
et al.

Publication Date

2020-07-20

Peer reviewed

Engineered Barrier System Research Activities at LBNL: FY20 Progress Report

Spent Fuel and Waste Disposition

Prepared for
US Department of Energy
Spent Fuel and Waste Science and Technology

LianGe Zheng, Laura Lammers, Patricia Fox, Chun Chang, Hao Xu, Sharon Borglin, Michael Whittaker, Chunwei Chou, Christophe Tournassat, Nithya Subramanian, Yuxin Wu, Peter Nico, Benjamin Gilbert, Tim Kneafsey

Lawrence Berkeley National Laboratory
June 04, 2020
LBNL- 2001331
SFWD Working Document: External Release

This page intentionally left blank.

Revision 6
10/07/2019

APPENDIX E

NTRD DOCUMENT COVER SHEET [1]

Name/Title of Deliverable/Milestone/Revision No.	Engineered Barrier System Research Activities at LBNL: FY20 Progress Report - M3SF-20LB010308062
Work Package Title and Number	Engineered Barrier System R&D – LBNL - SF-20LB01030802 Engineered Barrier System International Collaborations – LBNL SF-20LB01030806
Work Package WBS Number	1.08.01.03.08
Responsible Work Package Manager	Liange Zheng (signature on file) (Name/Signature)
Date Submitted	**06/04/2020**

Quality Rigor Level for Deliverable/Milestone[2]	☐ QRL-1 Nuclear Data	☐ QRL-2	☒ QRL-3	☐ QRL 4 Lab-specific [3]

This deliverable was prepared in accordance with Lawrence Berkeley National Laboratory (LBNL)
(Participant/National Laboratory Name)

QA program which meets the requirements of
X DOE Order 414.1 ☐ NQA-1 ☐ Other

This Deliverable was subjected to:

☐ Technical Review
Technical Review (TR)
Review Documentation Provided
☐ Signed TR Report or,
☐ Signed TR Concurrence Sheet or,
X Signature of TR Reviewer(s) below
Name and Signature of Reviewers
Mengsu Hu – Section 2-3 (signature on file)
Piotr Zaraycki – Section 4-5 (signature on file)
Pei Li – Sections 6-7 (signature on file)
Jonny Rutqvist – Sections 8 (signature on file)

☐ Peer Review
Peer Review (PR)
Review Documentation Provided
☐ Signed PR Report or,
☐ Signed PR Concurrence Sheet or,
☐ Signature of PR Reviewer(s) below
Name and Signature of Reviewers
Boris Faybishenko – Sections 1-9 (signature on file)

NOTE 1: *Appendix E should be filled out and submitted with each deliverable. Or, if the PICS:NE system permits, completely enter all applicable information in the PICS:NE Deliverable Form. The requirement is to ensure that all applicable information is entered either in the PICS:NE system or by using the FCT Document Cover Sheet.*

- *In some cases there may be a milestone where an item is being fabricated, maintenance is being performed on a facility, or a document is being issued through a formal document control process where it specifically calls out a formal review of the document. In these cases, documentation (e.g., inspection report, maintenance request, work planning package documentation or the documented review of the issued document through the document control process) of the completion of the activity, along with the Document Cover Sheet, is sufficient to demonstrate achieving the milestone.*

NOTE 2: *If QRL 1, 2, or 3 is not assigned, then the QRL 4 box must be checked, and the work is understood to be performed using laboratory specific QA requirements. This includes any deliverable developed in conformance with the respective National Laboratory / Participant, DOE or NNSA-approved QA Program.*

NOTE 3: *If the lab has an NQA-1 program and the work to be conducted requires an NQA-1 program, then the QRL-1 box must be checked in the work Package and on the Appendix E cover sheet and the work must be performed in accordance with the Lab's NQA-1 program. The QRL-4 box should not be checked.*

This page is intentionally left blank.

TABLE OF CONTENTS

This page is intentionally left blank.

LIST OF FIGURES

LIST OF TABLES

ACRONYMS

ALS	Advanced Light Source
API	Application Programming Interface
APS	Advanced Photo Source
ASPECT	Advanced Solver for Problems in Earth's ConvecTion
BBM	Barcelona Basic Model
BExM	Barcelona Expansive Model
BGR	Bundesanstalt für Geowissenschaften und Rohstoffe
BRGM	The Bureau De Recherches Géologiques Et Minières, France
CET	Cryo-electron Tomography
CG	Conjugate Gradient
CIEMAT	Centro de Investigaciones Energéticas, Medioambientales y Tecnológicas, Spain
C-M	Chemo-Mechanical
COLVARS	Collective Variables
CT	Computed Tomography
DECOVALEX	DEvelopment of COupled Models and their VAlidation against Experiments
DOE	Department of Energy, USA
DRS	Dielectric Relaxation Spectroscopy
EBS	Engineering Barrier System
EDZ	Excavation Disturbed Zone
ELSM	Extended Linear Swelling Model
ENRESA	National Radioactive Waste Corporation, Spain
ERT	Electrical Resistivity Tomography
FEBEX	Full-scale Engineered Barrier Experiment
FEPs	Features, Events, and Processes
FLAC	Fast Lagrangian Analysis of Continua
FY	Fiscal Year
GBM	Granular Bentonite Mixture
GDSA	Generic Disposal Systems Analyses
High T	High Temperature
HLW	High-level Waste
IC	Ion Chromatography

ICP-MS	Inductively Coupled Plasmas – Mass Spectrometry
ID	Inner Diameter
LBNL	Lawrence Berkeley National Laboratory
LLW	Low-level Waste
Low T	Low Temperature
LSTM	Long-Short Term Memory
MD	Molecular Dynamics
MGC	Modified Guoy-Chapman
MMT	Montmorillonite
NAGRA	National Cooperative for the Disposal of Radioactive Waste, Switzerland
NBS	Natural Barrier System
NS	Natural System
NWMO	The Nuclear Waste Management Organization, Canada
OD	Outer Diameter
PA	Performance Assessment
PDE	Partial Differential Equations
PMF	Potential of Mean Force
PWR	Pressurized Water Reactor
RWM	Radioactive Waste Management Limited, Quintessa Ltd
SAXS	Small-angle X-ray scattering
SFWST	Spend Fuel and Waste Science and Technology
SMD	Steered Molecular Dynamics
SURAO	Radioactive Waste Repository Authority, Czech Republic
TH	Thermo-Hydrological
THC	Thermo-Hydro-Chemical
THM	Thermo-Hydro-Mechanical
THMC	Thermo-Hydro-Mechanical-Chemical
THMCB	Thermal-Hydrological-(biogeo)-Chemical
TOUGH	Transport of Unsaturated Groundwater and Heat
TXM	Transmission X-Ray Microscope
UFD	Used Fuel Disposition
WHAM	Weighted Histogram Analysis Method
Wy-MMT	Wyoming Montmorillonite
XCT	X-ray Computed Tomography

XRD	X-ray Diffraction
μXCT	Microscale X-ray Computed Tomography
ZP	Zone plate

1. INTRODUCTION

The design of a radioactive waste repository typically involves a multi-barrier system, including the natural barrier system (NBS), i.e., the host rock and its surrounding subsurface environment, and an engineered barrier system (EBS). The EBS is to be constructed from the man-made, engineered materials placed within a repository. The repository includes the waste form, waste canisters, buffer materials, backfill, and seals. The most common buffer material for EBS is compacted bentonite, which features low permeability and high retardation of radionuclides. Extensive studies concerning the behavior of bentonite backfill in crystalline and argillite/shale geologic environments for nuclear waste disposal have been conducted by means of laboratory experiments, numerical modeling, and large-scale *in situ* tests in Underground Research Laboratories (URLs) in Switzerland, France, Belgium, and Japan.

This report includes the results of LBNL's research activities conducted according to the objectives and scope of the work packages "SF-20LB01030802 Engineered Barrier System R&D – LBNL" and "SF-20LB01030806 Engineered Barrier System International Collaborations – LBNL" of the Spent Fuel and Waste Science and Technology (SFWST) (formerly called Used Fuel Disposal) Campaign of the Department of Energy's (DOE) Office of Nuclear Energy. LBNL research studies included laboratory scale tests and modeling of the evolution of the EBS bentonite and associated coupled processes, and impacts of high temperature on parameters and processes relevant to the performance of crystalline and argillite repositories, including the evaluation of the technical basis for applying the maximum allowable temperature. The results of these studies are being addressing the technical elements necessary to evaluate the EBS design concepts. Emphasis is on the study of thermal, mechanical, and chemical processes that influence the performance of EBS, and the development of modeling capability for reliable assessment of these processes, and ultimately supporting the development of the GDSA model with detailed coupled THMC process models.

The research work was conducted both at LBNL and through collaboration in international programs to create a partnership bridge gaining advanced knowledge of nuclear waste disposal research from international URL activities. This report documents results of activities, which address key Features, Events, and Processes (FEPs), ranked in importance from medium to high, as listed in Table 7 of the Used Fuel Disposition Campaign Disposal Research and Development Roadmap (FCR&D-USED-2011-000065 REV0) (Nutt, 2011). Specifically, these research activities address FEP 2.1.04.01, Evolution and Degradation of Backfill/buffer. The work is also related to FEP 2.2.01, Excavation Disturbed Zone (EZD), for clay/shale, by investigating how coupled processes affect EDZ evolution; FEP 2.2.05, Flow and Transport Pathways; and FEP 2.2.08, Hydrologic Processes, and FEP 2.2.07, Mechanical Processes, and FEP 2.2.09, Chemical Process—Transport, by studying near-field coupled THMC processes in clay/shale repositories.

This report documents the following research activities:

Section 2 presents the results of the development and application of thermal-hydrological-mechanical-chemical (THMC) modeling to evaluate the EBS bentonite characteristics in argillite repository under different temperature (100 °C and 200 °C). This chapter contains three parts, the first part presents some new results, using the dual structure model – BExM to conduct a parametric study of the effect of the pre-consolidation pressure. The second part includes a description of the progress of the development of the simulator – TReactMech with new libraries, modified the coupling strategy from iterative two-way coupling to a sequential coupling method, and used it to simulate the high temperature in nuclear waste disposal sites. The third part provides a summary of using reduced order models for investigation of new constitutive relationships for bentonite. Section 2 was co-authored by Hao Xu and Liange Zheng.

Section 3 presents the results of sorption and diffusion experiments on bentonite samples. In this chapter, we focus on the diffusion of ^{3}H, U, and Se through compacted smectite. Specifically, we present the results from ^{3}H and U diffusion experiments from field-heated (95°C, 18 years) and cold-zone (20°C) FEBEX bentonite under different chemical conditions; plans for studying Se(VI) diffusion through compacted montmorillonite under different background electrolyte compositions, and plans for modeling the diffusion experiments. We note that experimental work was interrupted/delayed due to the shelter-in-place orders associated with the COVID-19 pandemic. Section 3 was co-authored by Patricia Fox, Christophe Tournassat and Peter Nico.

Section 4 presents the progress on an integrated set of experiments, molecular simulations, and thermodynamic modeling to develop a predictive understanding of ion exchange-driven swelling and collapse of montmorillonite clay. We report on the development of an X-Ray transparent micro-oedometer system for the measurement of montmorillonite swelling pressure as a function of the dry bulk density and the aqueous solution composition. Initial work focused on pure homoionic NaCl and KCl solutions as well as NaCl+KCl mixtures. Preliminary data are presented from *in situ* X-Ray scattering experiments. To develop a theoretical understanding of microstructural evolution, we applied our newly published structural model for cis-vacant smectite clay (Subramanian et al., 2020) to simulate the free energy of mixing crystalline layer states and find that highly unfavorable mixing energetics can drive phase separation in mixed layer state systems. Section 4 was co-authored by Benjamin Gilbert, Nithya Subramanian, Laura Lammers, Francis Claret and Stephane Gaboreau.

Section 5 presents a research plan for a newly added research activity on the development and validation of a microscopic model of coupled transport processes in bentonite and using this model to determine cost effective augmentation strategies to increase the bulk thermal conductivity of hydrated bentonite. Because this activity was added in March 2020, we only report a research plan and some preliminary results, which will serve as a foundation for a larger scale effort in FY20-21 to stably increase the thermal conductivity of bentonite above 2 W/mK at temperatures relevant to modern nuclear waste storage design concepts. Section 5 was co-authored by Michael Whittaker, Benjamin Gilbert and Piotr Zarzycki.

Section 6 presents the results of coupled THMC modeling for understanding the THMC evolution of bentonite in FEBEX-DP. From FY16 to FY19, extensive model calibrations were conducted, which provided a coherent explanation of THMC data collected at the FEBEX *in situ* test. In FY20, the modeling work included the use the THMC model to explore the long-term alteration of bentonite. Besides, a long-term THC model was also used to assess the necessity of using the THMC model for studying the long-term alteration of bentonite, especially geochemical alteration. Section 6 was co-authored Liange Zheng and Hao Xu.

Section 7 presents the results of modeling in support of the HotBENT field test that is currently under construction in Grimsel, Switzerland. In April 2020, the design for HotBENT was finalized in terms of the type of bentonite and the designed conditions of bentonite barrier. We developed a THC model to predict the evolution of one of the bentonites (Woyming bentonite) that will be used in the HotBENT. Section 7 was authored by Liange Zheng

Section 8 presents a summary of the benchtop-scale laboratory experiment, HotBENT-Lab, which provides a laboratory analog of the HotBENT experiment, to obtain a more comprehensive set of characterization and monitoring measurements. The primary goal of this laboratory experiment is to obtain well-characterized datasets for (1) understanding bentonite THMC processes under heating and hydration for model parameterization and benchmarking, (2) comparison with field-scale test results from HotBENT, and (3) development of a prototype experimentation platform for future studies of bentonite under conditions of high temperature. In the report we discuss the monitoring results until March 2020. A planned dismantling of the column was delayed by COVID19 pandemic. The section

is co-authored by Sharon Borglin, Yuxin Wu, Chun Chang, Chunwei Chou, Tim Kneafsey, Liange Zheng, and Hao Xu.

Section 9 summarizes the main FY20 research accomplishments and proposed future work activities.

This page is intentionally left blank.

2. INVESTIGATION OF THE IMPACT OF HIGH TEMPERATURE ON EBS BENTONITE WITH THMC MODELING

2.1 Introduction

In the underground Engineered Barrier System (EBS), bentonite is expected to be used as a buffer material to isolate the disposed nuclear waste from the surrounding environment. Bentonite is characterized by swelling properties, absorption capabilities for radionuclides, and low permeability. The complexity of the underground multi-processes and the interaction between the bentonite buffer and the NS (Natural System) makes it difficult to predict long-term evolution of bentonite buffer. This chapter is aimed at utilizing the coupled Thermo-Hydro-Mechanical-Chemical (THMC) model to evaluate the behavior of EBS bentonite and the NS clay formation.

Zheng et al. (2015) investigated the coupling between chemical and mechanical processes via an Extended Linear Swelling Model (ELSM) and the double structure Barcelona Expansive Model (BExM) (Sánchez et al., 2005; Gens, 2010; Guimarães et al., 2013). However, the ELSM does not accurately describe the transient state of swelling, neglects the history of mechanical change, and is unable to account for the impact of cations exchange on the bentonite swelling. BExM linked mechanical process with chemistry, so the model could simultaneously incorporate the effects of exchangeable cations, ionic strength of pore water, and abundance of swelling clay on the swelling stress of bentonite. Two scenarios were presented: (1) a case in which the peak temperature in the bentonite near the waste canister is about 200 ^{o}C and, (2) a case in which the temperature in the bentonite near the waste canister peaks at about 100 ^{o}C. The comparison of these two cases delineates the impact of temperature on the coupled process in bentonite.

In FY20, we continued working on THMC modeling of bentonite and the transition to the new simulator – TReactMech. This chapter contains three parts: (1) the first part presents some new results using the dual-structure BExM model to conduct a parametric study on pre-consolidation pressure; (2) TReactMech (Sonnenthal et al., 2015; 2018) with new libraries, which modified the coupling strategy from iterative two-way coupling to a sequential coupling method, and used it to simulate the high temperature cases in nuclear waste disposal; (3) In the third part, we summarize the studies on using reduced order models for investigations of new constitutive laws for bentonite.

2.2 Generic Model Development with BExM

Because the model used in this report is similar to that described in previous report (Liu et al., 2013; Zheng et al., 2014; Zheng et al., 2015; Zheng et al., 2016; Zheng et al., 2017), we only briefly describe each element of the THMC model here, focusing on the parametric study condcuted in FY20.

2.2.1 Double structure model

The dual structure model, Barcelona Expansive Model (BExM), considers the elasto-plasticity at the macrostructure, and incorporates a microstructure into the model to form a dual structure, which enables simulating the behavior of expansive soils, such as the dependency of swelling strains and swelling pressure on the initial stress state and on the stress path, strain accumulation upon suction cycles and secondary swelling. In the model design, the microstructure can swell to invade the macro-porosity, depending on the mechanical confinement and the load level. This is relevant when considering permeability changes during the soil swelling, because fluid flow takes place mostly through the macro-porosity, which is not proportional to the total strain and deformation of the expansive soil. Details regarding concept and equations to describe the mechanical behavior of micro-structural and macro-structural levels and the interaction between structural levels are given there, but they can be found in Zheng et al. (2019). A one-way coupling approach, in which chemical changes affect mechanical behaviors of bentonite through the

evolution of volume fraction of smectite, exchangeable cation concentration, and ionic strength (via osmotic suction), is taken into account through BExM.

2.2.2 Simulator

In this study, the numerical simulations are conducted with TOUGHREACT-FLAC3D, which sequentially couples the multiphase fluid flow and reactive transport simulator, TOUGHREACT (Xu et al., 2011), with the finite-difference geomechanical code FLAC3D (Itasca, 2009). The coupling of TOUGHREACT and FLAC3D was initially developed in the work by Zheng et al. (2012) to provide the necessary numerical framework for modeling fully coupled THMC processes. Recently, the numerical code was expanded with multiple constitutive models, such as the dual structural BExM and Extended Linear Swelling Model (ELSM).

2.2.3 Modeling scenarios

The model is applied to a hypothetical bentonite-backfilled nuclear waste repository, which involves a horizontal nuclear waste emplacement tunnel at 500 m depth in Opalinus clay (Figure 2-1). The case is a pseudo 2D model with the *y*-axis aligned parallel to the tunnel, with a 1 m thickness in the *y*-direction. The *z*-axis is vertical, and the horizontal *x*-axis is orthogonal to the tunnel direction. Note that while the canister is modeled as a heat source with mechanical properties of steel, the THC changes in the canister and its interactions with the EBS bentonite are not considered for the sake of simplicity.

An initial stress field is imposed by the self-weight of the rock mass. Zero normal displacements are prescribed on the lateral boundaries of the model. Zero stress is applied to the top, and vertical displacements are prevented at the bottom. Liquid pressure is constantly constrained at the top and bottom, and the model domain is in a hydrostatic state. The initial temperature of 11 ºC was assigned at the top, and of 38 ºC at the bottom, with a thermal gradient of 27 ºC /km along the depth (i.e., the *z*-axis). The model simulations were conducted in a non-isothermal mode with a time-dependent heat power input. The power curve in Figure 2-1 was scaled from representative heating data from the U.S. DOE's SFWD campaign for PWR used fuel for the current "high T" case. This heat load is then scaled in the 2D model to represent an equivalent line load, which depends on the assumed spacing between individual waste packages along an emplacement tunnel. The heat load corresponds to an initial thermal power of 520 W/m along the length of the heater. The EBS bentonite has an initial water saturation of 65% and the argillite (Opalinus clay) is fully saturated. From time zero, the EBS bentonite undergoes simultaneously re-saturation, heating, chemical alteration, and stress changes.

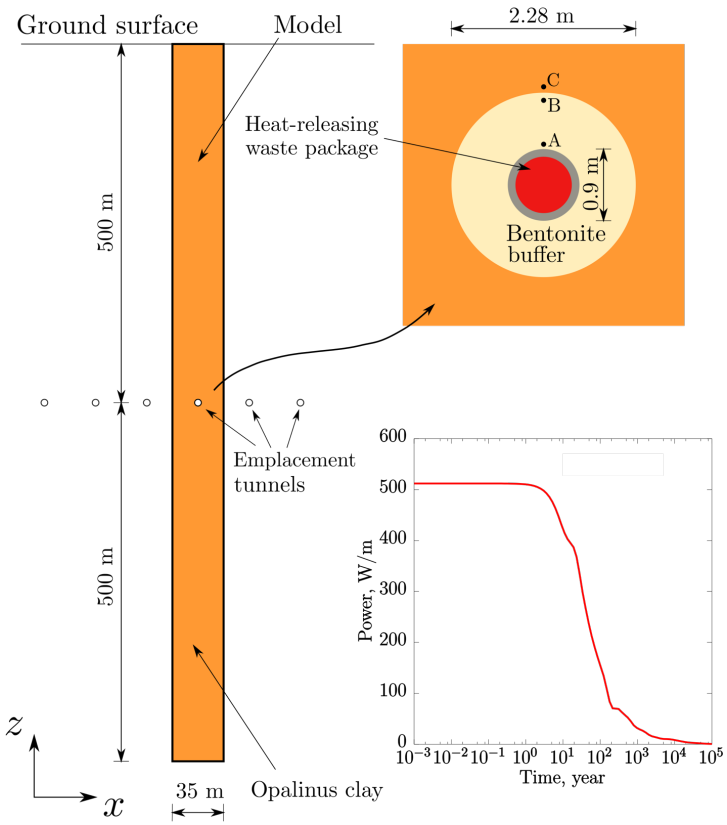

Figure 2-1. Domain for the test example of a bentonite back-filled horizontal emplacement drift at 500 m (Rutqvist et al., 2014). Modeling monitoring points: A--in the bentonite near the canister, B--in the bentonite near the EBS-NS interface, C--in the Opalinus clay near the EBS-NS interface. Power curves used in simulations to generate a 200 ºC peak temperature in the buffer.

2.2.4 Model results on pre-consolidation pressure, p_0^*.

With BExM, we conducted several simulations with different pre-consolidation pressure, p_0^*, to investigate the variety of bentonite response under THMC processes. In BExM, p_o is the yield/pre-consolidation pressure at the current suction, while p_o^* is the associated yield stress at full saturation. These two variables are two points on the locus of Loading-Collaspse (LC) curve defined in BExM, and the locus with respect to the suction forms the range of the elastic domain. If the stress path of p reaches the locus, the macro-structural plasticity will occur. The value of p_0^* ranges from 5 to 12 MPa based on the reported values in several published papers (Sanchez et al., 2005, 2008; Guimarães et al., 2013; Lloret et al., 2003) using BExM. To study the effect of this parameter on the elasto-plastic behavior, we computed three cases, $p_0^* =$ 4 MPa, 6.5 MPa and 8 MPa (noted as cases 1, 2 and 3, respectively). Figure 2-2 displays the stress path at Points A and B on p-s_m plane for these 3 cases. Figure 2-2a shows that no intersections or overlapping between p and p_0 are found in all 3 cases, indicating that Point A in all cases remains inside the elastic domain, and the LC curve path of p_0 in the space evolve quite similar in three cases. Figure 2-2b shows that p at Point B in Case 1 intersects with the path of p_0 at around 2.5 MPa when the bentonite is just fully saturated, indicating the yield threshold was reached. Stress collapse will happen at Point B in Case 1, and the material will consequently lose some swelling capacity.

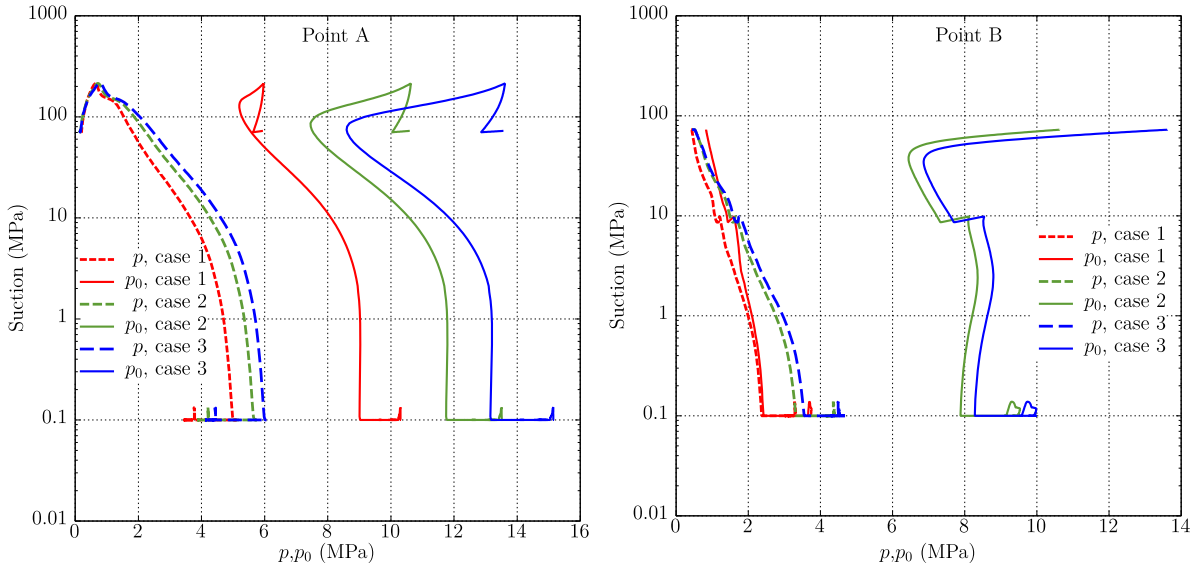

(a) Stress path of Point A on p-s_m plane. (b) Stress path of Point B on p-s_m plane.

Figure 2-2. Simulation results of stress at Points A and B with different initial p_0^*.

As these 3 cases illustrate, initial p_0^* affects the behavior of the material. However, the value p_o varies depending on the historical stress path and the sample preparation process. Although the sample was carefully compacted, the heterogeneity of material's density induced distinct internal stress paths.

2.3 TRANSITION TO A NEW SIMULATOR AND PLATFORM

2.3.1 Introduction

In FY19, as a part of the GDSA framework, we started to move our work to the Linux platform with a new numerical simulator – TReactMech, which has been recently developed at LBNL. However, the convergence in mechanical calculations was likely not well achieved, especially when PETSc (an acronym for Portable, Extensible Toolkit for Scientific Computation) library was used for parallel computing, and the iterative two-way coupling induced very tiny time increments, resulting in extremely long computational time in our high T case. In FY20, we used the deal.II library to reconstruct the mechanical module. The deal.II library is an open source Finite Element library written in C++, which supports a broad variety of PDEs for different types of problems, such as mechanics, fluid flow, heat transfer, etc. (Bangerth, 2019; Arndt et al., 2019). It also provides interfaces to numerous programs and libraries, such as PETSc and Trillions for parallel computing, GPU (an acronym for Graphics Processing Unit) support via CUDA (an acronym for Compute Unified Device Architecture), HDF5 (the Hierarchical Data Format version 5) for data structures, etc. (Bangerth et al., 2007). Figure 2-3 shows one example developed with the deal.II library for parallel computing. The deal.II is initially programmed for adaptive mesh refinement (Bangerth et al., 2007; 2012), so it supports multiple mesh formats or result formats both for input and output. Although the built-in C++ classes in deal.II are not easily understandable and implemented, after getting familiar with them, it's more easily to modify PDEs for any specific scenario. Moreover, the C++ class in deal.II is optimized for better memory access following the hierarchical structure of the memory and cache.

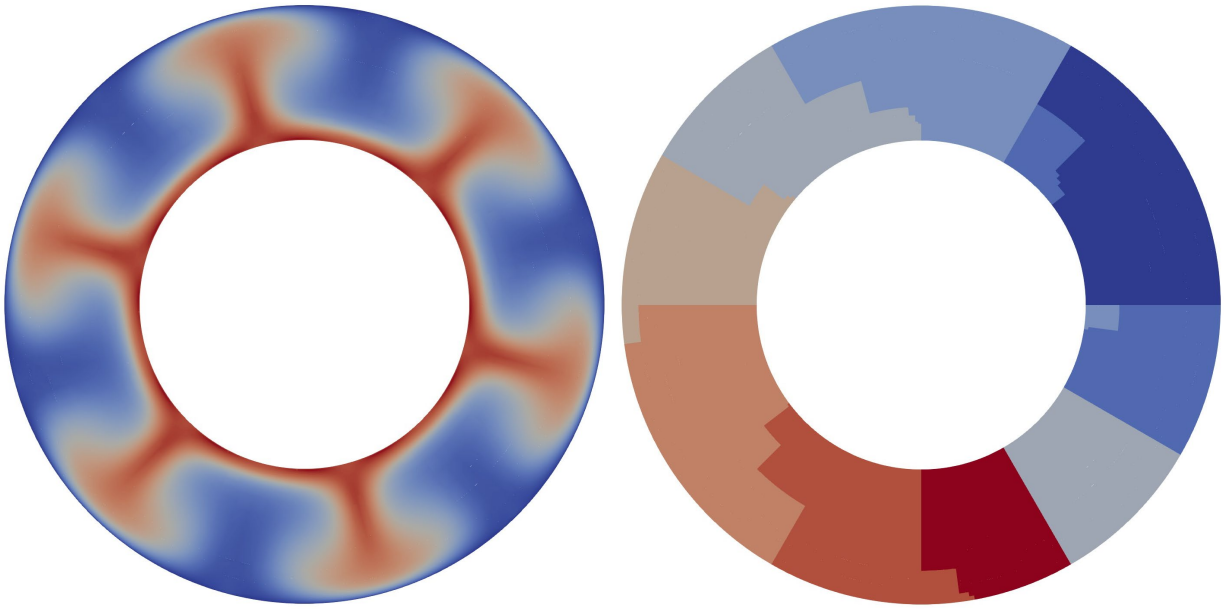

a) b)

Figure 2-3. Numerical simulation results of TH processes in the Earth's mantle with an open source code ASPECT (Advanced Solver for Problems in Earth's ConvecTion) developed with the deal.II library: (a) Temperature results; and (b) Partition of the whole domain with 8 CPUs. The results are based on the work by Kronbichler et al. (2012).

For the flow part in the simulator, we modified the code slightly to transfer from Intel FORTRAN compiler to GNU compiler. The reason to the change is that because the Intel compiler uses stack for many variables in the program, it is faster but may cause stack overflow and segmentation fault errors. On Linux, users need to increase the stack limit when compiling the source code and running the program. The GNU compiler uses heap for variables, which is a little slower than the stack, but safer. Another advantage of using the GNU compiler is that we can use more open source tools to diagnose the source code or to link with our program.

The current code only combines mechanics with Thermo-Hydraulic module, since some bugs related to OpenMP were found in the chemical part. After we diagnose and fix more code bugs, we will attach the chemical part back to the simulator. The coupling strategy includes the application of the sequential coupling method developed by Kim et al. (2012), which is widely used in the DECOVALEX-2019 project (Xu et al., 2020). This coupling method is performing, and the convergence is better than that in the previous version of two-way coupling in TReactMech, which induced a very tiny time increment. Now, the code uses mixed-languages compiling, C++ for mechanics, and FORTRAN for TH processes. Some variables used in both parts, like pore pressure, are declared as global variables stored in the memory, which can be accessed by any function in C++ and FORTRAN. A a result, no more files output and reading are required.

2.3.2 3D THM modeling verification

In this section we used the same benchmark case (Zheng et al., 2019), a consolidation case of a homogeneous saturated porous medium around a constant point heat input power, to verify the implementation of the new coupling method. For simplicity, we don't present all details, but rather only present a comparison between the numerical results and analytical solutions (Booker and Savvidou, 1985; Smith and Booker, 1993). The only change is the domain size, which is a cube of 20 m×20 m×20 m, the

heat power (only 17.5 W), and output points. Temperature, pressure, stresses and displacements evolution up to 100,000 hours are printed at the monitoring points as listed in Table 2-1.

Table 2-1. Points for numerical results for the 3D THM benchmark.

Points	(x, y, z) coordinates	Quantity
P1	(0.275, 0, 0)	Temperature, pressure
P2	(0.35, 0, 0)	Temperature, pressure
P3	(0.45, 0, 0)	Temperature, pressure
P4	(0.275, 0.35, 0.45)	Temperature, pressure, stress
P5	(0.3, 0.4, 0.5)	Displacement

The results of 3D THM numerical modeling and analytical calculations of temperature are plotted in Figure 2-4 . Figures 2-4a, b display the temperature changes at Points P1, P2, P3 and P4; Figure 2-4c presents the displacement changes at Point P5; and Figures 2-4d,e show the normal stress and shear stress changes at Point P4.

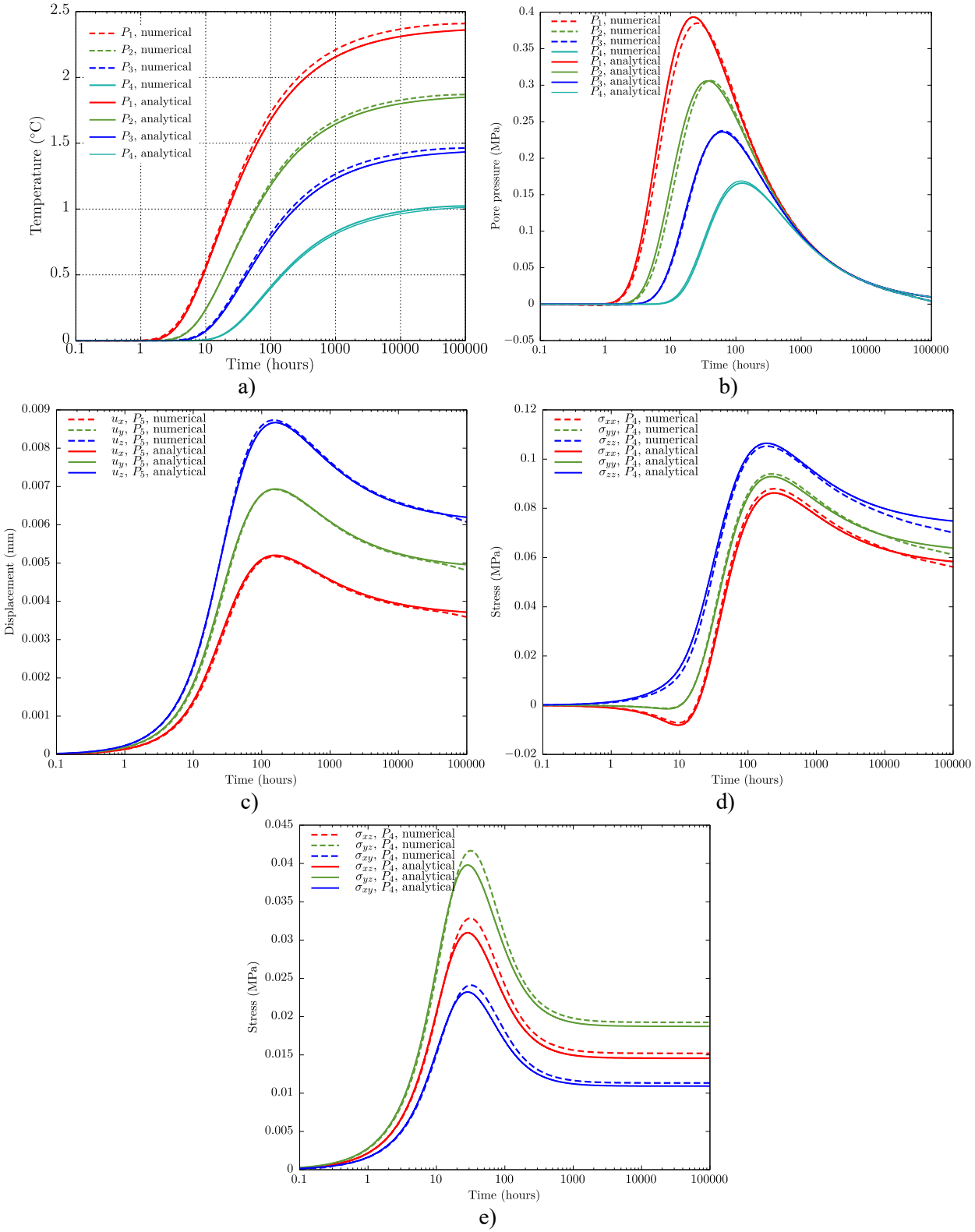

Figure 2-4. Simulation results of 3D THM modeling: (a) Temperature evolution at P1, P2, P3 and P4; (b) Pore pressure evolution at P1, P2, P3 and P4; (c) Displacement changes at P5; (d) Normal stress changes at P4; and (e) Shear stress changes at P4.

A good agreement between numerical simulations and analytical solutions is obtained, which verifies the correctness of the THM models' computation using the new simulator.

We used the uftrace, a profiling tool for C/C++ program developed by a group of Korean computer engineers (Kim, 2020), to analyze the code performance. Its functionality is similar as gcov and valgrind, but provides more interfaces to other tools, such as Chrome and Flame Graph (Gregg, 2019), to visualize the function calling. Because the model comprises of over than 20,000 elements, the debug mode of the program generates a large amount of profiling data. Because Chrome is used more frequently for web applications and has a limitation on the data size, we used Flame Graph tool to show the function calling.

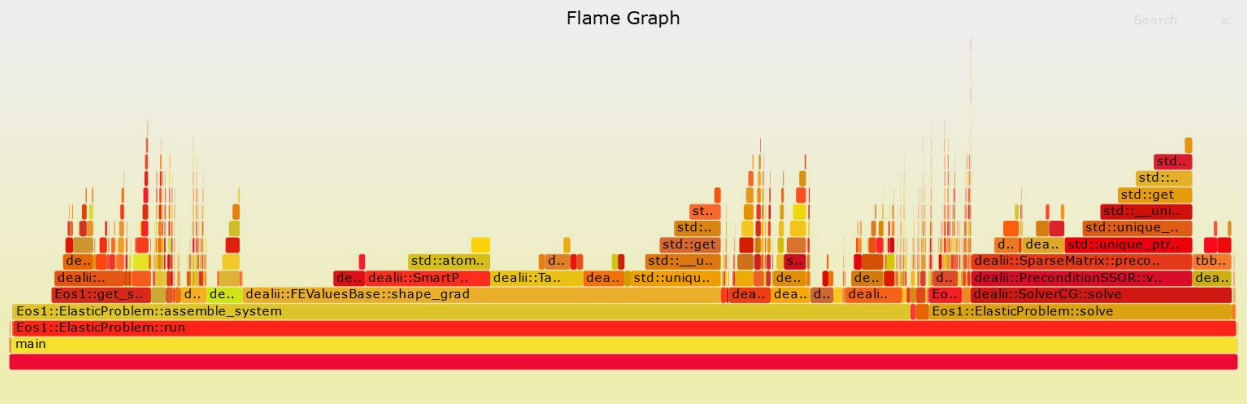

Figure 2-5. CPU time flame graph of the mechanical calculation in one time step.

Figure 2-5 shows the graph of CPU running time of each function, and the horizontal length illustrates that the time length is proportional to the main function. This hierarchical graph shows the function calling relation during just one time increment in mechanical calculations. The parent function is at the lower level, and the child function called by this parent function is placed on top of the parent function. For example, main function creates the Eos1 object, and calls its public member function Eos1::ElasticProblem::run to start the problem. Then, Eos1::ElasticProblem::run calls the private member function Eos1::ElasticProblem::assemble_system to assemble the linear system, and so on. Usually, in the graph, sharper the function is and closer the time of the child function is to its parent function, more efficient the code is. From Figure 2-5, the most expensive and inefficient function is dealii::FEValuesBase::shape_grad, which calculates the gradients of the shape function to form the A matrix in the linear equation system $Ax = b$. Since the element number is not small, this function needs to be called numerously, and it's inevitable for the calculation. But if the material is linear elastic and the small deformation is assumed, it is only called in the first-time increment, which saves a lot of time for later computation in this specific case.

2.3.3 THMC modeling of bentonite in nuclear waste disposal

In this section, we present the results of simulations of a generic case similar to that described in Section 2.2.3. We generated a similar model following the same geological formation and used the same material of the EBS, such as steel cell at the center surrounded by FEBEX bentonite and Opalinus clay, shown in Figure 2-6. In this model, the depth of the same domain is 1000 m. For the canister and bentonite, the mesh was refined with 0.05 m×0.05 m elements to capture the detailed THM evolution.

During the heating period, the unsaturated bentonite is placed in the tunnel, but the surrounding clay is assumed being fully saturated. The material properties were kept the same as in the previous case.

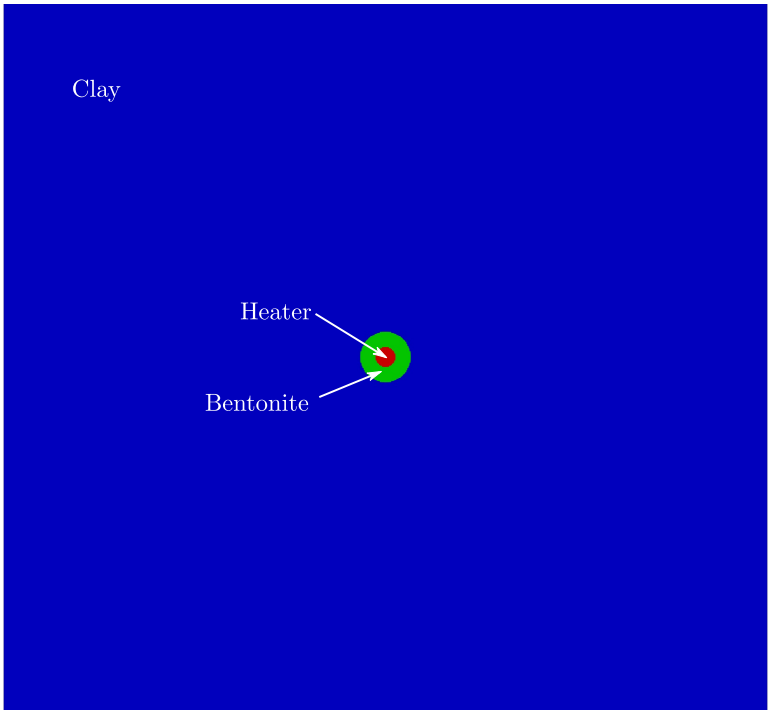

Figure 2-6. Simulation domain of the new "high T" case.

In this case, we didn't simulate the excavation process before the heating phase. Figures 2-8 and 2-9 demonstrate the simulated results of temperature and liquid saturation at Points A and B. But, unfortunately, there was a convergence issue in the flow computation. The simulation crashed around about 7 years before the planed temperature peak was reached. Figure 2-7 display the temperature distribution at the crash time point. As this figure shows, the temperature at the canister already reached 200 ^{o}C. Figure 2-9 displays that the liquid saturation at point B gradually increased to close to fully saturation, while the liquid saturation at A increased slower, which is different from our previous simulation with TOUGHREACT-FLAC.

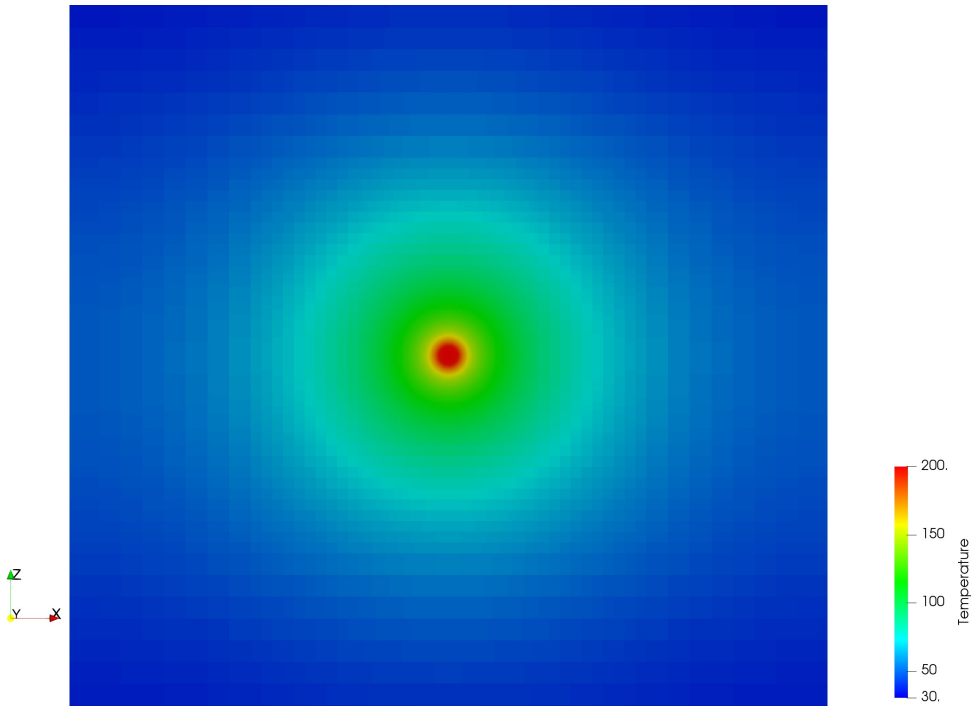

Figure 2-7. Simulation results of temperature at around 7 years.

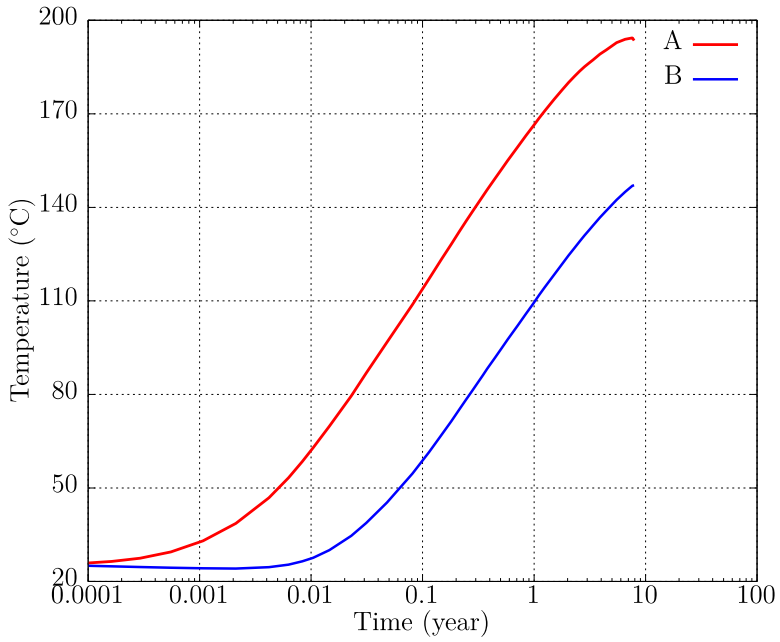

Figure 2-8. Simulation results of temperature, at Points A and B in "high T" scenario.

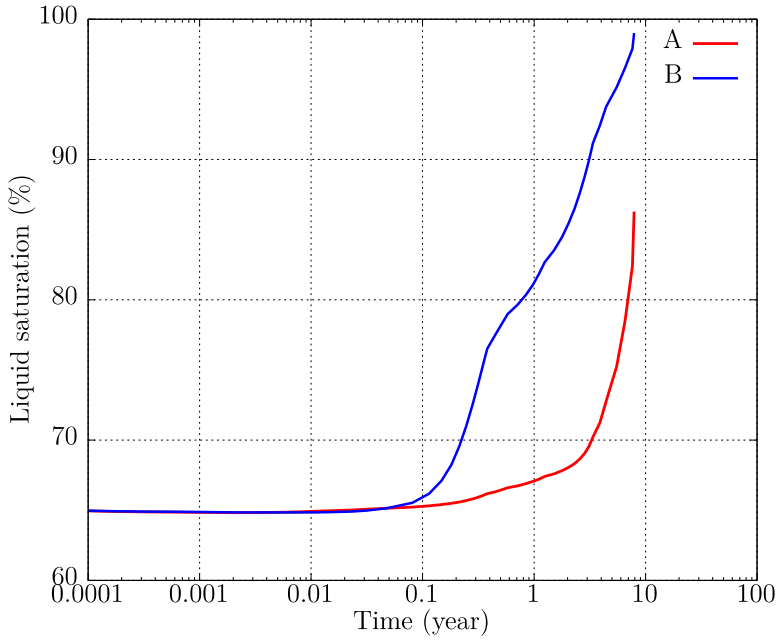

Figure 2-9. Simulation results of liquid saturation, at Points A and B in "high T" scenario.

Based on these results, the simulation ran well until the temperature peak was close, then the computation crashed in the flow part due to the oscillation between two-phase and a single-phase transition in bentonite. The hardiness of this transition is because the flow part uses different primary variables, for example, pore pressure (p) and temperature (T) are the state variables of a single phase, while gas pressure (p_g) and gas saturation (s_g) are the state variables of the two-phase system. Thus, during the two-phase calculation, the A matrix and the b vector in the linear equation system $Ax = b$ are related to p_g and s_g. Then, in the next time step for single phase, A and b are related to p and T. Since it's a nonlinear problem, we used an iterative solver - Conjugate Gradient (CG) solver, instead of the default direct solver. The CG solver is dependent on its preconditioner, which needs to be modified based on the A matrix and organization of sparse matrix in A. Also note that if a larger size of elements is used, the convergence will become better. For example, in the DECOVALEX project, we also considered the unsaturated bentonite buffer in the tunnels, but the elements sizes were about 1 m, so the convergence was not severe. But with a coarse mesh, we are losing detailed information for bentonite at different locations. The deal.II library has considered much about CG solver and its preconditioner, since the code developers did much works on that problem in the past years. We will investigate this issue and try to improve the robustness of the simulator with the help of the deal.II library. More work to improve the simulation is undergoing.

2.4 Summary and Future Work

In the past few years, we have dedicated our efforts to developing a series of coupled THMC models to evaluate the chemical alteration and associated mechanical changes in a generic repository and to consider the interaction between EBS bentonite and the NS clay formation. In FY20, we tested the BExM with a parametric study, improved the simulator TReactMech and modified it with a new coupling strategy. The achievements we have reached are as follow:

- We conducted a parametric study on pre-consolidation pressure in BExM for bentonite buffer under THMC processes. With this study, a distinct elasto-plastic behavior of bentonite was obtained,

revealing that the spatial heterogeneity of the sample may induce uneven performance inside the material.

- We have improved the simulator on Linux platform with the deal.II library, and modified the coupling strategy to a sequential coupling method. A good agreement between numerical simulations and analytical solutions is obtained, but in the THM simulation of high T case, the hydrological calculation failed to converge due to phase changes.

The further improve the coupled THMC model on the Windows platform to obtain a better understanding of the coupled processes contributing to chemical and mechanical alteration in EBS bentonites and NS argillite formations and answers questions regarding the thermal limit of EBS bentonite in clay repository, we are planning:

- To improve the convergence of hydrological part in the simulator with the deal.II library, and recalculate the high T case. Use this new library to conduct parallel computation and modify the chemical reaction part and link with the THM part. To investigate chemical-induced deformation in solid skeleton related to the change of solution compositions and to derive an improved coupling model for compacted clays following the framework of poromechanics.
- To derive reduced order model that can be integrated into the performance assessment model in GDSA. The importance of bentonite alteration and its impact on mechanical behavior needs to be integrated to PA model to assess their relevance to the safety of a repository. Specifically, we will first implement of bentonite swelling models such as linear swelling, state surface, BBM, and BExM into a parallel THMC simulator and then reduced order model will be developed based on the large number of THMC simulations.
- To use a physics-constrained data-driven computational framework to develop a constitutive function with the Long-Short Term Memory (LSTM) method-based strain-stress data search for simulation of clay behavior under thermal and hydration processes.
- To implement more constitutive models into the new simulator for better representation of different geomaterials, and continue working on coupled THMC modeling about different materials with the new simulator.

3. SORPTION & DIFFUSION EXPERIMENTS ON BENTONITE

3.1 Introduction

In order for nuclear energy to be viable, a long-term nuclear waste disposal repository capable of isolating high-level (HLW) and low-level radioactive waste (LLW) over the time scales necessary for the decay of long-lived radioactive isotopes (> 10^6 years) must be created. Most disposal options currently under investigation use clay media (*i.e.*, bentonite or shale) as engineered barriers or as the host rock for geologic storage (Altmann, 2008; Altmann et al., 2012; Delay et al., 2007; Guyonnet et al., 2009; SKB, 2011; Tournassat et al., 2015). Clays are good barriers for HLW due to their low hydraulic conductivity, which restricts contaminant mobility to slow diffusion-based transport, and their high adsorption capacity for radionuclides, which slows transport even further. Montmorillonite ($M^+_{0.33}(Al_{1.67}Mg_{0.33})Si_4O_{10}(OH)_2$) is the dominant clay mineral found in bentonite. It has a 2:1 layer-type phyllosilicate structure, with a large specific surface area (~750 m^2/g) and cation exchange capacity (~1 mol/kg), and strongly-sorbing surface complexation sites on clay edge surfaces.

In compacted clay, solute transport is controlled by diffusion, and adsorption of solutes to the clay can significantly retard transport. Uranium is the primary constituent of spent nuclear fuel, and the long half-lives of ^{238}U and ^{235}U (4.5 x 10^9 and 7.0 x 10^8 years, respectively) and high toxicity of U underscore the importance of understanding the transport of U through engineered barriers. U(VI) K_d (distribution coefficient) values for adsorption onto montmorillonite can vary over 4 orders of magnitude depending on aqueous chemical conditions, such as pH, partial pressure of CO_2, ionic strength, and Ca concentration (Tournassat et al., 2018). A limited number of studies have examined U(VI) diffusion through bentonite (García-Gutiérrez et al., 2003; Idemitsu et al., 1995; Joseph et al., 2017; Joseph et al., 2013; Ramebäck et al., 1998; Torstenfelt and Allard, 1986; Wang et al., 2005) and montmorillonite (Glaus and Van Loon, 2012; Tinnacher et al., 2016b). Most of these experiments have been conducted under conditions where U(VI) K_d values were relatively low (1-50 L/kg), with only a few studies performed at moderate U(VI) K_d values (93-310 L/kg, (Torstenfelt and Allard, 1986; Wang et al., 2005). This is likely due in part to the extremely long-time scales necessary for diffusion of strongly sorbing solutes. Joseph et al., (2017) found that the U(VI) had migrated only about 2 mm into the clay after 6 years of diffusion under relatively low U(VI) sorption conditions (K_d = 2.6-5.8 L/kg). Diffusion experiments with natural bentonite are complicated by changes in porewater chemistry during experiments due to processes such as dissolution of carbonates (*e.g.*, calcite) and cation exchange. This can lead to variable and unknown pH values and Ca and bicarbonate concentrations in the porewater during diffusion experiments, which in turn leads to dynamic changes in U(VI) aqueous speciation and adsorption during the experiments. Without a full understanding of the mechanistic factors underpinning U(VI) diffusion it is difficult to accurately predict the mobility of U(VI) in a waste disposal scenario.

While present at lower total amounts than U, ^{79}Se is a major driver of the safety case for nuclear waste disposal due to its long half-life (3.3 x 10^5 yr) and presence as relatively mobile anionic species under a range of chemical conditions (*e.g.*, HSe^-, SeO_3^{2-}, SeO_4^{2-}). Se redox chemistry is complex, with oxidation states ranging from -II to +VI over environmentally relevant conditions. While Se(-II) and Se(0) are relatively immobile due to the formation of low solubility precipitates, Se(IV) and Se(VI) exist as the oxyanions selenite (SeO_3^{2-}) and selenate (SeO_4^{2-}) and are highly mobile in water due to their high solubility. Se adsorption to clay minerals is quite low compared to other important radionuclides such as U. K_d values for selenite adsorption to smectite are in the range of 1-10 L/kg (Missana et al., 2009; Montavon et al., 2009) compared to values up to 10^4 for U(VI) (Tournassat et al., 2018). Selenite and selenate adsorption to the clay minerals kaolinite and Ca-montmorillonite were studied by Bar-Yosef and Meek (1987) over the pH range 4-8. Both selenite and selenate adsorption decreased with increasing pH, with very low or negligible adsorption above pH 8 and selenate adsorption to kaolinite was lower than selenite adsorption (Bar-Yosef and Meek, 1987). Similar trends of lower selenate vs selenite adsorption and decreasing

adsorption with increasing pH are observed on iron oxides and oxyhydroxides (Balistrieri and Chao, 1987, 1990).

Selenite diffusion through bentonite has been investigated in several studies (García-Gutiérrez et al., 2001; Idemitsu et al., 2016; Wang et al., 2016; Wu et al., 2017). Idemitsu et al. (2016) measured apparent diffusion coefficient (D_a) values of 2.5 x 10^{-11} to 1.9 x 10^{-13} m^2/s over a range of dry bulk densities (0.8-1.6 kg/L), ionic strengths (0.01-1.0 M NaCl), and temperatures (10-55°C) for purified bentonite consisting of 99% montmorillonite. Measured D_a values for bulk bentonite (*i.e.*, with lower smectite content) under similar conditions are 1-2 orders of magnitude higher (Sato et al., 1995; Wu et al., 2014). Under anaerobic conditions, it is possible for Se(IV) to become reduced to Se(0) or Se(-II) (Charlet et al., 2012; Charlet et al., 2007; Ma et al., 2019). Due to the lower adsorption of selenate compared to selenite, selenate diffusion may be even higher than observed for selenite, although we could find no studies on selenate diffusion through bentonite in the literature.

Storage of HLW can result in transient high temperatures near the waste canisters resulting from radioactive decay. The effects of elevated temperature on the engineered barrier must be taken into account when designing a nuclear waste repository. The duration of the transient elevated temperature and temperature profiles in the engineered barrier can vary widely depending on the repository design and site-specific (*e.g.*, host rock) factors, however most HLW repository concepts impose a temperature limit of 100-200°C in the bentonite buffer, with elevated temperatures persisting for on the order of thousands of years (Johnson et al., 2002; Wersin et al., 2007; Zheng et al., 2015). Temperature effects on the bentonite barrier may include changes to the clay's hydrological and mechanical properties, changes to pore water chemical compositions, and changes to the clay and accessory mineral composition (Cuadros and Linares, 1996; Wersin et al., 2007; Zheng et al., 2015). In a previous study, we found that U(VI) adsorption to lab-heated (300°C, 7-weeks) and field-heated (95°C, 18-years) bentonite was lower compared to non-heated bentonite in batch experiments, with K_d values decreasing by approximately 50% and 30%, respectively (Fox et al., 2019). While some of the lower U(VI) adsorption could be explained by changes in aqueous U(VI) speciation, changes to the clay minerals was also considered to be important in the lower U(VI) adsorption.

In this chapter, we focus on the diffusion of ^3H, U, and Se through compacted smectite. In section 3.2, we present the results from ^3H and U diffusion experiments from field-heated (95°C, 18-years) and cold-zone (20°C) FEBEX bentonite under different chemical conditions. In section 3.3, we present plans for studying Se(VI) diffusion through compacted montmorillonite under different background electrolyte compositions. We note that experimental work was interrupted/delayed due to the shelter in place orders associated with COVID-19 pandemic. In section 3.4, we present plans for modeling the diffusion experiments.

3.2 FEBEX Diffusion Experiments

3.2.1 Materials and methods

3.2.1.1 Bentonite samples

Bentonite samples were obtained from the second dismantling of the FEBEX *in situ* heater test in 2015, after 18 years of heating. Detailed information on the heater test can be found elsewhere (Huertas et al., 2000). Briefly, bentonite was compacted into blocks ("bentonite rock") at 1650 kg/m^3 dry density, placed in a radial arrangement around two underground heaters and heated to a maximum of 100°C. The original FEBEX bentonite contained primarily smectite (92%), with minor amounts of quartz (2%), plagioclase (2%), cristobalite (2%), and traces of potassium feldspar, calcite, and trydimite (Fernández et al., 2004). The smectite is made up of a mixed layer illite-montmorillonite with approximately 11% of illite layers (Fernández et al., 2004). Based on results from adsorption experiments, we chose to focus on bentonite samples from two locations; one location in the heater test zone (BD-48) at a radial distance of 50 cm from the center axis and one location from a control non-heated zone (BD-59) at 50 cm. The section layout during

dismantling is described by Detzner and Kober (2015). Three replicate blocks, measuring approximately 10 x 12 x 14 cm, were used from each location. The blocks were split open and approximately 200 g of bentonite was removed from the center of each block and dried in an oven at 60°C for 1 week. The dried bentonite was then crushed by hand using a porcelain mortar and pestle, and sieved through a 0.063 mm sieve in order to remove sand particles and reduce sample heterogeneity. Equivalent weights of each replicate block were mixed together to form composite samples for the three locations. Average water contents were approximately 18% and 25% and historical *in situ* temperatures were approximately 95°C and 20°C for the 50-cm heater-zone and 50-cm cold-zone samples, respectively (Villar et al., 2018a; Villar et al., 2018b).

Composite FEBEX bentonite samples were purified in order to produce a purified clay sample (*i.e.*, without carbonate and other accessory mineral impurities) for U(VI) diffusion experiments. The purification procedure was adapted from Tinnacher et al. (2016a). The procedure included the following major steps: (1) dialysis against sodium acetate at pH 5 for carbonate mineral removal, (2) dialysis against NaCl to remove acetate and complete Na-saturation, (3) dialysis against water to remove excess salts, and (4) centrifugation to remove particles greater than 2 μm. Composite clay samples (20 g) were suspended in 200 mL of 1 M sodium acetate solution buffered at pH 5 with acetic acid, placed into pre-rinsed dialysis tubing (SpectraPor7, 8 kDa), and dialyzed against acetate buffer for 1 week, changing dialysis solution daily. The acetate buffer dialysis solution was then replaced with 1 M NaCl (dialyzed for one week), then with MilliQ water (dialyzed for two weeks), again changing dialysis solution daily. The clay suspensions were then transferred into plastic bottles and diluted and dispersed in MilliQ water to reach a clay concentration of approximately 15 g/L, and centrifuged at 1000 x *g* for 7 minutes. This centrifugation speed and time was deemed sufficient to remove all particles > 2 μm as calculated from Stoke's Law. The replicate < 2 μm clay fractions were then combined into a glass beaker, dried at 45°C and ground in ball mill with tungsten carbide balls.

3.2.1.2 Pre-equilibration of clay

In order to ensure that aqueous porewater chemical concentrations are constant during the diffusion experiments, purified clay samples were pre-equilibrated with the appropriate background electrolyte prior to packing in diffusion cells. 2 g of purified clay was suspended in 20 mL of electrolyte solution and the clay suspension was transferred to pre-rinsed dialysis tubing (SpectrPor7, 8 kDa). Clay samples were dialyzed against 1 L of background electrolyte for 2 weeks, changing dialysis solution at least 3 times and manually adjusting pH daily. After dialysis was complete, the clay suspension was transferred to 40 mL polycarbonate centrifuge tubes and centrifuged at 39,000 x *g* for 20 minutes. The supernatant was removed and the clay was dried at 45°C and ground in ball mill with tungsten carbide balls and stored at room temperature prior to packing the cells. At the time of packing, a subsample of each clay was dried at 150°C to determine the moisture content.

3.2.1.3 Diffusion experiments

Diffusion experiments were conducted with purified, pre-equilibrated FEBEX clay at a dry bulk density (ρ_d) of approximately 1.25 kg/L using the diffusion cell design shown in Figure 3-1. The diffusion cells used for experiments were machined in-house at Lawrence Berkeley National Laboratory and are based on the design of Van Loon et al. (2003), with dimensions adjusted to accommodate smaller samples. Preliminary experiments with stainless steel filters showed evidence of corrosion, therefore PEEK filters with a PCTFE ring were used instead (IDEX # OC-815, overall D=0.95 cm, filter D=0.74 cm, thickness=0.16 cm, pore size=5 μm).

Experiments were performed at room temperature in the presence of 0.1 M NaCl, 0.1 or 2.0 mM Ca, and pH 7.0 in equilibrium with atmospheric CO_2. The pre-equilibrated dry clay samples were carefully weighed into PEEK diffusion cells and compacted using a custom PEEK packing rod. Three phases of the diffusion experiment were conducted: (1) saturation, (2) tritiated water (^3H) diffusion, and (3) U(VI) diffusion. The

clay was saturated by circulating 200 mL of background electrolyte at both ends of the cell at approximately 1 mL/min using a peristaltic pump for 18-35 days. The background electrolyte solution was monitored for pH and dissolved Ca concentrations during saturation. After the saturation period, the ^{3}H through-diffusion phase was started by replacing the background electrolyte solutions with a high ^{3}H reservoir containing background electrolyte spiked with 30 nCi/mL ^{3}H (200 mL) at one end and a low ^{3}H reservoir containing only background electrolyte (20 mL) at the other end. The high concentration reservoir was sampled at the beginning and the end of the ^{3}H diffusion experiment and did not change significantly over that time period. The low ^{3}H reservoir was changed at time intervals of 2-48 hr, and the ^{3}H concentration was measured in the low reservoir samples by liquid scintillation counting. The concentration in the low reservoir never exceeded 2% of the concentration in the high reservoir. The ^{3}H diffusion was continued for 13-15 days. After this period, one end of the diffusion cell was plugged (low ^{3}H side) and the high ^{3}H reservoir at the other end was replaced with 20 mL of electrolyte solution spiked with 1 x 10^{-6} M U(VI), marking the start of the U(VI) in-diffusion experiment. Subsamples of the U(VI) solution reservoir were collected periodically for dissolved U(VI) and other metal measurement by ICP-MS and pH was measured directly in the U(VI) solution reservoir. U(VI) diffusion was continued for 31 days. U(VI) controls consisting of U(VI)-spiked electrolyte solution recirculating through the peristaltic pump (*i.e.*, without the diffusion cell) were performed in parallel. The U(VI) control reservoirs were monitored and sampled in the same manner as the U(VI) diffusion experiment reservoirs in order to check for U(VI) adsorption to tubing and reservoir containers. Note that the U(VI) diffusion experiment was completed for the two samples in the presence of 2 mM Ca; the U(VI) diffusion for the 0.1 mM Ca sample was interrupted.

At the end of the U(VI) diffusion period, the diffusion cells were disassembled and the clay plug was extruded using the PEEK packing rod and sliced into thin slices. The thickness of the clay slices was measured using a digital caliper with a precision of 0.1 mm. The clay slices were placed into 20 mL glass scintillation vials, dried at 150°C for 24 hours, and weighed to determine the exact dry clay weight for each slice. The PEEK filters were removed from each end of the clay plug, suspended in 10 mL of MilliQ water in a glass scintillation vial and shaken vigorously to dislodge any clay that was stuck to the filter. The filter was then transferred to a new vial and 10 mL of 0.15 M nitric acid was added to the filter to dissolve any adsorbed U(VI). The clay slices were extracted with 10 mL of 0.15 M ultrex grade nitric acid for 24-hours, then centrifuged at 39,000 x *g* for 20 min and filtered through a 0.45 μm PVDF syringe filter. Metal concentrations were measured in the nitric acid extracts by ICPMS. The small amount of clay which was removed from the filters with MilliQ water was dried at 150°C, weighed, and extracted in the same manner as the clay slices. Both the dry bulk density (ρ_d) and U concentrations in the clay plug are expressed in terms of the 150°C oven dry weight of clay. At room temperature, the clays had a water content of approximately 11%.

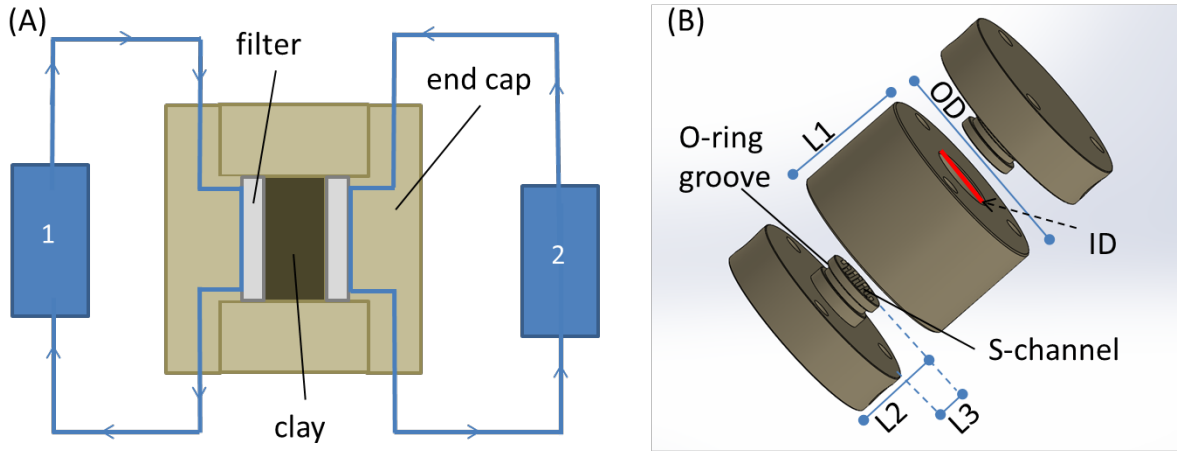

Figure 3-1. Schematic of diffusion cells machined in house. (A) Cross-sectional view of the diffusion cell showing the clay plug, filters and two solution reservoirs. During saturation and ^{3}H diffusion, both reservoirs are used, and during U(VI) in-diffusion, reservoir 2 is removed and the cell is plugged at that end. (B) Detailed schematic of the cell design, with groves for the o-rings and an S-shaped channel which allows the solution to distribute evenly over the entire filter of the diffusion cell. The dimensions for the cell are as follows: OD=30 mm, ID=9.5 mm, L1=17.8 mm, L2=12.2 mm, L3=4.9 mm. O-rings measure 7.5 mm ID and 9.5 mm OD.

3.2.1.4 Analytical techniques

Samples were analyzed for metal concentrations (U, Ca, Mg, Al, Si, and Fe) by ICP-MS (Perkin-Elmer Elan DRC II) after acidification and dilution with ultrapure (ultrex grade) 0.15 M nitric acid and internal standard addition. Samples were analyzed for ^{3}H using liquid scintillation counting (Perkin-Elmer Liquid Scintillation Analyzer Tri-Carb 2900TR) by mixing 4 mL of sample with 18 mL of Ultima Gold XR liquid scintillation cocktail.

3.2.2 Results and Discussion

3.2.2.1 Tritium (^{3}H) diffusion

Normalized mass flux (J_N, in m/day) reaching the low concentration reservoir was calculated using Equation 3-1:

$$J_N = \frac{C_{low} V_{low}}{C_{high} A \cdot \Delta t} \quad (3\text{-}1)$$

Where C_{low} is the concentration in the low concentration reservoir, C_{high} is the concentration in the high concentration reservoir, V_{low} is the volume of the low concentration reservoir (approximately 20 mL), A is the cross-sectional area of the diffusion cell (0.709 cm^2), and Δt is the time interval since the previous sampling event.

The normalized flux of ^{3}H is shown in Figure 3-2 for the purified FEBEX samples from the heated and cold-zones. Diffusive flux increased over the first 48 hr, reaching steady state thereafter for both samples. Note that the first sampling point for the heated-zone sample shows a higher apparent flux than subsequent points. This is due to the fact that the tubing for the low-concentration reservoir was mistakenly dipped in the high-concentration reservoir prior to starting the flow. The contaminated tubing was rinsed with MilliQ

water, however a small amount residual ^{3}H contamination remained. The average normalized flux at steady state (≥50-hr) ranged from 1.38 ± 0.13 x 10^{-3} m/day (cold-zone, 2 mM Ca) to 1.73 ± 0.17 x 10^{-3} m/day (heated-zone sample, 0.1 mM Ca) as shown in Table 3-1. Small differences in the normalized measured ^{3}H flux may result from small differences in cell packing, which can in turn affect porosity or pore structure (*i.e.*, pore constrictivity or tortuosity). However, it should be noted that the observed normalized fluxes are not significantly different from one another. Total porosity (ε) depends on bulk density, and can be calculated using Equation 3-2:

$$\varepsilon = 1 - \frac{\rho_d}{\rho_g} \tag{3-2}$$

where ρ_g is the crystal density of clay mineral layers (*i.e.*, grain density). For montmorillonite, ρ_g is approximately 2.84 kg/L (Bourg et al., 2006; Tournassat and Appelo, 2011). There is no measurable difference in the calculated bulk density or total porosity of the two samples (Table 3-1).

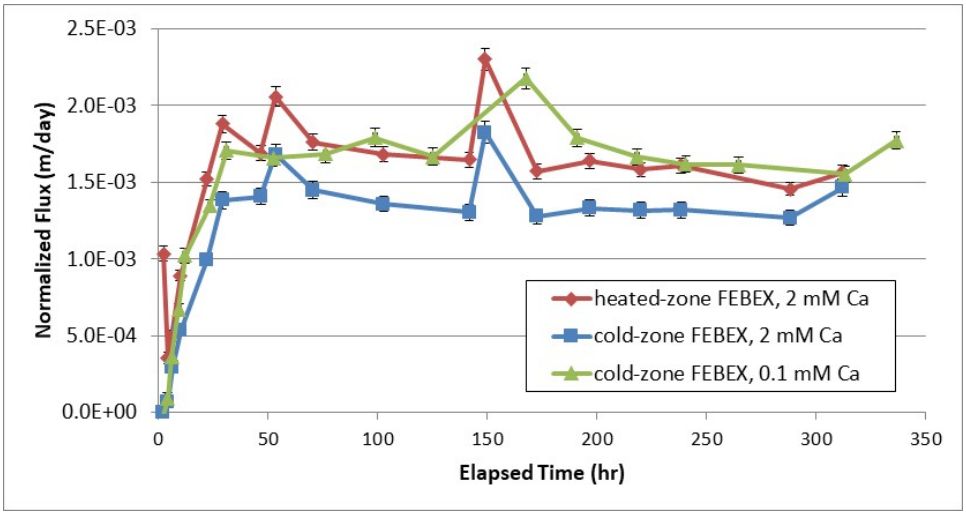

Figure 3-2. Tritium diffusion through heated-zone and cold-zone purified FEBEX bentonite at pH 7 in the presence of 2 mM or 0.1 mM Ca and 0.1 M NaCl. Diffusion is expressed as normalized mass flux as a function of time. Error bars represent the analytical error (standard deviation).

Table 3-1. Summary of diffusion cell properties.

Sample	ρ_d, kg/L	ε	Ca, mM	^{3}H Avg J_N, m/day[(a)]	U(VI) K_d, L/kg[(b)]
FEBEX, 95°C heated-zone	1.25	0.56	2.0	1.66 ± 0.16 x 10^{-3}	9,333
FEBEX, 20°C cold-zone	1.24	0.56	2.0	1.38 ± 0.13 x 10^{-3}	16,982
FEBEX, 20°C cold-zone	1.25	0.56	0.1	1.73 ± 0.17 x 10^{-3}	19,055

(a) The average normalized mass flux for ^{3}H during steady state (≥50 hr).

(b) U(VI) K_d values determined from batch adsorption experiments (Fox et al., 2019).

3.2.2.2 U(VI) diffusion

Dissolved U(VI) concentrations in the U(VI) reservoirs during the U(VI) diffusion experiments are shown in Figure 3-3. Dissolved U(VI) concentrations decreased over time for both samples and the control experiment. The decrease in U(VI) concentration in the control reservoir indicates that U(VI) adsorption onto tubing and container walls likely occurred. However, U(VI) concentrations in the sample reservoirs were lower than in the control reservoir, therefore the difference between the control and sample reservoirs represents the diffusive loss of U(VI). Tests with different types of tubing will be performed in order to minimize U(VI) adsorptive loss in future experiments. The two clay samples tested exhibited nearly identical U(VI) loss under these conditions. Interpretation of the U(VI) diffusion data is confounded by the small differences observed in ^{3}H diffusion and modeling will be required to separate the effects of pore structural differences (if significant) and U(VI) adsorption on the U(VI) diffusion. Figures 3-4 and 3-5 show the Ca concentrations and pH observed in the U(VI) reservoir solution during the experiment. Changes in Ca concentration were very small, while pH values varied within 0.2 pH units (6.8-7.2) over the course of the experiment.

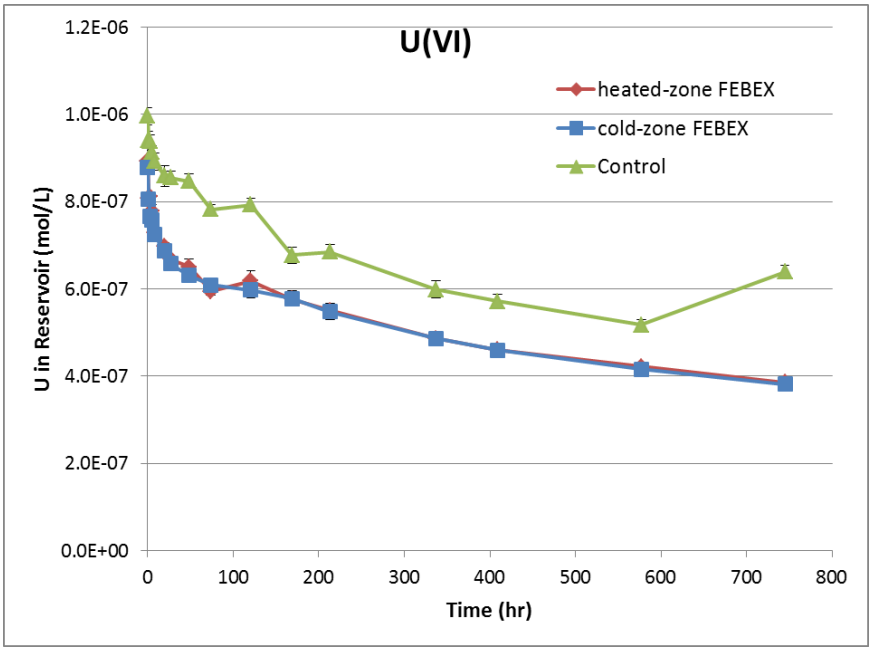

Figure 3-3. Dissolved U(VI) in reservoir during U(VI) diffusion experiments with purified heated-zone and cold-zone FEBEX clay. Concentrations are also shown for a control reservoir containing U(VI)-spiked background electrolyte that was recirculated through the peristaltic pump. Error bars represent analytical error.

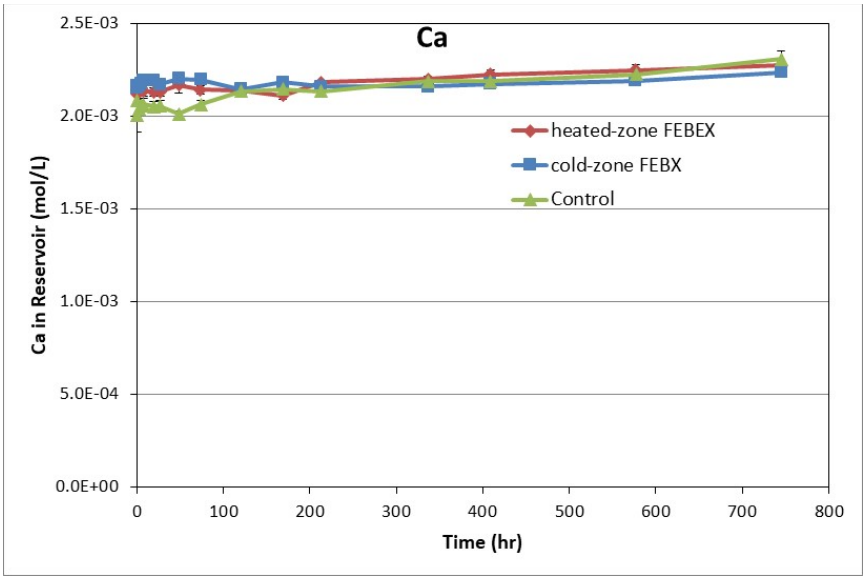

Figure 3-4. Dissolved Ca in reservoir during U(VI) diffusion experiments with purified heated-zone and cold-zone FEBEX clay. Concentrations are also shown for a control reservoir containing U(VI)-spiked background electrolyte that was recirculated through the peristaltic pump. Error bars represent analytical error.

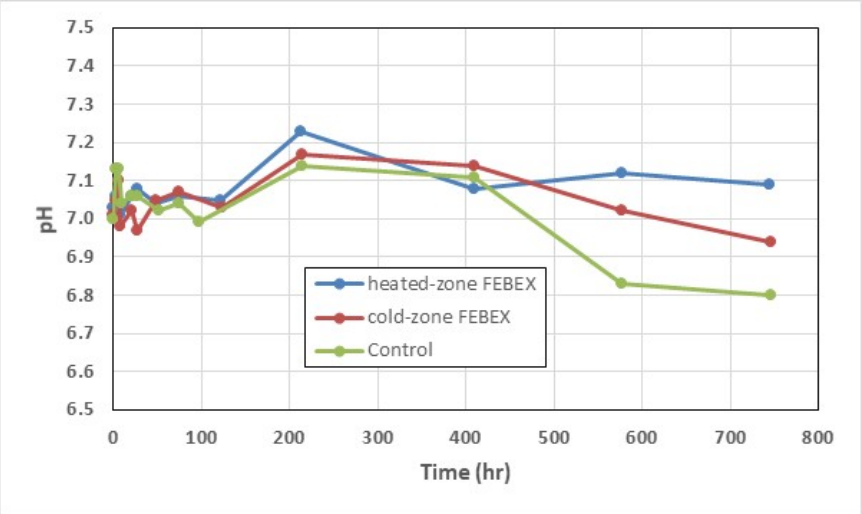

Figure 3-5. Measured pH in reservoir during U(VI) diffusion experiments with purified heated-zone and cold-zone FEBEX clay. pH values are also shown for a control reservoir containing U(VI)-spiked background electrolyte that was recirculated through the peristaltic pump.

3.2.2.3 Clay slicing

In order to determine the U(VI) diffusion profile in the clay, the clay plugs were sliced at the end of each experiment and total U and other metal concentrations were measured in the clay. The results for U and Ca are shown in Figure 3-6. Background metal concentrations extracted from the FEBEX clays which had been pre-equilibrated with 0.1 M NaCl and 2 mM Ca at pH 7.0 are shown in Table 3-2. U accumulated only in the first two slices of clay (<1 mm). No evidence for changes in concentrations of other elements from

background concentrations was observed. The net U recovered on the clay (after subtracting out the background U) was 2.6 ± 0.04 x 10^{-9} mol U and 2.3 ± 0.03 x 10^{-9} mol U for the heated and cold-zone samples, respectively. This agreed well with the 2.7 ± 0.3 x 10^{-9} mol net U lost from the reservoir for both samples (corrected for U lost to sorption to tubing and reservoir walls using concentrations in the control reservoir).

Table 3-2. Background metal concentrations in purified FEBEX clay which was pre-equilibrated with 0.1 M NaCl, 2 mM Ca, at pH 7.0 measured by nitric acid extraction.

Metal	Extracted Concentration (mol/g)	
	Heated-zone	Cold-zone
Mg	8.81± 0.38 x10^{-06}	7.65 ± 0.44 x10^{-06}
Al	1.48 ± 0.04 x10^{-04}	1.23 ± 0.04 x10^{-04}
K	1.84 ± 0.03 x10^{-05}	2.24 ± 0.04 x10^{-05}
Si	6.75 ± 0.28 x10^{-04}	6.70 ± 0.06 x10^{-04}
Mn	5.43 ± 0.10 x10^{-07}	5.08 ± 0.15 x10^{-07}
Ca	2.21 ± 0.03 x10^{-04}	2.25 ± 0.02 x10^{-04}
Fe	1.43 ± 0.02 x10^{-05}	1.19 ± 0.02 x10^{-05}
U	1.14 ± 0.03 x10^{-09}	9.25 ± 0.22 x10^{-10}
Sr	4.55 ± 0.13 x10^{-08}	4.73 ± 0.13 x10^{-08}

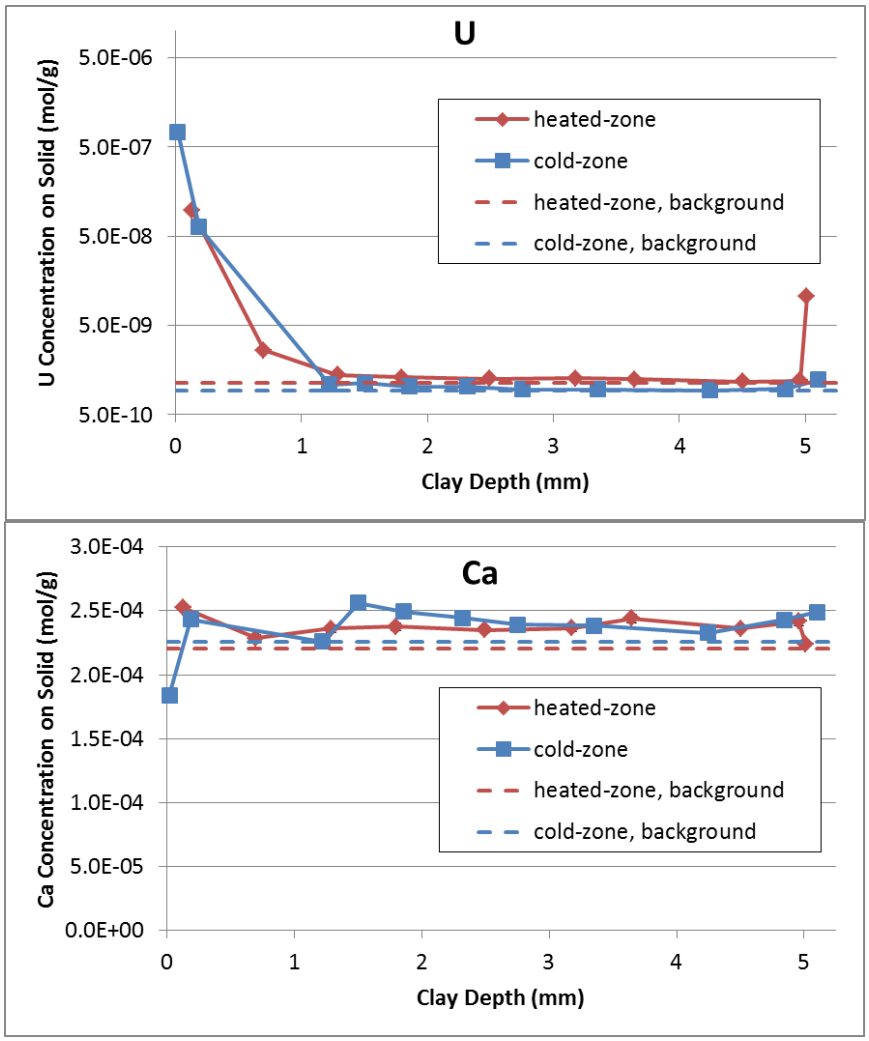

Figure 3-6. Top: U diffusion profile in clay at the end of the experiment for FBEEX clay equilibrated with 2 mM Ca. U is expressed as the total U concentration (note log scale of y-axis). The U(VI) inlet end of the cell is at a clay depth of 0.0 mm and the outlet end (plugged) is at 5.0 mm. Bottom: Ca profiles in the clay, expressed as total Ca concentration. Concentrations of U and Ca in the original pre-equilibrated clay are shown for reference. The data points are shown at the end of the clay depth, *i.e.*, the data point at 0.13 mm represents the clay slice from 0-0.13 mm, then point at 0.70 mm represents the clay slice from 0.13-0.70 mm, and so on.

3.3 Summary and Future Work

In FY20, diffusion experiments were conducted with 95°C heated and 20°C cold-zone purified FEBEX bentonite at a bulk density of 1.25 kg/L. The experiments were conducted at a constant ionic strength (0.1 M NaCl) at pH 7 in the presence of 0.1 mM Ca or 2 mM Ca. The average normalized ^{3}H flux at steady state (≥50-hr) for ^{3}H through-diffusion was not significantly different across samples, with values ranging from $1.38 \pm 0.13 \times 10^{-3}$ m/day to $1.73 \pm 0.17 \times 10^{-3}$ m/day. U(VI) in-diffusion experiments conducted in the presence of 2 mM Ca showed the diffusive loss of U(VI) from the high concentration reservoir was indistinguishable for the heated and cold-zone bentonite and U(VI) traveled less than 1 mm into the clay over the 30-day diffusion period. While lower U(VI) adsorption was previously measured on the heated-

zone FEBEX bentonite compared to the cold-zone bentonite, it is possible that differences in U(VI) diffusion due to differences in adsorption may only become apparent over much longer time periods than can be realistically tested in the laboratory. Reactive transport modeling of these results using CrunchClay is currently underway and will provide further insight into the geochemical conditions and time periods in which differences in U(VI) diffusion as a result of heating may be observed.

Future work will focus on the diffusion and redox transformations of Se through compacted montmorillonite. Experiments will be conducted under a single ionic strength (0.1 M) and three different electrolyte compositions: 0.1 M NaCl, 0.033 M $CaCl_2$, and 0.085 M NaCl + 0.005 M $CaCl_2$, representing pure Na, pure Ca, and a Na-Ca mixture, respectively. We hypothesize that Se(VI) diffusion will be different under these different electrolyte compositions due to both differences in aqueous Se speciation and differences in the clay swelling in the presence of Na and Ca. These experiments will also be modeled using CrunchClay.

A detailed understanding of selenium diffusion through and transformation within bentonite is critical for the successful design and implementation of engineered barrier systems due to the long half-life (3.3×10^5 yr) and high mobility of ^{79}Se. Se redox chemistry is complex, with oxidation states ranging from -II to +VI over environmental conditions relevant for deep geologic disposal, and each species has different mobility due to differences in adsorption, solubility, and charge. Over the next year, we plan to begin a detailed investigation of Se diffusion and reactivity in bentonite in order to better our understanding of its behavior in engineered barriers. This work will be done in close coordination with a modeling effort described in section 3.4. Our primary goal is to evaluate Se(VI) diffusion through compacted montmorillonite over a range of electrolyte compositions although future work will expand into important Se redox transformations driven by reactions with reduced constituents present in the EBS.

Se(VI) diffusion experiments will be conducted using a well-characterized, purified montmorillonite source clay (SWy-2). Through-diffusion experiments will be conducted using the same diffusion cells described in section 3.2.1.3 at a dry bulk density of 1.25 kg/L. Experiments will be conducted under a single ionic strength (0.1 M) and three different electrolyte compositions: 0.1 M NaCl, 0.033 M $CaCl_2$, and 0.085 M NaCl + 0.005 M $CaCl_2$, representing pure Na, pure Ca, and a Na-Ca mixture, respectively. We hypothesize that Se(VI) diffusion will be different under these different electrolyte compositions due to both differences in aqueous Se speciation and differences in the clay swelling in the presence of Na and Ca. Se(VI) aqueous speciation over the pH range of 5-8 is shown in Figure 3-7, where three major Se(VI) species with different charge dominate: SeO_4^{2-}, $HSeO_4^-$, and $CaSeO_4^0{}_{(aq)}$.

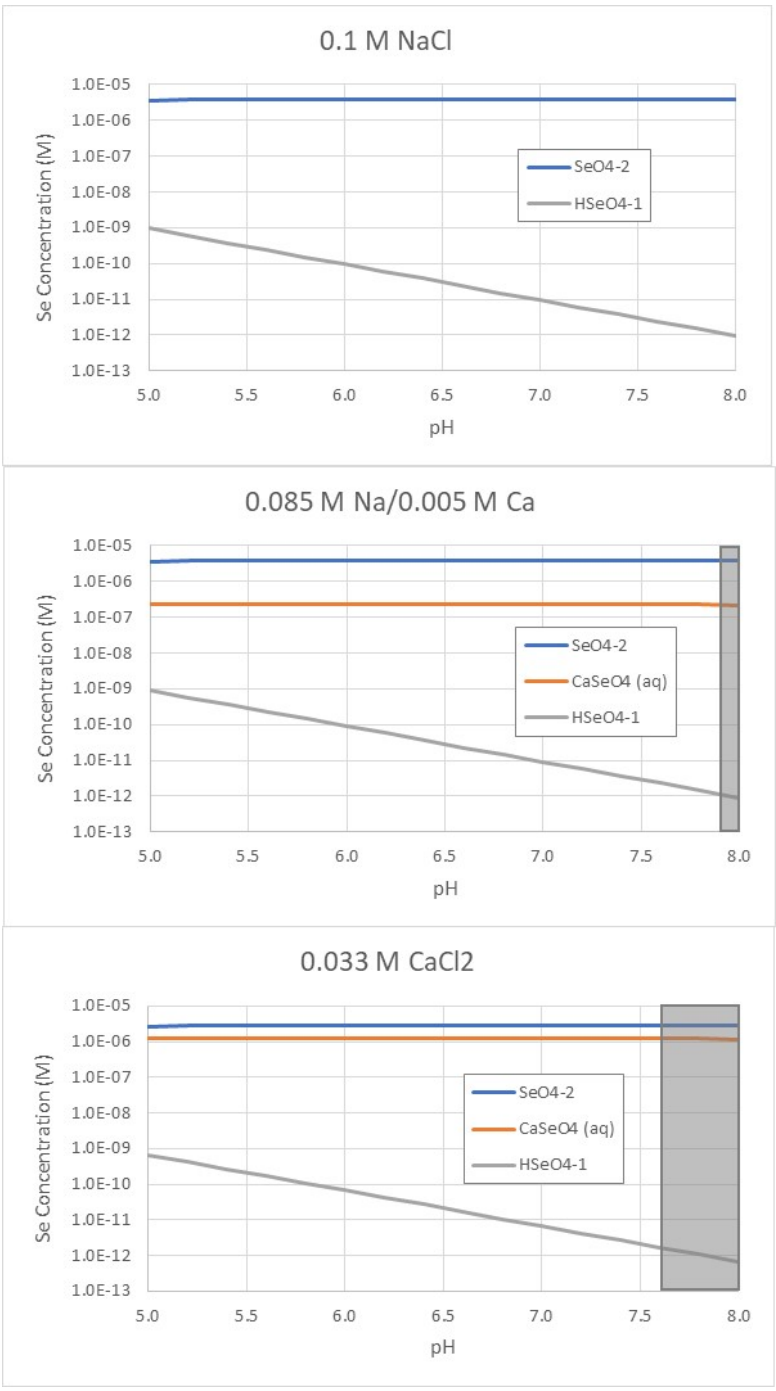

Figure 3-7. Aqueous speciation of Se(VI) as a function of pH in equilibrium with atmospheric CO_2 (380 ppm) for three different electrolyte compositions. Total Se(VI) concentration is 4 μM. The area shaded in grey represents conditions which are oversaturated with respect to calcite.

Modeling of diffusion experiments will be carried out using CrunchClay (Steefel et al., 2015; Tournassat and Steefel, 2019a) taking full advantage of the capabilities of this reactive transport code developed at LBL. CrunchClay is currently one of only two codes that can handle diffusion processes in the diffuse layer, in which the solution is not electroneutral, and for which coupled interdiffusion processes must be taken

into account to model diffusion properties with a mechanistic approach (Tournassat and Steefel, 2019b). CrunchClay has the ability to treat both electrical double layer and bulk porosity with differing anion and cation diffusivities, which makes it possible to simulate the diffusion of a range of tracers with different charges in a single run, and with the same input parameters. CrunchClay also has surface complexation and cation exchange modeling capabilities, thus making it possible to couple mechanistic adsorption models with diffusion models in clay media. Our goal is to derive consistent diffusion and adsorption parameters for Se, ^{3}H and other trace elements as a function of ionic strength and electrolyte composition, which will be probed experimentally in this project.

4. CHEMICAL CONTROLS ON MONTMORILLONITE STRUCTURE AND SWELLING PRESSURE

4.1 Introduction

Despite many decades of study, quantitatively predictive models for diffusion-driven mass transport through clay rich geomaterials remain elusive. Predicting mass transport through clays is difficult, because the material is largely nanoporous, and interactions between charged clay layers and nanopore fluid give rise to structural and dynamical fluid properties that cannot be quantified with existing continuum models. Our research focuses on montmorillonite (MMT), which is the dominant smectite clay mineral that makes up bentonite, which is expected to be widely used as a barrier material. Under confinement and under certain aqueous solution conditions, montmorillonite clays adopt crystalline swelling states, with defined water contents (Norrish, 1954; Smith et al., 2006; Rotenberg et al., 2009; Holmboe and Bourg, 2013). Multiple swelling states typically coexist at equilibrium (Bérend et al., 1995; Homboe et al., 2012), but there are no models available that can predict the distribution of swelling states as a function of solution composition, particularly in mixed electrolyte solutions. Moreover, perturbations to stress state or fluid chemistry will result in shifts to the equilibrium swelling state, leading to what is known as chemical-mechanical coupling. The central aim of this research is to develop an equilibrium model to predict clay swelling states in mixed-electrolyte solutions under varying stress states.

A molecular-level understanding of the interlayer and inter-tactoid forces causing swelling/collapse, influenced by the chemical composition and mobility of water and ions in the interlayers and pores, can provide valuable upscaling strategies to inform macroscopic models. Numerous physical and chemical variables have been shown to have a major influence on clay swelling – clay layer charge, water activity, electrolyte ion composition, and confining pressure being the dominant controlling variables (Sun et al., 2015; Teich-McGoldrick et al., 2015). Other factors, such as the crystalline alignment of individual clay layers, have been shown to depend on ion composition and are, therefore, likely to influence swelling (Whittaker et al., 2019). Traditional models implementing the DLVO and the Modified Guoy-Chapman (MGC) theory can reasonably predict osmotic swelling (in the case of symmetric monovalent, low ionic-strength electrolyte) provided molecular-level information (e.g. distance of closest approach) is available; however, these continuum model predictions break down for hydrates with basal spacing ~ *10-12 Å* (1-2 water layers) where water molecules need to be treated as discrete.

In this report, we present the progress on an integrated set of experiments, molecular simulations, and thermodynamic modeling to develop a predictive understanding of ion exchange-driven swelling and collapse of montmorillonite clay. In our previous reports (Zheng et al., 2019a,b), we focused on developing modeling and simulation approaches to understanding clay thermodynamics. Accomplishments from the prior funding period include development of molecular simulations approaches (Subramanian et al., 2020) that inform a new thermodynamic model for ion exchange driven clay swelling and collapse (outlined in Whittaker et al., 2019). Our FY 2020 efforts focus on transferring this knowledge to compacted clay systems accounting for non-zero effective normal stress. We report on the development of an X-Ray transparent micro-oedometer system for the measurement of montmorillonite swelling pressure as a function of dry bulk density and aqueous solution composition. Initial work focuses on pure homoionic NaCl and KCl solutions as well as NaCl+KCl mixtures. Preliminary data are presented from *in situ* X-Ray scattering experiments conducted at the Advanced Photon Source, Argonne National Laboratory. To develop a theoretical understanding of microstructural evolution, we applied our newly published structural model for cis-vacant smectite clay (Subramanian et al., 2020) to simulate the free energy of mixing crystalline layer states and find that highly unfavorable mixing energetics can drive phase separation in mixed layer state systems. Ongoing simulations of swelling free energy are being conducted using a potential of mean force (PMF) calculation method. Finally, these results are integrated into a

thermodynamic model, previously developed (Zheng et al., 2019a,b; Whittaker et al., 2019), to predict swelling pressure as a function of pore fluid composition in compacted bentonite.

4.2 Experimental Studies of Swelling Pressure and Microstructure in Compacted Montmorillonite

In early FY 2020, we set up a new X-Ray transparent micro oedometer system (Figure 4.1). This system is designed to measure the evolution of swelling pressure as a function of time during equilibration of a clay sample of fixed bulk density with an aqueous solution or with pure water. The swelling pressure is a key property of bentonite barriers for EBS. Swelling of the clay minerals causes closing of part of the pore space or preferential flow pathways (formed, for example, due to shrinkage), reducing permeability of the clay barrier. Macroscopic swelling pressure is a measure of the excess pressure required to obtain a defined water content and is equivalent to disjoining pressure for an infinite clay tactoid. Pressure in excess of the hydrostatic stress arises in clay interlayers from the sum of several forces, including electrostatic interactions, van der Waals dispersion forces, and especially the clay interlayer cation hydration energy. The latter quantity arises due to the relatively strong interaction between clay interlayer cations with their waters of hydration (cf. Norrish, 1954; Teppen & Miller, 2005). Together these forces promote water uptake and volumetric increase in clays at fixed pressure, and conversely pressure increase in clays with volumetric constraints.

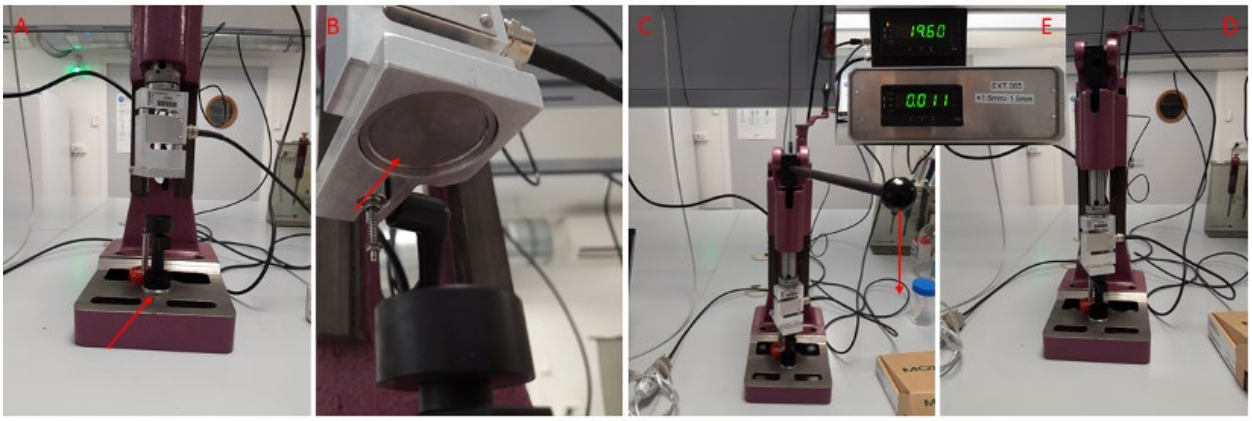

Figure 4.4. Photographs of the custom micro-oedometer showing (a) the position of the black PEEK cell on the holder, (b) the top contact with the force sensor, (c) the whole cell and holder illustrating the emplacement of the force sensor on the cell, (d) the cell configured for a measurement, and (e) the force (top) and displacement (bottom) sensors logging data.

Measurements of swelling pressures are typically made to obtain a swelling pressure curve, which gives swelling pressure as a function of clay dry bulk density for a given aqueous solution composition (Pusch, 1982; Liu et al., 2013). These measurements can be obtained using an oedometer, which measures the force on a stiff spring applied by a swelling material confined to a fixed volume. Briefly, clay is packed into a small cylinder bounded on either side by permeable filters and frits. The clay is confined by a displaceable piston. Miniscule displacements on the piston generate a force measurement, which is subsequently converted to pressure based on the geometry of the cell.

In this section, we detail the Oedometer configuration and provide some preliminary swelling pressure data for our study clay, Wyoming Montmorillonite SWy-3 obtained from the Source Clay Minerals Repository.

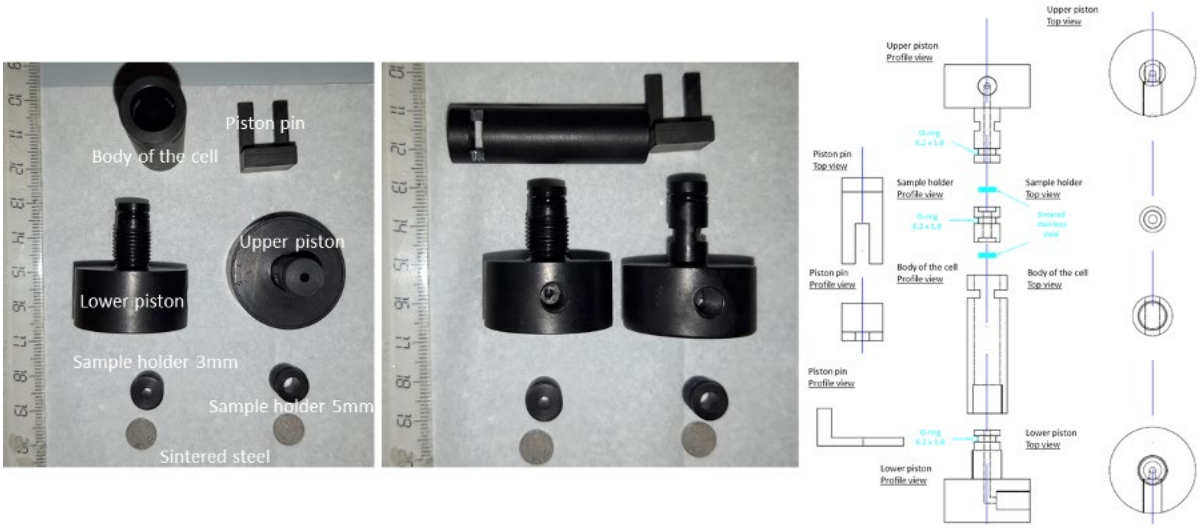

Figure 4.5. Close-up photographs of a micro-oedometer cell displaying the components and highlighting the fluid ports for equilibration of the clay with aqueous solutions. Assembly of the cell yields an internal cylindrical volume into which the clay is packed to obtain the desired dry bulk density.

4.2.1 Micro-Oedometer Cell Design

Custom micro-oedometer cells were developed for simultaneous measurement of basal spacings and overall microstructure by small-, mid-, and wide-angle X-Ray scattering performed on beamline 5-ID at the APS (described in the following section). These oedometer cells were designed to allow for aqueous solution to flow across the top and bottom of the clay sample, facilitating water and ion exchange. The micro-oedometer cells shown in Figure 4.2 consist of three primary components: upper and lower pistons and the cylindrical cell body. A pin is machined to align with a notch in the cell body to constrain the volume of the cell when it is removed from the oedometer, allowing for intermittent measurements. The top and bottom cell pistons were machined to allow for internal flow in a T-configuration, with influent and effluent ports in both pistons. This allows for flow of aqueous solution across the permeable steel frit that holds the clay in place, removing stagnant fluid and facilitating equilibration of the clay with the aqueous solution. Six identical cells were machined on-site at LBNL in January 2020, so many experiments can now be setup and equilibrated simultaneously.

For each cell, three internal geometries are possible. All three geometries have approximately identical internal heights (9 mm) but inserts provide variable diameter configurations (3 mm, 5 mm, and 9 mm; Figure 4.2). All cells are constructed with relatively X-Ray transparent PEEK material (TECAPEEK CF30, Ensinger Plastics), which is more transparent to X-Rays than hydrated clay. The different diameters were made to optimize for different critical measurements: The 3 mm cell is best suited to in-situ X-Ray scattering measurements, while the largest 9 mm cell gives the most sensitive measurement of swelling pressure. Thus, every set of swelling experiments conducted in the 3 mm cell at the APS will be reproduced in the 9 mm cell on the benchtop at LBNL.

4.2.2 Oedometer Swelling Pressure Measurements

Our collaborators at the French Geologic Survey (BRGM) were contracted to construct a custom oedoemeter apparatus of sufficiently small size to transport and install on the X-Ray synchrotron beamline at the Advanced Photon Source. The oedometer (Figure 4.1) measures force and displacement on the oedometer cell piston with two digital displays tied into a datalogging Excel macro for continuous time-

resolved swelling pressure measurements. The minimum force on the piston measurable by the apparatus is 10-20 N, which equates to a minimum accessible swelling pressure measurement of 160 kPa in the 9 mm cell and 1400 kPa on the 3 mm cell. These sensitivity values equate to a minimum bulk density of ~1200 kg/m^3 for the 3 mm cell and ~800 kg/m^3 for the 9 mm cell for swelling pressure measurement of Na-MMT in contact with pure water. These calculations illustrate the tradeoff between X-ray sensitivity and the ability to obtain swelling pressure measurements.

To prepare a sample, the bottom piston is fitted to the body of the cell, and a steel frit and filter paper are inserted into the cell to contain the clay. If smaller internal diameter cell configurations are desired, the appropriate insert is added at this time. Dried clay is precisely weighed to obtain the appropriate bulk density and then carefully packed into the cell. During packing we attempted to ensure an even density of clay throughout the column, although the manual nature of the packing means some variability will occur. A second filter paper and steel frit were placed on top of the clay, and then the top piston was inserted. Once the cell was assembled, the pin was put in place, and the cell was placed in the oedometer. The clay pack was then evacuated, and fluid of a known composition was introduced to the bottom (and optionally top) pistons. Fluid was allowed to flow continuously to ensure constant composition boundary conditions in the cell. Once flow was established, the pin was removed, and pressure logging began.

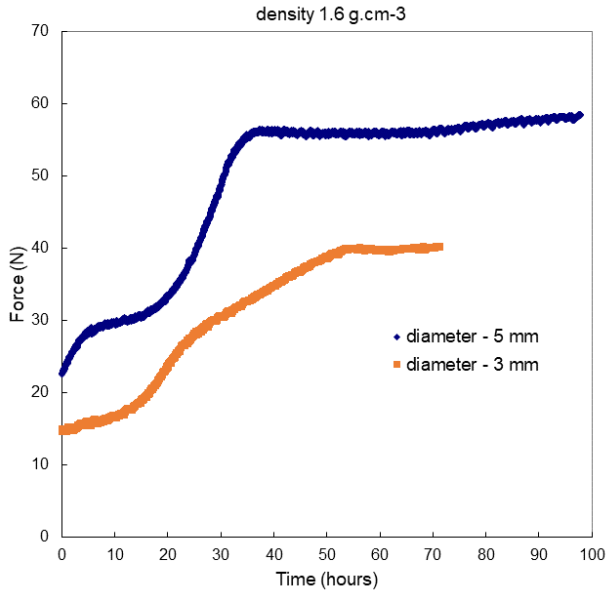

Figure 4.6. Force curves for montmorillonite swelling experiments in contact with pure water in the micro-oedometer (BRGM, *pers. comm.*).

4.2.3 Preliminary Swelling Pressure Results

Time resolved measurements of swelling pressure in montmorillonite clay displays interesting and unexpected behavior (Figure 4.3). Starting with an initially dry clay packed in the oedometer, early wetting by pure water led to a rapid increase in force. The force rise subsided at intermediate times, followed by a second pressurizing event. Final equilibration was achieved after ~30 and ~55 hours on the 5 mm and 3 mm cells, respectively. Final swelling pressures for these two experiments equal to 3.0 MPa for the 5 mm cell and 5.6 MPa for the 3 mm cell. The time required to obtain an equilibrium swelling pressure was variable and dependent on the initial dry bulk density and the cell geometry. Variation in equilibration times were also observed for identically packed clays, indicating a dependence on the heterogeneity and density

of the clay pack: clays packed more densely and with more force were slower to achieve the equilibrium swelling pressure.

One successful measurement of a swelling curve was obtained at LBNL prior to the lab-wide shut down in March 2020. This measurement was made on raw, untreated SWy-3 equilibrated with the pure MiliQ water packed to a dry bulk density of approximately 1.9 g/cm^3 in the 3 mm sample holder. The final force of 32.4 N corresponds to a swelling pressure of 4.6 MPa, which places the clay on a relatively low-pressure swelling curve compared to comparable Na-montmorillonite clays (Liu et al., 2013).

4.2.4 Planned Oedometer Measurements for Remainder of FY 2020

When on-site work is permitted to resume at LBNL, we have planned a systematic series of swelling experiments to prepare for anticipated beamtime at the APS. Briefly, we will generate a swelling curve by measuring equilibrium swelling pressure as a function of dry bulk density for the Na-treated SWy-3 montmorillonite clay in contact with pure MiliQ water in both the 3 mm and 9 mm sample holders. We will generate swelling pressure data for equilibration of the clay with aqueous solutions at a total 1 M concentration [KCl] + [NaCl] with variable K/Na ratios to generate swelling pressure data concurrent with the X-Ray scattering experiments reported in Whittaker et al. (2019). Finally, in FY20 we plan to perform a series of mixed-electrolyte swelling pressure measurements for NaCl + $CaCl_2$ mixtures more closely resembling fluids in contact with EBS bentonite barriers.

4.3 *In-situ* Microstructure by X-Ray Scattering at the Advanced Photon Source, Argonne, IL

The microstructure of clay, in particular the distribution of pore sizes and basal spacings, dictates the macroscopic transport properties of clay materials. We applied X-ray scattering to investigate the crystalline hydrate layer state distribution as a function of aqueous solution chemistry, using the micro-oedometer cell described in the previous section. X-ray scattering was performed at beamline 5ID-D of the Advanced Photon Source at Argonne National Laboratory. Simultaneous small-, medium-, and wide-angle X-ray scattering (SAXS/MAXS/WAXS) was collected on three Rayonix charge-coupled device detectors with sample-detector distances of 8505.0, 1012.1, and 199.5 mm, respectively. The wavelength of radiation was set to 1.2398 Å (10 keV), resulting in a continuous range of scattering vector, q = 0.0017–4.2 Å^{-1}, corresponding to real space distances between 370-1.5 nm.

Reflections from (020) and (110) planes of Mt layers in the WAXS region (q = 1–4.5 Å^{-1}) confirmed the presence of MMT and was used as an internal calibration standard. Constant (020) + (110) peak intensities throughout the experiment confirm that the volume and average orientation distribution of the layers did not change during the course of the experiment.

In the SAXS region (q < 0.1 Å^{-1}) a Porod slope of ~3 was the dominant feature. Fitting in the SAXS region was performed using a modified Guinier-Porod model (Moore et al., 1997) for thin platelets where the scattering intensity I at scattering vector q = $4\pi sin(\theta)/\lambda$), takes the form

$$I(q << 1) = Ae^{-\frac{R_g^2}{3}q^{-p}} \qquad (4.1)$$

where A is a pre-exponential intensity factor for the particle radius of gyration R_g and P is the Porod slope. The radius of gyration, R_g, defined as R_g^2=3/2R^2, was fixed at 560 Å based on the average particle radius calculated from AFM measurements of the particle size distribution. A Porod slope of P = -2.85 for Na-

MMT and -2.93 for K-MMT low q is characteristic of lamellar structures separated by interlayer water, with K-MMT slightly denser, as expected for a smaller basal spacing.

The MAXS region ($1.5 > q > 0.1$ Å^{-1}) was characterized by the presence of a strong diffraction peak at q_{001} = 0.331 Å^{-1} (19.0 Å) for Na-MMT and q_{001} = 0.398 Å^{-1} (15.9 Å) for K-MMT, characteristic of 3- or 2-water layer crystalline hydrates, respectively. Non-negligible peak asymmetry to the low-q side of the basal spacing peak has been frequently observed (Segad et al., 2012; Tester et al., 2016), but has been attributed primarily to Scherrer-type broadening. We use a recently described empirical peak profile function to fit the basal spacing peaks and higher order reflections. This function was necessary to fit the very broad tails of the peak profiles of both potassium- and sodium-saturated MMT and low-q asymmetry due to defective stacking motifs measured in cryo-TEM. The diffraction intensity, I, in the vicinity of a diffraction peak at q_d is given by

$$I(q) = C\left[1 + \frac{(q-\mu)^2}{\sigma\left(\frac{2\gamma}{1+e^{\alpha(q+\mu)}}\right)^2}\right]^{-\sigma} \tag{4.2}$$

were μ is the peak position, σ determines the extent of the tails, γ is a shape parameter, α defines the degree of asymmetry, and C is a constant proportional to the total intensity. This function yields higher-quality fits than Gaussian, Lorentzian, Pseudo-Voigt, Skewed-Gaussian, or combinations thereof.

Ion exchange between Na-MMT in 1 M NaCl and 1 M KCl were performed by flowing KCl solution over both the inlet of the oedometer cell. X-ray scattering patterns were collected at regular time intervals over the course of approximately 7 hours while simultaneously recording the swelling pressure. Profiles of the clay plug at intervals of 0.5 mm (approximately the height of the beam) were recorded at each timepoint to track the position of the exchange front.

Structural changes were observed over multiple length scales as a result of K^+ exchange for Na^+ (Figure 4.4). Clay mesostructure at the largest length scales remained relatively unimpacted by ion exchange (Figure 4.4a). Only subtle changes in the Porod slope (q < 0.25 Å^{-1}, >2 nm) that corresponded to densification upon the expulsion of interlayer water were observed. Importantly, this indicates that there is no appreciable change in mesoscale porosity (i.e., osmotic hydrates) during ion exchange at the high clay volume fractions employed in this study. Changes in porosity were confined to the nanoscale, with the collapse of the basal spacing from three water layers (q = 0.33 Å^{-1}, 1.9 nm) to two (q = 0.39 Å^{-1}, 1.6 nm). Collapse was also accompanied by a restructuring of the interlayer cations, which manifest as changes in scattering intensity at smaller scales (q > 0.5 Å^{-1}). The three-water-layer state in Na-MMT exhibited a second order harmonic peak at $2q$ = 0.66 Å^{-1}, which is indicative of bilateral symmetry. This confirms that the interlayer cations predominantly reside in a symmetric configuration about the interlayer midplane. However, the $2q$ harmonic peak for the two-water-layer state, which would be expected to occur at

0.78 Å^{-1}, is absent. This indicates that the cations in this state are in an asymmetric configuration relative to the interlayer midplane.

Using the change Porod slope, collapse of the basal spacing peak, and reconfiguration of interlayer cations as indications of the exchange front, the evolution of ion exchange was tracked along the 10 mm height of the clay plug over the course of 7 hours. Two important conclusions can be drawn from these experiments: 1) exchange of K^+ for Na^+ is slow on the experimental timescale, and 2) the exchange front is sharp. The exchange front traveled less than 0.5 mm in 7 hours (Figure 4.4b). Predominantly two-water layer hydrate coexisted with a small fraction of three-water-layer hydrate within the first 0.5 mm. Between 0.5 mm and 1 mm there was only a minor fraction of two-water-layer hydrate, and the rest of the clay plug remained unchanged.

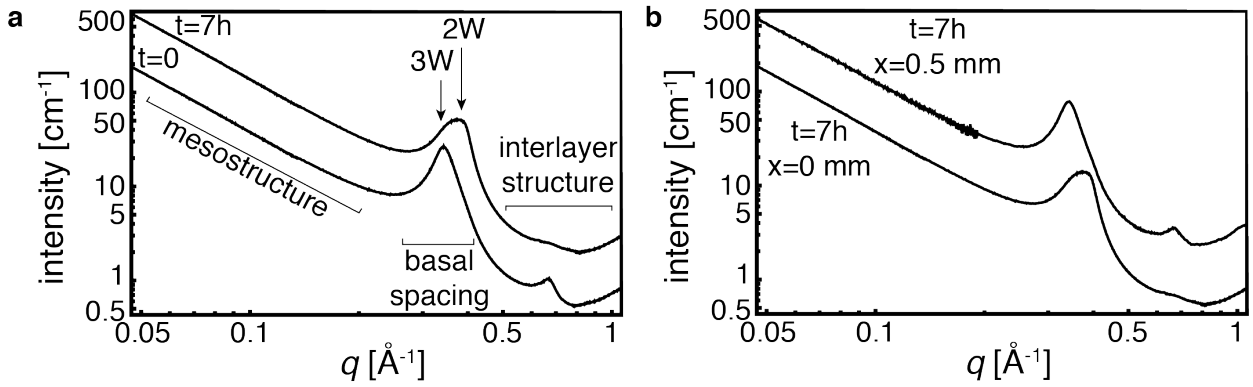

Figure 4.4. Ion exchange between Na-MMT and 1 M KCl tracked via X-ray scattering. Patterns collected at $t = 0$ and $t = 7$ hours following the start of aqueous KCl flow. Curves are offset for clarity.

4.4 Molecular Simulations of Ion Exchange and Swelling Thermodynamics for cis-vacant Montmorillonite

4.4.1 Problem statement

Decades of study has shown that crystalline swelling states in montmorillonite often coexist, and their relative proportions vary as a function of water activity (Berend, 1995; Ferrage, 2005; Holmboe et al., 2012). A mixture of coexisting swelling states was generally thought to yield an 'interstratified' structure with multiple distinct basal spacings (swelling states) within an MMT particle. However, recent cryo-TEM and X-ray scattering data indicate the presence of coexisting but physically separated MMT particles with proportions of the discrete swelling states that depend on the NaCl/KCl electrolyte composition (Whittaker et al., 2019). A clear understanding of swelling state distribution and its effect on the structure of MMT at the aggregate scale is critical to predict swelling pressure and transport properties as a function of solution composition and confinement.

To investigate the energetics of swelling and layer state mixtures, we performed molecular dynamics (MD) simulations of MMT hydrates in homoionic bulk solution. Classical molecular simulations serve as powerful tools to investigate the structure and energetics of equilibrium hydration states and the microstructures arising from phase coexistence of MMT. Several atomistic models have simulated the diffusion (Holmboe and Bourg, 2013), kinetics (Tournassat et al., 2016) and free energies of cation exchange (Rotenberg 2009; Teppen 2006; Lammers et al., 2017), and swelling thermodynamics (Hsiao and Hedström, 2017; Svoboda et al., 2018; Whitley and Smith, 2004) in various clay minerals. However, a quantitative evaluation of phase coexistence through the explicit modeling of mixed phases is missing in literature. Here, we employed the recently developed molecular structure for cis-vacant MMT (Subramanian et al., 2020) to investigate the energetic underpinnings of phase transition and coexistence in homoionic electrolytes. In particular, these simulations allow us to calculate the free energies of transition between swelling states and the excess free energies of mixing of mixed swelling states, in order to relax the assumption of ideal mixing.

4.4.2 Swelling Energetics

A phase transition corresponds to the adsorption or desorption of water molecules in the MMT interlayer to switch between swelling states. The calculation of free energy difference between stable hydrates yields the swelling free energy at a given solution composition. Significant focus has been dedicated to the estimation of swelling free energies using molecular modeling (Whitley & Smith, 2004; Smith et al., 2006, Honorio et al., 2017; Svoboda et al., 2018; Underwood & Bourg, 2020). These studies have calculated the swelling free energy for trans-vacant MMT, which has a centrosymmetric molecular structure. Available experimental data unambiguously show that Wy-MMT has a cis-vacant structure. Our recent study of water adsorption on cis-vacant MMT revealed that interlayer water is more structured and 'ice-like' due to a stronger hydrogen bonding network at the mineral/water interface. We believe that this could have an impact on the energetics of swelling/collapse mechanisms under various conditions (electrolyte type and concentration, pressure, temperature, etc.). Therefore, we computed the potential of mean force (PMF) between two MMT layers as a function of their basal spacing.

Each clay layer in our model contains 175 units cells of cis-vacant MMT, where structural hydroxyls occupy adjacent positions relative to the octahedral vacancy sites. The edges of clay layers perpendicular to the *x*-*z* plane were made unreactive with OH, OH_2 terminations that result in neutral edge charge. Isomorphic substitutions of Mg^{2+} for octahedral Al^{3+} were also randomly introduced to yield a structural charge of -0.57e per $O_{20}(OH)_4$ of clay. It must be noted that in cis-vacant MMT we did not impose a constraint preventing two adjacent Mg^{2+} substitutions. The two clay layers (9.35 nm × 9.05 nm) were immersed in bulk solution of 1M NaCl as shown in Figure 4.5. Although the electrolyte concentration is relatively high compared to solutions in the EBS context, it was chosen to be close in concentration to the phase transition boundary between the 2- and 3-water layer hydrates of Na-MMT. Interatomic interaction terms that represent the van der Waals and electrostatic forces are obtained from ClayFF (Cygan, 2004) for the mineral atoms and ions, and water interaction parameters use the SPC/E model (Berendsen et al., 1981). The pairwise Lennard Jones energy is calculated using the Lennard-Jones potential given by

$$E_{pair,ij} = 4\varepsilon_{ij}\left[\left(\frac{\sigma_{ij}}{r_{ij}}\right)^{12} - \left(\frac{\sigma_{ij}}{r_{ij}}\right)^{6}\right]$$

where r is the distance between two particles, and ε and σ are the maximum depth of the potential energy well and the distance of zero potential, respectively. The pairwise interaction terms between dissimilar atoms are calculated via Lorentz-Berthelot mixing rules – $\varepsilon_{ij} = \sqrt{\varepsilon_{ii}\varepsilon_{jj}}$ and $\sigma_{ij} = (\sigma_{ii} + \sigma_{jj})/2$. Coulombic interactions are calculated using $E_{coul,ij} = \frac{q_i q_j}{4\epsilon_0 r_{ij}}$ where q is the partial charge and ϵ_0 is the permittivity in vacuum. A cutoff distance of 15 Å is used to calculate short-range interactions and the Particle-Mesh Ewald's summation method with an accuracy of 99.99% is used to compute long range electrostatics. The system was equilibrated in the NPT (T = 298 °K) ensemble for 1 ns, following which, a steered molecular dynamics (SMD) simulation was performed over 3 ns in the NPT (P = 1 atm, T = 298 °K) ensemble. During the equilibration, the clay layers were held tethered to their initial positions. This is because the initial state of the simulation corresponds to an unstable dry state (0.25 H_2O molecules per unit cell of clay) and the electrostatic repulsive forces between the layers cause the layers to deform.

In the SMD run, the bottom MMT layer was tethered while the top MMT layer was translated along the *z*-direction with a constant velocity of 2 Å/ns by a harmonic stiff spring (Park and Schulten, 2004). The layers were allowed to be flexible during the translation. We then segmented the entire SMD run into trajectory windows of 1 Å change in basal spacing and used the initial step of each window as input to perform umbrella sampling. The umbrella sampling, which was implemented using the Collective Variables (COLVARS) library in LAMMPS (Fiorin, 2013), spanned 40 stages per window, and each stage sampled

the distance between the layers and the harmonic potential of the spring for a translation of 0.025 Å. The small size of umbrella windows ensured that there was sufficient sampling of the entire reaction coordinate (here, the reaction coordinate is the basal spacing) and overlap among the umbrella windows. Since the umbrella sampling approach imposes a biasing potential (here, the biasing potential is the harmonic potential of the stiff spring), we need an unbiasing algorithm to compute the PMF. We used the Weighted Histogram Analysis Method (WHAM) code (Grossfield) to extract the PMF profile from the umbrella sampling results. Ho et al. (2019) showed that the ClayFF parameter set does not predict the dry to one-water layer (0W – 1W) hydration process well. The authors of the study modified ClayFF to capture the dry to hydrated state transition. Since we used the traditional ClayFF parameters and because we are interested in the swelling states applicable to engineered barriers, our focus is restricted to the 2W to 3W transition.

We observed the 2W and 3W minima at basal spacings of 16.11Å and 18.89Å, respectively, from the PMF profile in Figure 4.6. It appears that the global minimum for the chosen electrolyte concentration corresponds to a 2W hydrate. Contrary to our experimental data, which suggest that NaMMT occurred as a stable 3W hydrate in dilute suspensions and 1M NaCl, the simulations showed that the most energetically favorable hydrate at this concentration was a 2W state. Additional simulations will be performed to identify the transition concentration where 2W clay becomes favorable. The water activity and the clay dry bulk density play a critical role in determining the stable MMT hydrate for a given solution. For clay layers in suspension, the water activity in solution was ~0.98; therefore, it was surprising that the 2W was clearly favored over the 3W state. This discrepancy might have been an artifact of the selected force-field potential model; however, there is plenty of evidence in literature for NaMMT commonly occurring in the 2W state. Svoboda et al. (2018) computed the PMF profiles for NaMMT suspended in pure water and 2.8 M salt solution, and concluded that the 3W state has the lowest free energy in pure water, whereas a lower hydration state (2W) was favored in the salt solution. X-ray diffraction (XRD) studies (Cases et al., 1992; Morodome and Kawamura, 2009) showed that the 3W hydrate occurs in significant proportions only at relative humidity (RH) of 0.93 or above. A model developed based on fitting XRD data (Holmboe et al., 2012) also validated this finding, and the fraction of 3W was small even at RH values higher than 0.96. Whitley and Smith (2004) found that at room temperature with RH = 1, NaMMT may exist as 2W, 3W, or even osmotic hydrates depending on preparation and clay dry density.

Further investigations are needed with pure water (0M NaCl) and higher electrolyte concentrations (perhaps 2M NaCl) to understand how the global minimum shifts as a function of ionic strength. From the PMF profile, we calculated the swelling free energy (2W – 3W) to be ~7 kJ/mol, which is consistent with reported literature (1-3kT). In comparison to reported values of swelling free energy for trans-vacant clay layers, we find that the swelling free energy for our cis-vacant structure is slightly higher.

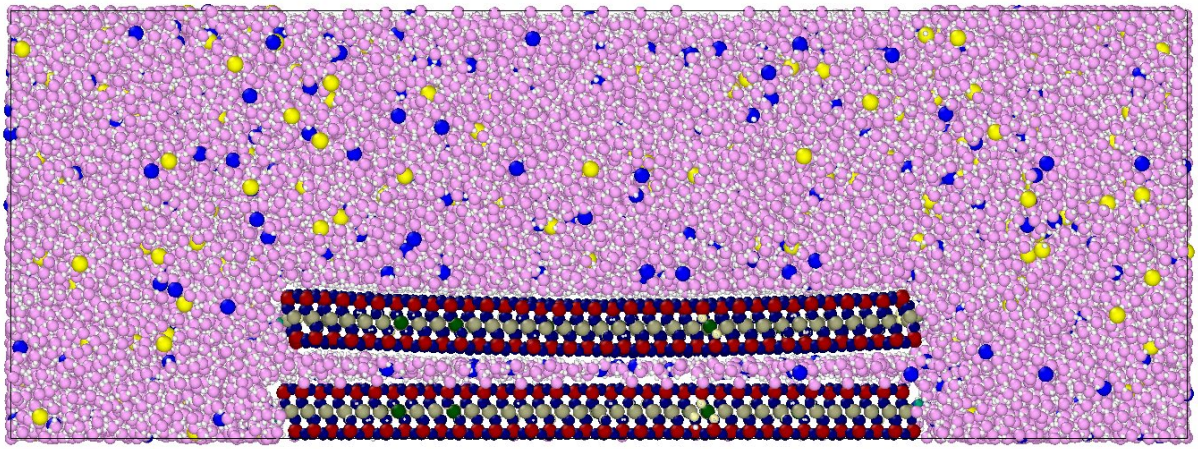

Figure 4.5. MMT layers immersed in bulk solution of 1M NaCl. Al atoms in the octahedral sheet are in gray, Mg substitutions in dark green, Si atoms in the tetrahedral sheet are in dark red, clay oxygen atoms in dark blue, terminal edge oxygen atoms in violet, water oxygen atoms are in pink, water and clay hydrogen in white, sodium ions in blue, and chloride ions are in yellow.

4.4.3 Layer State Mixing Energetics

We explicitly modeled interstratified mixed layer states to probe the energy penalties (if any) for the mixing of swelling states. The molecular models consist of four layers of MMT suspended in a bulk electrolyte solution of 1 M NaCl. The simulation volume was designed to be large enough to facilitate diffusion and exchange of interlayer water and ions with the bulk solution. The clay layers were placed at the center of a box (16.5 nm × 9.05 nm × Z), where Z was determined by the equilibrium basal spacing of the layer states. Periodic boundary conditions were imposed to the volume along all three dimensions, thus rendering the clay tactoid infinite in the y and z dimensions and finite along the x direction. The large x dimension of the box also ensured that we were able to extract bulk solution properties away from the clay mineral edges and that the particles do not interact across periodic boundaries. With 2W and 3W states as pure end-members, we generated mixed layer states by changing the proportions of these states in the tactoid. Figure 4.7 shows an interstratified clay particle with equal proportions of 2W and 3W phases. The starting point of the current model was the near-optimal values of hydration stoichiometry (~5 and ~4.8 H_2O molecules per $O_{20}(OH)_4$ per water layer for 2W and 3W, respectively) and equilibrium basal spacings (16 Å and 18.9 Å, respectively) we determined for 2W and 3W cis-vacant NaMMT from previous Grand Canonical Monte Carlo (GCMC) and μVT simulations (Subramanian et al., 2020), which were also validated by the results of the PMF profiles and corresponding swelling thermodynamics.

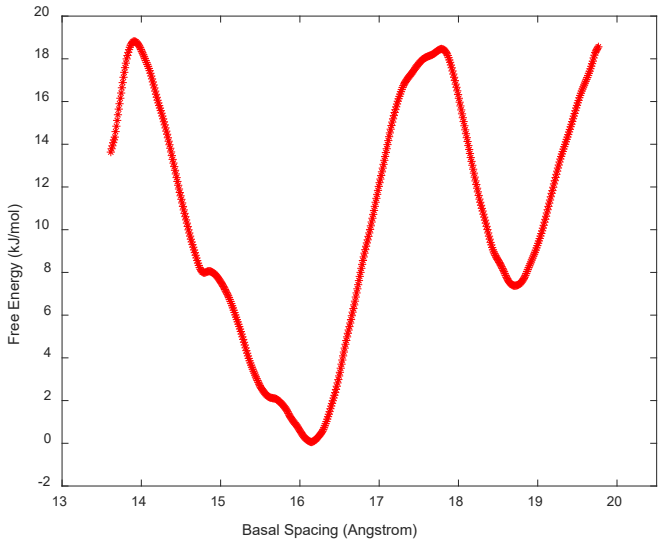

Figure 4.6. Potential of mean force profile of NaMMT swelling free energy in 1M NaCl.

The structures were equilibrated for 1 ns in the NVT ensemble (T = 298 °K) and 5 ns in the NPT (P = 1 atm, T = 298 °K) with a Nose-Hoover themostat and barostat. The equations of motion for the particles were solved using the Verlet algorithm with a 1 fs timestep. Production simulations were carried out in the same isothermal-isobaric ensemble for 3 ns over the course of which data was sampled.

The atoms of the clay particle, with the exception of the hydroxyls (including those in edge terminations), were held rigid during the equilibration. The pure end-member components equilibrated well under these conditions and resulted in uniform basal spacings. Based on the newly obtained basal spacings for 2W and 3W states in equilibrium with 1M NaCl solution, the mixed layer states were tethered in the z direction with a spring force of 5 eV/Å^2. We observed that without the tethering, the mixed states yielded non-uniform basal spacings (with 2W and 3W in the same interlayer) indicating that the interstratified configuration was energetically unfavorable.

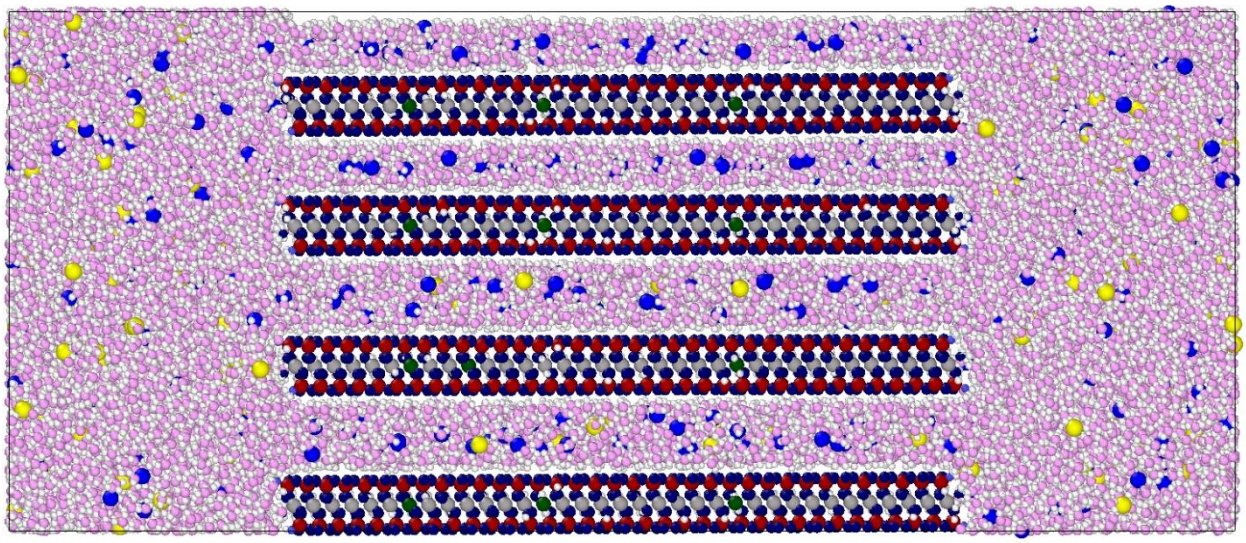

Figure 4.7. Simulation volume containing an interstratified clay particle with 50% 3W and 50% 2W fractions in 1M NaCl solution.

An analysis of the resulting average basal spacing in each mixed layer state (Table 1) shows that there are minor deviations from the equilibrium d_{001} values despite the applied spring force. The observed strains become generally larger as the relative proportion of the phase decreases in the mixture (16.01 Å for the 2W phase in 25%-75% mixture is the exception). Simulations of mixed layer states that did not impose a spring force (untethered configuration) confirmed that 2W interlayers displayed a tendency to expand whereas the 3W interlayers tended to collapse (see Figure 4.8). The applied spring force adds to the total enthalpy of the tethered system, but helps retain the solid solution in a physically meaningful configuration with uniform basal spacings.

Table 4-1. Calculated basal spacings of hydrates from simulations

Configuration	Bulk NaCl concentration (mol/dm^3)	d_{001} $(MMT2, MMT3)$ (Å)
100% MMT2	0.99	$(15.91 \pm 0.095, N/A)$
75% MMT2 – 25% MMT3	0.98	$(15.84 \pm 0.002, 18.27 \pm 0.005)$
50% MMT2 – 50% MMT3	1.01	$(15.37 \pm 0.001, 18.67 \pm 0.001)$
25% MMT2 – 75% MMT3	1.00	$(16.01 \pm 0.005;\ 18.83 \pm 0.009)$
100% MMT3	0.97	$(N/A, 18.94 \pm 0.03)$

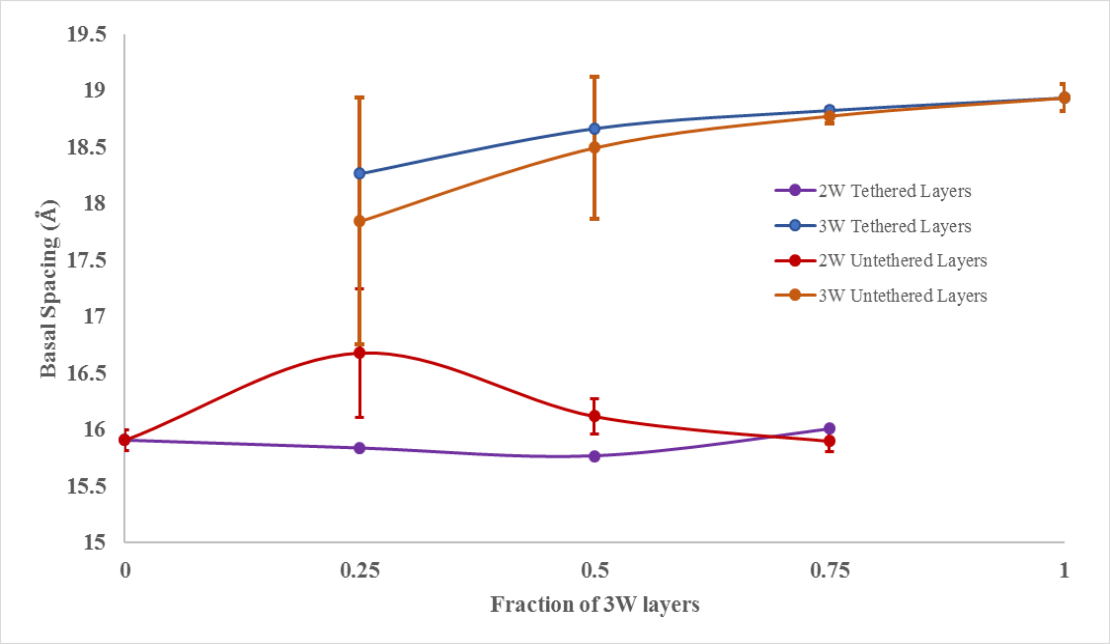

Figure 4.8. Average basal spacings in pure and mixed layer states with tethered and untethered (rigid) configurations. Fluctuations of layers in unstable states lead to large error bars in some cases.

We then calculated the enthalpies of formation of the pure and mixed layer states. The total internal energy output of the system (U_{total}) can be broken down into contributions from the clay hydrate and the bulk solution. Since the concentration of bulk solution (and therefore, water activity) was kept constant in simulations, we expect the internal energy per mole of solution ($\underline{U_{soln}}$) to be constant. This was verified by energy output from the bulk region of the simulation volume normalized by the number of moles of solution (n_{soln}) as shown in Table 4.2. Based on Equation 4.1, we calculated the total internal energy from the clay hydrate ($n_{clay}\underline{U_{clay}}$) in each of the pure and mixed layer states from the equation given by

$$U_{total} = n_{clay}\underline{U_{clay}} + n_{soln}\underline{U_{soln}} \tag{4.3}$$

Table 4.2. Solution concentration and total internal energy per mole of solution calculated after equilibration

Configuration	Bulk NaCl concentration (mol/dm^3)	$\underline{U_{soln}}(\frac{kJ}{mol})$
100% MMT2	0.99	-48.13
75% MMT2 – 25% MMT3	0.98	-47.67
50% MMT2 – 50% MMT3	1.01	-47.91
25% MMT2 – 75% MMT3	1.00	-47.69
100% MMT3	0.97	-47.17

Including the pressure-volume work done on the mixed layer hydrate to the total internal energy yields the mixing enthalpies (expressed in per molar quantities). Although the magnitude of bulk pressure ($P_{z,bulk}$) is significant, the change in basal spacing from the corresponding equilibrium values is small. Thus, the

contribution of the pressure-volume work term to the enthalpy of mixing is small, and was calculated from equations given by

$$\Delta \underline{H}_{mix} = \Delta \underline{U}_{mix} + \underline{PdV}_{mix} \quad (4.4)$$

$$\Delta \underline{H}_{mix} = \left[\underline{U}_{mixed,clay} - (x_{2W}\underline{U}_{clay,2W} + (1 - x_{2W})\underline{U}_{clay,3W})\right] + \frac{1}{n_{clay}}\left[(P_{z,bulk}) \times l_x l_y \times \Delta d_{001}\right] \quad (4.5)$$

The computed enthalpies of mixing from the molecular simulations indicate non-ideal mixing between the 2W and 3W phases, with the excess free energy of mixing being symmetric, thus exhibiting near-perfect regular solid solution behavior (see Figure 4.9). In the regular solution model, we calculated the excess free energies of mixing with ideal entropic components for each mixed layer state as described by the following equations:

$$\Delta \underline{G}_{mix} = \Delta \underline{H}_{mix} - T\Delta \underline{S}_{mix} \quad (4.6)$$

$$\Delta \underline{S}_{mix,ideal} = -R(x_{2W} ln x_{2W} + (1 - x_{2W}) ln\,(1 - x_{2W})\,) \quad (4.7)$$

Here, we find that the excess free energy of mixing of the 2W and 3W states is significantly higher than the free energy difference between them (swelling free energy determined in the previous section). The proximity in the free energy between the 2W and 3W hydrates will likely allow these phases to switch among each other completely as opposed to existing in mixed layer states. These calculations provide a thermodynamic basis for the absence of MMT layer state coexistence in NaCl solutions.

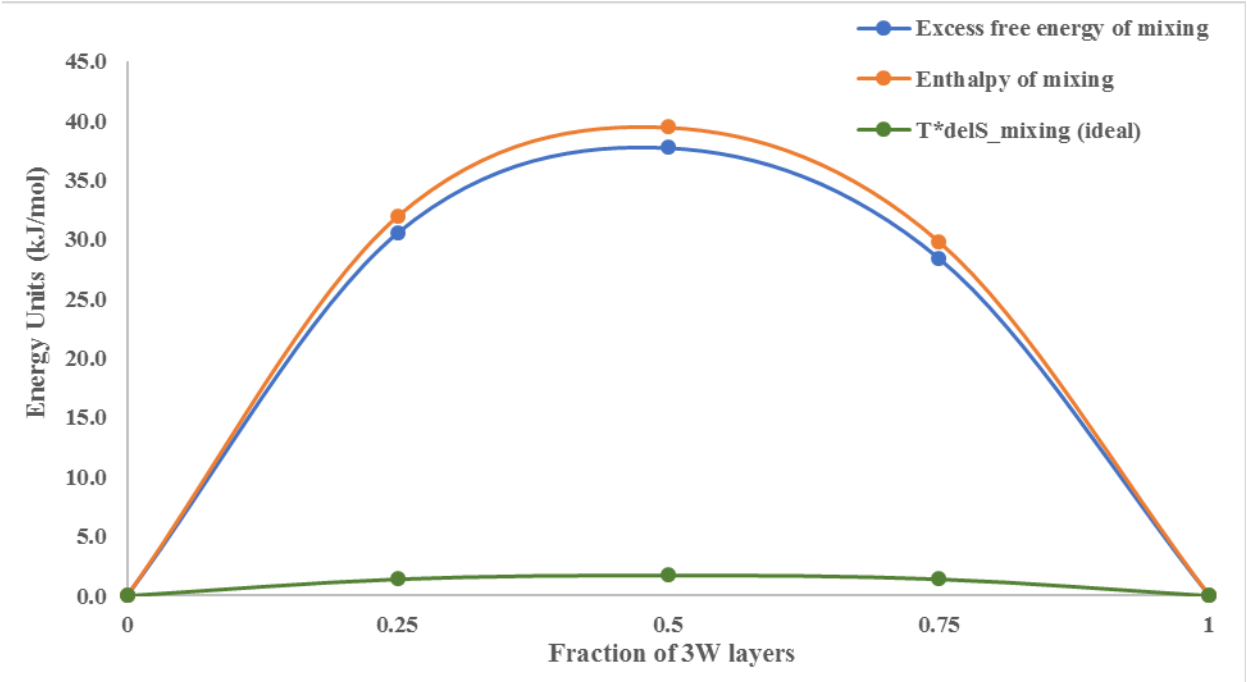

Figure 4.9. Excess free energy of mixing as a function of mole fractions of 3W hydrate in the solid solution

4.4.4 Ion Exchange Thermodynamics

Research has shown that swell/shrink reactions and ion exchange processes in smectites are tightly coupled. X-ray scattering data acquired recently (Whittaker et al., 2019) indicates a selectivity of the hydration states to ion adsorption. For example, during an exchange reaction of Na^+ for K^+, it was observed that the 3W particles were Na^+ rich whereas the 2W MMT particles were K^+ rich. The exchange of Na^+ for K+ was

found to drive the collapse of 3W MMT layers to 2W states. To better understand the coupling between hydration reactions and ion exchange reactions, we set up molecular simulations of layer states in a mixed electrolyte solution. These simulations will allow us to quantify the selectivity of layer states for ion adsorption.

Thermodynamic integration (TI) calculations were performed to calculate the free energies of ion exchange reactions between Na and K in the bulk aqueous solution. We start with one of the equilibrated end-member hydrate (2W) states in 1 M NaCl from the previous section. Then, 25% of Na ions in solution were randomly selected and progressively transformed into K ions by changing their pairwise interaction potentials in a series of 10 steps, using a coupling parameter $\lambda \in [0,1]$, with 0 representing Na, and 1 representing K, using equations given by:

$$\sigma(\lambda) = \sigma_{Na} + \lambda(\sigma_{Na} - \sigma_K) \tag{4.8}$$

$$\varepsilon(\lambda) = \varepsilon_{Na} + \lambda(\varepsilon_{Na} - \varepsilon_K) \tag{4.9}$$

At each step, an NPT equilibration for 3 ns follows the change in the Lennard Jones interaction parameters. The result at the end of the transformation yields a 2W hydrate in a mixed electrolyte solution containing 0.75M NaCl and 0.25M KCl. This series of progressive transformation steps will be carried out until we arrive at 2W hydrates with 0.5M, 0.75M, and 1M KCl (with decreasing NaCl concentration accordingly). The variation in the Hamiltonian of the system (the total energy of the system in our case) during the transformation as a function of the coupling parameter λ gives us the free energy for the exchange reaction. Along with the change in bulk electrolyte and the free energy associated with the exchange, we can also compute the selectivity of the 2W hydrate for ion adsorption as a function of aqueous composition.

4.5 Summary and Future Work

In FY20 we have conducted a comprehensive set of experiments and simulations, which provided deep insights into the thermodynamics of clay swelling in mixed electrolyte solutions. Experimental procedures are in place to generate a comprehensive swelling pressure data set in multicomponent electrolyte solutions as soon as laboratory work is resumed in FY20 and extended into FY21. The swelling pressure data will be compared against model expectations based on the thermodynamic approach described in Zheng et al. (2019) and Whittaker et al. (2019), with subsequent model refinements based on experimental outcomes. Additional X-ray scattering beamtime will be sought toward the end of FY20 to obtain additional microstructural data constraints, including the evolution of MMT microstructure, upon ion exchange in mixed electrolyte solutions including calcium. Additional simulations will be completed to determine swelling free energies for mixed electrolytes, but a different simulation technique is required to quantify interlayer ion exchange thermodynamics. These will be investigated further in FY21, using the thermodynamic integration technique described above.

This page was intentionally left blank.

5. MICROSCOPIC ORIGINS OF COUPLED TRANSPORT PROCESSES IN BENTONITE

5.1 Background and Proposal goals

Thermal processes play a major role in controlling the fate of nuclear waste disposed in geological repositories through coupled effects on hydration, mechanical and chemical (THMC) properties of the barrier/backfill material. Heat conduction away from the nuclear waste cannister has a significant impact on the design, construction and operation of any disposal system, and the ability to predict the thermal properties of a barrier/backfill is of high importance to the safety case for any design concept. Reducing the peak temperature of the barrier/backfill near the cannister, and thermal gradients between the cannister and host rock, will significantly improve the ability to predict the outcomes of specific nuclear waste disposal designs. However, the thermal conductivity of bentonite is a strong function the hydration state, which changes considerably with temperature(*Lee et al.*, 2016; *Tang et al.*, 2007), especially under irradiation(*Gu et al.*, 2001).

Initial work in this area focused on extending a model of the intermolecular forces that govern Mt structures and energetics (in preparation) to high mineral volume fractions where the properties of bentonite are strongly influenced by the details of the interfacial hydration structure(*Subramanian et al.*, 2020; *Zarzycki and Gilbert*, 2016) and the coupling between hydration and ion distributions at mineral interfaces are highly temperature dependent.

We propose to develop and validate a microscopic model of coupled transport processes in bentonite and to use this model to determine cost effective augmentation strategies to increase the bulk thermal conductivity of hydrated Bentonite. Results of preliminary work through FY19-20 will serve as a foundation for a larger scale effort in FY20-21 to stably increase the thermal conductivity of bentonite above 2 W/mK at temperatures relevant to modern nuclear waste storage design concepts.

5.2 Proposed Work

5.2.1 Model development

Here, we outline the model that has been developed during FY19-20, which will serve as a foundation for an upscaled effort in FY20-21. This model incorporates a range of experimental results on the properties of water and ions in the confinement of clay interlayers that collectively point to persistent non-equilibrium behavior in hydrated bentonite at elevated temperatures. We will show that non-equilibrium dynamics are the result of tightly coupled mobility of ions and water in the confinement of clay interlayers and their ability to mechanically deform the layers, which results in fluctuations that generate, and conduct, heat. We aim to determine the exact microscopic origins of thermal fluctuations and investigate the effects of chemical or structural alterations designed to enhance the thermal conductivity of Bentonite by amplifying these fluctuations.

Bentonite backfill can be considered to be a three-component composite material: mineral phases (predominantly montmorillonite, Mt), water, and electrolyte (Bourg and Ajo-Franklin, 2017). Thermal and ionic transport properties of Mt depend on the relative contributions from the mineral layers, the interlayer cations, water and the coupling between them. Pyrophyllite and mica are structural analogs of Mt that have thermal conductivities of 0.81 and 0.21 W/mK, respectively (Horai, 1971). Both minerals are highly electrically insulating and thermal transport is phonon-mediated. The lower conductivity of mica suggests that the presence of interlayer cations (i.e., K+) decreases the phonon mean free path, likely due to the low areal density of these cations relative to the tetrahedral and octahedral sheets. From this perspective, Mt

structural charge that is intermediate to pyrophyllite and mica would be expected to result in intermediate thermal conductivity. However, the thermal conductivity of fully-dense, anhydrous Mt exceeds that of pyrophyllite (1.0 W/mK) and may increase by a factor of two when fully saturated(Lee et al., 2016; Tang et al., 2007). The thermal conductivity of bulk water is 0.6 W/mK, and therefore understanding the anomalous thermal conductivity of Mt and its amplification when hydrated is imperative for improving the thermal properties of barrier materials.

Measurements of bentonite electrical conductivity reveal distinct mechanisms of diffusive ion transport at various temperatures and levels of hydration that elucidate the atomic-scale phenomena underlying thermal conduction in the absence of applied electric fields. The direct current (DC) electrical conductivity of anhydrous Mt is extremely low ($\sim 10^{-13}$ $\Omega^{-1}cm^{-1}$ at 80°C) and has a high activation energy of approximately 1 eV/ion for Na^+ ions (*Balme et al.*, 2010; *Kharroubi et al.*, 2012). Electrical conductivity of anhydrous Mt increases with temperature with Arrhenius kinetics, suggesting that ionic mobility is limited by individual hopping events between charge sites (*Belarbi et al.*, 1997). Each hop is highly unfavorable due to the high repulsive electrostatic potential from neighboring charges that originate over a relatively large region of the mineral.

Even small quantities of water increase the DC electrical conductivity of Mt by 10 orders of magnitude ($\sim 10^{-3}$ $\Omega^{-1}cm^{-1}$ at 20°C) (*Balme et al.*, 2010), and activation energies decrease rapidly with water content. For example, the activation energy for diffusion of Na-Mt with two layers of interlayer water is approximately 0.25 eV. This dramatic increase in ionic mobility relative to dry Mt is due to the effective screening of the long-range electrostatic potential by the relatively high dielectric permittivity of water ε_{water}. Bulk water has $\varepsilon_{water} = 80$, and therefore $\varepsilon_{water} \cong 10\varepsilon_{Mt}$. In the limit of full hydration, the length scale over which Coulombic interactions contribute appreciably to the forces felt by an ion is reduced by approximately a factor of 10. This reduction is anisotropic, occurring preferentially within the interlayer where water can penetrate. Therefore, water has a strong and chemistry dependent, but spatially anisotropic, effect on intermolecular interactions in Bentonite.

In addition to decreasing the activation energy for diffusion, the presence of water also gives rise to super-Arrhenian temperature dependence of the ionic conductivity, which is indicative of non-equilibrium conditions. The bulk thermal conductivity of Bentonite(*Lee et al.*, 2016; *Tang et al.*, 2007) has been shown to have a similar, non-Arrhenian, dependence on temperature. The activation energy for water diffusion in hydrated Mt is 0.12-20 eV (*Sanchez et al.*, 2008; *Sánchez et al.*, 2008), lower than that of the ions, and displays Arrhenian temperature dependence above 0°C. Thus, ionic mobility is strongly influenced by the presence of water, but is decoupled from water diffusion and proceeds via a distinct mechanism. This suggests that the overall thermal conductivity of Bentonite is largely controlled by the mobility of ions. However, ionic mobilities are highly dependent on the hydration state and strongly coupled to the structure of the charged mineral layers, and thus understanding the thermal conductivity of Bentonite requires explicit elucidation of these microscopic couplings.

Below 0°C, water within clay interlayers becomes supercooled and exhibits super-Arrhenian temperature dependence approaching a glass transition at ~120 K (*Sánchez et al.*, 2008). While these temperatures are not directly relevant to nuclear waste storage, this behavior is a well-studied example of non-equilibrium dynamics exhibited by the same system that are analogous in many ways to the behavior observed for interlayer cations at elevated temperatures. In both cases, super-Arrhenian diffusivities exhibit a 'glass-transition' temperature, below which dynamics are quenched and above which dynamics are activated, but starkly contrast the 'hopping' type ion diffusion that occurs in anhydrous clays, or for water above 0°C.

Glassy, supercooled water in between clay layers results from the geometrical inability to form a critical nucleus of crystalline ice. We propose that hydrated clay minerals are supercooled liquid crystals resulting from the geometrical inability of neighboring layers to find a local energy minimum that also satisfies global charge neutrality. Disordered structural charge on either side of an interlayer cannot be compensated by the same number of cations in each interlayer, on average (Figure 5.1). We hypothesize that the anomalous

thermal conduction of hydrated Bentonite arises from a transition between interactions dominated by long-range electrostatics observed in pyrophyllite, mica, and anhydrous Bentonite to local, hydration-mediated interactions that reduce the local system energy but globally unfavorable configurations. We propose to apply an Ising model for the charge, hydration, and structural state of a mineral layer (Figure 5.1) (*Chamberlin*, 1999) based on supercooled liquids that describes how the structure of Bentonite responds to different chemical, hydration, and thermal conditions.

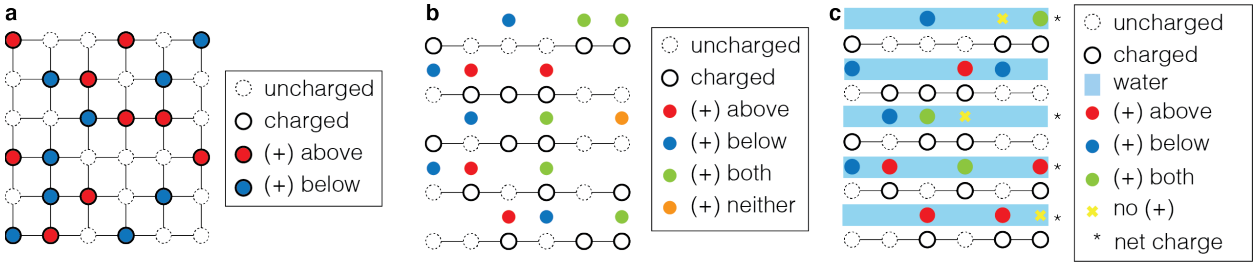

Figure 5.1. Using model for microscopic transport in clay minerals: (a) Face-on view of clay layer with x = 0.5 (solid circles). For a single layer, charge neutrality is maintained when half of the interlayer cations (red, blue) are located on each side of a layer. (b) Charges become dissociated from structural charge sites when anhydrous layers are stacked, but because electrostatic forces are long-range, the charge distribution finds a minimum energy state. (c) Interactions become highly anisotropic and local when water is introduced because it screens charge laterally, leading to net charge states within interlayers.

5.2.2 Model validation

Microscopic model validation relies primarily on cryo-electron tomography (CET) to determine the three-dimensional structure of hydrated bentonites (*Whittaker et al.*, 2020) with near atomic resolution (*Whittaker et al.*, 2019), and dielectric relaxation spectroscopy (DRS) to probe the behavior of water in the confinement of clay interlayers and at elevated temperatures. These techniques are complimentary because water is effectively transparent in CET, while it dominates the signal of DRS. We have recently shown that Na^+ and K^+ ions in Mt tactoids reside in distinct sites within the interlayer, either partially dehydrated and directly bound to the clay mineral surface or fully hydrated and approximately 0.3 nm (approximate molecular diameter of water) away from the mineral surface. The relative proportions of these binding configurations are chemistry-specific and control the swelling state of the clay (Fig. 2). Thus, we expect these distinct structures to exhibit vastly different DRS spectra that will reveal important information about the ability of water to modulate the interactions between ions and clay that control heat transport.

Bulk thermal conductivity measurements will be performed over a range of chemical, hydration, and temperature conditions using custom designed therm-oedometer cells. Cell concepts are based on the sorption and diffusion cells described in the chapter 3 (Sorption and diffusion experiments on bentonite) and the X-ray transparent oedometer pressure cells described in chapter 4 (Chemical controls on montmorillonite structure and swelling pressure). Therm-oedometer cells will be modified with a plane-source thermoelectric heating element and sheet temperature sensor at opposite ends of the Bentonite plug for *in situ* application of temperature gradients and measurements of thermal conductivity. These multifunctional cells will have the capacity to facilitate simultaneous chemical, uniaxial pressure, and thermal stimuli with real time measurements of swelling pressure, uniaxial temperature gradient, and X-ray scattering or tomography. Initial cell designs will be completed in the remainder of FY19-20 and early FY20-21, with fabrication and testing to following.

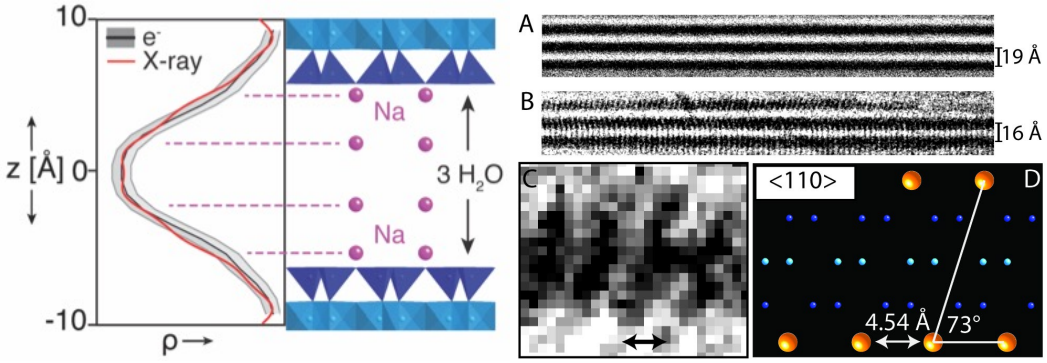

Figure 5.2. Ion binding sites in Mt tactoids. (Left) Electron density (ρ) profile determined by X-ray scattering and cryo-transmission electron microscopy (cryo-TEM) of Na-Mt, showing two types of binding sites within a three-water-layer hydrate. (A) Na-Mt in 1 M NaCl, with 19 Å spacing corresponding to a three-water-layer hydrate. (B) K-Mt in 1 M KCl with 16 Å corresponding to two-water-layer hydrate. (C) Enlarged region of (B), showing atomic contrast adjacent to the mineral interface consistent with bound K ions. (D) Atomic model of cations in a clay layer, showing spacing and geometry reflected in (C). Taken from ref (*Whittaker et al.*, 2019).

5.3 Expected outcomes

Our model predicts two important consequences for the thermal conductivity of bentonite. The first is that a local equilibrium is not possible without macroscopic rearrangement of mineral layers, and therefore microscopic gradients of ions and water are pervasive in bentonite unless or until the mineral is chemically altered to redistribute structural charge. The second is that a 'turbostratic' rearrangement of layers, as is observed in natural bentonites, may minimize the free energy of a given local arrangement, but that any structural fluctuations away from this arrangement will alter the energetic landscape and drive ion and water fluxes. These phenomena represent two important couplings between the chemistry and mechanical deformation of mineral layers in bentonite whose ultimate consequence is to create microscopic fluxes that generate entropy, and therefore, heat. We anticipate that this model can be used to quantify the specific interactions/fluctuations through which heat is transferred and make predictions about deliberate chemical or structural alteration that may augment heat conduction.

With further development in FY20-21, we expect to be able to identify and test bulk chemical modifications to Bentonite that enhance the thermal conductivity beyond 2 W/mK. For example, fluorine functionalization of the Mt octahedral sheet reduces hydrophilicity and may significantly alter the dielectric properties of confined water to more effectively screen interlayer charge and sustain dynamic fluctuations that drive thermal transport. Alternatively, mixing bentonite with aromatic hydrocarbons, such as chemical precursors to graphite, may facilitate the *in-situ* formation of thermally conductive carbon nanomaterials that enhance the thermal conductivity of bentonite.

6. UNDERSTANDING THE THMC EVOLUTION OF BENTONITE IN FEBEX-DP— COUPLED THMC MODELING

6.1 Introduction

The safety functions of EBS bentonite include limiting transport in the near field; damping the shear movement of the host rock; preventing the sinking of canisters (if emplaced in the center of the tunnel), limiting pressure on the canister and rock, and reducing microbial activity. To assess whether EBS bentonite can maintain these favorable features when undergoing heating from the waste package and hydration from the host rock, we need a thorough understanding of the thermal, hydrological, mechanical, and chemical evolution of bentonite under disposal conditions. Despite of numerous laboratory, field, and numerical studies, there is a lack of studies on coupled THMC processes. As part of SFWST program, a series of coupled THMC models have recently been developed for a design of a generic disposal system in clayey host rock with the EBS bentonite (Liu et al., 2013; Zheng et al., 2014; Zheng et al., 2015b; 2016; 2017;2018; 2019a). However, model validation was difficult due to the lack of THMC data from long-term, large-scale experiments. The FEBEX *in situ* test (ENRESA, 2000), which has been operated for 18 years, provides a unique opportunity of validating coupled THMC models.

The FEBEX-DP project is comprised of extensive THMC and biological characterization tests of bentonite, along with the development of numerical models. In the FEBEX *in situ* test, two heaters surrounded by bentonite blocks about 0.7 m thick were emplaced in a tunnel excavated in granite. The heaters were switched on in 1997. Heaters #1 and #2 were dismantled in 2002 and 2015, respectively. LBNL/DOE joined the FEBEX-DP project in FY15. The ultimate goal is to use THMC data from FEBEX-DP project to validate THMC models, and, therefore, enhance our understanding of coupled THMC process. From 2015 to 2017, extensive THMC characterization of bentonite samples, collected during the dismantling of Heater #2, was carried by partners of FEBEX-DP. Ion concentrations in the pore-water of bentonite were obtained via an indirect method, aqueous extract, and these concentrations were used to initially constrain the chemical model. In FY18, the geochemical models were used to infer the "true" ion concentrations in pore-water from aqueous extract data for one of the sections, and the developed coupled THMC model reasonably explained all the THM data and the trend of the chloride concentration in the pore-water of bentonite. In FY19 (Zheng et a., 2019a), the "true" ion concentrations in pore-water from aqueous extract data for another section were inferred by geochemical modeling; key processes that control the hydration of bentonite were re-evaluated, especially regarding the necessity of including thermal osmosis in the flow model to explain the relative humidity and water content data (Zheng et al., 2019b); chemical models were refined and used to explain the sulfate time series data. From FY16 to FY19, extensive model calibrations were conducted, and finally in FY19, the THCM model provided a coherent explanation of THMC data collected at the FEBEX *in situ* test. In FY20, the modeling work is, therefore, aimed at using the THMC to explore the long-term alteration of bentonite. The first question we are now trying to address is the necessity of using the THMC model (as appose to THC model) for studying long-term alteration of bentonite, especially geochemical alteration. THMC model is computationally expensive and numerically more unstable than THC model, while upgrading of THMC code using parallel computing and a better solver can alleviate the issue. Using the THC model could be beneficial in terms of a computation time and simulation stability, given that the performance assessment is most likely a THC simulation, not THMC simulation.

6.2 A brief description of FEBEX experiments

The FEBEX *in situ* test was conducted at the Grimsel URL from 1997 to 2015 (ENRESA, 2000). It consisted of five basic components: the drift, the heating system, the bentonite barrier, the instrumentation, and the monitoring and control system. The main elements of the heating system are two heaters (#1 and

#2), 1 m apart. Heaters were placed inside a cylindrical steel liner. Heaters were at a constant-temperature control mode to maintain a maximum temperature of 100 ºC at the steel liner/bentonite interface 20 days after the heating started. The bentonite barrier is made of blocks of highly compacted bentonite. The average values of the initial dry density and the gravimetric water content of compacted bentonite blocks were 1.7 g/cm^3 and 14.4%, respectively.

The *in-situ* test began on February 27, 1997, and went through two dismantling events. Table 2-1 presents the operation timeline. Comprehensive post-mortem bentonite sampling and analysis program was performed during both dismantling events (Bárcena et al., 2003; Garcia-Sineriz et al., 2016). After Heater #2 was switched off and a short cool-off time period, dismantling was carried out from the shotcrete toward the bentonite section by sections, and the types of monitoring and sampling are shown in Figure 2-1 (Garcia-Sineriz et al., 2016).

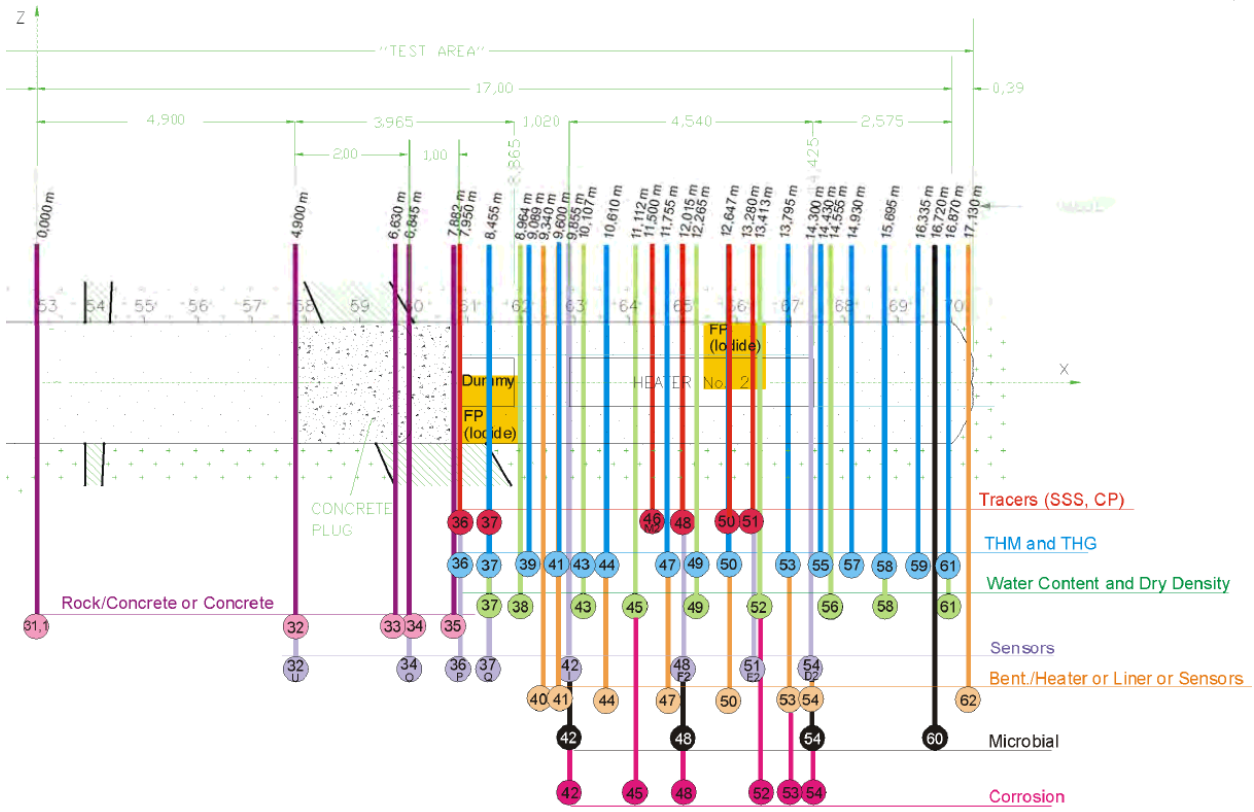

Figure 6-1. Section layout during the dismantling operation of Heater #2, showing the types of monitoring and sampling (Detzner and Kober, 2015)

The sensors installed in the bentonite blocks were used to measure temperature, relative humidity and stress. The bentonite samples that were taken after dismantling of test sections were used to determine the water content and dry density. The dismantling of Heater #1 in 2002 and Heater #2 in 2015 (Table 2-1) provides two snapshots of measured water content, dry density, and ion concentrations in pore water of bentonite, which are important for understanding the temporal evolution of the key THM processes. More detailed description of the FEBEX *in situ* test and available THM data were given in Zheng et al. (2018).

Table 6-1. Timeline of the FEBEX *in situ* test.

Event	Date start	Time (days)	Time (years)
Commencement of heating by Heater #1	2/27/1997	0	0.0
Shutdown of Heater #1	2/2/2002	1827	5.0
Sampling after Heater #1 was dismantled	5/2/2002	1930	5.3
Shutdown of Heater #2	4/24/2015	6630	18.2
Sampling after Heater #2 was dismantled	7/3/2015	6700	18.3

Zheng et al. (2018) described in detail the types of chemical data available in the FEBEX *in situ* test. Ion concentration in the pore-water of granite was collected and measured in the two boreholes parallel to the *in situ* test tunnel, which can be used to evaluate the diffusion of water from bentonite into granite. However, the chemical data for the solid phase are too scattered to be used to determine the spatial trend; data for exchangeable cations are problematic, but could be used with caution; the concentration data were not directly measured and geochemical modeling was involved to infer the ion concentration in pore water from data obtained by aqueous extract. Ion concentrations in pore water of bentonite still the primary data to validate model.

6.3 Model Development

Since FY15, the model interpretation of the FEBEX *in situ* test started from a simple TH model and gradually increased the level of complexity until a coupled THMC model was developed. In FY19, the model effort focused on evaluating key processes that control the hydration of bentonite and a comprehensive interpretation of chemical data. In this section, we briefly present the model setup: more details about the model development can be found in Zheng et al. (2016; 2017).

6.3.1 Simulator

Zheng et al. (2016, 2017) carried out numerical simulations using TOUGHREACT-FLAC3D, which sequentially couples the multiphase fluid flow and reactive transport simulator, TOUGHREACT V2 (Xu et al., 2011), with the finite-difference geomechanical code FLAC3D (Itasca, 2009). The coupling of TOUGHREACT and FLAC was initially developed by Zheng et al. (2012) to provide the necessary numerical framework for modeling fully coupled THMC processes. Modeling was conducted using a linear elastic swelling model (Zheng et al., 2012; Rutqvist et al., 2014) to account for swelling resulting from changes in saturation and pore-water composition, and the abundance of swelling clay (Liu et al., 2013; Zheng et al., 2014). A recent addition to the code is the capability of simulating non-Darcian flow (Zheng et al. 2015b) and thermal osmosis. In FY18, the code was upgraded by replacing TOUGHREACT V2 (Xu et al., 2011) with TOUGHREACT V3.0-OMP (Xu et al., 2014). In comparison with TOUGHREACT V2 (Xu et al., 2011), TOUGHREACT V3.0-OMP (Xu et al., 2014) has the several major improvements (see http://esd1.lbl.gov/research/projects/tough/software/toughreact.html), one of the them is the OpenMP parallelization of chemical routines on multi-core shared memory computers, which significantly decreases the computation time.

6.3.2 Modeling setup

Because the hydration of bentonite during the test was fairly symmetrical, we used an axi-symmetrical mesh (Figure 2-3) to reduce computation time, so that we can focus on the key coupling processes. However, such a model can only be used to interpret and predict the THMC behavior in the “hot sections,”

i.e., Sections 41-54 (specifically Section 49) of the bentonite block surrounding the heater, shown in Figure 6-2.

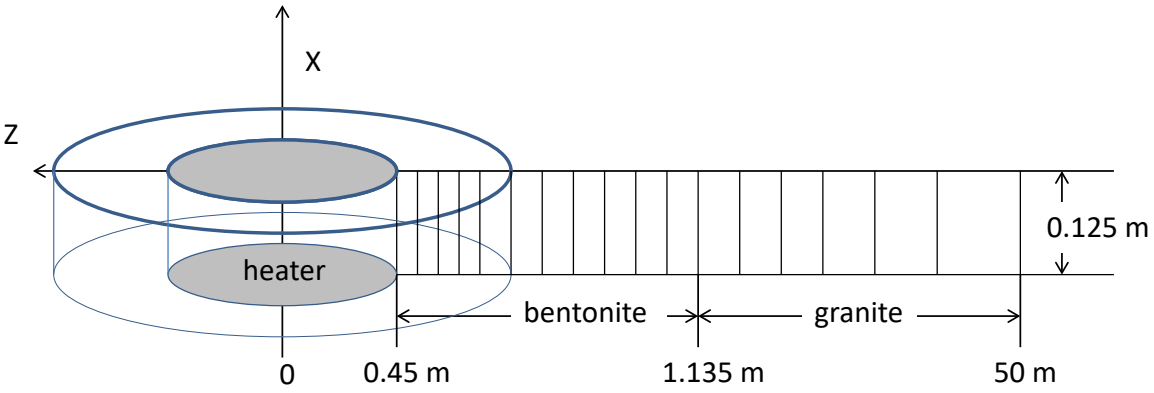

Figure 6-2.Mesh used for the model, shown not to the scale.

The model domain includes two material zones: one for the bentonite, and the other for the granite. The first two nodes (1 and 2) are located on the external wall of the heater (r = 0.45-0.46 m). Bentonite is located within 0.45 m < r < 1.135 m. The remaining domain up to 50 m is used to simulate the granite. The simulation time starts on February 27, 1997, and ends on July 3, 2015, a total of 6700 days (18.3 years).

The initial temperature of 12 ºC was uniform over the model domain. A constant temperature of 100 ºC was prescribed at the heater/bentonite interface (r = 0.45 m), and temperature was assumed to remain constant at its initial value of 12 ºC at the external boundary (r = 50 m), because the thermal perturbation induced by the heaters over the time frame of the experiment did not extend to this boundary.

The bentonite initial gravimetric water content was 14%, corresponding to a degree of saturation of 55% and a suction of 1.11×10^5 kPa. The boundary conditions for flow included: 1) no flow at r = 0.45 m, and 2) a liquid pressure of 7 bars at r = 50 m.

The model considers non-isothermal two-phase (air and water) flow, with each individual phase fluxes given by a multiphase version of Darcy's law. For the vapor flow in the air phase, in addition to Darcy flow, mass transport can also occur by diffusion and dispersion according to Fick's law. In the current model, both conductive (Fourier's law) and convective heat flux were considered in the model, and thermal conductivity is the key parameter. Details of THM model were given in Zheng et al. (2018).

In Zheng et al. (2016), we tested two mechanical models for bentonite: a linear swelling model and dual structure Barcelona expansive clay model (BExM), and found out that both models led to similar fits to measured THM data. Both methods have pros and cons: BExM provide a mechanistic description of the swelling of bentonite, but it is more computationally expensive and parameters are difficult to calibrate, whereas linear swelling models has simple parameterization and parameters can be easily calibrated, but it does not describe correctly the transient state of swelling. Eventually, for the THMC model of the FEBEX *in situ* test, we use a method that is somewhat in between--the state surface approach.

6.3.3 Chemical Model

Although Zheng et al. (2018) presented a detailed description of the chemical model, we provide here a summary of this model to facilitate the discussion in next section.

The development of the chemical model requires the knowledge of initial chemical compositions of bentonite and granite, i.e., the initial mineralogical and pore water concentrations. The mineral phases and their volume fraction are summarized in Table 2-2. Note that these publications provide concentrations as mass fractions, which were converted to volume fractions (ratio of the volume for a mineral to the total volume of medium) using a porosity of 0.41. Note that in the table the minerals with zero volume fractions are the secondary minerals that could be formed.

Table 6-2. Mineral volume fraction (dimensionless, ratio of the volume of a mineral to the total volume of medium) FEBEX bentonite (ENRESA, 2000; Fernández et al., 2004; Ramírez et al., 2002; Villar et al., 2018) and granite (Zheng et al., 2011).

Mineral	**FEBEX Bentonite**	**Granite**
Calcite	0.00472	0
Smectite	0.546	0
Gypsum	0.00059	0
Quartz	0.018	0.37
Cristobalite	0.0059	0.00
K-Feldspar	0.0059	0.35
Plagioclase	0.0059	0.27
Dolomite	0.0	0
Illite	0.0	0
Kaolinite	0.0	0
Siderite	0.0	0
Ankerite	0.0	0
Anhydrite	0.0	0
Chlorite	0.0	0

FEBEX bentonite blocks have an initial gravimetric water content of 13.5–14% (ENRESA 2000). Table 6-3 summarizes the bentonite pore water composition from aqueous extract data and the pore water composition for granite, which were used for modeling.

Table 6-3. Pore-water composition (concentrations are mol/kg water, except for pH) of FEBEX bentonite (Fernández et al., 2001) and granite (Zheng et al., 2011).

	EBS Bentonite: FEBEX	Granite
pH	7.72	8.35
Cl	1.60E-01	1.31E-05
SO_4^{-2}	3.20E-02	7.86E-05
HCO_3^-	4.1E-04	3.97E-04
Ca^{+2}	2.2E-02	1.81E-04
Mg^{+2}	2.3E-02	1.32E-06
Na^+	1.3E-01	3.76E-04
K^+	1.7E-03	7.80E-06
Fe^{+2}	2.06E-08	2.06E-08
$SiO_2(aq)$	1.1E-04	6.07E-04
AlO_2^-	1.91E-09	3.89E-08

In the chemical model, we consider aqueous complexation, cation exchange, surface complexation and mineral dissolution/precipitation. Details of aqueous complexes and their disassociation constants for reactions, solubility and reaction rate for minerals are given in Zheng et al. (2018)

6.4 Coupled THMC Model

The ultimate goal of using a coupled THMC model is to interpret the data collected in the FEBEX *in situ* test and to understand the THMC evolution of bentonite under simulated repository conditions. Once the coupled THMC model can simultaneously match the measured temperature, relative humidity, water content, stress, aqueous concentrations, and mineral phase changes, we can further use it to predict the long-term alteration of bentonite buffer under different conditions, such as under higher temperature, as was done by Zheng et al. (2015a). In this section, we first recap the model results for the base THMC model developed from FY16 to FY19, and then present the results of simulations with longer running time to show the evolution of bentonite barrier in the long run.

6.4.1 Base THMC model

From FY16 to FY19, the model for FEBEX *in situ* test evolved from the TH model (Zheng et al., 2016) to THMC model that can reasonably interpret THMC data collected at the test site (Zheng et al., 2018, 2019a, 2019b).

Because TH model overestimated the relative humidity data (Zheng et al., 2016), water content data, additional processes were added seeking better match between data and model. First, mechanical effects, using the state surface approach, were added to the model to simulate the swelling of bentonite, expanding the model from a TH to a THM model. As a result of the swelling, the porosity changed, as did the permeability. Variable permeability as a function of the dry density was used. Second, another coupled process, thermal osmosis, was added to the model, using a calibrated thermal osmotic permeability.

The calibrated THMC model, referred to as the base THMC model in this report, was able to provide a reasonable match to the measured temporal evolution of temperature (Figure 6-3) , relative humidity (Figure 6-4), and measured spatial distribution of water content at 5.3 years and 18.3 years (Figure 6-5), stress at several radial distances (Figure 6-6), and the chloride concentrations measured at 5.3 years (Figure 6-7) and 18.3 years (Figure 6-8). This confirmed the necessity of using a THM model to explain the hydrological behavior of bentonite. However, TH and THMC models led to similar temperature profiles, as demonstrated in Figure 6-3, indicating it was not necessary to use a full THM/THMC model to calculate temperature

evolution. The TH model overestimated significantly the water content data at 18.3 years, but only slightly at 5.3 years, signifying the importance of having long-term data for calibration.

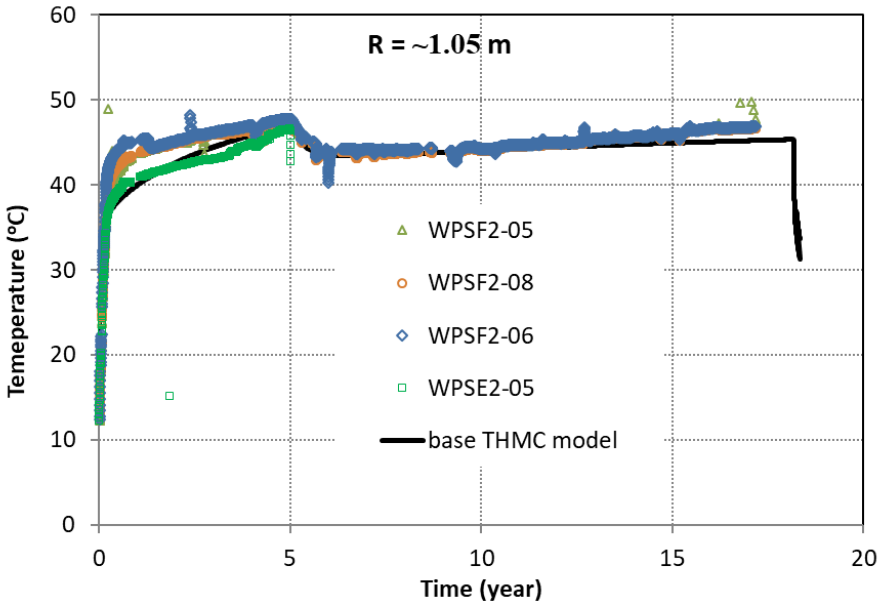

Figure 6-3. Measured temperature by sensors at different locations, but the same radial distance (1.05 m) and results from the base THMC model.

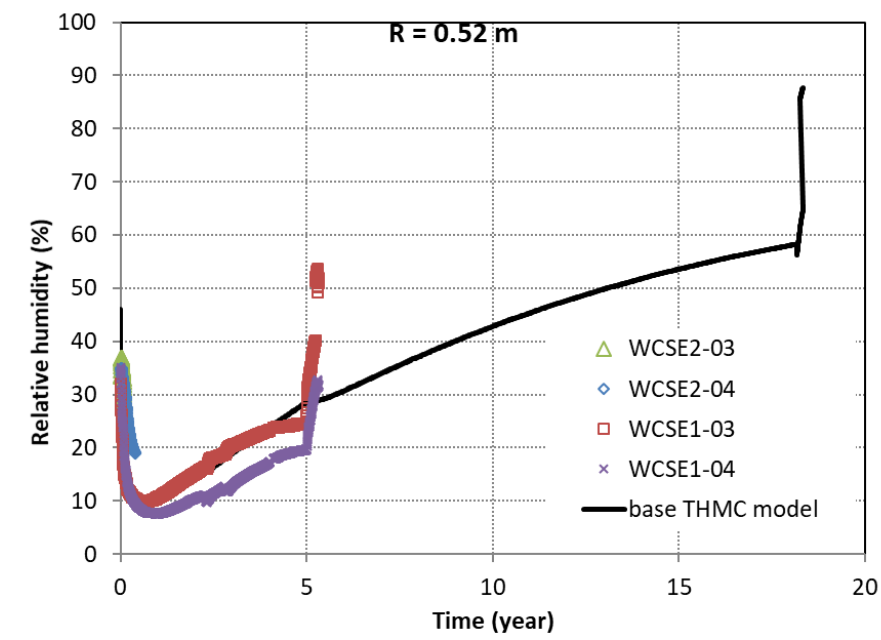

Figure 6-4. Relative humidity data measured from sensors at different locations, but the same radial distance (0.52 m), and model results from the base THMC model.

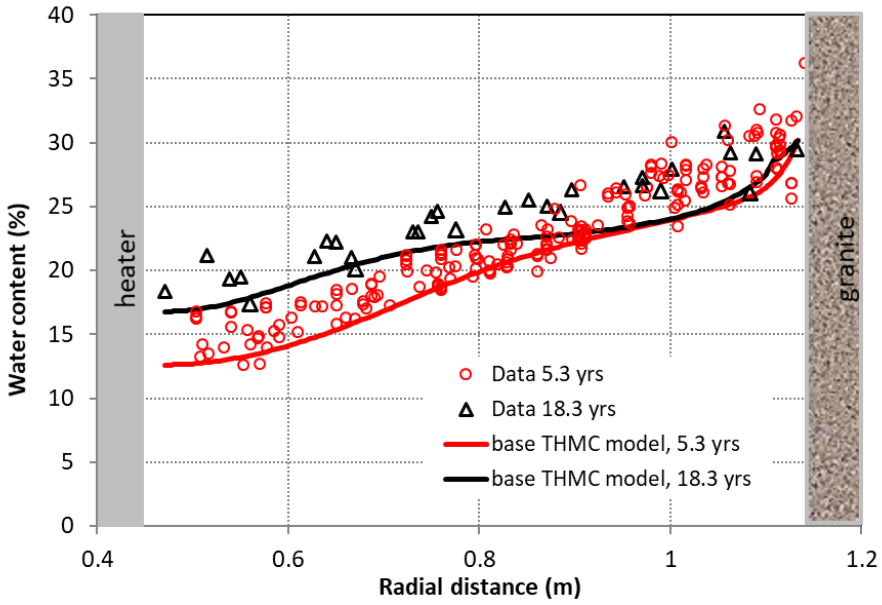

Figure 6-5. Measured water content at 5.3 years and 18.3 years, and results from the base THMC model.

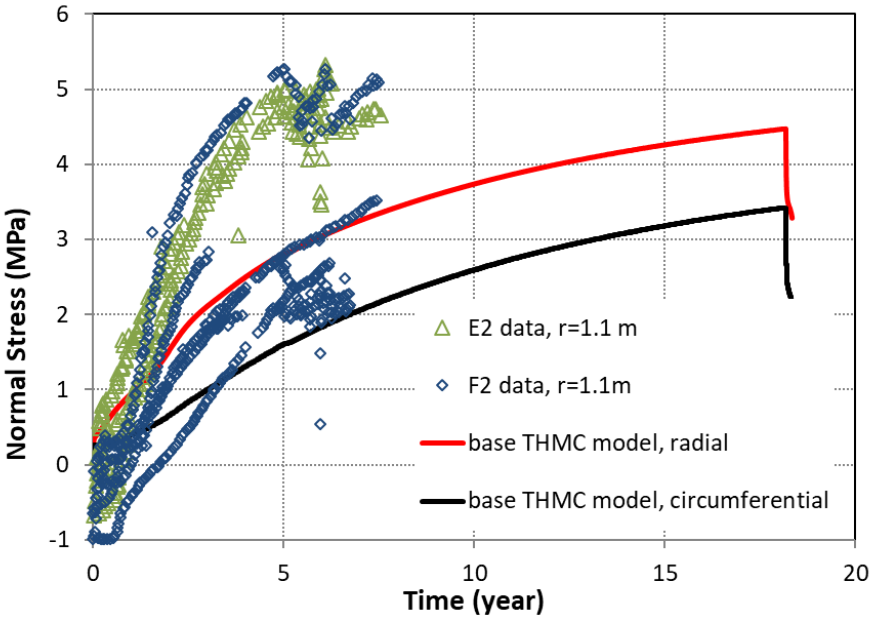

Figure 6-6. Measured stress by sensors at different locations (from sections E2 and F2, see ENRESA, 2000), but the same radial distance (1.1 m), and results from the base THMC model.

Geochemical evolution is the consequence of coupled THMC processes. THM processes strongly affect the geochemical evolution, but usually not vice versa, which is why a great deal of efforts was dedicated to have a sound THM model that can match the THM data. Once the THM processes are relatively well established, before we study the possible chemical reactions, we need to constrain the transport process. While the advection of chemical species is fixed in the THM model, diffusion has to be calibrated in the chemical model.

Because chloride is only controlled by transport processes, its temporal and spatial evolution is a good indicator of the transport processes. The THMC model nicely fit the data near the heater (Figure 6-7), indicating that the chloride concentration could be fairly high at the canister-bentonite interface. If such a trend persists for an extended time period until the canister is fully corroded, the high chloride concentration might significantly affect the degradation of waste. As granite pore water (which has much lower chloride concentration than bentonite pore water) penetrates into the bentonite, it dilutes significantly the bentonite pore water, and the chloride concentration is reduced near the granite at the radial distance between 0.8 and 1.1 m. Meanwhile, bentonite pore water was pushed further near the heater by advection and evaporation causes an increase in the chloride concentration, as manifested by the high chloride concentration near the heater.

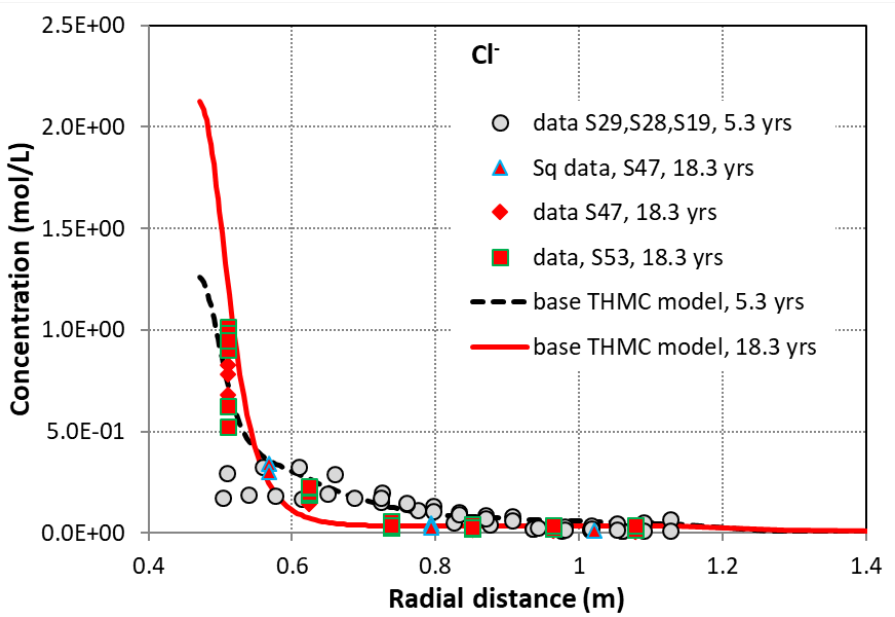

Figure 6-7. Calibrated chloride concentration data at 5.3 years from aqueous extract test for Sections 29, 28, and 19 (Zheng et al., 2011), calibrated chloride concentration data at 18.3 years from aqueous extract test for Section 47 ("data S47, 18.3 yrs") and Section 53 ("data S53, 18.3 yrs"), chloride concentration data from squeezing test for Section 47 ("Sq data, S47, 18.3 yrs"), and model results from the base THMC model.

The base THMC model (Zheng et al., 2018, 2019a) also showed that the key coupling processes that were required to match THM data and chloride concentration include vapor diffusion, porosity change due to swelling, permeability change as a function of dry density, and thermal osmosis.

The concentration profile of pH, bicarbonate and sulfate were largely determined by chemical reactions. The potassium profile (Figure 6-8) is largely shaped by transport processes, despite potassium is affected by cation exchange and precipitation of illite. The pH profile is an example of the effect chemical reactions. Because of the buffer by surface protonation, the spatial profile of pH is also fairly flat, except in the area near the granite and the heater (Figure 6-9). The increase in pH in bentonite pore water at the vicinity of heater is related to the dissolution of montmorillonite (Figure 6-10).

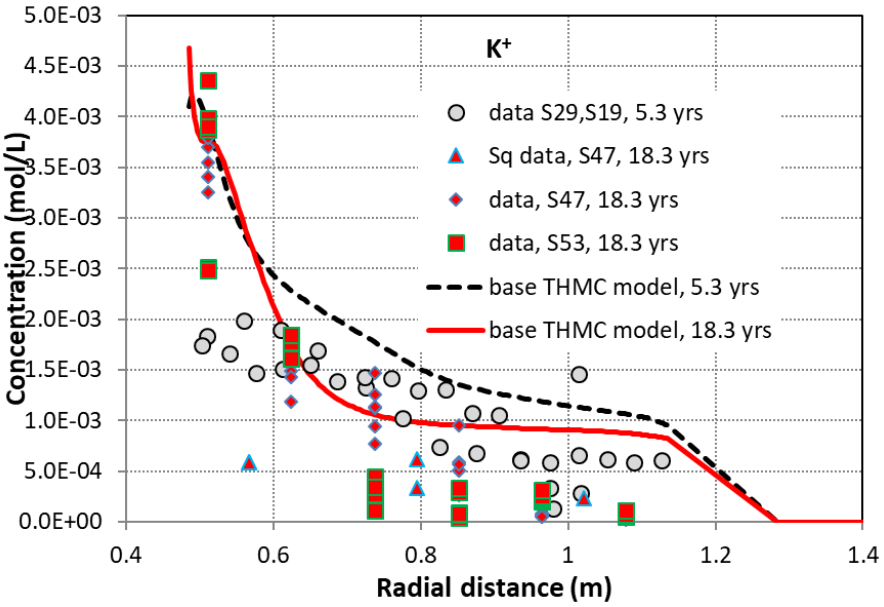

Figure 6-8. Calibrated potassium concentration data at 5.3 years from aqueous extract test for Sections 29, 28, and 19 (Zheng et al., 2011), calibrated chloride concentration data at 18.3 years from aqueous extract test for Section 47 ("data S47, 18.3 yrs") and Section 53 ("data S53, 18.3 yrs"), chloride concentration data from squeezing test for Section 47 ("Sq data, S47, 18.3 yrs"), and model results from the base THMC model.

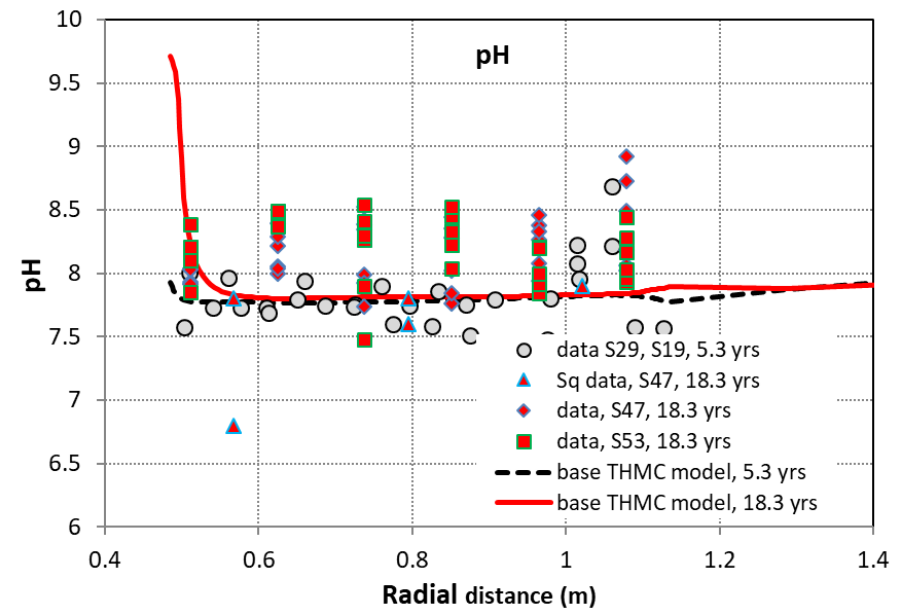

Figure 6-9. Calibrated pH data at 5.3 years from aqueous extract test for Sections 29, 28, and 19 (Zheng et al., 2011), calibrated chloride concentration data at 18.3 years from aqueous extract test for Section 47 ("data S47, 18.3 yrs") and Section 53 ("data S53, 18.3 yrs"), chloride concentration data from squeezing test for section 47 ("Sq data, S47, 18.3 yrs"), and model results from the base THMC model.

Apparently, the evolution of clay minerals, namely smectite and illite, has great implications to the long-term stability of the bentonite barrier. While many laboratory heating tests are often too short to show significant change in clay minerals or conditions in the laboratory tests are very different from the *in situ* conditions, and the implications of these test results require interpretation. The mineral characterization of the samples collected after the final dismantling provides insight into the possible change of clay minerals after long-term heating and hydration. Unfortunately, given the large variation of the illite fraction in the illite/smectite mixed layer between samples, it is impossible to delineate if there is any increase or decrease of the illite mass fraction by comparison with the reference bentonite. Models show illitization near the heater, as manifested by illite precipitation and

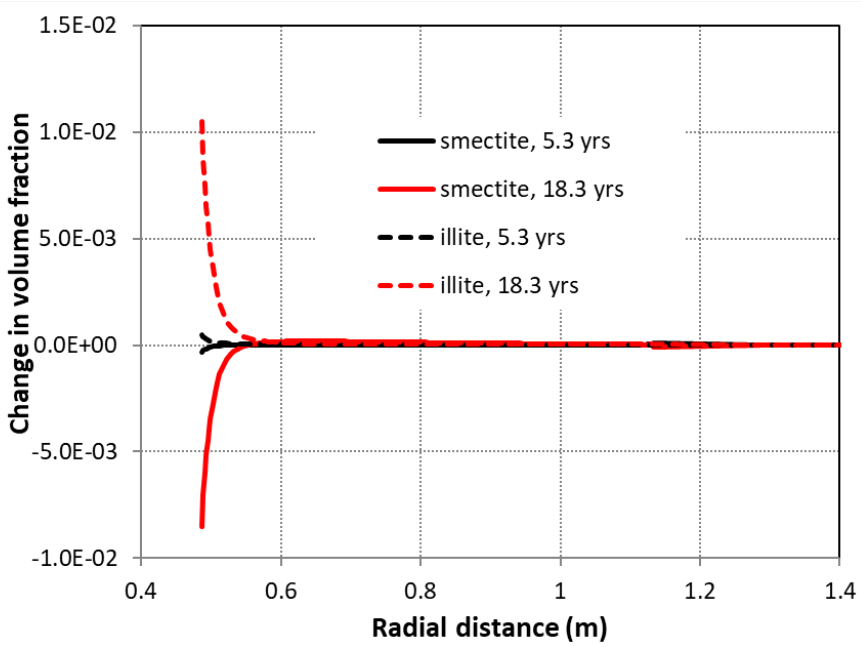

montmorillonite dissolution, but on the order of less than 1%, which cannot be proved or disapproved by the data.

Figure 6-10. Model results of smectite and illite volume fraction change at 5.3 years and 18.3 years. Negative values mean dissolution, and positive values means precipitation.

6.4.2 The long-term evolution

One of the most challenging issues for performance assessment of geological disposal of high-level radioactive waste is the prediction of long-term evolution of the repository. Typically, the safety performance assessment requires an evaluation for up to 100,000 years. But this is way beyond the time any experiment can run. So far, the longest experiment is the FEBEX *in situ* test that had been running for 18 years, which is much shorter than the required safety evaluation time. What researchers in the community of radioactive waste disposal can best do is to build a validated numerical model to carry out long-term predictions. After the THMC models were tested to make long-term predictions of the evolution of the bentonite barrier, we extended the base THMC model to conduct longer time predictions. Meanwhile, long-term THC modeling was also conducted. The THMC and THC models attempt to answer some questions. The first question is that how long it takes for the bentonite to be fully saturated, and the second question is whether high ion concentrations in pore water are expected in bentonite in the vicinity of a canister in the long run. As we see in the previous section, high Cl concentration was observed in the area near the heater. Such high concentration might have an important implication for the corrosion of a canister and even the

waste degradation. But after bentonite becomes fully saturated, do concentrations remain at a high level? And the third question is related to the long-term evolution of smectite. The THMC model for the FEBEX *in situ* test showed a relatively small amount of illitization (dissolution of smectite and precipitation of illite) at an area near the heater after 18 years of heating and hydration. The question is whether there will be a significant amount of illitization in such conditions, if we run the model much longer? The last question is whether the THC model results are substantially different from THMC results at the later time (e.g., after bentonite becomes fully saturated). To answer these questions, we presented the results of two simulations here. The first one is a THMC model running for 200 years. The model keeps all other conditions the same except the heat decay curve was applied to the heater, it is named the "THMC model" when discussing results. The shape of the function is similar to that used in Rutqvist et al. (2011) for a 2D model, but the magnitude is scaled down so that the temperature in the EBS close to the heat source is around 100 ºC. Then, a THC model, which is similar to the THMC model with two differences: (1) there is no mechanical calculation, and (2) permeability and porosity are constants, unlike that in the THMC model permeability and porosity changes due to mechanical (swelling) process in bentonite.

Figure 6-11 shows the evolution of temperature at several radial distances for the THMC and THC models. As we learned from the modeling exercise for FEBEX *in situ* tests (Zheng et al., 2016), the difference in calculated water content from the THC and THMC models does not lead to noticeable differences in calculated temperature profile, because resulting thermal conductivity (which is a function of water content) is quite small.

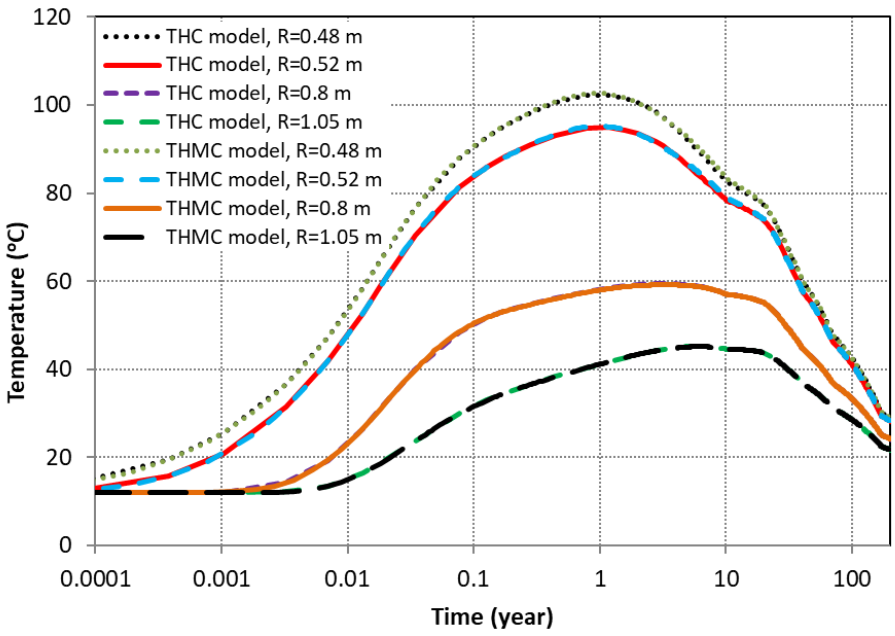

Figure 6-11. Temporal evolution of temperature at several radial distances using the THC and THMC model.

Using THMC model instead of the THC model for the interpretation of the FEBEX *in situ* test (see previous sections) were largely driven by fitting the relative humidity at the area near the heater (i.e., at a radial distance of 0.48 m). In Figure 6-12, relative humidity (RH) at radial distances of 0.48 m and 0.8 m are indeed quite different in the early time (< 20 years) for the THC and THMC models. The RH difference is about 10-15%. However, as bentonite is close to the full saturation in about 35 years, when the RH is about 92-97%, THC and THMC models are very similar. Both models show that after the majority of the area of

bentonite buffer becomes full saturated, a small, 3-5 cm away from the heater, maintained high RH, 97%, but not full saturation for a long time.

Both models show that inside the bentonite barrier at the near vicinity of the heater/canister, the evolution of the relative humidity goes through 3 phases. An early desaturation phase that lasts about 1 year and is featured with a sharp decrease of relative humidity; a rapid re-saturation phase, which ends around 35-40 years in the current model; and then bentonite barrier enters into a slow re-saturation phase: relative humidity at R = 0.48 m increases from 92% at 35 years to 97% at 200 years in the THMC model. However, whether the relative humidity in bentonite near the heater stays around 97% or 100% might be important for corrosion and waste degradation.

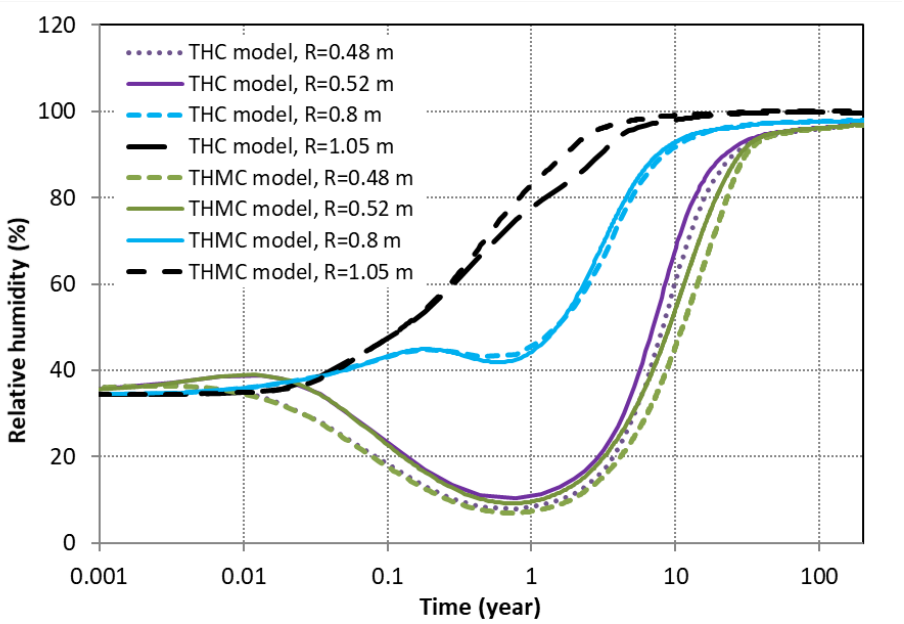

Figure 6-12. Temporal evolution of relative humidity at several radial distances in the THC and THMC models.

Similar to the relative humidity, the water saturation degree from THC and THMC model is just marginally different after 50 years (Figure 6-13) despite differences in the early times. It seems that hydrologically THC and THMC models are quite similar in the long run.

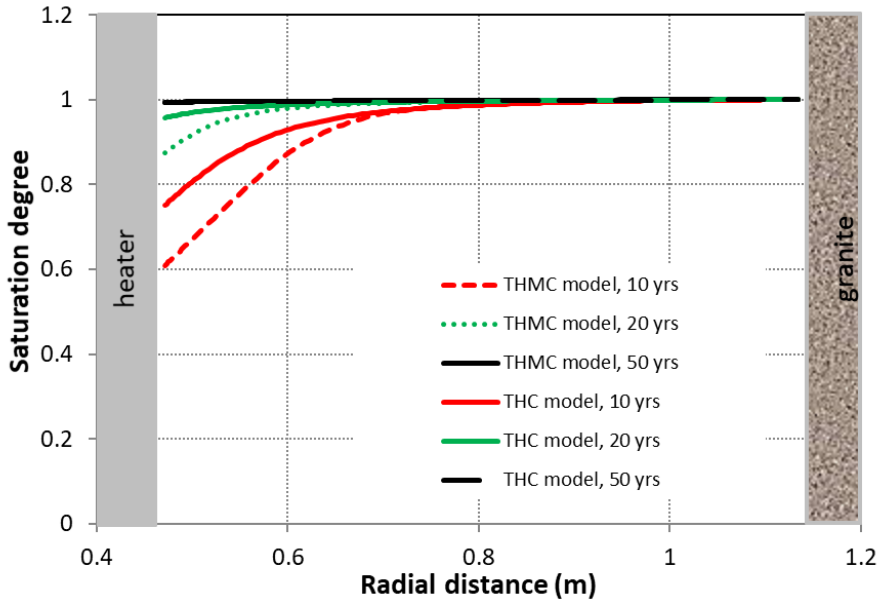

Figure 6-13. Radial distribution of the saturation degree at several times in the THC and THMC models.

In the FEBEX *in situ* test, high ion concentrations in the pore water of bentonite were observed. For example, as shown by chloride concentration profiles in Figure 6-7, the chloride concentration reaches about 2 mol/L near the heater. Such high concentrations are largely the result of evaporation. Then, the question is whether the concentration will decrease when the bentonite barrier becomes fully saturated. Figure 6-14 shows that chloride concentration is almost evenly distributed in the bentonite barrier with a concentration of about 0.1 mol/L, slightly lower than the initial chloride concentration in the pore water of bentonite (0.16 mol/L). The THC and THMC models give quite similar results.

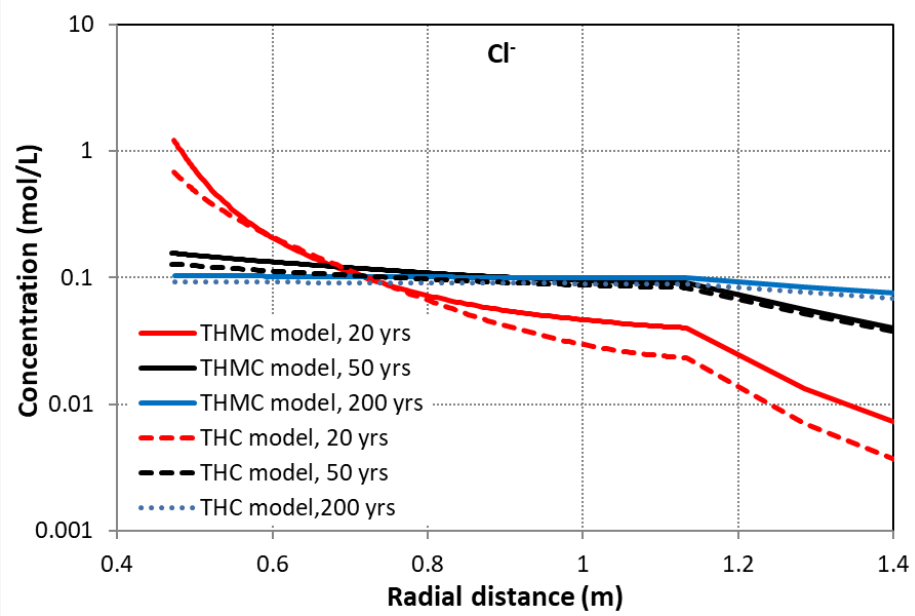

Figure 6-14. Spatial profiles of chloride concentration at several time points in the THC and THMC models.

As we found out from previous modeling work (e.g., Zheng et al., 2016; 2017), the concentration profiles of cations (calcium, potassium, magnesium, and sodium) were largely shaped by transport processes despite their concentration levels being affected by mineral dissolution/precipitation and cation exchange. Like for chloride, the spatial profile of potassium flattens out in the bentonite barrier: the concentration near the heater is just slightly higher than that near the granite. However, unlike chloride, the potassium concentration in THC and THMC models are quite different. It indicates that early chemical reactions history has a long-term effect on the reactive species like potassium.

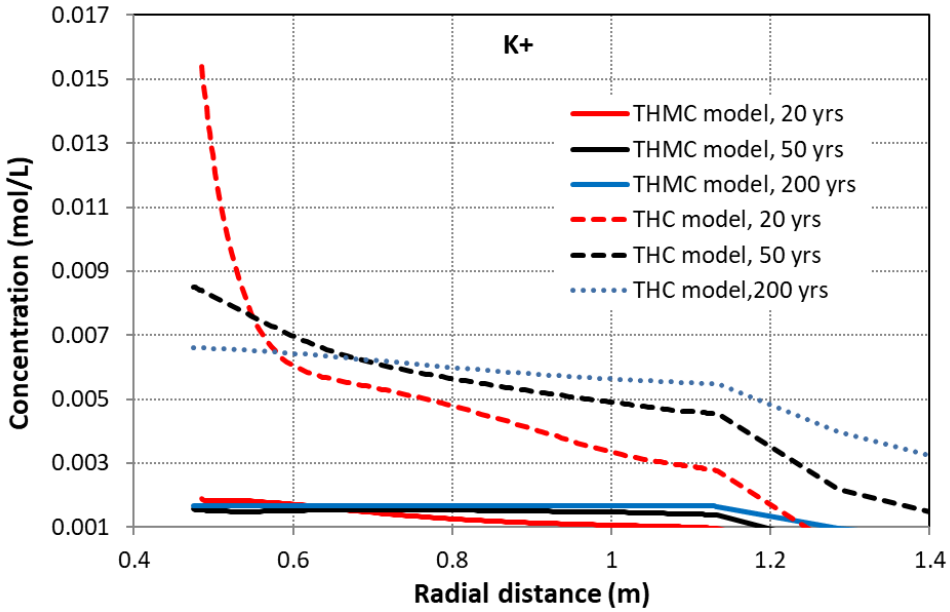

Figure 6-15. Radial profiles of potassium concentration at several times in the THC and THMC models.

Illitization (transformation of montmorillonite to illite) was one of the major concerns that led to the establishment of a thermal limit of 100 ºC for the argillite and crystalline repository with bentonite barrier throughout the world (Zheng et al., 2015). The base THMC model shows that montmorillonite dissolves and illite precipitates (illitization is usually expressed as the dissolution of montmorillonite and precipitation of illite, but here we only show the dissolution of montmorillonite) in bentonite near the heater with an amount less than 1% after 18 years, which was neither disapproved nor approved by the data, because the data for mineral phase were too scattered (Zheng et al., 2018). It is known that illitization is a very slow process (Zheng et al., 2015a). The question raised here is, if the model runs longer, will there be a significant amount of illitization? By comparing the calculated montmorillonite volume fraction change at 50 years and 200 years (Figure 6-16), for the environment of FEBEX bentonite in the granite host rock, illitization does not proceed further. If we compare the THC and THMC models, the difference is significant: in the area with the montmorillonite dissolution, the THC model predicts a double amount of montmorillonite dissolution; in the area very close to the heater, THC model predicts re-precipitation of montmorillonite, whereas THMC model does not.

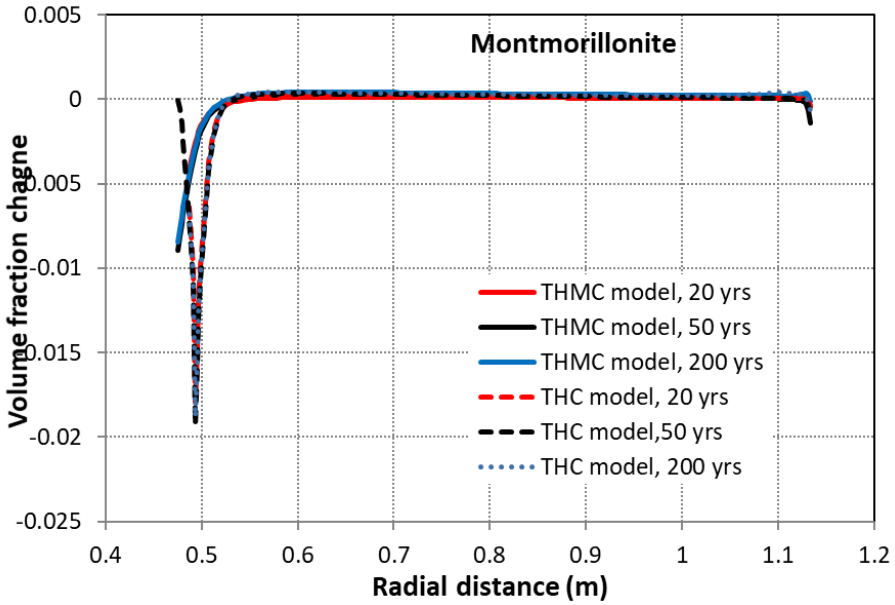

Figure 6-16. Model results for montmorillonite volume fraction change at several times in the THC and THMC models.

At the time of preparation of this progress report, THMC simulation was very slow, only running up to 200 years. The THC model is running to 10,000 years. Figure 6-17 shows the model result for montmorillonite at 1000 years and 10,000 years. Comparing results for 200 years, model results do not show further dissolution or precipitation of montmorillonite at areas near the heater (the radial distance of ~0.47-0.5m), but in the rest of area, there is a precipitation of montmorillonite, especially near the granite.

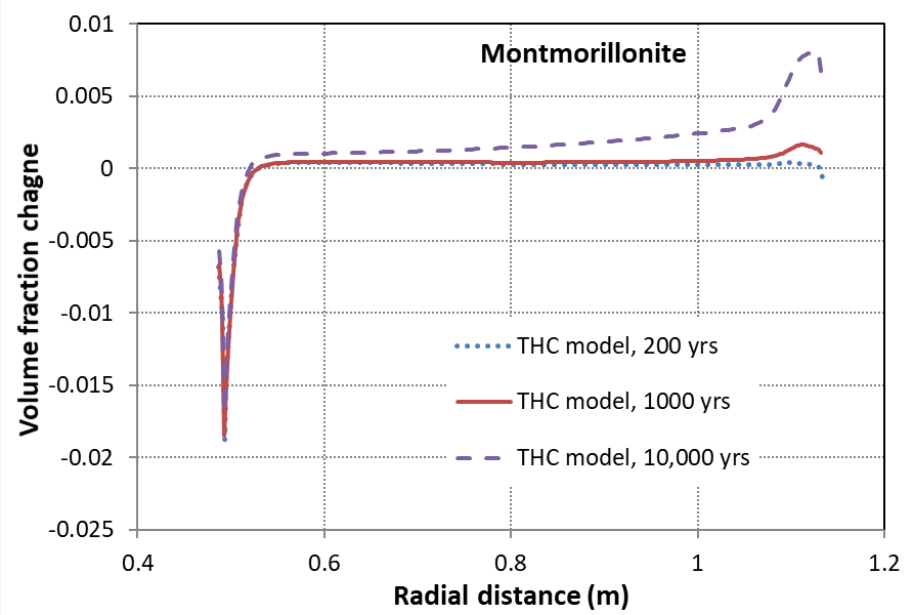

Figure 6-17. Model results for montmorillonite volume fraction change at 200 years, 1000 years, and 10,000 years in the THC model.

6.5 Summary and Future work

The FEBEX *in situ* test, which lasted more than 18 years, is extremely valuable for validating the coupled THMC model and improving our understanding of the evolution of the bentonite barrier throughout heating and hydration. The ultimate goal is to use THMC data from FEBEX-DP to validate the THMC models, and therefore enhance our understanding of coupled THMC processes in bentonite.

From FY16 to FY19, extensive model calibrations were conducted, and finally, in FY19, the THCM model provided a coherent explanation of THMC data collected at the FEBEX *in situ* test. In FY20, the modeling work is therefore to use the THMC model to explore the long-term alteration to bentonite. The first question we are trying to address is the necessity of using the THMC model for studying long term alteration of bentonite, especially the geochemical alteration. The use of the THMC model is computationally expensive and numerically more unstable than the THC model, while up-gradation of the THMC code, using parallel computing and the better solver, can alleviate this issue. Using the THC model could be beneficial in terms of the computation time and simulation stability, knowing that the performance assessment is most likely based on THC simulations, not THMC simulations.

The following results of simulations were obtained:

- In terms of the hydrological behavior, the THMC and THC modeling results are similar for the period of 50 years despite of a remarkable difference for the first 30 years.
- Evolution of conservative species (e.g., chloride) based on the results of THMC and THC modeling are similar
- The evolution of reactive species (e.g., potassium) based on the results of THMC and THC modeling are different, indicating that the reaction history in THMC and THC models in the early time (<30 years) have a long-term effect.
- Bentonite will become fully saturated in 30-40 years based on the model with a heat decay function, and the bentonite barrier is expected to homogenize in most areas.
- High chemical concentrations in bentonite near the heater, which were observed in the field test, are predicted to disappear after bentonite becomes fully saturated.
- Illitization will continue for 50 years, but won't proceed. However, the THC model shows more illitization in area near the heater compared to the THMC model.

In the remaining time of FY20 and FY21, we will continue improving the stability and numerical efficiency of TOUGHREACT-FLAC and finish the long-term THMC simulations. In addition, a reactive transport model will be developed to study the geochemical changes at the interfacial areas, including the bentonite/concrete interface and the bentonite/steel interface.

This page is intentionally left blank.

7. MODELING IN SUPPORT OF HOTBENT, AN EXPERIMENT STUDYING THE EFFECTS OF HIGH TEMPERATURES ON CLAY BUFFERS/NEAR-FIELD

7.1 INTRODUCTION

Several international disposal programs have recently initiated investigations of whether clay-based barriers can withstand temperature higher than the 100 °C threshold for bentonite that is usually considered in mined repository designs. For example, the SFWST campaign has been investigating the feasibility of direct geological disposal of large spent nuclear fuel canisters, currently in dry storage (Hardin et al., 2014), which are expected to result in much higher emplacement temperature. Even for small canisters with 2 or 4 PWR, allowing a thermal limit go higher can significantly decrease a footprint of the repository, and, therefore, reduce the cost of the repository. The performance of bentonite barriers in the <100 °C temperature range is underpinned by a broad knowledge based on laboratory and large-scale *in situ* experiments. Bentonite characterization at above 100 °C is less common, although for temperature up to about 150 °C no significant changes in safety-relevant properties were determined (e.g. Cheshire et al., 2014). At temperature above 150 °C, it is possible that a potentially detrimental temperature-driven physical-chemical response of materials (cementation, illitization) may occur, the characteristics of which are highly dependent on, and coupled with, the complex moisture transport processes induced by strong thermal gradients. The impact of such complex processes on the performance of a repository cannot be realistically reproduced and properly (non-conservatively) assessed at a small laboratory scale. Such an assessment needs to be conducted by large-scale *in situ* experiments at URLs, where the most relevant features of future emplacement conditions can be adequately reproduced.

Potential options for a targeted high-temperature experiment (150 °C to 200 °C) in a crystalline rock environment are currently being considered under the leadership of NAGRA with several international partners. The proposed HotBENT experiment will be conducted in the well-characterized FEBEX drift at the Grimsel Test Site. The benefit of such a large-scale test, accompanied by a systematic laboratory program and modeling effort, is that the temperature effects can be evaluated under realistic conditions of strong thermal, hydraulic and density gradients, which cannot be reproduced in the laboratory. This will lead to the development of improved mechanistic models for the prediction of temperature-induced processes, including chemical alteration and mechanical changes, which can then be used for the performance assessment (PA) analysis of high-temperature scenarios. The key question is whether higher repository temperature would trigger mechanisms that compromise the various barrier functions of the engineered components and the host rock. If the barrier function is (at least partially) compromised, the PA analysis can evaluate whether a reduced performance of a sub-barrier (or parts thereof) would still provide an adequate performance.

HotBENT partners include NAGRA(Switzerland), U.S. DOE (USA), SURAO (Czech Republic), NUMO (Japan), RWM (UK), BGR (Germany), ENRESA (Spain), Obayashi (Japan). Participation in the HotBENT testing would be beneficial for DOE. Substantial cost savings would be achieved in the design of a repository, if HotBENT demonstrates that the maximum temperature of bentonite backfill can be raised without drastic performance implications.

LBNL/DOE was part of the HotBENT project since the very beginning, including the initiation of the idea of large-scale high temperature field test (Vomvoris, et al., 2015) and using numerical models to support the design of the experiment. For example, Zheng et al. (2018) developed the models of a simple geometric setup, both 1D or 2-D, with consideration of coupled thermal, hydrological, mechanical and chemical (THMC) processes. Zheng et al. (2019) developed a 3D THM model to further understand the evolution of all the design components. However, these simulations were conducted based on bentonite parameters that are similar to those of the FEBEX bentonite in the *in-situ* test (ENRESA, 2000). In April 2020 (Kober et

al, 2020), the design for HotBENT was finalized. In this report, we provide the results of THC modeling to predict the evolution of Woyming bentonite that will be used in the HotBENT

7.2 Status of HotBENT

The final design of HotBENT is shown in Figure 7-1. In this design, the test is composed of 4 modules that differ in heating temperature, bentonite parameters, time length and with or without concrete liner. Module H4 locates closest to the instrumentation area. A 2-meter-long heater will be emplaced on top of bentonite pedestals and then surrounded with granular bentonite mixture (GBM). Pedestals are bentonite blocks. Bentonite used in module H4 is the BCV bentonite, a type bentonite from Czech Republic. Module H4 targets a heater at temperature of 175 ºC, and is planned to run for 5 years. Module H3 is similar to module H4, except the bentonite is Wyoming bentonite. Module H2 is identical to module H3 in design, except it will run for longer time. One lesion learnt from modeling the FEBEX *in situ* test (Zheng et al., 2018) is that multiple temporal snapshots of spatial distribution of key THMC results are critical for finding the "right" model and enhance the predictability of modeling. Modules H2 and H3 will provide two snapshots of THMC evolution of Wyoming bentonite. Module H1 has similar design to module H2, but with two differences: first, temperature will be 200 ºC for the heater rather than 175 ºC for the heater in module H2, and second, a concrete liner will be installed to the rock wall of the test tunnel.

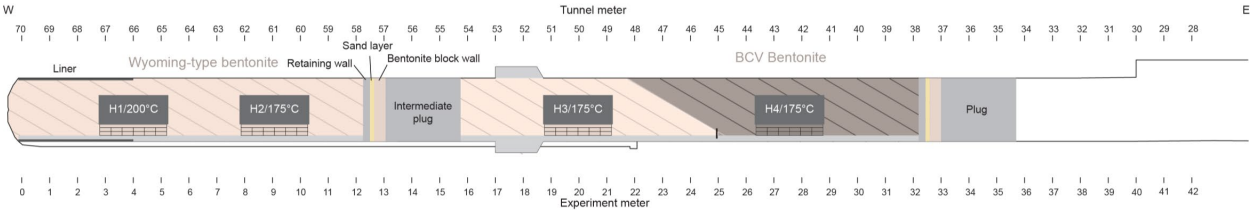

Figure 7-1. Design of modules for HotBENT (Kober et al, 2020).

Bentonite blocks will be used to build a pedestal below the heater and the rest of space will be filled with GBM (Figure 7-2). The target dry density for bentonite blocks is 1.78 g/cm^3 and for GBM is 1.5 g/cm^3. The Wyoming type Na bentonite is Laviobent_GN0318, formerly known as MX-80.

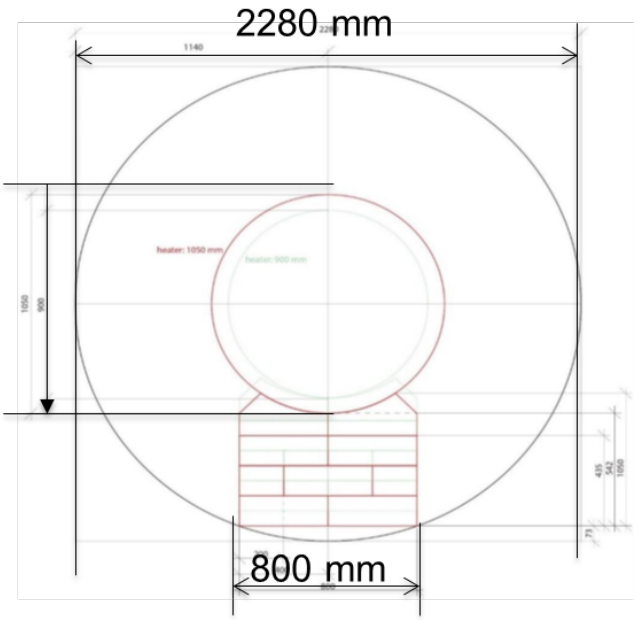

Figure 7-2. Cross section of HotBENT experiment at areas with heaters (Kober, et al., 2020)

The time schedule for the HotBENT experiment is given in Figure 7-3, but adjustment might be expected as the experiment enters into construction.

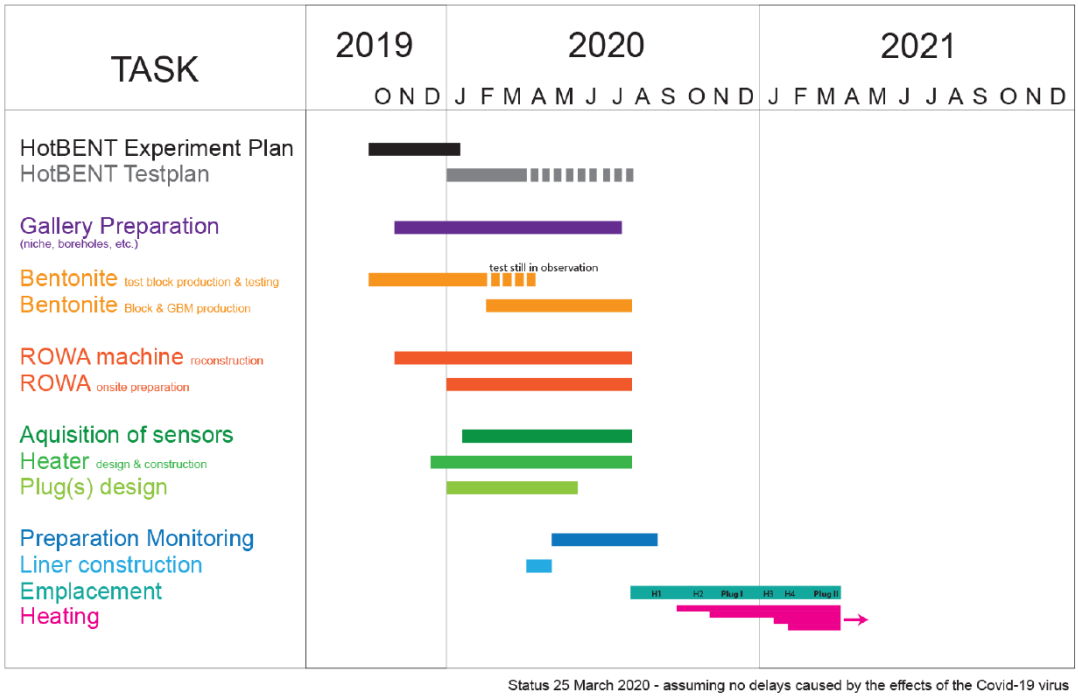

Figure 7-3. Time-schedule for the HotBENT experiment (Kober, et al., 2020)

7.3 Predicative Model for HotBENT

7.3.1 Introduction

While working with the NAGRA and HotBENT partners to finalize the design of the HotBENT test and an instrumentation plan, LBNL also conducted simulations to further understand what's expected in the HotBENT test. Zheng et al. (2017; 2018; 2019) conducted 1D axi-symmetrical simulations based on the THMC model for FEBEX *in situ* test and 2-D THC modeling assuming the FEBEX bentonite. Finsterle (2017) developed a 3D TH model for varioius scenarios to facilitate the design of the field test. As in the final design, two types of bentontie are going to be used: MX-80 and BCV bentonites. In this report, we developed a 1D axi-symmetric THC model to study the geochemical changes of MX-80 bentontie in HotBENT.

7.3.2 Model Development

The model was developed based on the THMC model for the FEBEX *in situ* test (see Chapter 6), with two major differences: the bentonite is Wyoming bentonite (MX-80) instead of FEBEX bentonite, and the hydraulic pressure in granite is 2 MPa instead of 0.7 MPa. The natural hydraulic pressure surrounding the FEBEX tunnel is around 7 bars (ENRESA 2000). In order to ensure a speedy hydration of bentonite in HotBENT, artificial hydration by pressurizing the granite around the tunnel will be used and the target pressure would be 2 MPa.

7.3.3 Simulator

The numerical simulations in Zheng et al. (2016, 2017) were conducted with TOUGHREACT-FLAC3D, which sequentially couples the multiphase fluid flow and reactive transport simulator, TOUGHREACT V2 (Xu et al., 2011), with the finite-difference geomechanical code FLAC3D (Itasca, 2009). The coupling of TOUGHREACT and FLAC was initially developed by Zheng et al. (2012) to provide the necessary numerical framework for modeling fully coupled THMC processes. It was equipped with a linear elastic swelling model (Zheng et al., 2012; Rutqvist et al., 2014) to account for swelling as a result of changes in saturation and pore-water composition and the abundance of swelling clay (Zheng et al., 2014). In FY18, the code went through a major upgrade by replacing TOUGHREACT V2 (Xu et al., 2011) with TOUGHREACT V3.0-OMP (Xu et al., 2014). In comparison with TOUGHREACT V2 (Xu et al., 2011), TOUGHREACT V3.0-OMP (Xu et al., 2014) has the several major improvements (see http://esd1.lbl.gov/research/projects/tough/software/toughreact.html), one of the them is the OpenMP parallelization of chemical routines on multi-core shared memory computers, which significantly decreases the computation time.

7.3.4 Modeling setup

Unlike the FEBEX *in-situ* test, in which pre-fabricated blocks were used everywhere, in HotBENT, bentonite blocks will be used to build a pedestal below the heater, and the rest of space will be filled with granulated bentonite mixture (GBM) (Figure 7-3). However, to take advantage of existing model and use it as a precursor for the 2-D cross-sectional model, we still use an axi-symmetrical mesh (Figure 7-4), despite of knowing that the hydration won't be totally axi-symmetrical, because of the pedestal bentonite blocks have different properties from GBM. Such practice saves computation time, so that we can focus on the key coupling processes. Because the geochemical alteration will mostly be triggered by the interaction between granite water and bentonite, and geochemical interaction between pedestal and GBM is only limited to the near vicinity of their interface (Zheng et al., 2018), current modeling results are expected be valid for areas far away from the pedestal.

The model considers two material zones: one is for the bentonite, and the other is for the granite. The first two nodes (1 and 2) are located on the external wall of the heater (r = 0.45-0.46 m). Bentonite is located within 0.45 m < r < 1.135 m. The remaining domain up to 50 m is used to simulate the granite. The simulation is conducted for 10 years.

The initial temperature of 12 ºC is uniformly distributed. A constant temperature of 200 ºC is prescribed at the heater/bentonite interface (r = 0.45 m), while the temperature is assumed to remain constant at its initial value of 12 ºC at the external boundary (r = 50 m), because the thermal perturbation induced by the heaters over the time frame of the experiment does not extend to this boundary.

The initial a gravimetric water content of bentonite is 14%, which corresponds to a saturation degree of 55% and a suction of 1.11×10^5 kPa. The boundary conditions for flow include: 1) no flow at r = 0.45 m, and 2) a liquid pressure of 2 MPa at r = 50 m, as the area surrounding the tunnel will be pressurized by constantly injecting Grimsel groundwater with a target pressure of 2 MPa through 4 boreholes locating roughly 2 m away from the tunnel wall (Kober et al., 2020) .

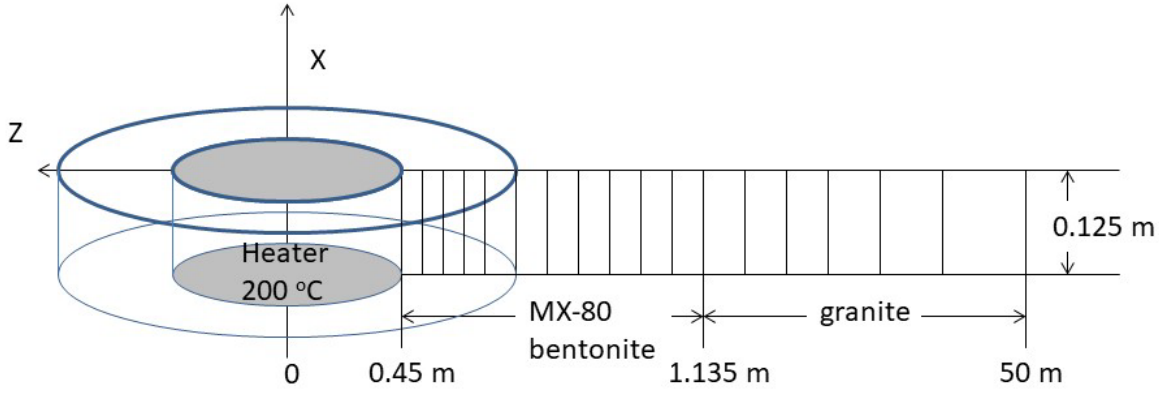

Figure 7-4. Mesh used for the model, shown not to the scale.

7.3.5 The TH model

The model considers non-isothermal two-phase (air and water) flow, with each phase fluxes given by a multiphase version of Darcy's law. For the vapor flow in the air phase, in addition to Darcy flow, mass transport can also occur by diffusion and dispersion according to Fick's law. In the current model, both conductive (Fourier's law) and convective heat flux are considered in the model, and thermal conductivity is the key parameter. Thermal behavior is relatively well understood because it is less affected by coupled processes in comparison with hydrological and chemical processes, and the relevant parameters can be reliably measured.

The thermal conductivity of bentonites is affected by the degree of compaction (dry density) and water saturation. Figure 7-5 shows the measured thermal conductivity for MX-80 at different dry density. In the current design, the granulated bentonite mixture has a target dry density of ~1.45 g/cm^3. We use a linear relationship implemented in TOUGH2 (Pruess et al., 1999) to represent the thermal conductivity and water saturation relationship:

$$K_{th} = K_{wet} + S_l(K_{wet} - K_{dry}) \qquad 7\text{-}1$$

where K_{wet} is the thermal conductivity under fully saturated conditions, K_{dry} is the thermal conductivity under dry conditions, and S_l is the liquid saturation degree. K_{wet} and K_{dry} are given in Table 7-1.

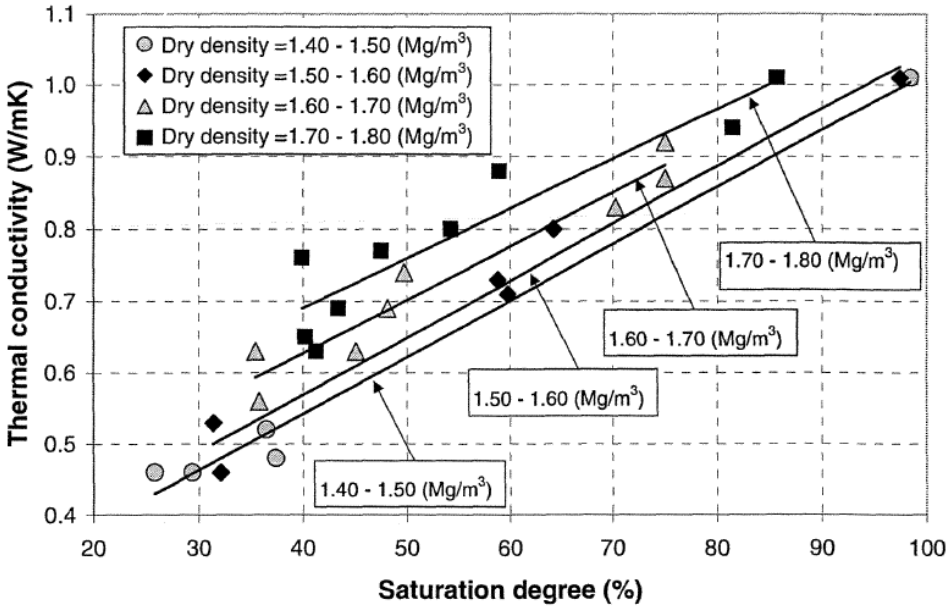

Figure 7-5 Thermal conductivity vs saturation degree for different dry density (Tang and Cui, 2006)

According to the sensitivity analysis, based on the THMC model for the FEBEX *in situ* test, the key parameters affecting the hydration of bentonite are permeability of granite, relative permeability, retention curves of bentonite, the vapor diffusion coefficient and permeability of bentonite. Granite is fractured media and should be represented by fractures and matrix. Just as previous models for *in situ* tests (Samper et al., 2008a; Sánchez et al., 2012b), the current model also assumes that granite is a homogeneous porous medium, which can be simulated based on a model of an equivalent permeability. Based on the total water flow from the tunnel wall at the entire length of the test zone (ENRESA, 2000), permeability of fractured granite is estimated to range from 5×10^{-18} to 8×10^{-18} m^2. ENRESA (2000) also reports that the most frequent permeability is 1×10^{-18} m^2, but it seems be more representative of the rock matrix. Zheng et al. (2011) used 8×10^{-18} m^2, Kuhlman and Gaus (2014) estimated permeability of 6.8×10^{-19} m^2, and Sánchez et al. (2012b) used a surprisingly small value of 8.18×10^{-21} m^2. Based on the published values, it seems that a permeability value between 7×10^{-19} to 8×10^{-18} m^2 is plausible. Based on the evaluation in Zheng et al. (2015a), a permeability of 2×10^{-18} m^2 is used (Table 7-1).

The capillary pressure (retention curve) is calculated by the van Genuchten function as:

$$P_{cap} = -\frac{1}{\alpha}\left(\left[S^*\right]^{-1/m} - 1\right)^{1-m} \qquad 7\text{-}2$$

where P_{cap} is the capillary pressure (Pa), $S^* = (S_l - S_{lr})/(1 - S_{lr})$ and S_l is the water saturation, S_{lr} is the residual water saturation. S_{lr} is 0.1 for bentonite and 0.01 for granite. The values of α and m for the FEBEX bentonite are given in Table 7-1 (Zheng et al., 2019).

Table 7-1. Thermal and hydrodynamic parameters.

Parameter	Granite	Bentonite
Grain density [kg/m^3]	2700	2780
Porosity ϕ	0.01	0.46
Saturated permeability [m^2]	2.0×10^{-18}	3.69×10^{-20}
Relative permeability, k_{rl}	$k_{rl} = S$	$k_{rl} = S^3$
Van Genuchten $1/\alpha$ [1/Pa]	4.76×10^{-4}	1.1×10^{-8}
Van Genuchten m	0.7	0.45
Compressibility, β [1/Pa]	3.2×10^{-9}	5.0×10^{-8}
Thermal expansion coeff. [1/^{o}C]	1.0×10^{-5}	1.5×10^{-4}
Dry specific heat [J/kg-^{o}C]	793	1091
Thermal conductivity [W/m-^{o}C] dry/wet	3.2/3.3	0.4/1.0
Effective vapor diffusion coefficient (m^2/s)	1.03×10^{-4}	1.03×10^{-4}

Note: in the relative permeability function, S is water saturation

The effective permeability of bentonite plays a critical role in determining the hydration of bentonite. It is the product of intrinsic permeability (k) (or saturated permeability, absolute permeability) and relative permeability (k_r). Relative permeability, $k_r=S_l^3$ (where S_l is water saturation degree), has been consistently used by different models (Zheng et al., 2011; Sánchez et al., 2012b; Kuhlman and Gaus, 2014) for FEBEX bentonite, and we use the same function for MX-80 here.

The stress-dependence of permeability for low-permeability sedimentary rock is fairly well known (e.g., Ghabezloo et al., 2009; Kwon et al., 2001). Many empirical relationships have been put forward to describe the permeability changes with effective stress. Villar (2005) derived an empirical relationship by fitting the permeability-dry density data as:

$$\log k = -2.94\rho_d - 8.17 \qquad 7\text{-}3$$

where ρ_d is dry density. Equation 7-3 give an initial permeability of 3.69×10^{-20} m^2 for GBM.

Kiverant et al. (2018) reported that the grain density of Wyoming bentonite varied between 2.773 and 2.806 g/cm3, with an average of 2.78 g/cm3. Karnland (2010) reported a slightly lower grain density of the bentonite MX-80 than Kriverant et al. (2018), which ranged from 2.75 to 2.78 g/cm^3, and a value of 2.75 g/cm^3 was used in their Buffer Production report. In this report, we used a grain density of 2.78 g/cm^3. With a target dry density of bentonite of 1.5 g/cm^3, we calculated a porosity of 0.46.

Taking into account coupled transport phenomena, thermal, hydraulic and chemical gradients all have effects on the heat, liquid and solute fluxes. Thermal osmosis is a coupled process that can produce a fluid flux. Zhou et al. (1999) showed that additional coupled flow terms due to a temperature gradient had a significant effect on the distribution of capillary pressure and saturation in a THM model of a thick cylinder heating test. The flux of fluid caused by thermal osmosis v_{to} can be written as (Dirksen, 1969):

$$v_{to} = -k_T \nabla T \qquad 4\text{-}1$$

where T is temperature and k_T is the thermo-osmotic permeability ($m^2/K/s$). Liquid flux caused by thermal osmosis term can be added to Darcian terms (Ghassemi and Diek, 2002; Zhou et al., 1999). In current model, k_T of 1.2×10^{-12} $m^2/K/s$ is used.

7.3.6 Chemical Model

The establishment of the chemical model requires first the knowledge of initial chemical conditions in bentonite and granite, i.e., the initial mineralogical and pore water compositions. In this report, the mineralogical composition for MX-80 bentonite were taken from Karnland (2010). Table 7-2 shows the mass fraction and Table 7-3 shows the volume fraction (ratio of the volume for a mineral to the total volume of medium) using a porosity of 0.46 (see Table 7-2). Because tridymite, a polymorph of silica, was not found in the database, in the model we assumed that tridymite thermodynamically is the same as quartz. Note the minerals assigned the zero initial volume fraction are the secondary minerals that could be formed.

Table 7-2. Mass fraction of mineral measured from the XRD analysis of five consignments of the Wyoming MX-80 material (Karnland, 2010). Column under "Wym" are the average.

Phase	WySt	WyL1	WyL2	WyR1	WyR1m	WyR2	Wym	plus	minus
Montmorillonite	82.5	79.5	79.8	82.7	83.9	80	81.4	2.5	1.9
Illite	0.7	0.8	0.7	0.8	0.8	0.7	0.8	0.1	0.1
Calcite	1.3	0	0	0.1	0	0	0.2	1.1	0.2
Cristobalite	0.2	1.4	2.5	0.6	0.7	0	0.9	1.6	0.9
Gypsum	1.4	0.7	0.9	0.7	0.8	1.1	0.9	0.5	0.2
Muscovite	2.4	5.1	2.6	3.5	4.4	2.5	3.4	1.7	1
Plagioclase	4.6	2.4	4	3.2	2.3	4.7	3.5	1.2	1.2
Pyrite	0.8	0.6	0.6	0.6	0.3	0.9	0.6	0.3	0.3
Quartz	2.6	2.5	3.8	3	2.8	3.2	3	0.8	0.5
Tridymite	1.7	5	3.8	3.9	3.1	5.1	3.8	1.3	2.1

Table 7-3. Mineral volume fraction (dimensionless, ratio of the volume for a mineral to the total volume of medium) MX-80 bentonite (Karnland, 2010) and granite (Zheng et al., 2011).

Mineral	MX-80 Bentonite	Granite
Calcite	0.00108	0
Smectite	0.439	0
Gypsum	0.00486	0
Quartz	0.0162	0.37
Cristobalite	0.0367	0.00
K-Feldspar	0.000	0.35
Plagioclase	0.0189	0.27
Dolomite	0.0	0
Illite	0.00432	0
Kaolinite	0.0	0
Siderite	0.0	0
Ankerite	0.0	0
Anhydrite	0.0	0
Chlorite	0.0	0
Muscovite	0.01836	0
Pyrite	0.00324	0

The initial pore water composition in MX-80 varies with dry density and water content (Bradbury and Baeyens, 2003). Because the target dry density of bentonite in granulated bentonite mixture is 1.5 g/cm^3, we take the values reported in Bradbury and Baeyens (2003), shown in Table 7-4). The pore water composition for granite (Table 3-7) is taken from Zheng et al. (2011).

Table 7-4. Pore-water composition (mol/kg water except for pH) of MX-80 bentonite (Bradbury and Baeyens, 2002; Bradbury and Baeyens, 2003) and granite (Zheng et al., 2011).

	MX-80 Bentonite	Granite
pH	8	8.35
Cl	6.75E-02	1.31E-05
SO_4^{-2}	1.04E-01	7.86E-05
HCO_3^-	8.8E-04	3.97E-04
Ca^{+2}	9.47E-03	1.81E-04
Mg^{+2}	7.06E-03	1.32E-06
Na^+	2.43E-01	3.76E-04
K^+	1.23E-03	7.80E-06
Fe^{+2}	2.06E-08	2.06E-08
$SiO_2(aq)$	1.1E-04	6.07E-04
AlO_2^-	1.91E-09	3.89E-08

In the chemical model, we consider aqueous complexation, cation exchange, surface complexation, and mineral dissolution/precipitation. Details of aqueous complexes and their disassociation constants for reactions, solubility and reaction rate for minerals are given in Zheng et al. (2018)

7.4 Model Results

7.4.1 TH Results

With constant heating at 200 ºC at the heater, a point 3 cm away from the heater is quickly heated to 190 ºC (Figure 7-6), in the middle of the bentonite barrier the temperature is about 128ºC, and the temperature in bentonite 6 cm away from granite is about 97 ºC (Figure 7-6). The temperature at the bentonite/granite interface is 87 ºC (not shown in the figure). The temperature in granite decreases to 75 ºC at about 1.6 m away from the heater, and to 40 ºC at 4 m away from the heater (Figure 7-6). At a 10 m depth in the granite (R=11 m), the temperature is about 20 ºC. Thermal disturbance penetrates about 25 m into the granite.

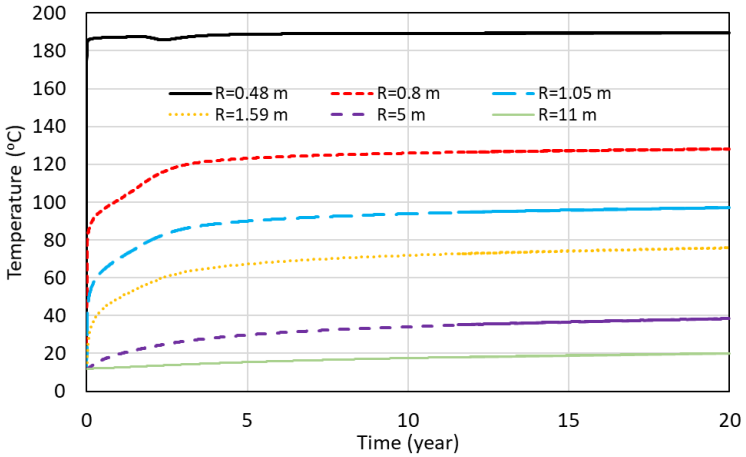

Figure 7-6. Temporal evolution of temperature at several radial distances, note that bentonite/granite interface locates at R = 1.13 m.

Typically, bentonite near the heater goes through desaturation/re-saturation cycling: evaporation due to high heat dries the bentonite, and re-saturation occurs once the hydraulic pressure overcomes the vapor pressure. However, the time span of such a cycle depends on the temperature, permeability of bentonite, and hydraulic pressure in granite. Model results showed that re-saturation for HotBENT is much faster than the FEBEX *in situ* test (Zheng et al., 2019), because permeability of bentonite is higher and hydraulic pressure in granite is higher, despite of higher temperature.

Figure 7-7 shows the evolution of liquid saturation at several radial distances, and Figure 7-8 shows the radial profiles for several times. Most parts of bentonite become fully saturation in about 3 years, but an area about 3 cm away from the heater remains slightly unsaturated (95% to 98% liquid saturation) until the end of simulation, because hydraulic pressure cannot exceed the high gas pressure (Figure 7-9) at this area. Note that pore pressure, shown in Figure 7-9, is the gas pressure for unsaturated condition, and liquid pressure for full saturation. Another indicator that a small area near the heater remans unsaturated is that the relative humidity of 92% at R=0.48 m remains stable until the end of simulation after bentonite goes through a desaturation (decrease in relative humidity) and re-saturation.

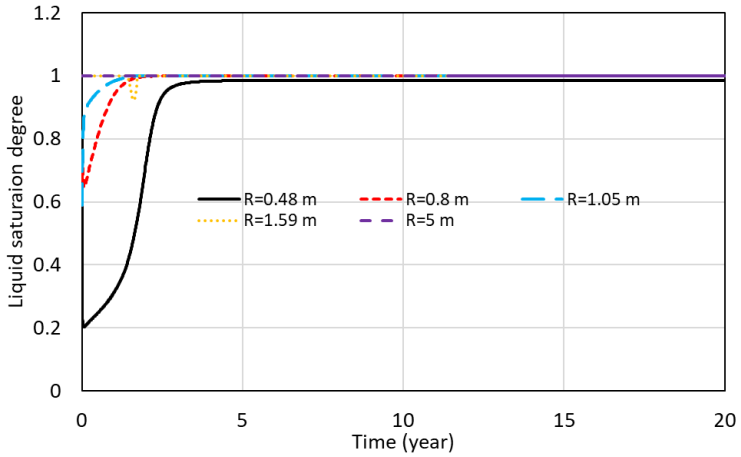

Figure 7-7. Temporal evolution of liquid saturation at several radial distances. Note that points at *R*= 0.48, 0.8, and 1.05 m are located within the bentonite barrier, and the rest of the points are located in granite.

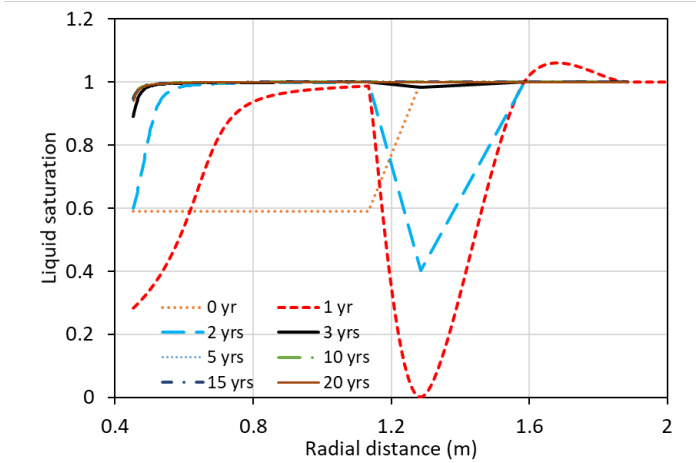

Figure 7-8. Spatial profiles of liquid saturation at several times. Note that the bentonite/granite interface is located at *R* = 1.13 m.

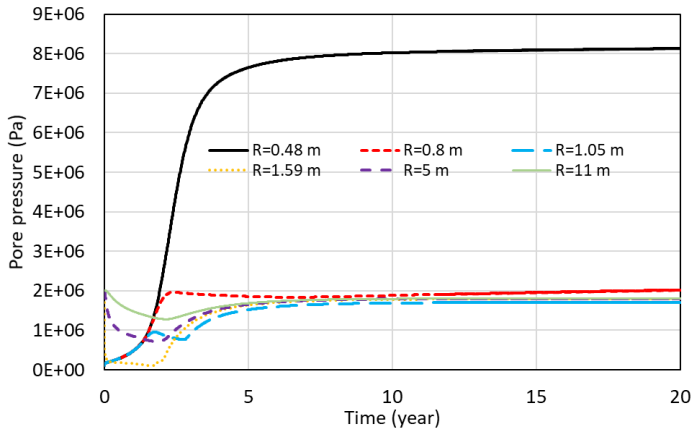

Figure 7-9. Temporal evolution of pore pressure at several radial distances. Note that points at *R*= 0.48, 0.8, and 1.05 m are located within bentonite barrier, and the rest of points are located in granite.

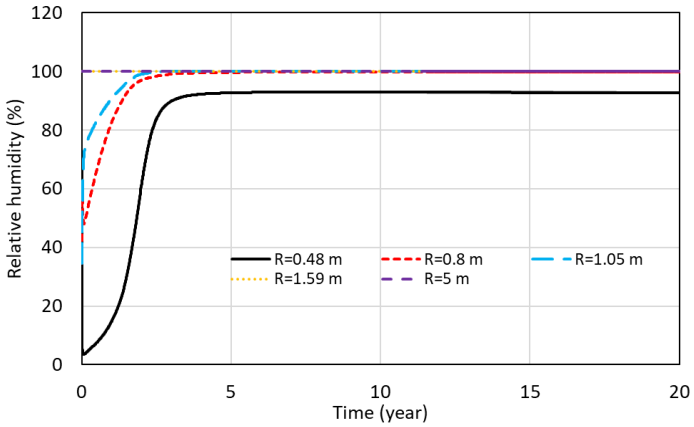

Figure 7-10. Temporal evolution of relative humidity at several radial distance, note that points at *R*= 0.48, 0.8 and 1.05 m are located within bentonite barrier, and the rest of points are located in granite.

7.4.2 Chemical Results

The evolution of conservative chemical species, i.e., Cl, as shown in Figure 7-11, is controlled by three major processes: water displacement, diffusion, and evaporation/condensation. As granite water infiltrates into the bentonite, it displaces bentonite pore water and pushes the bentonite pore water towards the heater. Evaporation caused by heating generates vapor and vapor move outwards to the relatively cooler area and condenses. The evaporation leads to an increase in concentration, whereas condensation results in a decrease in concentration. Because of the concentration difference between bentonite pore water and granite water, diffusion also occurs with ions moving from bentonite to granite for most species. As a result of the combination of these processes, the Cl profile can be divided into three areas: from radial distance of 0.45 m to 0.48 m, a narrow area (referred as "evaporation zone") with a high concentration due to continuous evaporation, and from radial distance of 0.48 m to 0.8 m, a condensation area (referred as "condensation zone") that is characterized by a gradually decreasing concentration. Because of the continuous condensation, the concentration in the "condensation zone" can be lower than in the granite water; from the radial distance of 0.8 m to the bentonite/granite interface, an area is featured with a concentration gradient decreasing from bentonite to granite due to diffusion, which is referred as "diffusion zone." Please note the

subdivision onto three zone is rather descriptive, and the temporal and spatial distribution of these zones changes with time.

Despite of other chemical reactions are involved in the transport of sulfate, its radial and temporal distributions (Figure 7-12) are similar to those of chloride, which is consistent with findings from the THMC model for the FEBEX *in situ* test (Zheng et al., 2018). The MX-80 bentonite contains a small amount of gypsum that quickly dissolves uniformly along the entire bentonite barrier (Figure 7-13), leading to a uniform rise of the sulfate concentration shortly after the simulation starts, but later it behaves just like chloride, and the spatial distribution is dominated by transport processes including displacement by penetration of granite water, evaporation/condensation, and diffusion.

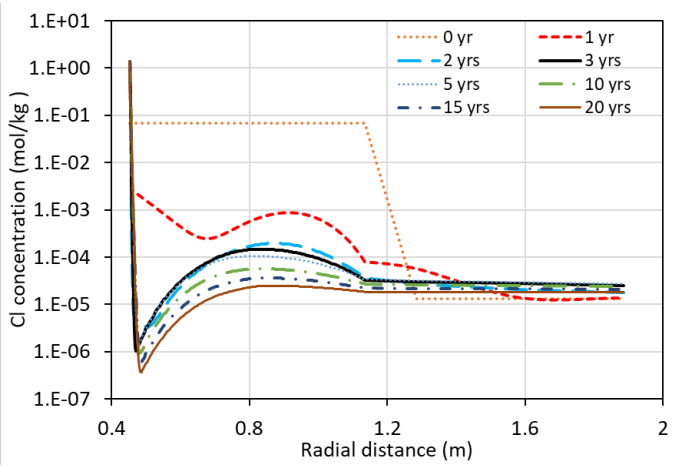

Figure 7-11. Radial profiles of Cl concentrations at several times. Note that bentonite/granite interface is located at $R = 1.13$ m.

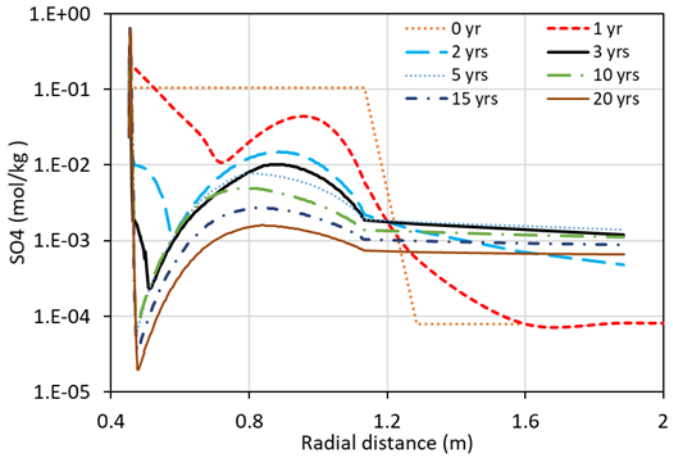

Figure 7-12. Radial profiles of SO_4 concentrations at several times. Note that bentonite/granite interface is located at $R = 1.13$ m.

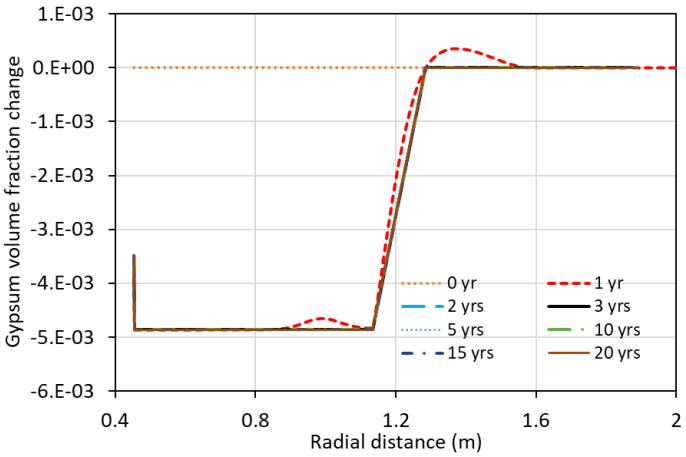

Figure 7-13. Radial profiles of gypsum volume fraction change at several times. Negative values mean dissolution, and positive values indicate precipitation.

Calcium is involved in many chemical reactions including calcite and gypsum dissolution/precipitation, cation exchange, which regulate the calcium concentration level, but the radial trend of calcium (Figure 7-14) follows that of chloride: an "evaporation zone" that is characterized by high concentration, an "condensation zone" that features low concentration and a "diffusion zone" that shows the decreasing concentration from bentonite to granite. Calcite dissolution/precipitation and precipitation of the anhydrite are the major reactions that affect the concentration of calcium. Evolution of calcite roughly follows the three zones, but changes spatially and temporally. Model shows precipitation in the "diffusion zone." In the "condensation zone," dissolution dominates, but precipitation appears at the boundary between the "diffusion zone" and the "condensation zone." There is re-precipitation in the "evaporation zone," i.e. calcite dissolves in the first 5 years and then re-precipitates, although the volume fraction therein is still lower than the initial value (negative value in Figure 7-15). Precipitation of the anhydrite is also observed in the model (Figure 7-16). Both gypsum and anhydrite are calcium sulfate minerals, but gypsum is the hydrous form, with two water molecules in the chemical formula. Anhydrite is more stable, when the temperature is higher than 43 ºC (Zheng et al., 2011), which is why precipitation of anhydrite is usually expected under the conditions of HotBENT.

Like calcium, magnesium (Figure 7-17) follows the spatial trend of chloride, and can roughly be divided into three zones. The chemical reaction that changes the concentration of magnesium is cations exchange, which will be discussed later in the section.

The radial profile of sodium (Figure 7-18) similar to that of chloride, showing very high concentration up to 3 mol/kg near the heater at the "evaporation zone." But they are also affected by the dissolution of plagioclase (Figure 7-19) and cation exchange.

Potassium concentrations (Figure 7-20) are similar to other major cations. Dissolution/precipitation of illite and muscovite interplay with the aqueous potassium that is strongly affected by transport processes, and display similar spatial patterns as aqueous potassium. In the "diffusion zone," illite dissolves and muscovite precipitates; in the area between "diffusion zone" and "condensation zone," illite precipitates and muscovite dissolves, but in the "condensation zone," close to the "evaporation zone," illite dissolves and muscovite precipitates; and in the "evaporation zone," illite precipitates and muscovite dissolves.

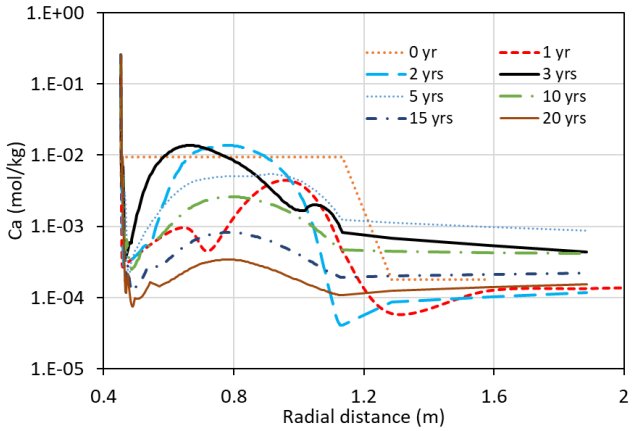

Figure 7-14. Spatial profiles of Ca concentration at several times. Note that bentonite/granite interface locates at $R = 1.13$ m.

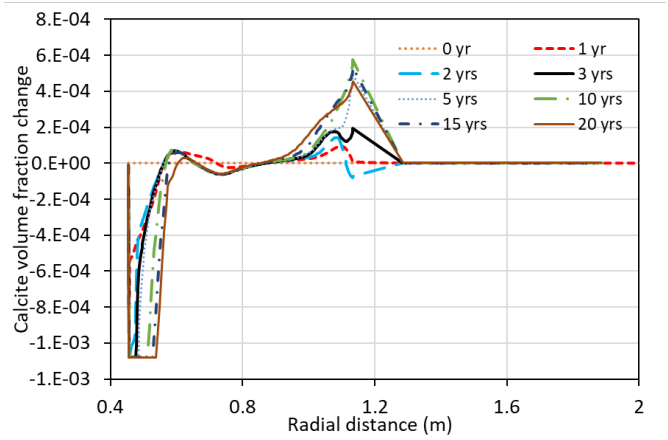

Figure 7-15. Radial profiles of calcite volume fraction change at several times. Negative values mean dissolution and positive values indicate precipitation.

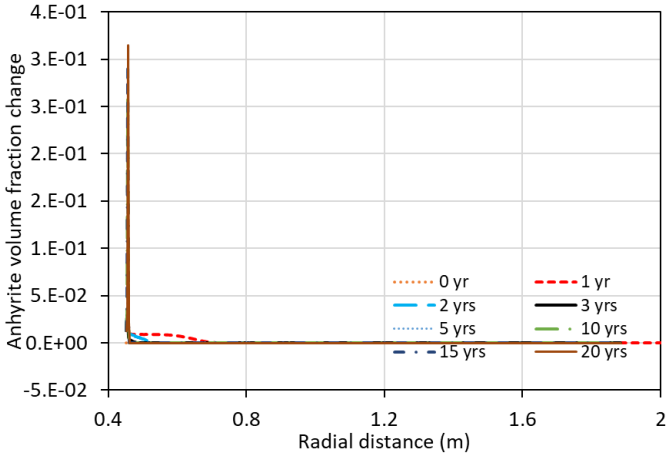

Figure 7-16. Radial profiles of anhydrite volume fraction change at several times. Negative values mean dissolution and positive values indicate precipitation.

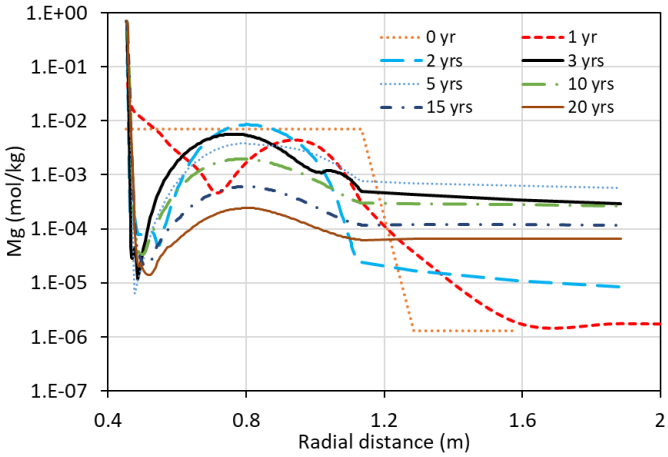

Figure 7-17. Radial profiles of Mg concentration at several times. Note that bentonite/granite interface is located at $R = 1.13$ m.

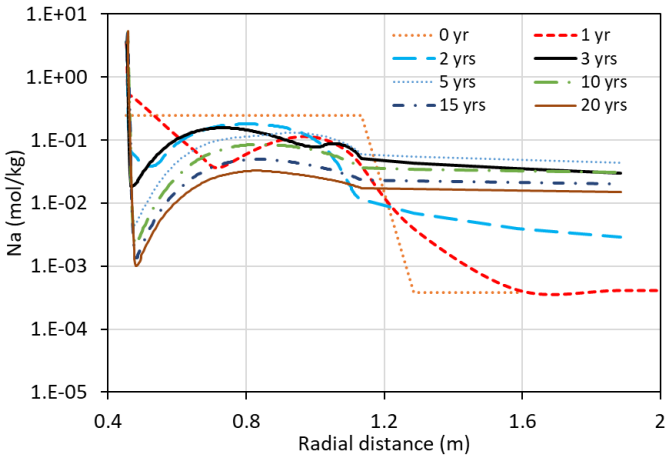

Figure 7-18. Radial profiles of Na concentration at several times. Note that bentonite/granite interface is located at $R = 1.13$ m.

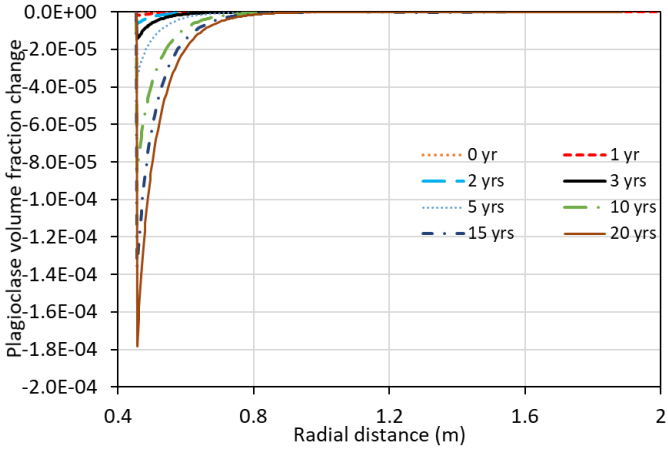

Figure 7-19. Radial profiles of plagioclase volume fraction change at several times. Negative values mean dissolution and positive values indicate precipitation.

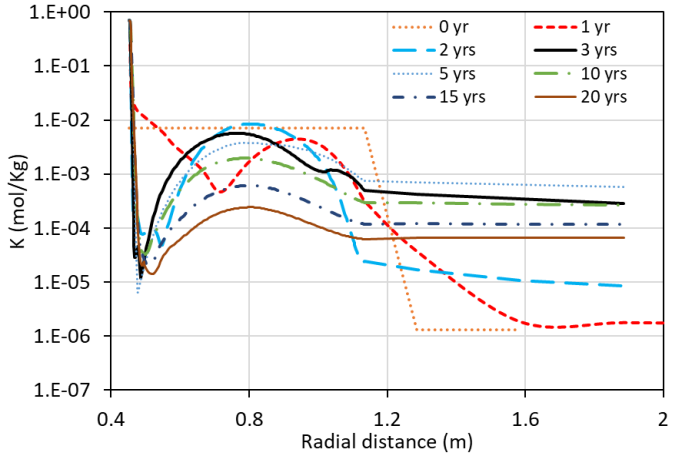

Figure 7-20. Radial profiles of K concentration at several times. Note that bentonite/granite interface locates at $R = 1.13$ m.

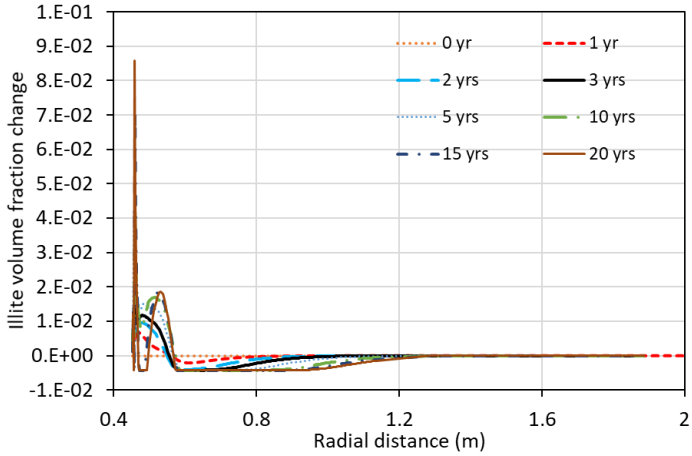

Figure 7-21. Radial profiles of illite volume fraction change at several times. Negative values mean dissolution and positive values indicate precipitation.

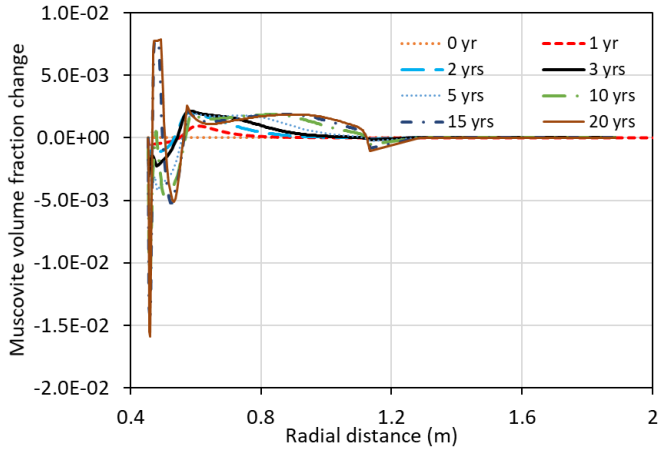

Figure 7-22. Radial profiles of muscovite volume fraction change at several times. Negative values mean dissolution and positive values indicate precipitation.

Simulations using the THMC model of FEBEX *in situ* test (Zheng et al., 2018) showed that pH and bicarbonate behave differently compared to other reactive species (i.e., sulfate, Ca, Mg, Na, K), and they do not follow the spatial pattern of conservative species (e.g., Cl), indicating chemical reactions, rather than transport processes dominating the evolution of pH and bicarbonate. The current predictive model for HotBENT shows the same. In most areas, pH is buffered by the surface protonation, but in the "condensation zone," right next to the evaporation zone in a very narrow area, continuous condensation and mineral dissolution drive the pH to 3. The dissolution of muscovite, smectite, and precipitation tends to decrease the pH, whereas the dissolution of calcite leads to an increase in pH, but the combined effect is that pH drops significantly. The rise of pH at areas near the granite in early time (1 year) is likely caused by the interaction between the bentonite pore water and granite water.

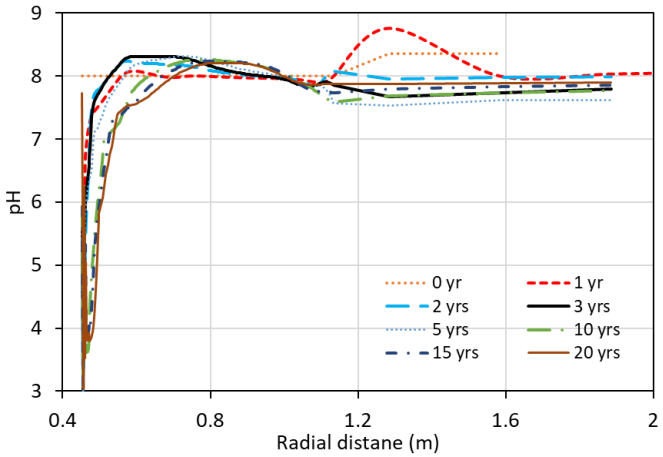

Figure 7-23. Radial profiles of pH at several times. Note that bentonite/granite interface is located at $R = 1.13$ m.

The spatial distribution of bicarbonate is controlled dominantly by reactions rather than by transport processes. The evolution of CO_2 gas trapped in the bentonite pore water and dissolution/precipitation of calcite are major reactions that are responsible for the changes in bicarbonate concentration.

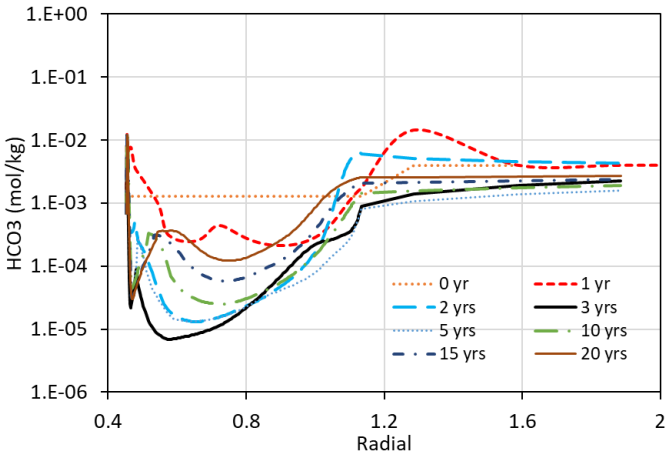

Figure 7-24. Radia profiles of bicarbonate concentration at several times. Note that bentonite/granite interface locates at R = 1.13 m.

The key mineral in bentonite that is a major concern for the long-term stability of bentonite barrier is smectite (Zheng et al., 2015a). Based on the results of the FEBEX *in situ* test (Zheng et al., 2018), comparison of smectite mass fraction in bentonite samples that were collected after 18-years of heating, and hydration with reference bentonite (reserved, represent the state of bentonite before the test) did not show a clear difference, because the data were too scattered. But the model for FEBEX *in situ* test (Zheng et al., 2018) showed bentonite in the narrow area close to heater loss about 1% smectite. The current model predicts a significant dissolution of smectite (Figure 7-25) in an area about 3 cm thick next to the heater because of strong and continuous evaporation near the heater, meanwhile illite precipitated at the same area (Figure 7-22).

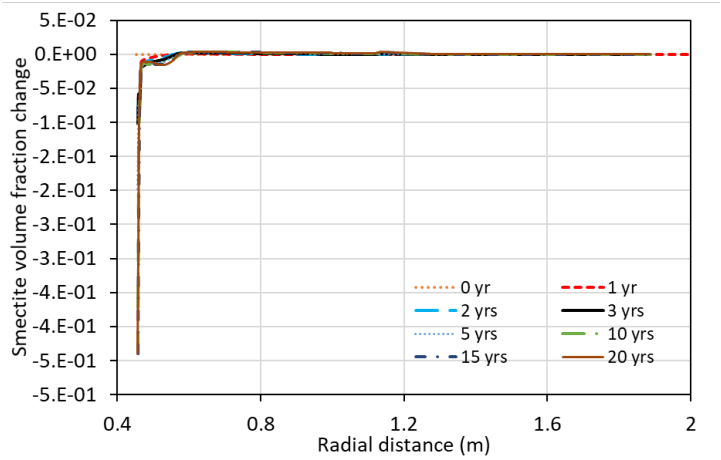

Figure 7-25. Radial profiles of smectite volume fraction change at several times. Note that bentonite/granite interface is located at *R* = 1.13 m.

In general, based on the results of modeling, changes in minerals phases occurred mostly in areas close to the heater by the end of the planned prediction time of 20 years. In an area very next to the heater, about 3 cm thick with radial distance from 0.45 m to 0.48 m, model showed the dissolution of smectite (Figure 7-25), precipitation of illite (Figure 7-22) and anhydrite (Figure 7-16), quartz (Figure 7-26) and cristobalite (Figure 7-27). Calcite, muscovite, and plagioclase dissolved initially, but started to precipitate at a later time, although the volume fractions of these minerals at the 20 years are still lower than their perspective initial values. Changes of siderite, ankerite, albite, and anorthite have not been shown by the model.

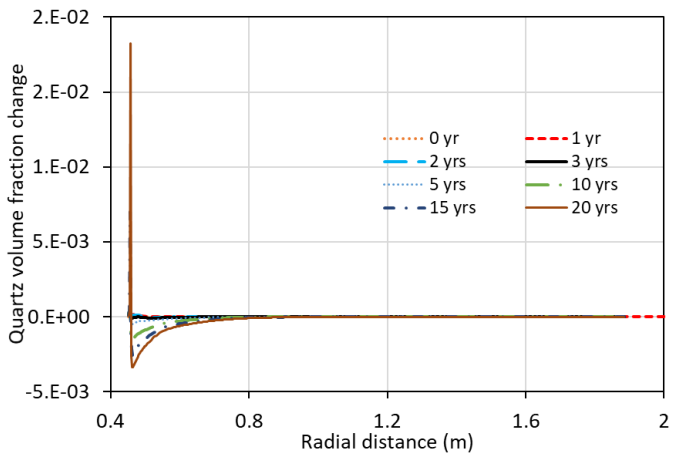

Figure 7-26. Radial profiles of quartz volume fraction change at several times. Note that bentonite/granite interface is located at R = 1.13 m.

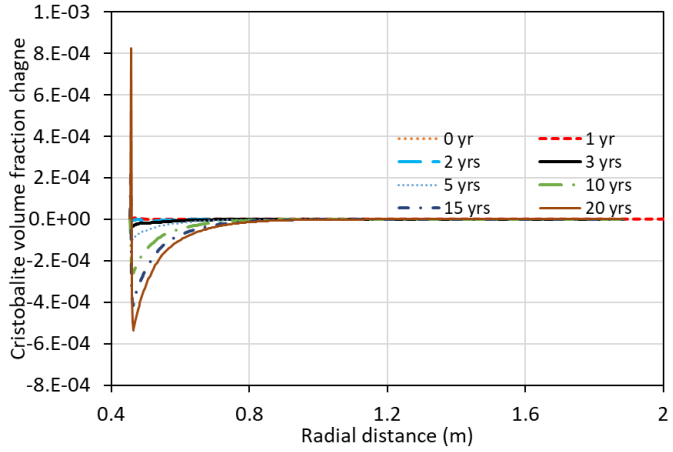

Figure 7-27. Radial profiles of cristobalite volume fraction change at several times. Note that bentonite/granite interface is located at R = 1.13 m.

The spatial distribution of exchangeable cations is the result of the interplay between exchangeable cations with their aqueous counterparts and competition between different exchangeable cations for the exchange sites. In most areas in the bentonite barrier, exchangeable Ca (Figure 7-30) and K (Figure 7-29) are loaded to the exchangeable sites, whereas exchangeable Na (Figure 7-28) and Mg (Figure 7-31) are released from exchangeable sites. But the model showed an opposite trend in the area close to the heater: exchangeable Ca (Figure 7-30) and K (Figure 7-29) are released from the exchangeable sites, whereas exchangeable Na (Figure 7-28) and Mg (Figure 7-31) are loaded to exchangeable sites.

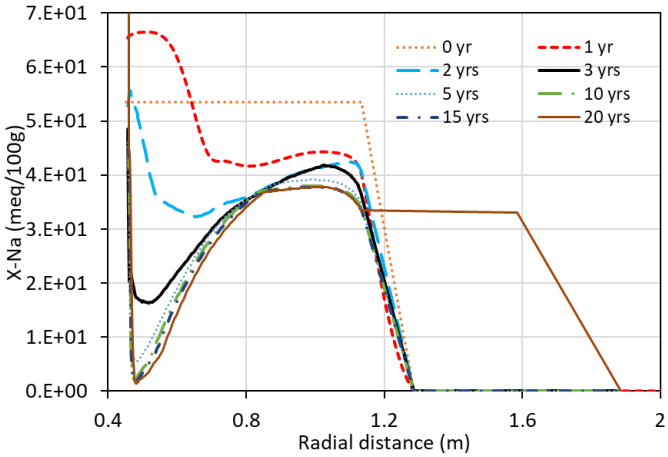

Figure 7-28. Radial profiles of exchangeable Na at diferent times. Note that bentonite/granite interface is locates at $R = 1.13$ m.

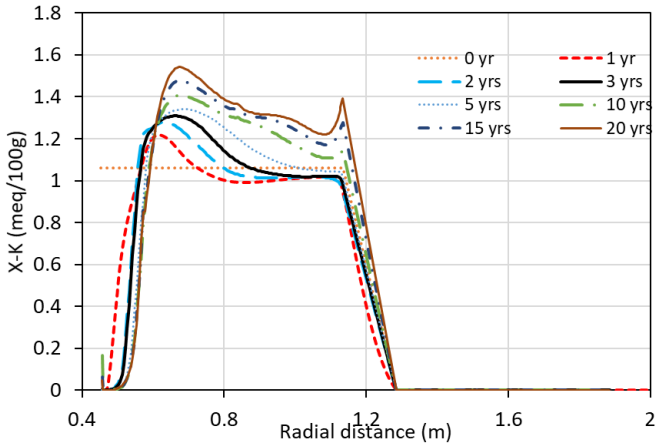

Figure 7-29. Radial profiles of exchangeable K at several times. Note that bentonite/granite interface locates at $R = 1.13$ m.

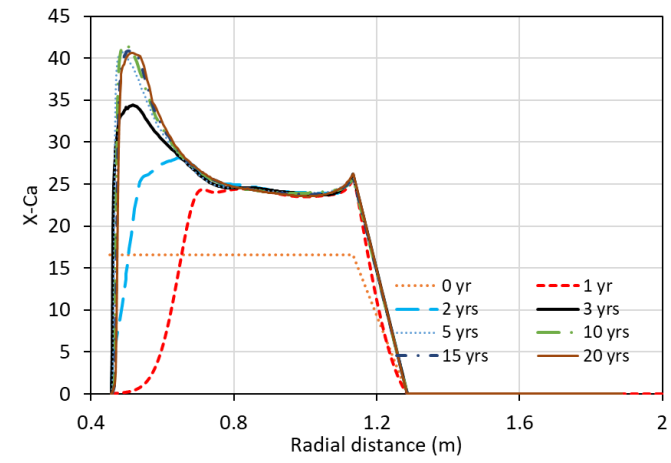

Figure 7-30. Radial profiles of exchangeable Ca at several times. Note that bentonite/granite interface is located at $R = 1.13$ m.

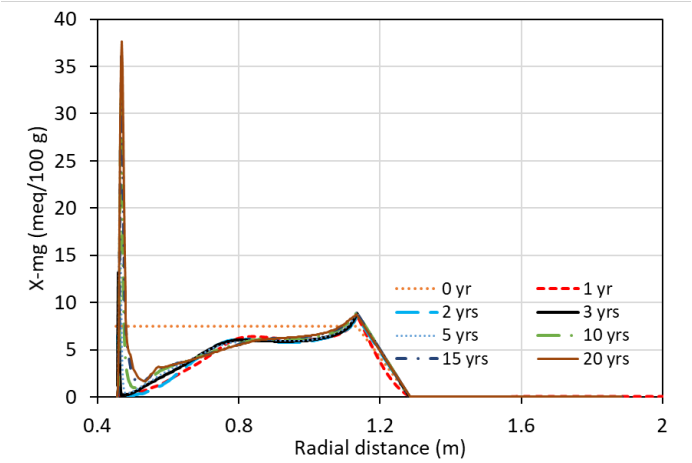

Figure 7-31. Radial profiles of exchangeable Mg at several times. Note that bentonite/granite interface is located at $R = 1.13$ m.

7.4.3 Sensitivity of simulations of chloride concentration to heater temperature

Accumulation of high ions in the close vicinity of the heater had been observed in the FEBEX *in situ* test and the corresponding interpretative models (Zheng et al., 2018), and also is shown in the current model as the "evaporation zone." The "condensation zone" with a low concentration that is located a bit further away from the heater than the "evaporation zone" was also observed in FEBEX *in situ* test. The concentration level in the "condensation zone" in the current model, however, is much lower than that having ever been observed in the FEBEX *in situ* test, and for some species, the concentration is even lower than that in the granite water. Considering that the heater was 100 ºC in FEBEX *in situ* test, a sensitivity run, assuming the heater has a temperature of 100 ºC, was conducted. Chloride concentration profiles shown in Figure 7-32 are similar to the chloride concentration profile in the FEBEX *in situ* test (Figure 7-33). In HotBENT, because of 200 ºC heater temperature, evaporation in the close vicinity of the heater is much stronger and condensation in the area further away from the heater is also stronger than that in the case with 100 ºC heater temperature. Note that permeability of the bentonite barrier in HotBENT is about 17 times higher than that in FEBEX *in situ* test, which may have also caused the difference in the concentration profiles.

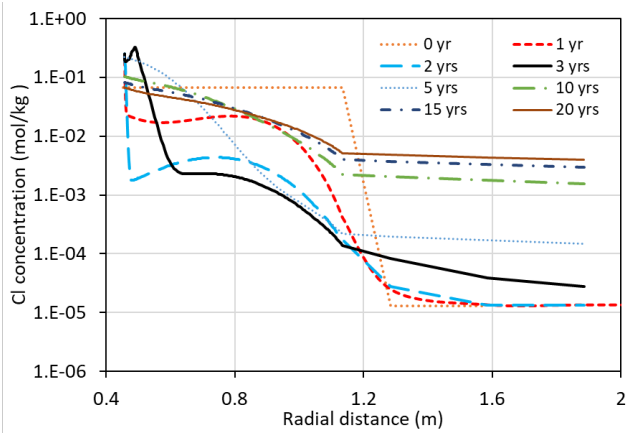

Figure 7-32. Radial profiles of Cl concentration at several times. Note that bentonite/granite interface is located at $R = 1.13$ m.

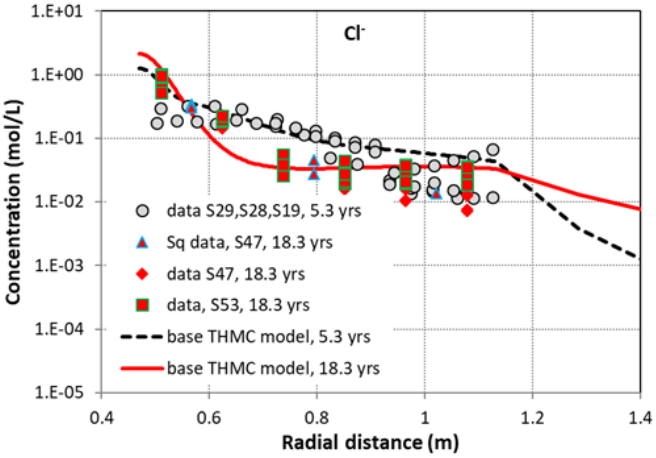

Figure 7-33. Calibrated chloride concentration data at 5.3 years from aqueous extract test for Sections 29, 28, and 19 (Zheng et al., 2011), calibrated chloride concentration data at 18.3 years from aqueous extract test for Section 47 ("data S47, 18.3 yrs") and Section 53 ("data S53, 18.3 yrs"), chloride concentration data from squeezing test for Section 47 ("Sq data, S47, 18.3 yrs"), and model results from the THMC model, modified from Zheng et al. (2018).

7.5 Summary and Future Work

In this report, we, therefore, developed a THC model to predict the evolution of Woyming bentonite (MX-80) that will be used in the HotBENT. Modeling of coupled THC processes affected by high temperature, relatively high permeability and high hydraulic pressure, combined with the effect of artificial hydration, generated the results that have not been observed in FEBEX *in situ* test (Zheng et al., 2018). Modeling results can be summarized as follows.

With a heater temperature of 200 ºC, temperature at the bentonite/granite interface is expected to reach 87 ºC. In about 3 years, most of bentonite would become fully saturated, but a narrow zone about 3 cm thick in the close vicinity of heater would remain unsaturated with a water saturation degree from 95% to 98% until 20 years.

The narrow unsaturated zone is where the most remarkable chemical changes are expected to occur, because of the continuous strong evaporation (referred as "evaporation zone" in this report). Ion concentrations are

expected to increase up to 2-3 mol/kg due to the dissolution of smectite, precipitation of illite, anhydrite, quartz and cristobalite, very high exchange Na and Mg and very low exchange of Ca and K at the cation exchangeable sites. Modeling showed the development a chemically active area a little further away from the heater and right next to the narrow unsaturated zone. It is referred to as the "condensation zone," in which chemical changes are induced by continuous condensation of vapor that is generated in the "evaporation" zone. In this area, model showed a significant dilution of the bentonite pore water, dissolution of most aluminum-silicate minerals, except muscovite, very high exchange of Ca and K, and very low exchangeable Na and Mg at the cation exchangeable sites.

Measurements of chemical concentrations in bentonite in a narrow zone close to the heaters may become a challenging problem, when modules H3 and H4 in HotBENT are dismantled after 5 years of operation.

The 1D model sheds light on the potential chemical changes in MX-80 bentonite in HotBENT, but the hydraulic calculation is not entirely faithful to the condition of HotBENT, because of the existence of pedestal underneath the heater. Currently, a 2D cross-section model (Figure 7-34) is under development.

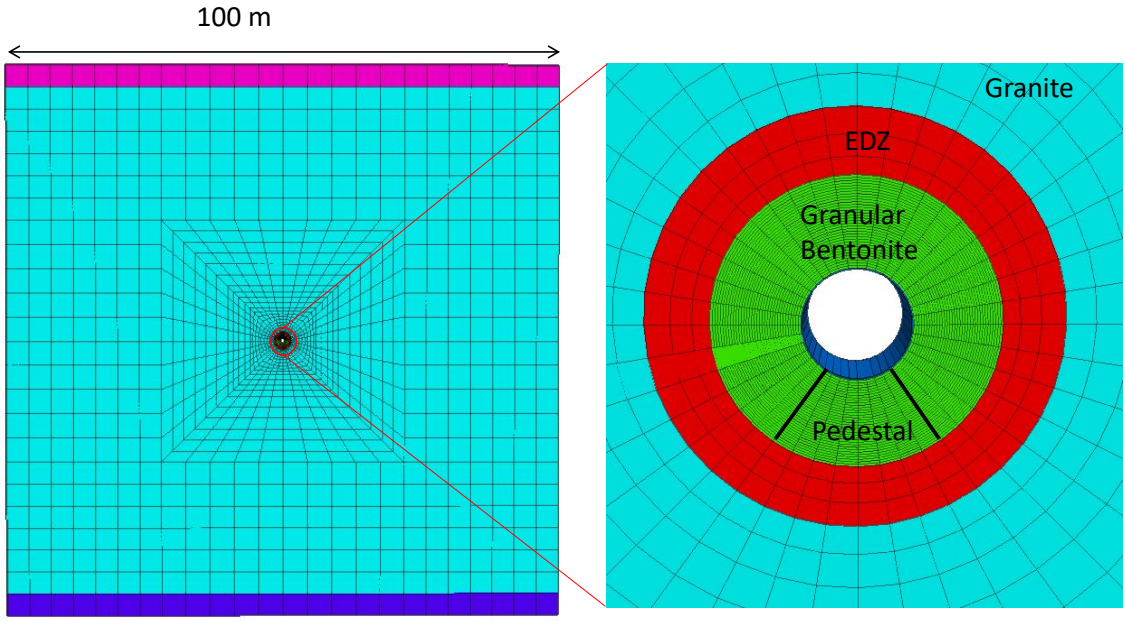

Figure 7-34. 2D cross-sectional mesh for the THC model.

In the remaining time of FY20 and FY21, we will continue making model predictions for the HotBENT, to help design a monitoring protocol and guide future measuring plan. Specifically, we will

1. Develop a 1D THC model for BCV bentonite,
2. Extend the 1D axi-symmetrical THC model for MX-80 to THMC model
3. Develop a 2D THMC model for MX-80 and BCV bentonites.

8. HEATING AND HYDRATION COLUMN TEST ON BENTONITE

8.1 Introduction

This Chapter of the report details of laboratory-scale experimental results in support of the HotBENT field-scale experiment, which is designed to study THMC behavior during long-term heating of clay to 200°C. This effort is built upon previous efforts of long-term laboratory-scale clay heating experiments conducted at lower temperatures (Fernández, 2010; Gómez-Espina, 2010; Villar, 2008). This benchtop-scale laboratory experiment, HotBENT-Lab, provides a laboratory analog of the HotBENT field experiment to obtain a comprehensive set of characterization data and monitoring measurements, which are difficult to conduct at the field scale. The primary goal of this laboratory experiment is to obtain well-characterized datasets to (1) improve understanding of bentonite THMC processes under heating and hydration for model parameterization and benchmarking, (2) compare the HotBENT-Lab data with HotBENT field-scale test results, and (3) develop a prototype of an experimentation platform for future studies of bentonite under conditions of high temperature.

In support of this effort, and as described in the FY18-19 report, the HotBENT-Lab experiment a cylindrical pressure column was constructed to reproduce realistic heating and hydration conditions of the field-scale experiment. The design of the experimental apparatus and monitoring tools are based on estimated ranges of temperature and pressure, ability to accommodate characterization methods, i.e., X-ray computed tomography (CT) and ERT, and safety. In order to better separate the effects of heating and hydration, two identical test columns are used, with the control column undergoing only hydration, and the experiment column experiencing both heating and hydration.

8.2 HotBENT-Lab Design

8.2.1 Column design

A schematic diagram of the column design is shown in Figure 8-1, and was described in detail in the FY18-19 progress report. To review, clay was packed in an Aluminum 7071 pressure column designed to withstand a maximum working pressure of 1000 psi (~6.9 MPa) at 200°C. The inner diameter (ID) of the column is 6.5 inches, an outer diameter (OD) is 7.5 inches, and a height is 18 inches. A cartridge heater of 12-inch-long and 0.25-inch OD is housed in a titanium shaft of 3/8 inch OD penetrating through the center of the column. Using MX-80 bentonite (Cetco), we packed two columns at an initial gravimetric water content of 15%, and a bulk dry and wet density of ~1.2 and 1.5 g/cm^3. A 0.25-inch thick layer of sand pack (12/20 mesh grain size) was installed between the clay column and the column wall as a high-permeability boundary. Hydration was achieved by flowing a synthetic brine (Table 8-1) continuously through the sand layer via a flow port at each of the end caps (Figure 8-2) via a syringe pump (ISCO pumps, 500 ml capacity).

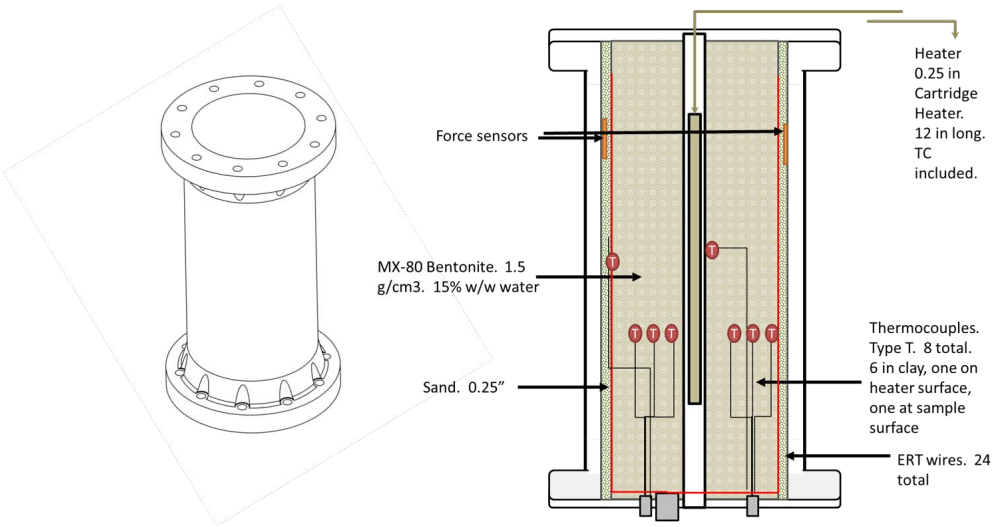

Figure 8-1. Schematic diagram of the column design for HotBENT-Lab experiment. Left: 3D rendering of the column exterior; right: interior design of the bentonite column, showing locations of sensors and the heater. The 1.5 g/cm^3 in the figure represents the bulk wet density of packed clay.

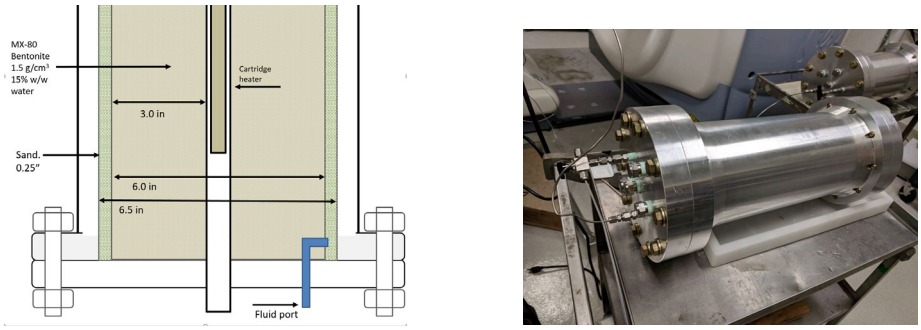

Figure 8-2 Schematic diagram showing the geometry of the different components of the test column (left) and an image of the completed column (right)

Table 8-1. Chemical composition of the artificial groundwater used to saturate the column (from Bradbury and Baeyens, 2003)

Compound	Molarity (mM)	Ion	Molarity (mM)
$NaHCO_3$	0.798	Na	243
Na_2SO_4	104	C	0.881
NaCl	34.2	SO_4	104
KCl	1.23	Cl	68.3
$CaCl_2$*$2H_2O$	9.35	K	1.23
$MgCl_2$*$6H_2O$	7.06	Ca	9.46
CaF_2	0.109	Mg	7.06
$SrCl_2$	0.0831	F	0.218
Si	0.183	Si	0.183
		Sr	0.0831

8.2.2 Characterization and monitoring

To characterize the sample during the heating process, the following techniques were employed:

X-ray CT imaging

X-ray CT images were collected to provide a 3D visualization of the density distribution in the column, which can be used to visualize density changes due to water saturation, clay swelling or structural deformation during the experiments. A GE Lightspeed 16 medical CT scanner was used to scan the experimental columns periodically throughout the experiment. Based on the column dimensions, the spatial resolution of the CT images is 400 × 400 × 625 μm. Because of the large weight of the experimental columns (~55 lbs), a cart/lift is used to move the columns onto and off the CT scanner table. Alignment of the scans is achieved via markings on the CT table and on the outside of the column, as well as key features in the CT images (high and low-density anomalies) inside the column during post processing. The post processing and analysis of the obtained CT scan images are conducted using self-developed codes in ImageJ software (Rasband, 1997–2020).

Continuous temperature monitoring

Temperature monitoring was conducted using thermocouples (type T) installed in the column. A total of 8 thermocouples were installed in each column between the heater shaft and the column wall. The distances of other thermocouples from the heater shaft were 0 (on the heater), 0.5, 1, 1.5 2, 2.5, 3, and 3.5 inches (the latter was on inside of the column wall). These feedthrough-coupled thermocouples, with an accuracy of 0.1°C, were acquired from Conax Technologies. The temperature readings from the thermocouples were recorded at 30s intervals with a data logger (Keithley 2701) throughout the experiment. In addition to the thermocouples inside the columns, additional temperature measurements were taken on the outside wall of the column.

Time lapse electrical resistivity tomography (ERT) monitoring

The ERT data acquisition is conducted using a DAS-1 ERT system (Multi-phase Technologies), combining electrodes used to send electrical current or measure electrical potential. Measurements were conducted using a pre-defined monitoring schedule (see Figure 8-3). A total of ~2600 data points were collected for a single resistivity survey in each column, which takes ~ 40 minutes. The voltage used for ERT data acquisition was targeted at < 50 V, but it varied depending on the resistivity of the tested clay and its hydration status during the experiment. Both the heated and unheated columns were configured to allow for sequential data collection during the same data acquisition event. Tri-hourly data collection is designed for the initial stage of the experiment, and this frequency was adjusted based on the observed rate of changes during the experiment and was was reduced for the longer term experiment. Data collection was autonomously carried out via a control software. Analysis of the post-experiment collected datasets included data quality assessment, inversion and visualization. The open software BERT (boundless ERT, Gunther and Rucker, 2013) and Paraview (Kitware, NY) were used for data inversion and visualization.

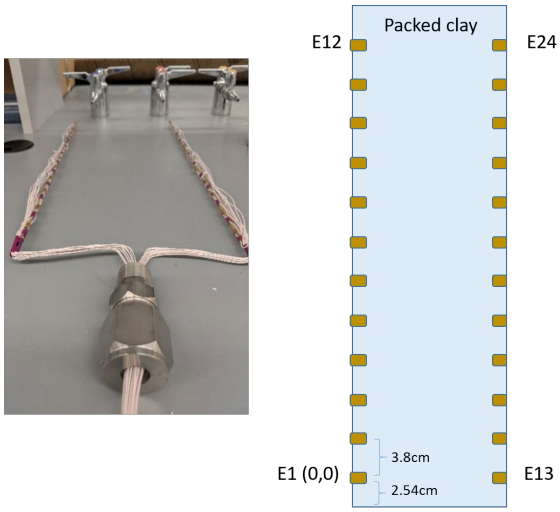

Figure 8-3. ERT monitoring design and a geometric layout of the column.

Influent and effluent fluid geochemical analysis

The fluid (Table 8-1) used to hydrate the bentonite was sampled and analyzed to monitor geochemical changes in the bentonite system. Changes in water chemistry are being used to understand the geochemical processes in the column due to evaporation, dilution, diffusion and other transformations. Samples collected from the experiments were filtered, acidified, when necessary, prepared and analyzed using the standard Ion Chromatography (IC) and Inductively Coupled Plasmas – Mass Spectrometry (ICP-MS) protocols.

Pre- and post- experiment clay analysis following a gradient from the heater

The post-experiment clay analysis data will be compared with those from the pre-experiment clay samples to understand changes in physical, chemical and hydrological characteristics of bentonite due to hydration and heating, including gravimetric water content analysis and mineralogical analysis with X-ray Diffractometry (XRD). Preliminary measurements have been made on the pre-experiment clay and more extensive tests are planned when the experiment is dismantled.

Lab petrophysical studies

In addition to the heating and hydration experiments conducted in the pressure column, parallel experiments with non-pressurized and smaller columns were set up for petrophysical model studies. The main goal of such studies is to determine petrophysical correlations that can be used to link indirect geophysical measurements to parameters of interests. For instance, resistivity-moisture content correlations can be determined from the results of such studies, so the electrical resistivity map acquired from the pressure columns can be translated into a moisture distribution map. Such studies can also be used to acquire water content-density calibration datasets for CT images as well as for porosity- permeability correlation studies.

8.3 Experimental Operation

Packing and startup of the system occurred in June 2019, and hydration and heating have been continuous since inception. Two columns have been continuously operated, a heated and unheated column. After the baseline scan and testing other components, hydration and heating were started. A schematic diagram of the experimental setup with the column and supporting components is shown in Figure 8-4.

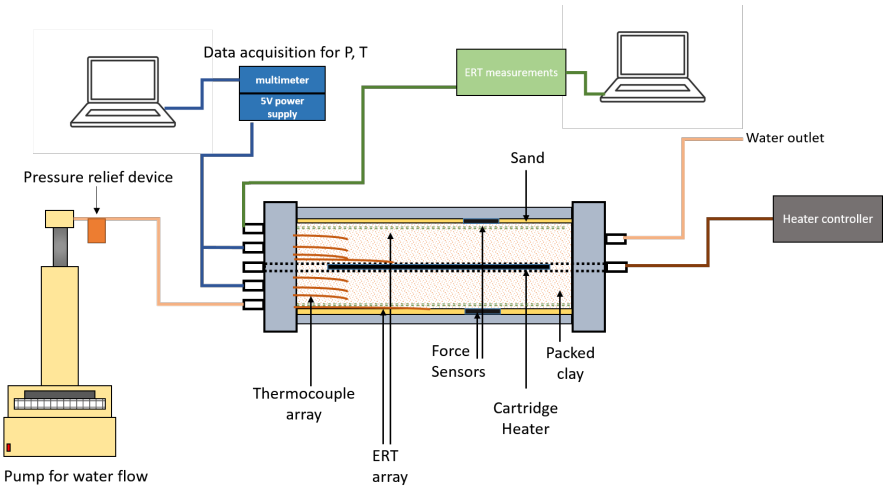

Figure 8-4. Schematic diagram of the entire experimental setup including the column, flow control, and sensors. The inner diameter (ID) of the column is 6.5 inches, an outer diameter (OD) is 7.5 inches, and a height is 18 inches.

8.4 Preliminary Results

8.4.1 X-ray CT

Baseline CT

The baseline CT image provides information on the clay and sand packing, and the layout the column sensors. The cross-sectional CT images of the Column 1 (C1), which was used for the heating and a hydration experiment, is shown in Figure 8-5. The color scale in the images is CT numbers that are proportional to the bulk density. In general, the higher numbers (i.e., brighter color) represent higher density. As shown on the image, the bright yellow color on the column perimeter represents the Al pressure column. The white shining spots are either the copper electrodes, the copper wires connecting the electrodes, or the metal in the pressure sensors. Blue color represents low-density features, which include the interior open space of the heater shaft, penetrating through the middle of the bentonite column, and some lower density features created during packing. The brownish color between the column and the clay pack represents the sand layer packed into the column with the purpose to evenly saturate the bentonite. Visible strikes running horizontally across the column are resulting from the dry packing process. Overall, the density variability as the artifact of packing is generally very small. We selected a representative 2D image (marked by the yellow dotted line in Figure 8-5) to discuss the clay hydration subject to heating in Section 8.4.2*c*.

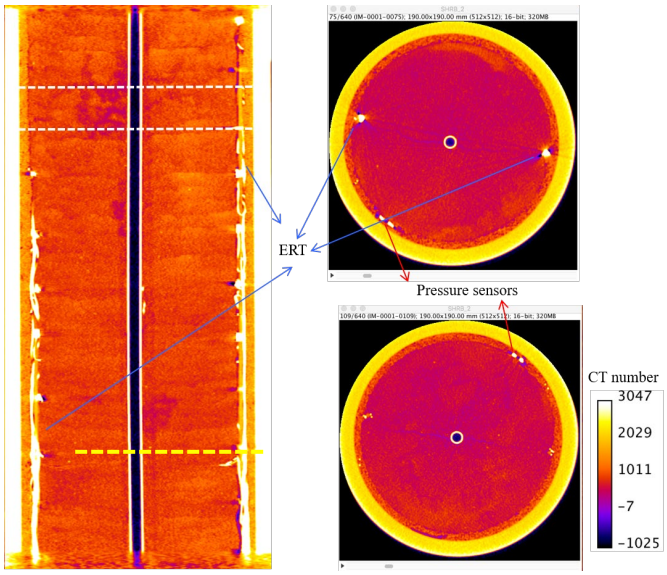

Figure 8-5. Cross sectional CT images of Column 1 that is used for a heating and hydration experiment. The two circular cross sections are from locations marked with the dashed lines on the vertical cross section image on the left. The yellow dashed line indicates locations of the 2-D image selected in Figure 8-11.

The cross-sectional CT images of Column 2 (C2), which was subject to hydration only, are shown in Figure 8-6, which show similar density features in this column, but some visible variances can be observed as well. Noticeably, some local low-density features on the top of the column are visible resulting from uneven packing. In addition, a seemingly slightly larger lateral heterogeneity exists, which is also related to packing. In Section 8.4.2*b*, we will discuss two representative 2D images (marked by the yellow dotted line in Figure 8-6) of the clay that was subject to hydration only.

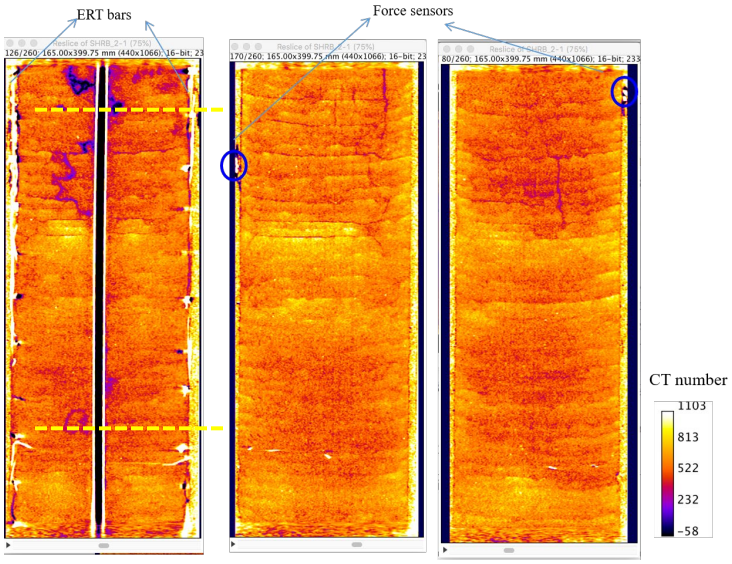

Figure 8-6. Cross sectional CT images of Column 2 that are used for hydration only experiment as the control. The three different cross sections represent different slices at different depths in the axis-normal direction. The two yellow dotted lines indicate locations of the two 2D image selected for the time series presentation in Figure 8-10.

A 3D rendering of C1 is shown in Figure 8-7, and a similar image for C2 is shown in Figure 8-8, with marked key features.

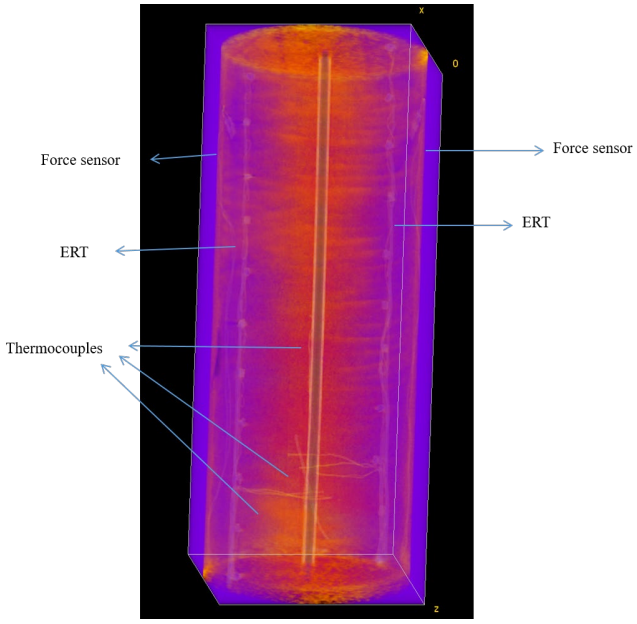

Figure 8-7. 3D CT image of C1 with key instrumentation—thermocouples, ERT and force sensors, and sensor wires.

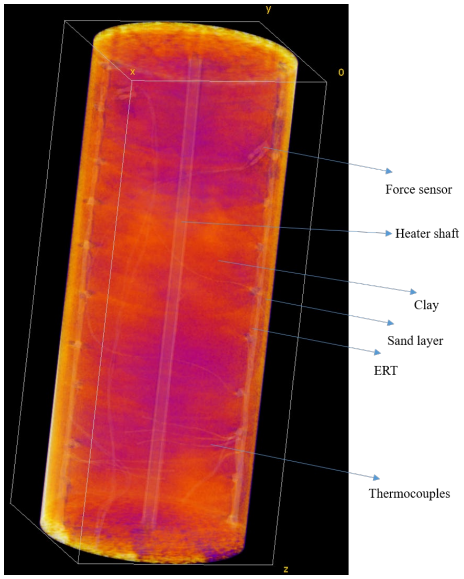

Figure 8-8. 3D CT image of C2 with key features indicated.

Overall, the CT images provide well-defined visualization of the column density structure. This can be used to determine precise locations of the sensors and boundaries in the sample column, which are needed for interpreting and modeling the behavior of the system as experimental data are being collected. Additionally,

the images can be used to understand changes in density and structure during clay hydration and heating. We built the relationship between CT number vs. density by scanning columns compacted with bentonite clay of different bulk wet density. Figure 8-9 represents calibration curve, which was used to interpret the correlation between the CT number and the clay density for both of the heated and non-heated columns. It should be also noted that the clay density is dependent on the bulk dry density and water content, i.e., the value increases with increasing water content and clay dry density. Also noted that no hysteretic or dynamic wetting-drying processes were considered in Figure 8-9 as it was built on static conditions with pre-packed columns

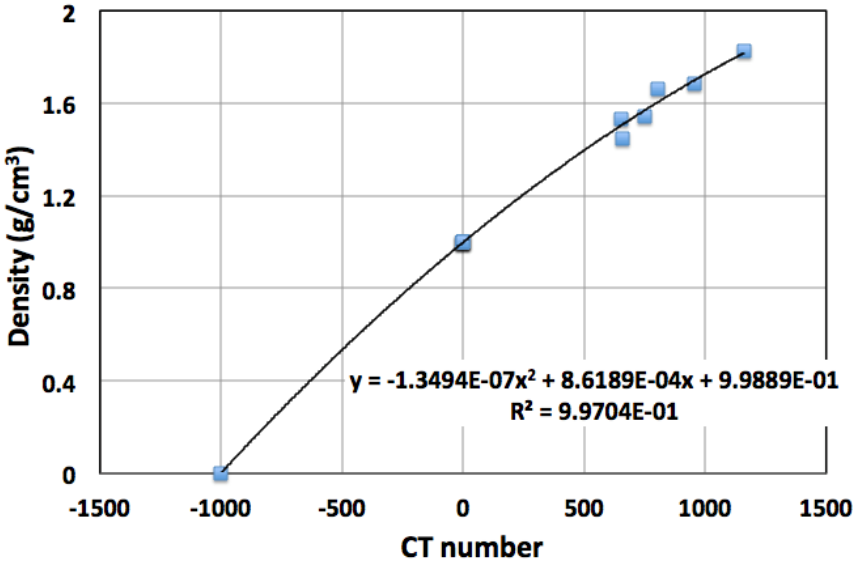

Figure 8-9. The calibration curve used to interpret the correlation between the CT value and density.

We have kept running the experiments and monitoring the density distributions and temporal changes in both columns through frequent CT scans for 255 days. In the following sections, we will present the 3D density map of Column 2 subject to hydration, and column 1--to both hydration and heating. Comparison will focus on (1) the temporal changes of 2D and 3D clay density distributions due to water intrusion, swelling and structural deformation during hydration in the non-heated column, and hydration and heating in the heated column, (2) the swelling and deformation of clay subject to hydration and heating by image-tracking the transit movement of the thermocouple sensors, and (3) the density averaged over the entire clay column and its changes as a function of time.

2-D hydration

Figure 8-10 depicts examples of 2D images of CT density map during the first 8 days, when Column 2 was subjected to hydration. The sub-image at T=0 day shows the initial density map when bentonite clay was packed with a CT density of 1.43 g/cm^3, close to the wet density of 1.46 g/cm^3 measured from the wet clay mass and column volume. The peripheral sand layer has a higher density of 1.67 g/cm^3, presenting a clear boundary (marked by the black dotted line) to the packed clay. The two bright spots of high CT density are the ERT arrays near the sand-clay boundary, while the one in the center indicates the stainless-steel shaft with the heater inserted. We also observe a fracture with a low apparent density (see the blue arrow) due to the uneven packing.

At T=1 day, we first injected gas CO_2 into both columns, followed by brine injection to fully saturate the sand layer. After that, brine injection was kept constant at a rate of 0.11 mL/min under 120 psi. From the 2D CT images, once brine was introduced into the column at T=1 day, the density of the sand layer increased to 1.85 g/cm^3. From T=1 day to 2 days, there exists a density segmentation between the top and bottom portions of the sand due to gravity. After that, we were able to keep a constant density boundary (i.e., a constant water saturation boundary) in the sand layer via maintaining a constant water injection rate (see the density distribution at T=4 and 8 days). The fluid pressure was also maintained constant and monitored by pressure transducers at the inlet and outlet ends. The white arrows in Figures 8-10(A) and (B) indicate the brine intrusion front, based on the CT density difference. Figure 8-10(C) shows the corresponding changes in the average density vs. radial distance from the center shaft as a function of time. At T=1 and 2 days, we observe the increase in CT density near the clay-sand boundary due to brine intrusion. At T= 4 days, a peak CT density occurred 54 mm away from the center shaft (see Figure 8-10(A)), with a continuous density reduction at locations towards the shaft and the clay-sand boundary. The peak density propagates further into the clay, and at T=8 days, it reaches 41 mm away from the shaft. The density reduction near the clay-sand boundary may be attributed to clay swelling subject to hydration. At this point (T=8 days), CT density was affected by both water content and solid migration/displacement. This clay swelling may also compact the interior clay and contribute to the density increase to the peak value in addition to water intrusion. The average clay density, shown in this 2D image, increased from 1.43 g/cm^3 at T=0 day to 1.61 g/cm^3 at T=8 days due to hydration.

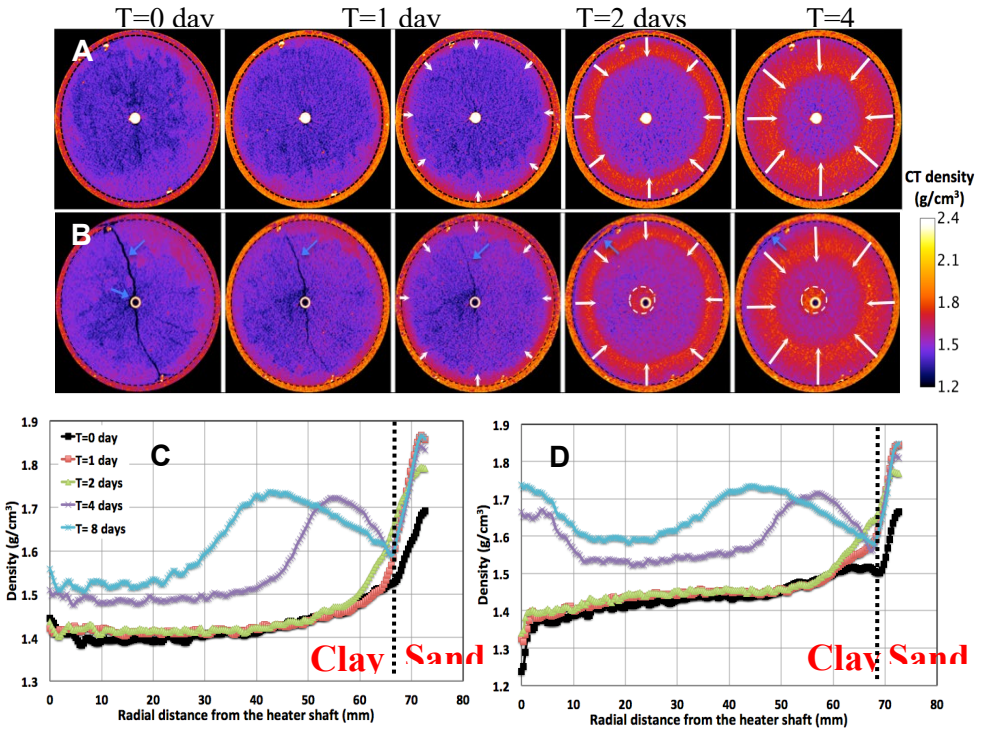

Figure 8-10. (A) 2D images showing the typical hydration process in the non-heated column. (B) 2D images showing the impact of an initial fracture on brine hydration in the non-heated column. (C) and (D) are corresponding average density vs. radial distance from the heater shaft for (A) and (B). The black dotted lines represent the clay-sand boundaries, the white dashed lines indicate the density increase around the heater shaft. The white and blue arrows show the hydration direction and sealing of fracture and boundary gaps due to clay swelling. The 2D images represent locations marked by the yellow dashed lines in Figure 8-6.

Figures 8-10(B) and (D) also demonstrate the impact of initial clay fracture on the 2D hydration process. After brine was injected into the sand layer at T=1 day, the fracture across the center shaft gradually self-sealed due to clay swelling. The fracture cannot be observed at T=4 days at the CT resolution. We also observe in the figure that clay swells at the sand-clay boundary and fills the low-density gap (see the blue arrow at T=4 and 8 days). After that, the sand density remains constant at 1.84 g/cm^3. The graph of the average density vs. distance to the heater shaft in Figure 8-10(D) indicates a density increase close to the shaft at T=4 and 8 days, after the fracture is sealed. More detailed images and a discussion will be presented in Section 8.4.1*d*. In this case, the average density increased from 1.43 g/cm^3 at T=0 day to 1.65 g/cm^3 at T=8 days, higher than the average density increase in the non-fractured case.

2-D heating and hydration

After we injected brine in the sand layer at T= 1 day, we turned on the heater in Column 1 at T= 2 days. Figure 8-11(A) shows the CT density at T= 2 days after heating, when the temperature of clay on the heater shaft (monitored by a pre-emplaced thermocouple) was increased to 150 °C. The temperature was then gradually increased to 175 °C and 200 °C at T=4 and 8 days, and kept constant afterward. Similar closure of fracture in the clay column and gap at the clay-sand boundary (see the blue arrows) indicate the swelling of clay subject to hydration. After increasing the heater temperature at T=2 days, a sharp drop of density occurred around the heater shaft shown in Figures 8-11(A) and (B). Meanwhile, the clay density increased near the clay-sand boundary due to hydration. Figure 8-11(C) shows the density reduction close to the sand-clay boundary at T=4 days, as well as the density peak at 45.5 mm from the heater shaft, indicating the swelling of clay occurred after hydration initiated from the sand-clay boundary. Comparing the peak density locations shown in the non-heated column (Figures 8-10(B) and (D)), we may infer a faster hydration process in clay subject to heating from the center. At T=4 and 8 days, the clay density around to the heater shaft (<15 mm) rebounded quickly to ~1.40 g/cm^3, similar to the density at initial conditions at T=0 day, i.e., prior to hydration and heating. It should be noted that this density rebound occurred before the hydration front arrived. Additional interpretation and analysis of the results of investigations will be given in Section *8.4.1f*.

Figure 8-11(C) presents the average CT density of clay over the 2D image in the three cases (Figures 8-10(A),(B) and Figure 8-11(A)), and their changes as a function of time. The overall density values increased with time after hydration. Comparison of the three cases indicates the highest CT density near the fracture, while heating (up to 200°C) led to the lowest density. A better understanding of the preferential brine flow path and heating hydration processes needs a detailed analysis of 3D images showing the dynamic and spatial CT density changes.

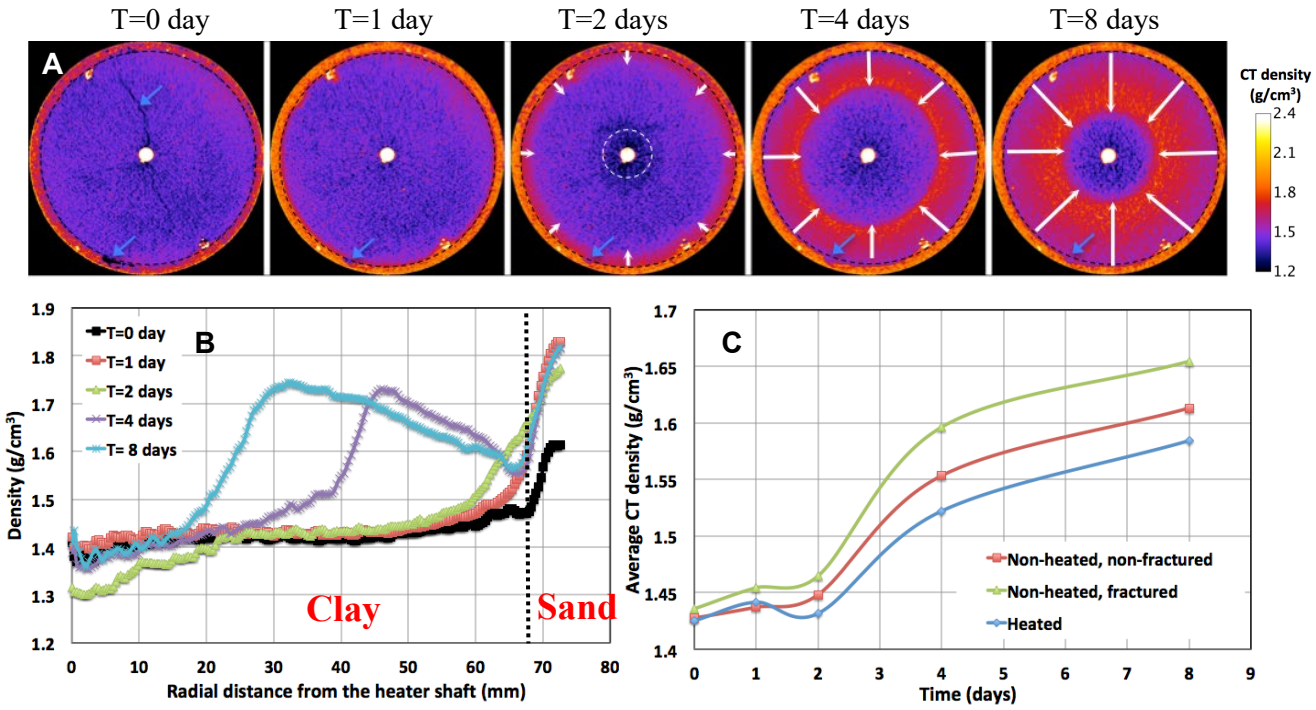

Figure 8-11. (A) 2D images showing the typical processes of heating and hydration in Column 1. (B) the corresponding average density vs. radial distance from the heater shaft. (C) The average density vs. time for the three cases. The black dotted lines represent the clay-sand boundaries. The white and blue arrows show the hydration direction and sealing of fracture due to clay swelling.

3-D hydration

Figure 8-12 depicts the 3D orthogonal view of CT density distribution and temporal changes in the non-heated column. The color bar bounds density changes from 1.2 to 2.4 g/cm^3, and a brighter color indicates a higher density. The image at T=0 day shows the initial conditions and density distribution after packing, including the heater and heater shaft in the center (white color), the sand layer surrounding the clay (orange color), the ERT bars emplaced at the sand-clay boundary (white line in the top slice, the other ERT bar was emplaced in the opposite position that cannot be directly seen in the figure), and clay packed between the sand layer and the central shaft (blue to orange color). The density variations, bedding layers and the dark fracture patches (bounded by the white dotted lines) close to one end of the column are attributed to uneven packing. The uneven packing, especially the fracture patches, affect the hydration process and induce preferential brine flow pathway. The CT density of clay averaged over the entire column is 1.46 g/cm^3, similar to the measured value of 1.44 g/cm^3 by weighing the clay mass used for packing and the column volume.

At T=1 day, we saturated the sand layer with brine and kept flowing at 0.11 mL/min under 120 psi. Hydration was then initiated and indicated by the changes of clay density. At T=8 days in Figure 8-12, the increase of CT density in the column indicates the considerable hydration. The density distribution, however, is not uniform. As shown in the figure, the high-density front represents the hydration front, which has advanced halfway towards the center shaft. We also observe great density reduction at the sand-clay boundary relative to the hydration front. This can be attributed to the more considerable reduction in clay dry density by swelling after hydration. The clay swelling initiated at the sand-clay boundary may push and

compact the interior clay, and contribute to the high-density hydration front. We also show at T=8 days the seal of the fracture patches by swelling, which hinders the propagation of hydration along the center shaft (see the magnified image, Figure 8-12). The clay swelling meanwhile smoothens the density variations and impedes preferential flow of brine from the surround sand layer. All these are in favor of retardation of radionuclide and securing the spent nuclear fuel and waste disposal. At T= 255 days, the overall density distribution become more uniform.

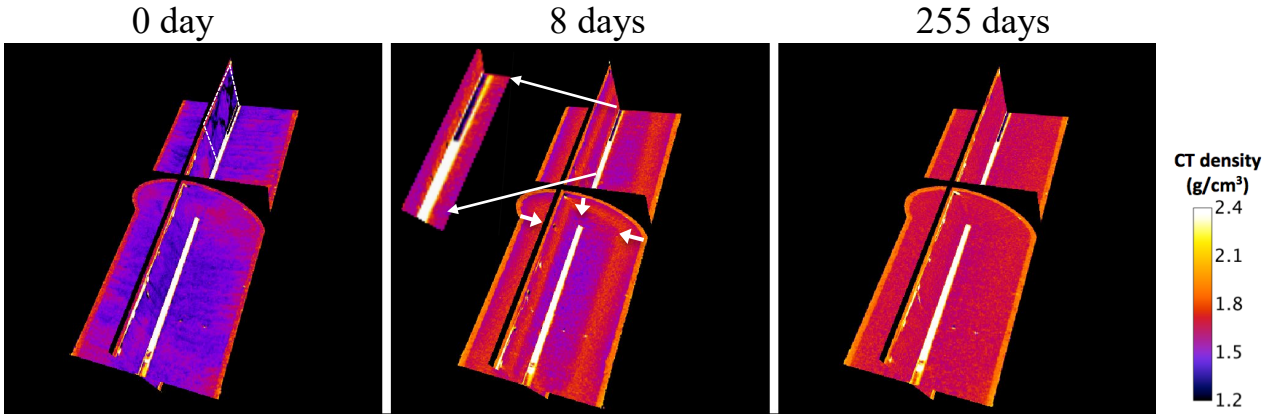

Figure 8-12. The 3D clay density maps showing the spatial and temporal variations of clay density in the non-heated column. The sub-image at T=0 day shows the initial condition after packing, with the uneven-packing induced fracture marked by the white dotted box. The white arrows at T=8 days depict the continuous hydration from the surrounding sand layer, while the magnified image at T=8 days presents the preferential water intrusion along the center shaft at early time.

The 3D images indicate radial symmetry of hydration distribution from the sand layer to the center shaft. We thus applied the radially averaged images to show the 3D hydration process. For each CT scan, the obtained CT image stack was first orthogonally reconstructed by rotating a line at 360° around the center shaft. Then, an image was obtained by averaging over the 360° radially reconstructed images, and the CT number was converted into the density using the calibration curve shown by Figure 8-13.

Figure 8-13 shows the time-lapse images of the non-heated column subject to clay hydration from the sand layer up to 255 days. Note that each sub-image was radially averaged, and the density profile along a single line (e.g., the white dotted line at t=255 days) represents the average density vs. radial distance from the heater shaft, as shown in Figure 8-13(B). Figure 8-13 (A) clearly shows that the hydration was initiated from the peripheral sand layer and the top and bottom boundaries, where brine invaded the clay column from gaps between the column end caps. The hydration along the center shaft, however, stopped at T=8 days, because of clay swelling and sealing of the gaps after hydration (also see the 3D images in Figure 8-12). The continuous propagation of hydration occurred from the peripheral sand layer, as indicated by the temporal changes of the peak density in Figure 8-13 (B). At T=33 days, the hydration front approached the center shaft. After that, the clay density increased at a location close to the shaft, along with the density reduction in the middle part (~40 cm from the shaft), resulting in a more uniform density distribution in the entire column.

The clay swelling and density reduction along the sand-clay boundary can also be observed at early times (T=4 and 8 days) in Figure 8-13 (A) and (B). The swelling of clay at the boundary may compact the interior clay, resulting in the sharp density increase ahead of the hydration front. For example, in Figure 8-13 (B) and at T=4 days, at the distance of <40 mm from the center shaft, the density of clay increased by ~0.05 g/cm^3, when compared to the density at T=2 days. At T=8 days, the density increased another 0.03 g/cm^3 ahead of the hydration front (<20 mm from the center shaft). As hydration continued and propagated to the center, the compaction weakened, the density at the sand-clay boundary gradually rebounded, along with

the density reduction in the middle part. These induced flattening of the density profile along the white dotted line perpendicular to the center shaft, and the uniform density distribution in the entire column. The magnified CT image shown in Figure 8-13 (A) depicts a relatively uniform density distribution close to the center shaft, with thermocouple sensors attached on the shaft shown in bright spots. The frequent X-ray CT images and changes in clay density represent the spatial and temporal dependent processes of increasing saturation and clay swelling due to hydration. At T=255 days, the column averaged clay density was stable at 1.68 g/cm^3, 0.21g/cm^3 higher than the initial value before hydration.

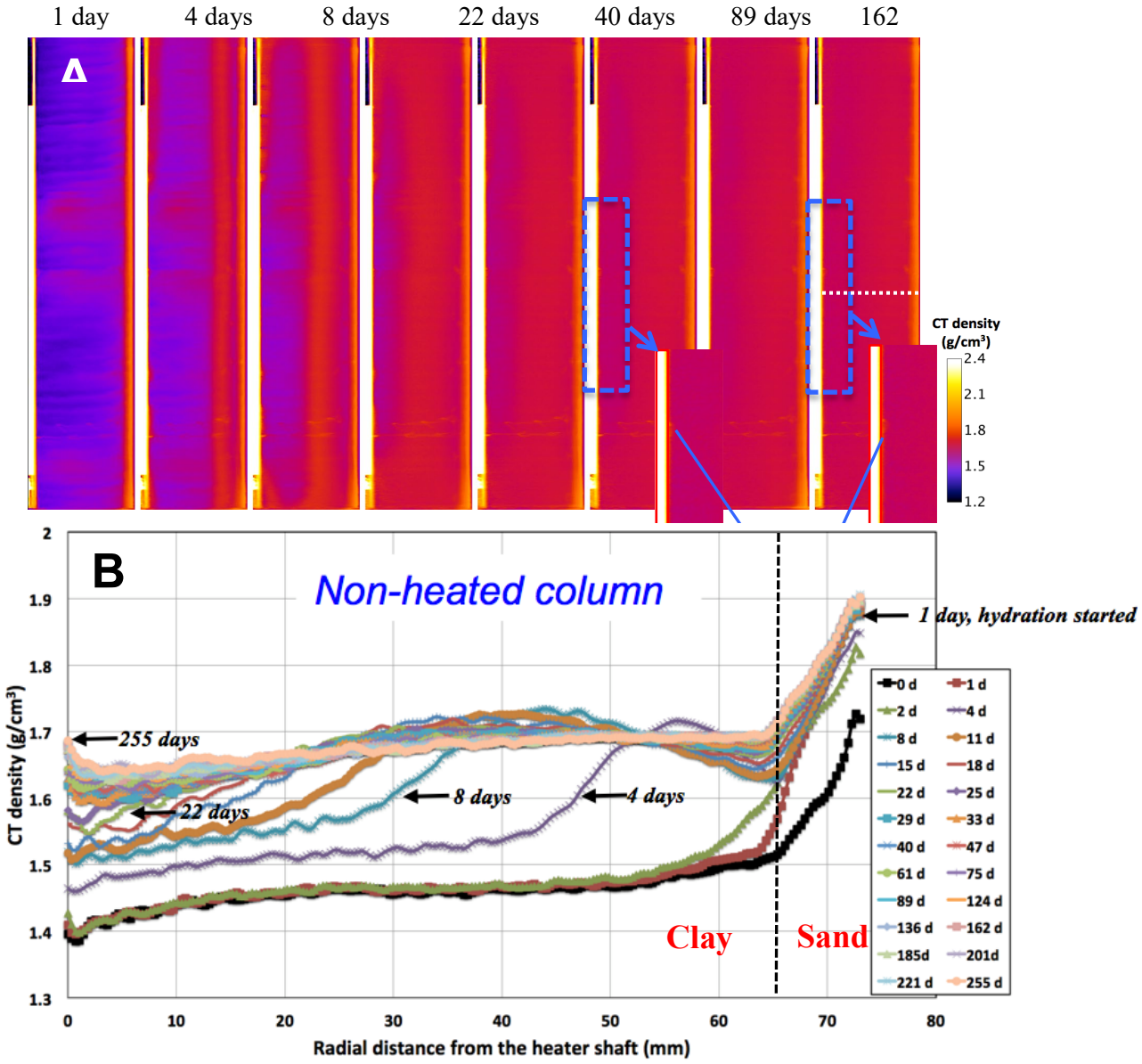

Figure 8-13. (A) The radially averaged density map and changes with time for the non-heated column subject to hydration only. (B) The average density vs. radial distance from the heater shaft along the white dotted line in (A). The magnified image in (A) (bounded by the blue dotted box) showing the density distribution close to the center shaft at T=89 and 255 days. The blue arrows in (A) mark the bright spot of thermocouple sensors.

3-D heating hydration

In the heated column at T=1 day, we also saturated the surrounding sand layer with brine and kept it flowing at 0.11 mL/min under 120 psi. At T=2 days, we turned on the heater and kept the temperature of clay on the heater shaft constant at 200 °C since T=8 days. Figure 8-14 depicts the 3-D density distribution and changes with time in the heated column, while Figure 8-15 shows the radially averaged density map (A) and the average density profile vs. radial distance from the heater shaft (B). Image at T=0 day presents an initial condition similar to that in the non-heated column. The column averaged CT density was 1.44 g/cm^3, close to the measured value of 1.41 g/cm^3 by weighting the packed clay mass. The image also presents the patterned layers and density variations, as well as the fracture close to one end of the column. At T=8 days, we observe similar (1) swelling of clay and sealing of the fracture after hydration, (2) density reduction at the sand-clay boundary due to clay swelling, and (3) clay density increase ahead of the hydration due to compaction.

Differing from the non-heated column, however, Figures 8-14 and 8-15(A) at T=8 days present a dry-out zone of a lower density close to the heater shaft. Because of heating, the average density within this dry-out zone was 1.32, 1.38, and 1.40 g/cm^3 at T=2, 4, and 8 days, respectively, lower than the values of 1.43, 1.52 and 1.56 g/cm^3 within the same region of the non-heated column. The heating, thus, induced a larger density gradient (thus, larger gradient of water content) and vapor outward transport (from the innermost heating zone) and condensation in the middle part as temperature decreased (also see Figure 8-15(B)). The hydration front approached the location 5 mm away from the middle shaft at T=25 days, after that a dry-out zone sustained. At T=255 days, the dry-out zone was confined in location <5mm away from the heater shaft, while the overall density distribution in the column became more uniform.

Within the dry-out zone, we observe bright, high-density deposition on the heater shaft, as shown by the magnified image in Figure 8-14 at T=255 days. More frequent CT images (Figure 8-15(A) and (B)) indicate the deposition initiated at T=75 days (the sharp increase in the CT density in the dry-out zone in Figure 8-15(B)), followed by the quick increase to 1.83 g/cm^3 until T=124 days. After that, the density increased slowly and stabilized at 1.89 g/cm^3 at T=255 days. The deposition also occurred along the heater shaft, as shown in Figure 8-15(A). We assume the high-density deposition was caused by mineral precipitation as water vaporization in the dry-out zone and continuous transport of dissolved mineral species with hydration to the dry-out zone. We will dismantle the column and collect the pore fluid and clay samples for more detailed chemical analysis.

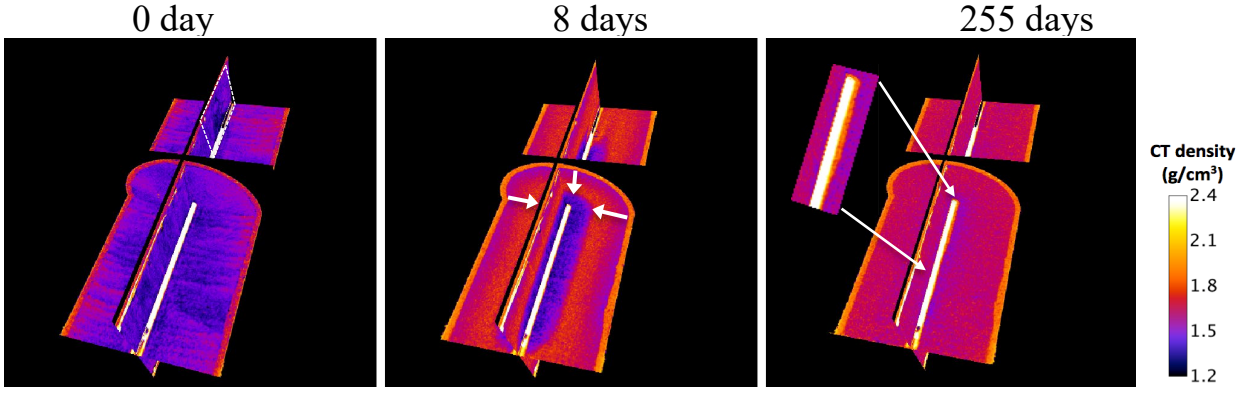

Figure 8-14. The 3-D clay density map and temporal variations in the heated column. The sub-image at T=0 day shows the initial condition after packing, with the uneven-packing induced fracture marked by the white dotted box. The white arrows at T=8 days depict the continuous hydration from the surrounding sand layer. The magnified image at T=255 days presents the bright high-density deposition on the heater shaft subject to heating and water vaporization.

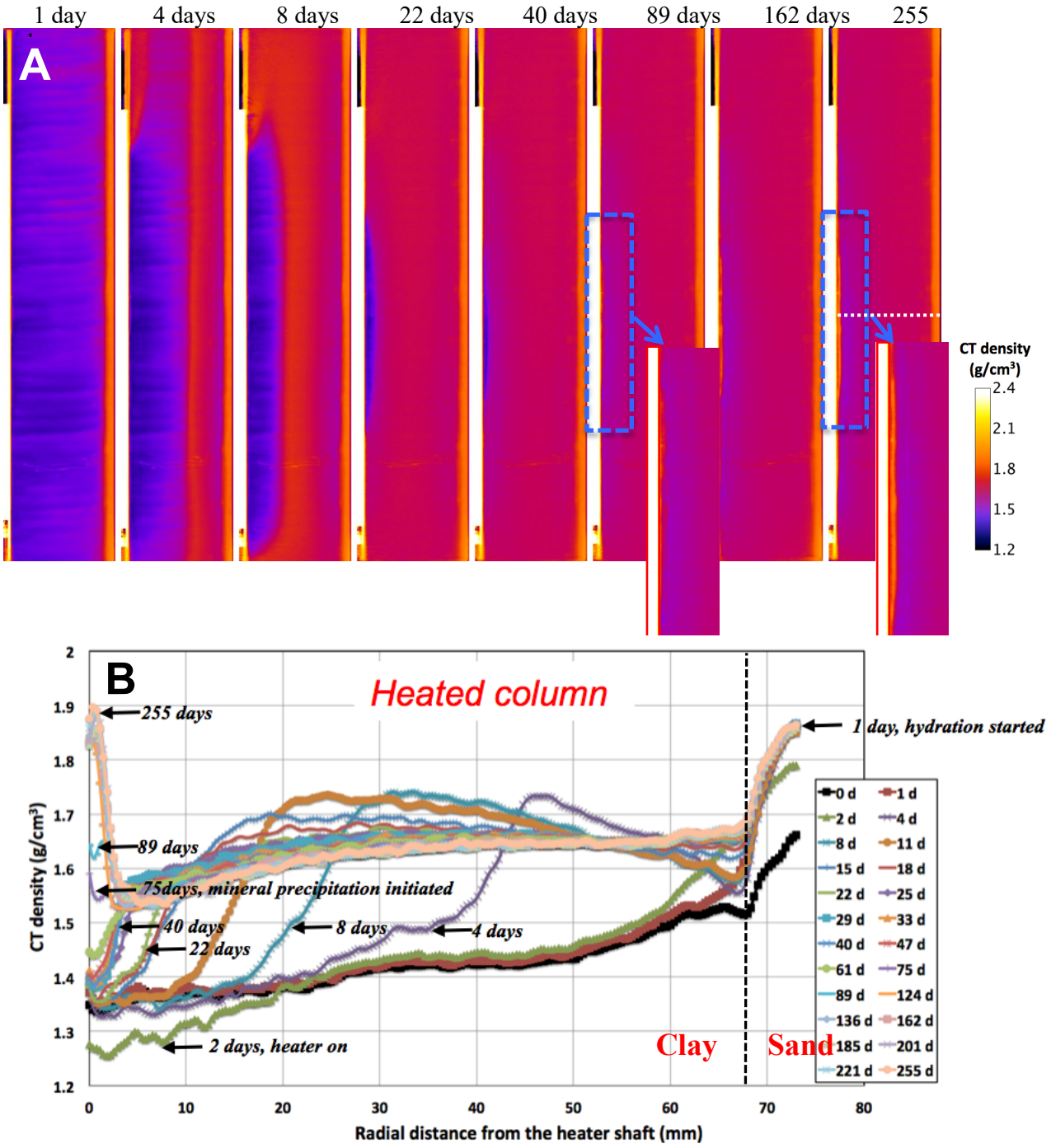

Figure 8-15. (A) The radially averaged density map and changes with time for the heated column subject to heating and hydration. (B) is the average density profile vs. radial distance from the heater shaft along the white dotted line in (A). The magnified image (bounded by the blue dotted box in (A)) shows the density distribution and bright high-density deposition on the heater shaft at T=89 and 255 days.

Deformation subject to hydration

We have shown in previous images potential clay swelling and compaction subject to hydration and heating through the dynamic changes of clay CT density. The clay swelling and compaction subject to hydration were further investigated by the transit movement of the thermocouple sensors (induced by the deformation of surrounding clay) through frequent CT images. We selected 2D CT images that present the bright spots representing thermocouple sensors, and tracked their distance to the central shaft and monitor the changes as a function of time. Figure 8-16(A) depicts the 2-D CT image selected from the non-heated column at different times. The white arrows mark the initial position of the exterior thermocouple before hydration, which was 48 mm away from the center shaft. The T=1day image shows the surrounding sand layer saturated with brine (orange color), the packed clay (purple color), and the brightly white shaft at the center, as well as the ERT bars emplaced at the sand-clay boundary.

As shown in Figure 8-16(A), as the high-density hydration front propagated into the clay column at T=4 days, the considerable clay swelling at the sand-clay boundary induced a significant density reduction. Meanwhile, the thermocouple was pushed towards the center shaft along with the compaction of surrounding clay (see the offset of the bright spot relative to the white arrow). At T= 8 days, the offset reached maximum as the hydration front approached the thermocouple. After that, as the hydration continued and the front passed the thermocouple, the thermocouple was pushed back slowly to its original location, as indicated by the reduced offsets between the bright spot and the white arrow (see the images at T=8 days and 255 days).

To better illustrate the process, we measured the distance between the center shaft and the thermocouple, and plotted in Figure 8-16(B) the changes as a function of time (marked by the red dotted line). The displacement was calculated by subtracting the initial distance between the thermocouple sensor and the center shaft (thus the displacement at T=0 day was normalized as 0). We define the negative displacement when the thermocouple was pushed toward the center shaft, and positive displacement when the thermocouple was pushed away from the center shaft relative to its initial position. Figure 8-16(B) also present the changes in the clay CT density around the thermocouple (the blue curve), with the density peak representing the hydration front. As shown in the figure, before the hydration front arrived at T= 8 days, the displacement continuously decreased from 0 mm to the minimum value at -2.3 mm. Most clay is compacted by the strong hydration and swelling along the sand-clay boundary. After the hydration front arrived, the deformation gradually rebounded back along with the clay swelling at the surrounding clay and more interior locations closer to the center shaft. This might have also caused the slow decrease in the clay CT density around the thermocouple. At T=255 days, the CT density and displacement were relatively stable at 1.68 g/cm^3 and -0.9 mm. These indicate the coupled processes of hydration and clay swelling, as well as their spatial and temporal dependent behaviors.

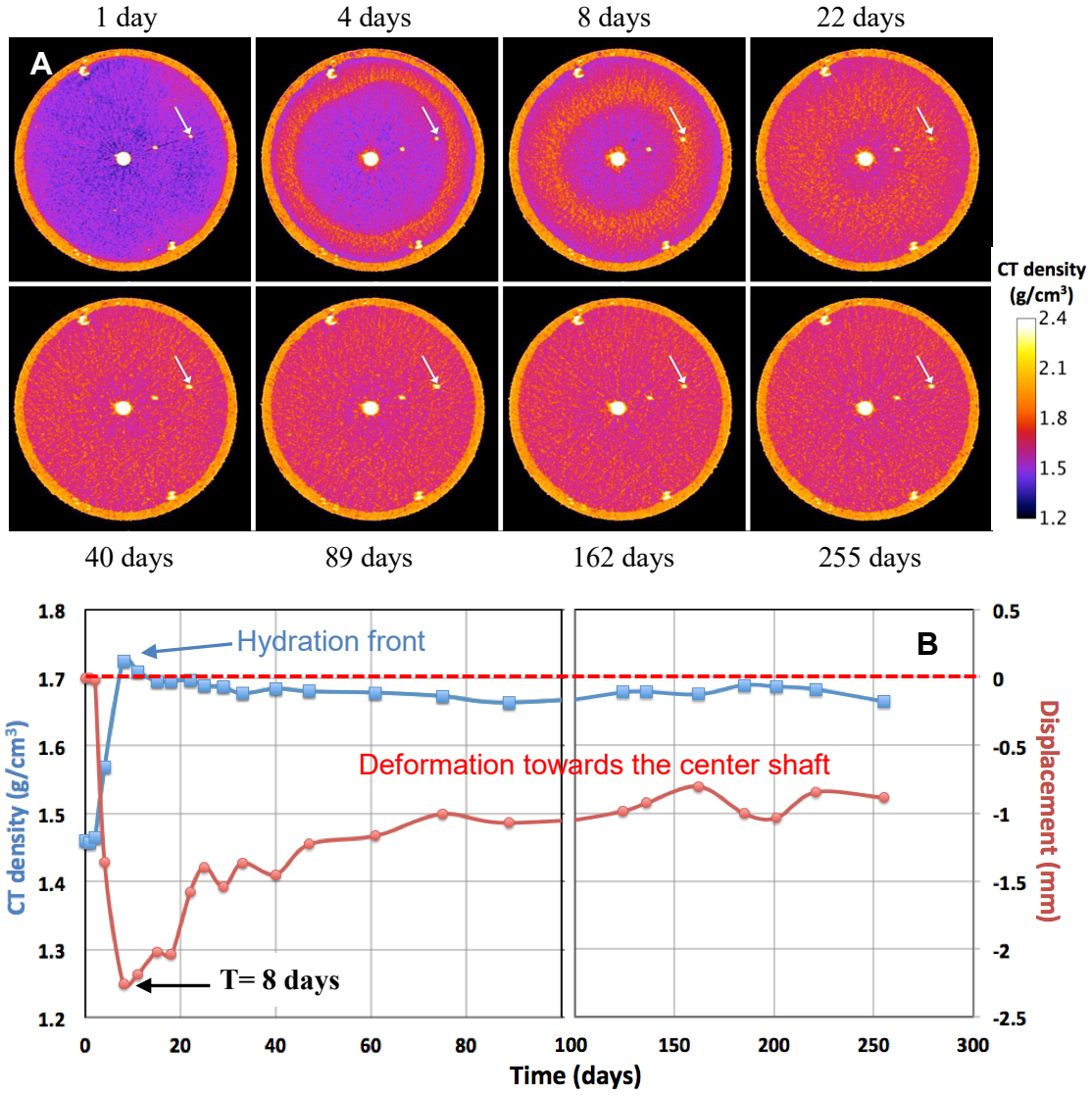

Figure 8-16. (A) The time-lapse 2D CT images showing the transit movement of the thermocouple sensor along with the dynamic CT density changes of clay in the non-heated column. (B) Comparison of the displacement of the thermocouple sensor vs. surrounding clay CT density. The white arrows in (A) mark the initial position of the thermocouple sensor.

Deformation subject to heating and hydration

Figure 8-17(A) presents the 2-D time-lapse CT images and transit movement of the thermocouple (originally 11 mm from the heater shaft) in the heated column. We turned the heater on at T=2 days and maintained the temperature on the heater shaft constant at 200 °C since T=8 days. Differing from the observations in the non-heated column, the inward movement of the thermocouple at early time (1-8 days) was followed by the backward movement to its original location at T=22 days. After that, the thermocouple sensor continuously moved outward to the sand-clay boundary and maintained a constant offset at T=255 days. The deformation and clay density around the thermocouple further quantify the coupled processes subject to heating and hydration. In Figure 8-17(B), as we turned the heater on at T=2 days, the local clay

density sharply reduced from the initial value of 1.40 g/cm^3 to 1.32 g/cm^3 due to water vaporization, followed by a quick rebound to 1.41 g/cm^3 at T=4 days. The continuous reduction in the displacement also confirms that most of the interior clay is dominated by compaction after the hydration, and clay swelling initiate at the sand-clay boundary. At T= 8 days, the deformation reached minimum values at -1.1 mm toward the heater shaft. It should be noted that, compared to that in the non-heated column, the local clay subject to heating and compaction is higher in its bulk dry density, thus obtained higher swelling potential once in contact with brine. When the hydration front arrived, the local and more interior clay swelled, and continuously pushed the thermocouple sensor back to its initial position at T=22 days. After that, the initially drier and tighter clay continued to swell and moved the thermocouple further away from its initial position by 1 mm at T=255 days. Note the temperature of the thermocouple increased with time and kept constant at 140 °C after T=89 days, lower than the water boiling temperature of 175°C under 120 psi. This enabled the hydration and swelling of clay to occur. The clay subject to heating and hydration shows a more considerable and complex process of deformation.

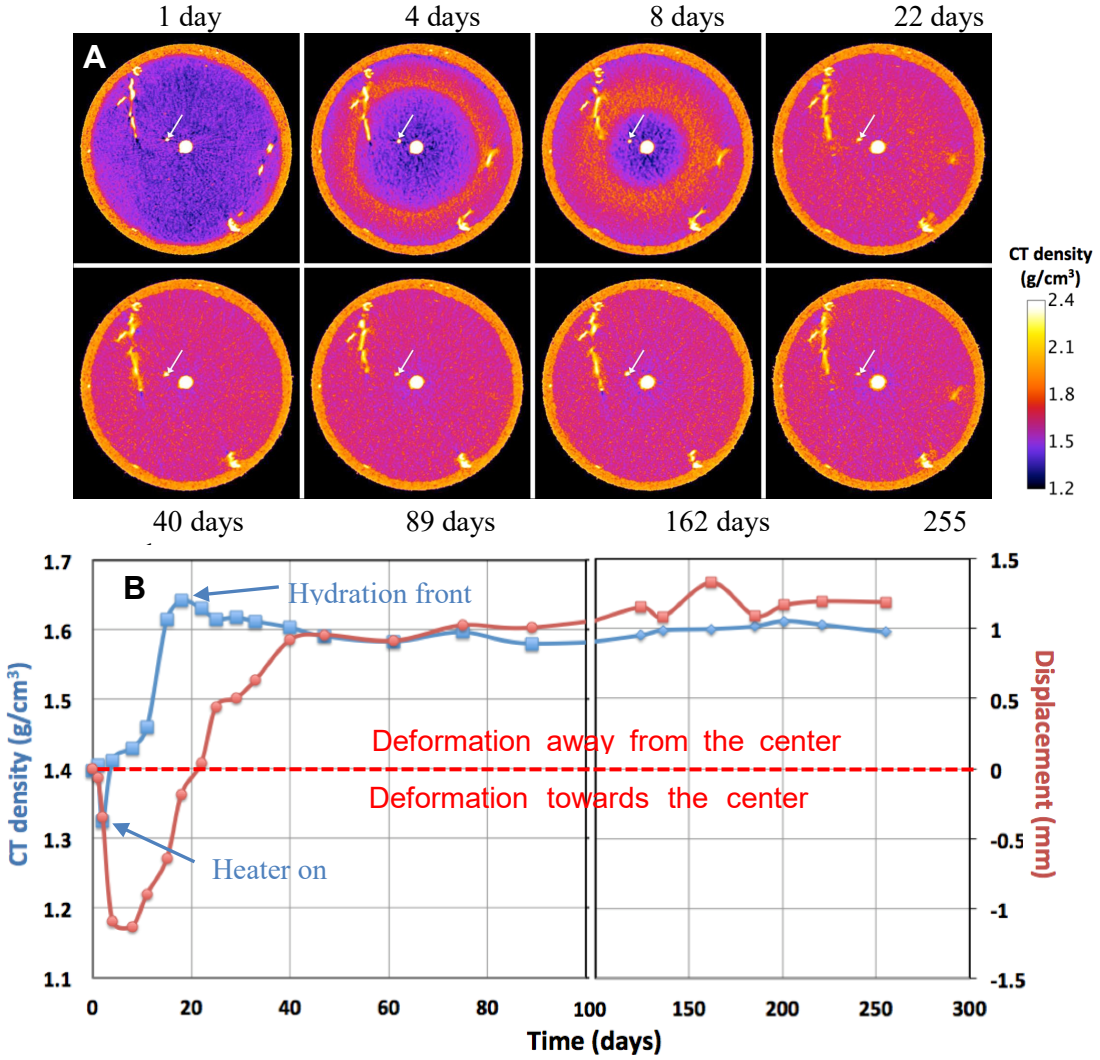

Figure 8-17. (A) The time-lapse 2D CT images showing the transit movement of the thermocouple sensor along with the dynamic CT density changes of clay in the heated column. (B) Comparison of the displacement of the thermocouple sensor vs. surrounding clay CT density. The white arrows in (A) mark the initial position of the thermocouple sensor.

h. Deformation at different locations

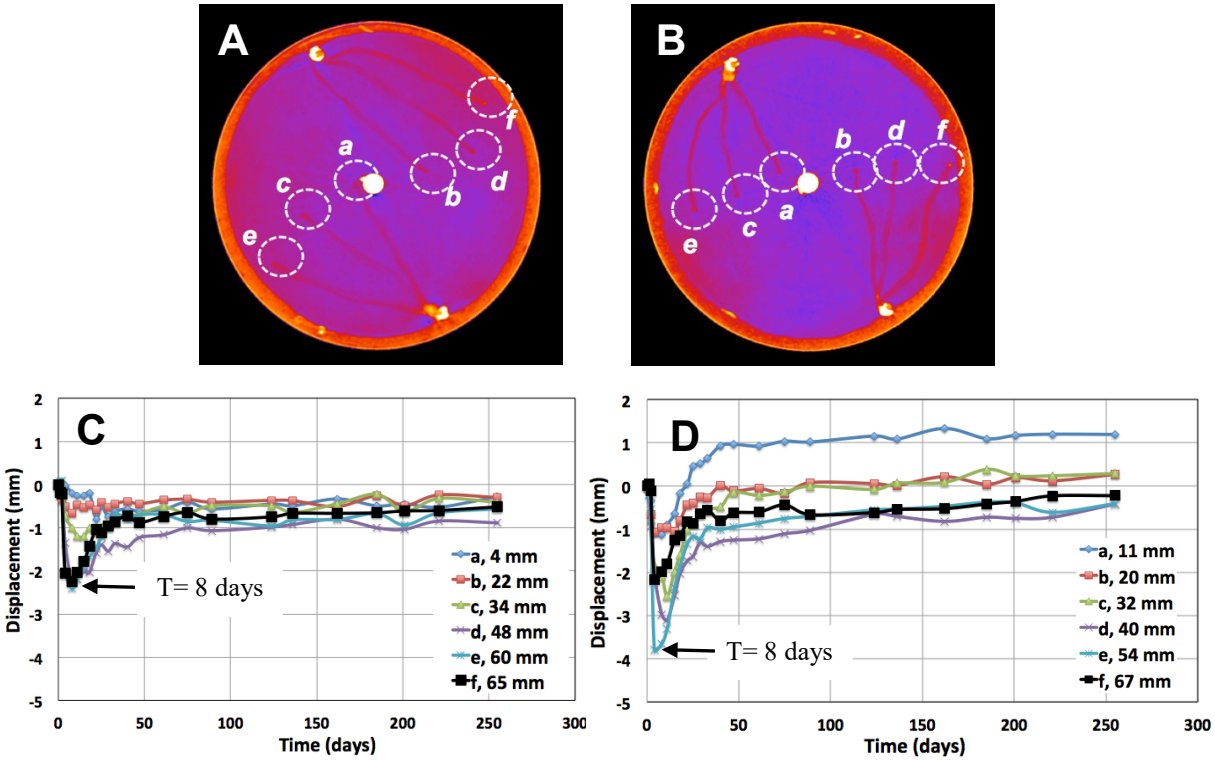

Figure 8-18. The six thermocouple sensors that are used for tracking clay deformation at different locations in the non-heated (A) and heated (B). (C) and (D) present the displacement changes relative to their original positions vs. time for the six thermocouple sensors. The legend marks the initial position of each thermocouple relative to the center shaft.

We investigated the spatially variable deformations of clay by tracking all six thermocouple sensors emplaced in both of the non-heated and heated columns. Figures 8-18(A) and (B) present the locations of each thermocouple sensor in the non-heated (A) and heated (B) columns. Figures 8-18(C) and (D) depict their displacements and variations as a function of time up to 255 days. In both columns, thermocouple *a* was closest to the center shaft, while thermocouple *f* was closest to the sand-clay boundary. Thermocouples *b, c, d, e* located 20 to 60 mm away from the center shaft. In the non-heated column, as shown in Figures 8-18(A) and (C), all six thermocouples showed similar trending of displacement variations vs. time. For instance, at early time (1-8 days), all thermocouples along with their surrounding clay were compacted toward the center shaft with continuous decrease in displacement. Spatially, the displacement decreased from exterior to interior clay, where deformation was confined by the rigid boundary at the center. After that, as hydration propagates to the center, all the thermocouples were pushed backward to their initial positions. The displacements for all the thermocouples thus gradually rebounded and kept constant at -0.4 to -0.9 mm relative to their initial positions.

Figures 8-18(B) and (D) show the initial locations of the six thermocouple sensors in the heated column, and their displacement changes vs. time. Comparing to the non-heated column in Figure 8-18(C), the clay presents more considerable deformation subject to heating and hydration. The deformation could be both inward (negative displacement values) and outward (positive displacement values), depending on the location and time. At early times (1-8 days), all thermocouples along with their surrounding clay were similarly compacted toward the heater shaft by swelling at the sand-clay boundary. The displacement

values, however, ranged from -1.0 to -3.8 mm, showing larger compaction than that in the non-heated column at -0.2 to – 2.4 mm. This indicates larger compaction induced by hydration and clay swelling at the sand-clay boundary when heating at the center. Note the clay CT density (1.58 g/cm^3) at the clay-sand boundary (marked by the black dotted line) at T=8 days in the heated column is lower than that in the non-heated column (1.63 g/cm^3). While more water was sucked into the column by larger water saturation gradient, the reduced clay CT density indicates larger reduction in clay dry density after more considerable swelling. It should be also noted that for thermocouple *f*, the compaction and displacement were limited by the clay available for swelling as its location was too close to the clay-sand boundary.

Thermocouple *a* was discussed in details in the previous section. While the other thermocouples more or less recovered to their initial positions, the displacement of thermocouple *a* was affected by larger heating-induced swelling, as it was closest to the clay dry-out zone. It can be inferred that more interior clay would be drier as temperature increases beyond water boiling point. More considerable clay swelling at some locations (e.g., around the thermocouple *a*) of favorable temperature and water content (i.e., the local temperature is high enough to vaporize pore brine but still below water boiling temperature so that the subsequent hydration is allowed) may hinder fracture development at the shaft-clay interface by heating, thus is in favor of securing the spent nuclear fuel and waste disposal.

Average density change of the clay columns

Through the frequent X-ray CT imaging, we are able to calculate the average CT clay density over the entire clay column, and show in Figure 8-19 the density increase after hydration in Column 2 (the non-heated column) and in Column 1 (the heated column) subject to heating and hydration. In the non-heated column, the clay density increased quickly once hydration started and at T= 22 days, the average density was 1.68 g/cm^3, increased by 0.21 g/cm^3, when compared to the initial condition. After that, the value kept relatively constant until T=255 days. By comparison and in the heated column, the density increased faster and at T= 15 days, the density increase reached the peak value of 0.21 g/cm^3. After that, clay density decreased slowly, but was 0.2 g/cm^3 higher than the initial one, and finally stabilized at 1.64 g/cm^3 at T= 255 days. Overall, Figure 8-19 presents a faster hydration of clay and density increase subject to heating and hydration, followed by a slow density reduction and finally stabilized. The observed bright deposition on the heater shaft after 75 days in the heated column indicates potential mineral precipitations and chemical interactions (e.g., indicated by Section 8.4.2), and coupled THMC processes of bentonite clay subject to heating and hydrations. As we discussed earlier, these processes are spatial and temporal dependent. We will dismantle both columns and collecte clay and pore water samples for detailed mineralogical and chemical analysis. These will help in understanding the complex processes and provide a complete dataset for modeling the behavior of bentonite based EBS system, which is key to the evaluation and prediction of its performance in the long term.

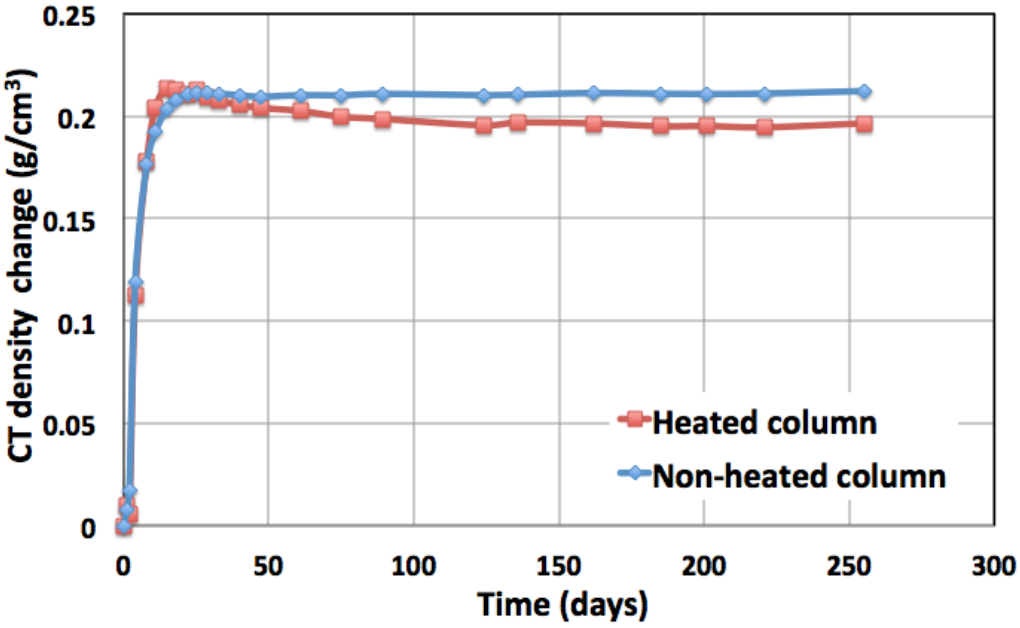

Figure 8-19. The CT density changes in the heated Column 1 and non-heated Column 2.

8.4.2 Geochemistry

Effluent water was collected, weighed and sampled from the influent mixture (see Table 8-1) and from the effluent of both columns (Figure 8-20). In the heated column, the effluent showed the sulfur reduction (also identified observed through the smell of sulfide), excess of silicon and potassium, and calcium, magnesium retention.

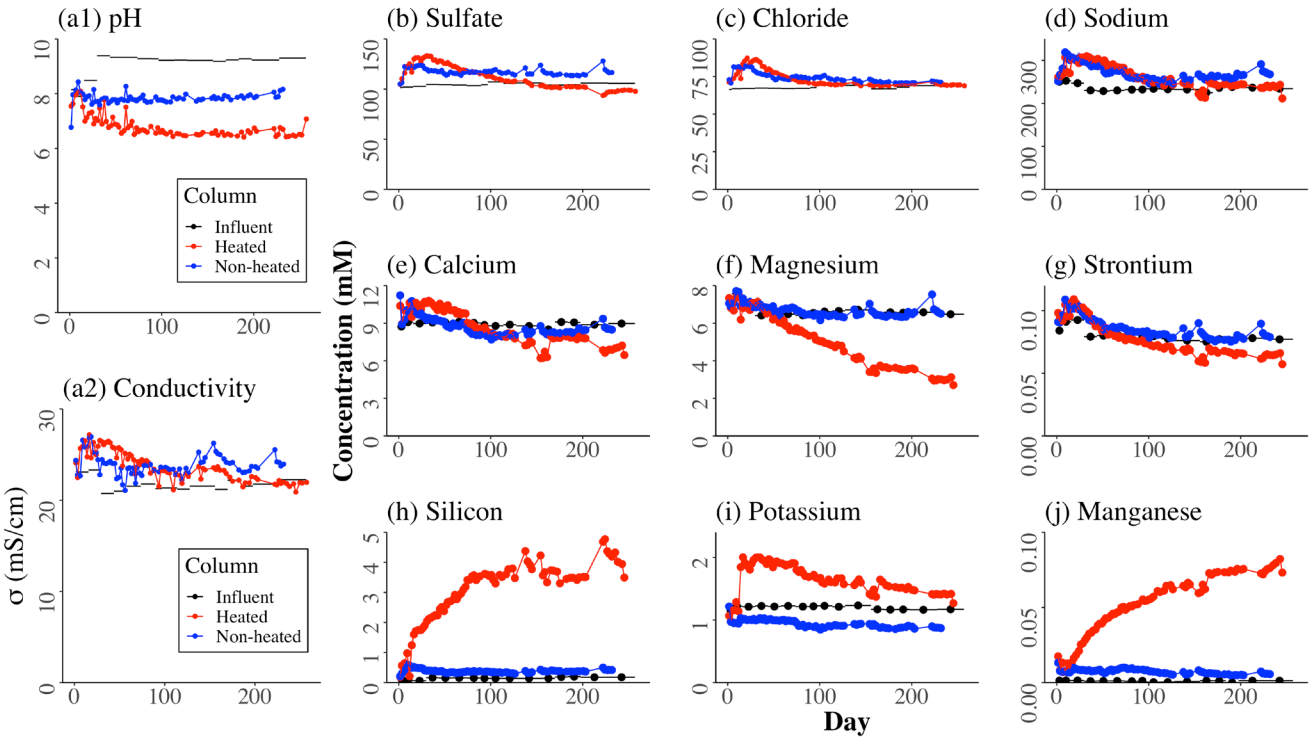

Figure 8-20. Influent and effluent geochemistry results. (a) pH and conductivity, (b-d) anions and (e-j) cations concentration in mM.

8.4.3 ERT

In HotBent-Lab experiment, we evaluated the potential of using the electrical resistivity tomography as a long-term field monitoring technique for the bentonite barrier system. Under heating and hydration, the clay enfolds much of the information in its electrical resistivity, and water content is one of the dominant parameters of interest. Temporal variation and spatial distribution of moisture in the barrier system are crucial for evaluating bentonite sealing properties and for THLM modelling, while obtaining spatial water content data at the field scale is challenging due to site accessibility and sensor availability under the thermal and geochemical conditions of the operation. With the electrodes embedded into the clay as part of the packing processes, time lapse ERT would be able to provide continuous and dynamic visualization of the changes in the bentonite. In this section, we would be discussing (a) ERT data acquisition, processing and visualization, (b) calibration between resistivity and water content using physics-based model and laboratory data (including CT, temperature, effluent chemistry) from lab petrophysical experiments and *in-situ* measurements in the columns, and (c) the application of the calibration for the ERT time lapse imaging to generate temporal water content distribution maps. The limitations of current setups and improvements that could be made would also be addressed.

ERT data acquisition, processing and visualization

Our current ERT setup included (1) an electrical impedance tomography system (MPT DAS-1) and (2) 24 square copper electrodes (0.5 by 0.5 cm) evenly spaced on a pair of fiberglass rods (12 electrodes on each rod, inter-electrode distance was 3.8 cm) (Figures 8-1, 8-3). The rods were positioned at the sand-clay boundary opposite at each other from the central shaft, with the electrodes embedded inside the clay. The wires were soldered onto the copper, wrapped along the rods, exited through a feed-through port on the

end-cap and connected back to the system. The materials of the rods and the wires were chosen to withstand the operation temperature and saline conditions, and the aluminum column and the titanium heater shaft were painted with electrically-insulated silicone gel to minimize current conduction from the metals.

During an ERT data acquisition, electrical potential was applied through two selected electrodes, and the potential difference was measured between multiple combinations of the other electrodes in pair. The electrical potential was applied in the frequency domain at 1 Hz with a target voltage at 10 V. The measurement sequence followed dipole-dipole electrode configurations (a combination of skip-0, 1, 2, 4, 6, 11 arrays) with 3 stacks, summing up to 1326 lines of data in one acquisition. Our current setup allowed for automatic and simultaneous imaging of both columns with a specifiable time interval (on a tri-hourly basis), and the data were remotely retrieved, thus offering the opportunity to provide spatially and temporally dense datasets. A python-based algorithm BERT (Gunther and Rucker, 2013) was used for ERT data simulations and for generating a 3D electrical resistivity distribution in the clay. Figure 8-21 shows the numerical mesh used to perform forward and inverse simulations. The inversion results can be opened in software such as paraview that allows for inspecting the internal structures at desirable cross-sections and performing spatial analyses.

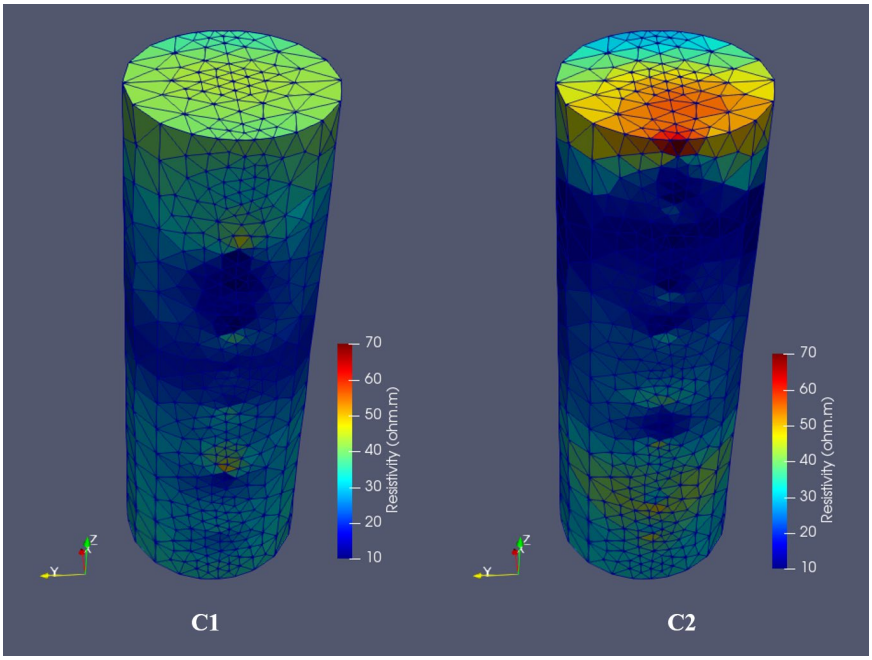

Figure 8-21. Numerical mesh used for ERT inversion and 3D visualization of the electrical resistivity structure of the columns after packing (T=0 day). C1 is the heated column, and C2 is the non-heated.

As was shown in the CT analysis, heating and water infiltration could be described as radial processes. Therefore, radial-averaged resistivity along the column depths was calculated as part of the post inversion data processing. Since the electrode rods were planted at two ends of the *x*-axis, the major electrical current flow paths were along the rod or in a cross-well manner, therefore giving higher data coverage of the ERT inversion model near the *x*-axis (Figure 8-22 (A)). As the distance to the electrode rods increased, the data coverage decreased, generating bigger and sparser cells in the numerical mesh. In this analysis, we only included the data inside the high coverage cuboid bounded by the red lines (Figure 8-22 (A)). When calculating the radial-averaged resistivity, a 1 cm (radius) by 1 cm (depth) mesh grid was adopted for

interpolation, using the inverse distance weighing with 2 cm (chosen as the electrode half space) moving window (Figure 8-22 (C)). Figure 8-22(C) also shows three column depths, which would later be used to compare with CT: (1) thermocouple depth z = 11cm, (2) mid-heater depth z = 21cm, and (3) mid-column range with depths between z = 11 and 31 cm.

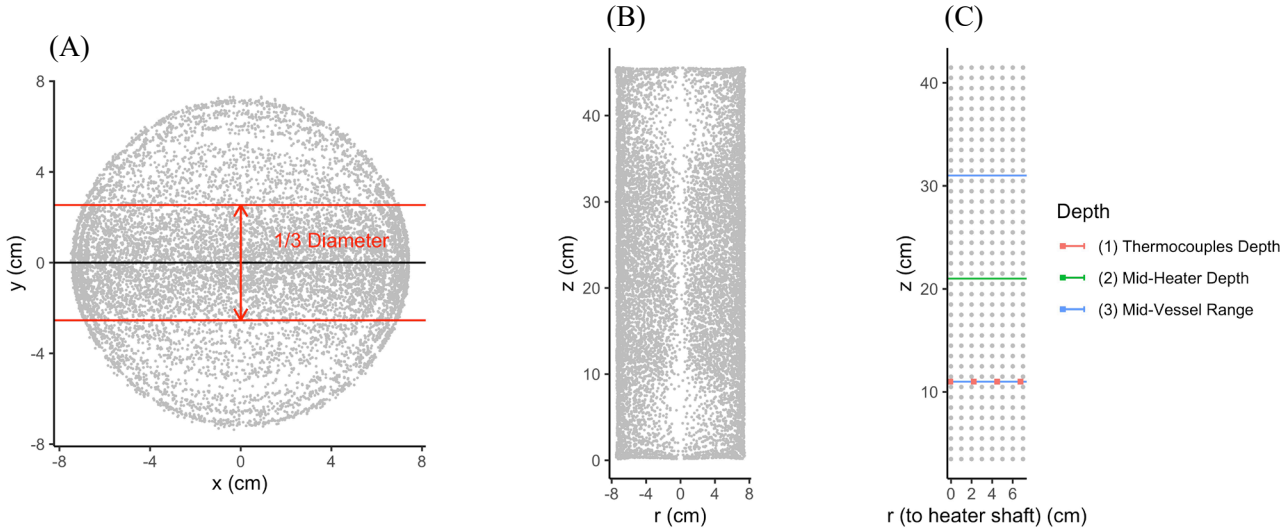

Figure 8-22. Radial data coverage of the ERT inversion model in (A) cross-sectional and (B) bird's-eye view. Each point is the center of a cell from the numerical mesh (Figure 8-21) and carried a resistivity value. (C) Mesh grid for radial-averaged resistivity and selected depths for joint analyses with CT.

The resistivity of the clay depends heavily on its saturation degree. On the dry end, Figure 8-21 shows generally similar resistivity structures of both columns packed for 21% (v/v) volumetric water content and 1.2 g/cm^3 dry bulk density. At this water content, more than 95% of the resistivity values fell in the range of 15~40 Ωm, with a noticeably higher anomaly approaching 70 Ωm at the top of non-heated column (C2). Due to the dryness of the material, contact resistance between the electrodes and the clay was relatively high (>10 kΩ) during the pre-flow acquisition. High contact resistance reduces signal to noise ratio, thus the data quality. Since the flow started, contact resistance of most electrodes has significantly decreased (<10^3 Ω), and mean resistivity value already dropped down to 5 Ωm on day 1. However, a small magnitude of anomaly (~2 Ωm) persisted at the top-center of the non-heated column (Figure 8-23). Based on CT images, this region did not remain particularly dry and could have initially undergone faster fluid saturation due to the fractures near the end-caps. Because the ERT data coverage in this region was short (Figure 8-22(B)), and the contact resistance of few (1 or 2) electrodes remained high (~10 kΩ), the resistivity in this zone could have been overestimated.

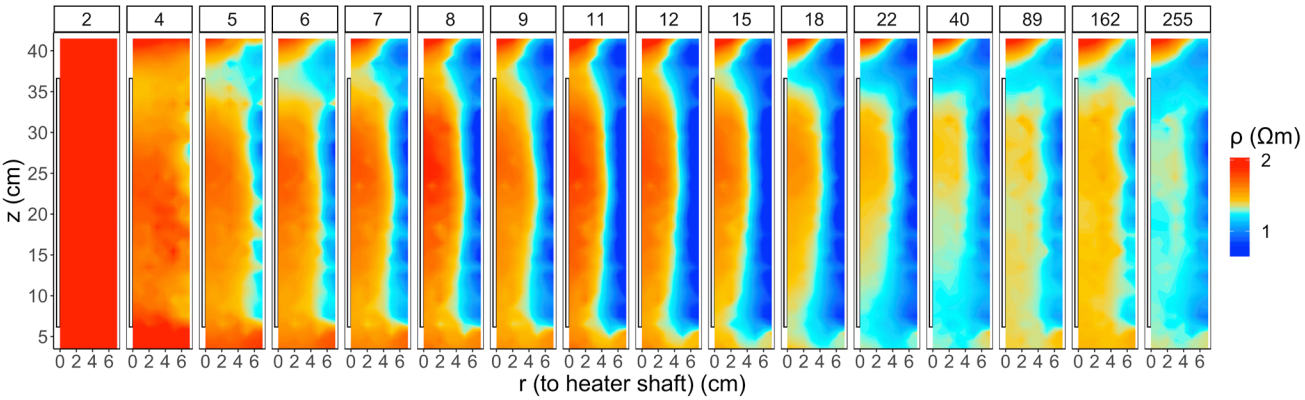

Figure 8-23. Radial resistivity map of the non-heated column (C2) after flow started (day 2 to 255). Flow was along the positive *z* direction. Color bar is log-scaled from 0.8 to 2.0 Ωm.

Time-lapse ERT of the non-heated column captures the sprawl of a low resistivity zone that matched with the CT images both spatially and temporally. From CT images (Figure 8-13), we to see (1) an overall increase in CT density on day 4 due to clay water uptake, with the high-density front reaching half of the radial distance by day 8, (2) a vertical low-density zone started to develop along the sand-clay boundary on day 4 due to clay swelling, and which slowly faded after day 22, and (3) low clay density remained in only the mid-center zone after day 22, while the top and bottom of the central shaft had higher density due to saturation through end-caps. Figure 8-23 shows similar development in terms of resistivity: (1) starting from day 4, low resistivity spots emerged near the sand-clay boundary and progressively migrated inward between day 5 and 22, (2) a highly conductive region (deep blue) developed near the sand-clay boundary and gradually dialed down after day 22, and (3) if we exclude the resistivity anomaly near the top-center, the mid-center zone remained the most resistive, and the top and bottom of the heater shaft seemed to have lower resistivity. Comparing the two datasets, the increase in CT density was found to be well aligned with the decrease in resistivity. Until the clay started to swell, CT density decreased because locally water displaced high density minerals, while the resistivity continued dropping following the increasing water content trend. This one-way relationship between higher water content and lower resistivity makes interpreting time lapse ERT straight forward in the non-heated column.

On the other hand, the ERT of the heated column was coated with the temperature effect in addition to the changes in water content. As the temperature rises (below the boiling point of saturation fluid, around 175 ºC at the applied pressure of 120 psi), the resistivity of the clay drops due to more vigorous movements of ions in the pore water and on the clay surfaces. Between day 4 and 12, Figure 8-24 captures a low resistivity zone moving inward due to water saturation. Compared to CT, the drying near the heat source was less pronounced, because the increase in temperature competed with the decrease in water content in terms of resistivity trend. After day 15, the distribution of resistivity over the entire column became homogeneous. On day 12 and 13, we improved the exterior insulation, thereby the clay temperature increased significantly. Between day 15 and 89, the clay gradually warmed up (Figure 8-25), which visually masked the effect of water content on resistivity. As the temperature of the clay reached stability in the range of 100-140 ºC around day 120, low resistivity zones were spotted both near the sand-clay boundary due to high water content and near the heater due to high temperature. In order to decouple the temperature from the water content variation, our lab setting provided great opportunities for ERT-CT joint analysis to relate time lapse ERT to moisture dynamics, structural change, and the diffusion processes.

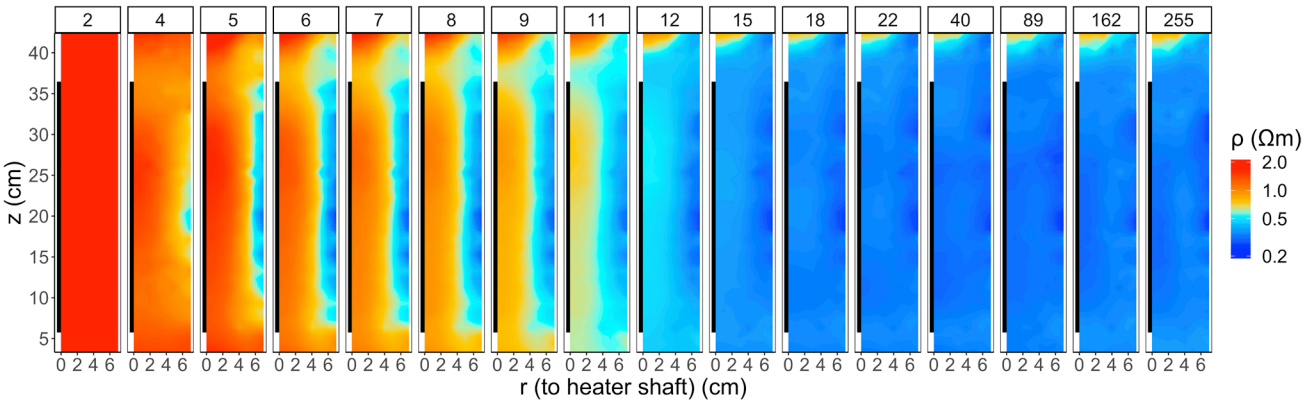

Figure 8-24. Radial resistivity map of the heated column (C1) after flow started (day 2 to 255). The black rectangle at the center (r < 0 cm) is the location of the heater. Color bar is log-scaled from 0.2 to 2.0 Ωm.

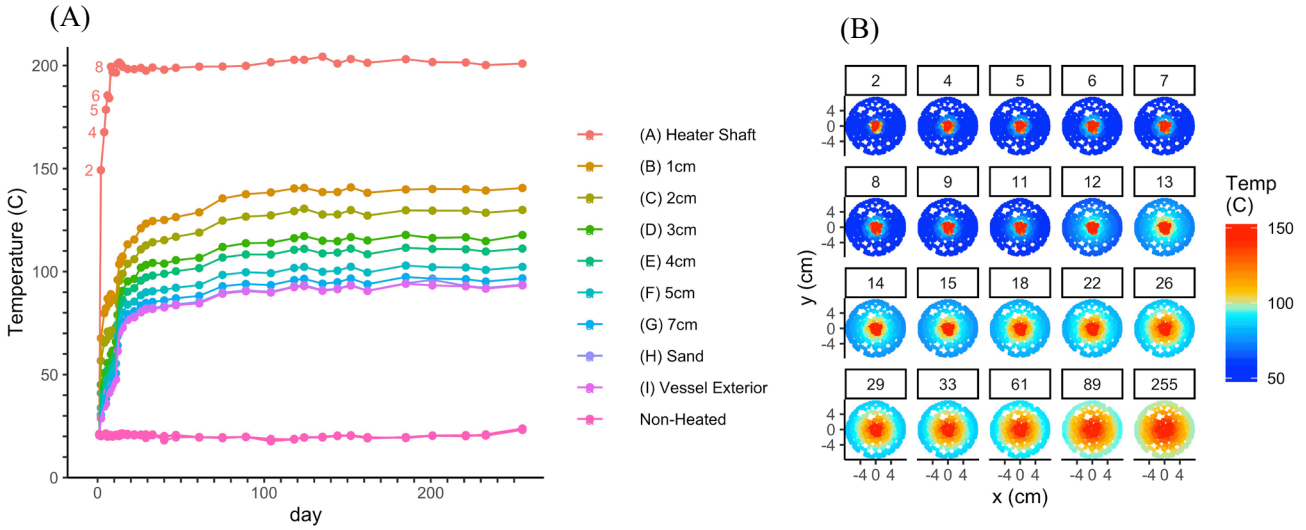

Figure 8-25. (A) Temporal temperature trend measured with the thermocouples in heated (A through I) and non-heated columns. (B) Radially-interpolated temperature distribution in heated column on selected days (days 2 to 255). Color bar is scaled from 50 to 150 degree Celsius.

(a) Calibration between resistivity and water content

One of the main objectives of HotBent-Lab is to establish, improve and validate a material-specific relationship between resistivity and water content. As discussed above, high water content increases the electrical current flow paths through pore fluid connectivity, and high temperature enhanced the movement of the electrolytes in pore fluid and cations on clay surfaces. In addition, chemical diffusion affects the electrical conductivity of the pore fluid, and mechanical compaction (and swelling) affects the porosity and the pore structure (Figure 8-28). A typical petrophysical relationship between resistivity and the four factors mentioned above for rocks and porous media can be described by Archie's Law:

$$\rho = \Phi^{-m} S^{-n} \sigma_f^{-1} \tag{8-1}$$

where **ρ** is the resistivity of the media (Ωm), **Φ** porosity (m^3/m^3), **m** (-) cementation factor (typically lies between 1.5 ~ 4.0 and increases with cementation), **S** degree of saturation (m^3/m^3), **n** (-) saturation factor (typically ~ 2), $\boldsymbol{\sigma_f}$ conductivity of pore fluid (S/m).

Since montmorillonite, the main mineral component of the MX-80 bentonite, has high surface conductance, resistivity is expected to decrease with the increasing amount of clay mineral present. The Waxman-Smits Model (8-2), a modified version of Archie's Law, incorporates an additional surface conductance term, **bQv**, and is more suitable for clay application. Table 8-2 summarizes the parameters used in the WS model.

$$\rho = \Phi^{-m} S^{-n} \left(\sigma_f + \frac{b Q_v}{S} \right)^{-1} \tag{8-2}$$

$$Q_v = cec * D_{grain} * \frac{1 - \Phi}{\Phi} \tag{8-3}$$

where b is the equivalent ionic conductance of clay exchange cations (S/m cm^3/meq) as a function of σf and temperature T, and Q_v is the cation exchange capacity per unit pore volume (meq/cm^3) as a function of porosity, cec cation exchange capability (meq/g), and D_{grain} grain density (g/cm^3). The value of cec was held constant at 0.75 meq/g, and D_{grain} = 2.75 g/cm^3 was based on the SKB TR-10-60 technical report (Karland, 2010) for MX-80 bentonite.

Table 8-2. Waxman-Smits Model Parameters

Processes	Parameters in WS Model	Function of	Formulae
Mechanical	Porosity (Φ)	Dry bulk density (BD_{clay})	$\Phi = 1 - BD_{clay}/D_{mineral}$
	Cementation exponent (m)	Pore network connectivity	Fitting Parameter
Hydrological	Saturation (S)	Dry bulk density, water content (θ)	$S = \theta/\Phi$
	Saturation exponent (*n*)	Continuity of pore network when unsaturated	Fitting Parameter
Thermal and Chemical	Pore fluid conductivity (σf)	Temperature (T), Effluent Conductivity measured at 20C (σ_{20})	$\sigma_f = \sigma_{20}(1 - (20 - T) * 0.02)$
	Clay cation conductance (*b*)		$b = \left(1 - 0.83e^{-e^{\sigma f\left(-2.38+\frac{42.17}{T}\right)}}\right) * (-3.16 + 1.59\ln(T))^2$ (Dacy & Martin, 2006)

The calibration was provided in two trials: (1) initial fit of WS model parameters (*m* and *n*) using separately packed calibration columns, and (2) second fit using *in-situ* ERT and CT observations (Figure 8-26(A))). The final goal is to correlate the time lapse ERT with column-level porosity, effluent fluid conductivity and spatial temperature data, and apply the WS model to obtain the water content distribution maps (Figure 8-26(B)).

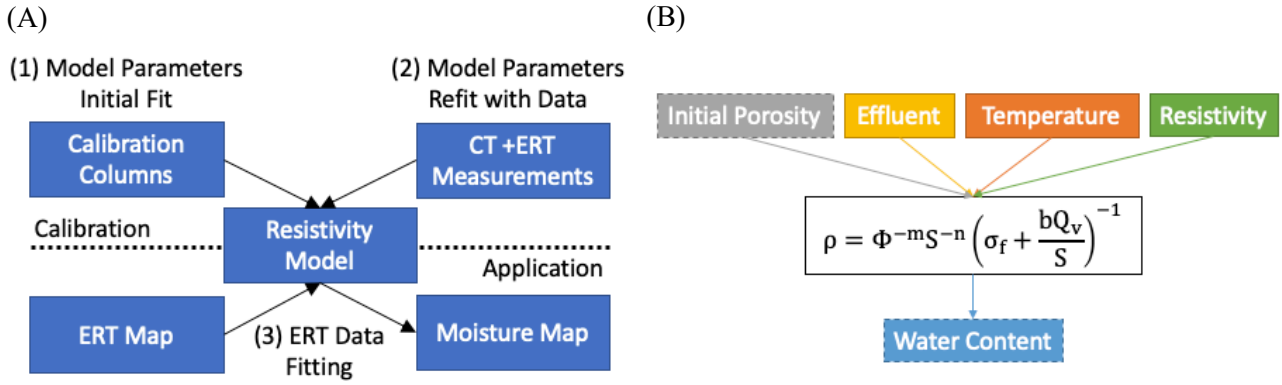

Figure 8-26. (A) Schematic flowchart of petrophysical and *in-situ* calibration (1, 2) and ERT-water content fitting (3). (B) The Waxman-Smits Model as the resistivity model and the desirable model inputs and deliverable.

In parallel to the main columns, we prepared several bentonite clay columns of various water content and dry density with the fluid of the same composition (σ20 ~ 2 S/m, Figure 8-20(A2)) (Table 8-3). For each column, an averaged CT value from the CT scan plus resistivity at a range of temperatures were measured. Resistance was measured with PSIP instrument (Ontash & Ermac) at 1 Hz frequency, which is consistent with the ERT data acquisition, and resistivity was calculated with geometric factor pre-determined with fluid of known conductivity. Because the columns were not pressurized, the maximum measurement

temperature was more or less confined to the water boiling point at the ambient pressure. The water content and dry density of each column were determined after oven-dried at 160 °C for at least 48 hours. The calibration of CT number and CT density has been shown in Figure 8-9. The parameters for Waxman-Smits Model were fitted: cementation exponent m = -3.8 and saturation exponent n = -3.0.

Table 8-3. Properties of the petrophysical calibration columns used for CT and ERT calibration.

Calibration Column	Gravimetric (oven-dry)		CT Calibration		ERT Calibration			
	Dry Bulk Density (g/cm³)	Wet Bulk Density (g/cm³)	CT No.	Calibrated CT Density (g/cm³)	Porosity (m³/m³)	Water Content (m³/m³)	Temp (oC)	Saturated
SC1	0.83	1.53	651	1.50	0.70	0.69	20, 50, 65, 80, 100	Y
SC2	1.02	1.66	807	1.61	0.63	0.63		Y
SC3	1.17	1.38			0.57	0.21		
SC4	1.32	1.82	1160	1.82	0.52	0.49		Y
SC5	1.09	1.69	957	1.70	0.60	0.59	20	Y
C1	1.20	1.45	657	1.51	0.56	0.24	20, 60, 75	
C2	1.29	1.54	752	1.57	0.53	0.25	20	
C3	1.15	1.38			0.58	0.22	20 – 60 by 5C	

To evaluate how the fitted parameters (m and n) can be used with the datasets from the pressured cells, we selected ERT and CT data at two vertical depths (thermocouples at z = 11 cm and the mid-heater at z = 21 cm) and registered them at six radial distances as the training/testing dataset (Figure 8-27). Here, we jointly addressed the observations previously made in CT and ERT sections: for the heated column, the resistivity itself showed no radial discrimination because of the competing thermal and hydration processes, whereas CT retained the radial density difference created by the central heat source. For the non-heated column, the outer region had lower resistivity, in agreement with higher CT density closer to the sand layer. At the thermocouple depths, CT values were radially similar due to early water infiltration through the heater shaft, and the radial resistivity difference was also slightly smaller comparing to the mid-heater depth. Initial swelling created high water content near the sand layer, creating dips of CT value (locally replacing minerals with water) and resistivity.

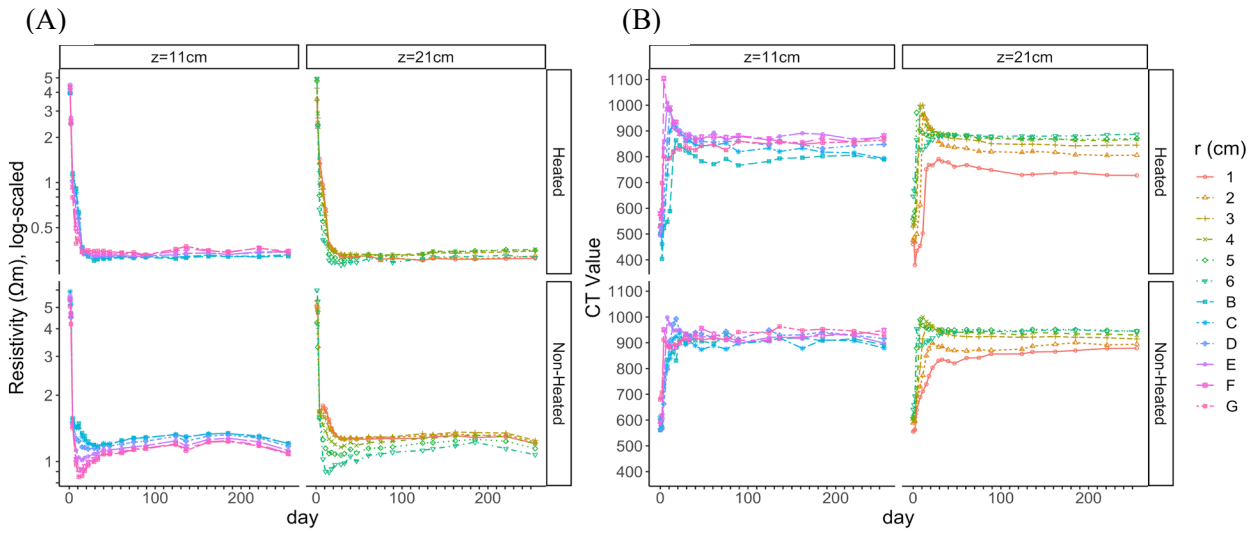

Figure 8-27. Temporal (A) resistivity (after day 1) and (B) CT trend of heated (top) and non-heated (bottom) columns at two selected depths. Data in the left panel were sampled adjacent to the thermocouples labeled as B-G, where B was closer to the heater and G to the sand-clay boundary. Data in the right panel were sampled at 6 radial distances (1 to 6 cm) from the heater shaft at the mid-heater depth (*z*=21cm).

Figure 8-28(A) shows where the testing data from the non-heated column fall on the WS model. Non-heated column was chosen for visualization because the temperature was homogeneous, and the results could be easily displayed on a 2D surface. The background is the WS model fitting results with the parameters from the calibration columns (m = -3.8, n = -3.0), temperature of 20 °C, and effluent conductivity of 2.5 S/m, and it is colored-coded by water content: the higher water content corresponds to the lower resistivity. A single water content crosses through multiple CT values because of different dry density, which could be due to different packing targets or local clay swelling or compaction. The firm line crosses through our dry bulk density at 1.2 g/cm^3, and the dashed line crosses through the saturated conditions. Due to its high swelling capacity, bentonite could be saturated at highly variable water content depending on the local dry density. From the fitting, the horizontally parallel trend indicates that the WS resistivity model is more sensitive to water than to the clay content and its surface conductance. The testing dataset from the CT and ERT measurements is plotted as data points in Figure 8-27.

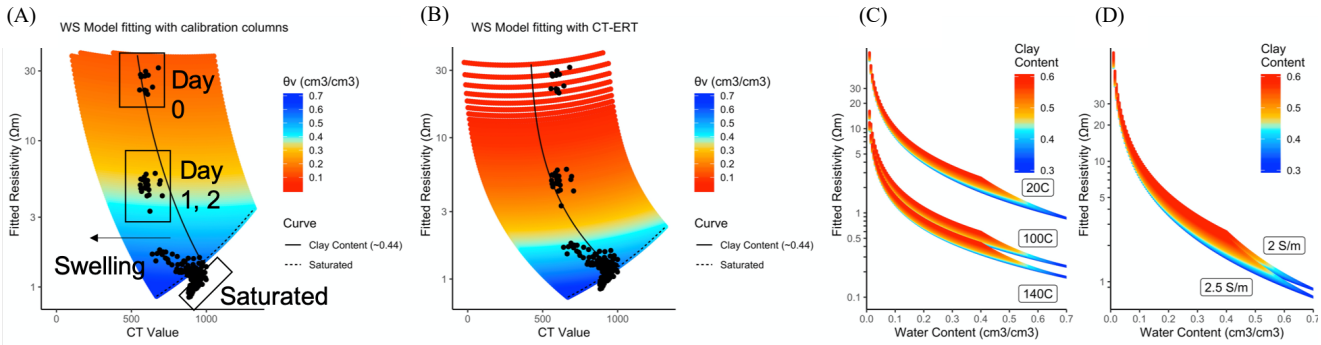

Figure 8-28. Model fitting results based on (A) calibration columns, and (B) column ERT plus CT data, demonstrating the effects of dry density (clay content), (C) temperature, and (D) fluid conductivity on the resistivity.

Two types of mis-fits are shown in Figure 8-28(A). The model overestimated the saturated resistivity, because many data points fell beneath the model fitting space, which would have led to overestimation of water content without CT constraints. Also, the model overestimated the unsaturated resistivity. Based on this fitting, the water content was 0.2 on day 0 and 0.3 to 0.4 on day 1 and 2. However, CT profile showed that CT density did not change much (r < 6 cm) between days 0 and 2, except for the center zone of the heated column (Figure 8-10, 8-11). Therefore, the resistivity difference between day 0 and days 1 and 2 was less likely from the water content, but from the suboptimal contact between dry clay and electrodes on day 0. The four unsaturated calibration columns used in this fitting were also packed at a similar water content (0.21 to 0.25), but without flow. Therefore, the contact resistance remained high and could decrease data quality of data interpretation.

This overestimation indicates the need for an adjustment of the WS model parameters based on the actual data collected from the pressured columns. The cementation exponent (m) was refitted with the saturated data from the training dataset (r > 6cm), and the saturation exponent (n) was refitted with the unsaturated data from day 1 and 2, assuming a homogeneous 21% initial water content based on oven-drying tests. The reason for only using data from days 1 and 2 in this refit was that clay displacement became more significant after day 4 (Figure 8-16 to 8-18). Movement of clay particles could change the local saturation, but was not easily distinguishable from CT data, as the water content was also simultaneously increasing. The following new WS model parameters were fitted as m = -3.4 and n = -1.9, with the saturation exponent approaching the common value of ~2 (Figure 8-28(B)). With constraint from the CT value, this adjusted WS model was applied to the rest of the testing dataset to fit the water content. Figure 8-29 shows both the drying and wetting of the clay in the heated column, extracting the water content information from the resistivity data based on the model fitting.

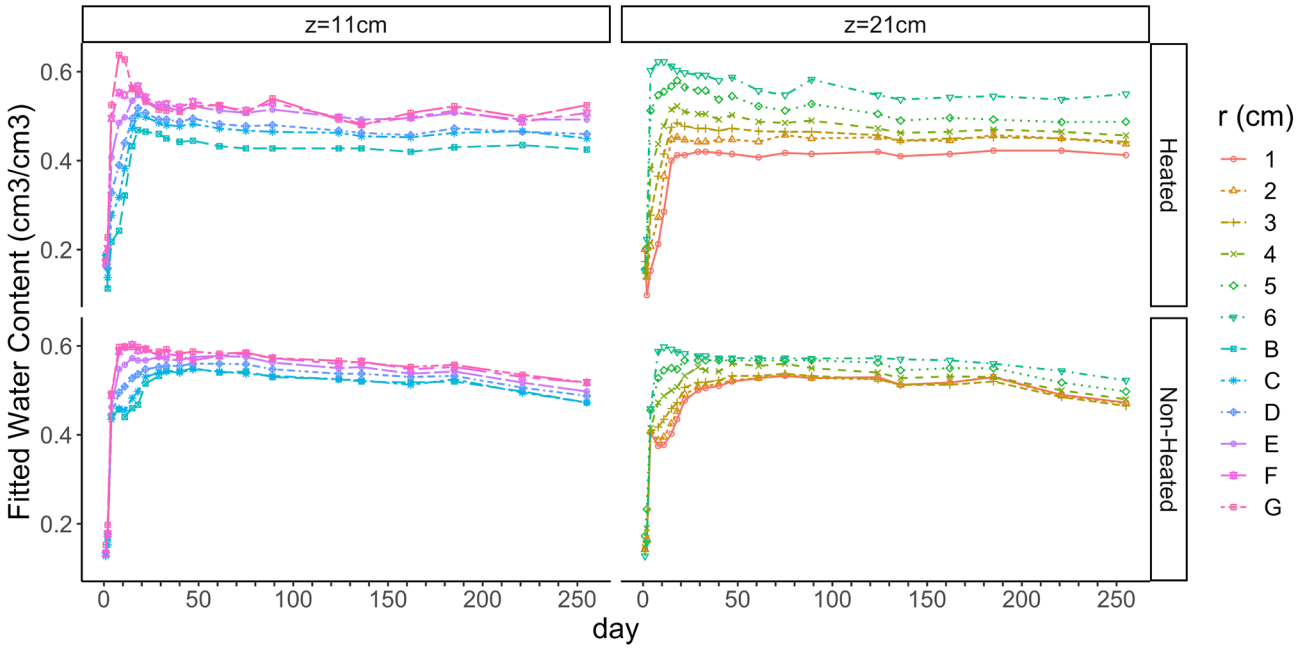

Figure 8-29. Temporal water content trend of heated (top) and non-heated (bottom) columns at thermocouple depth (z = 11cm) and mid-heater depth (z = 21cm) after day 2. Thermocouple (B) was closer to the heater, and (G) was closer to the sand-clay boundary.

(b) From ERT time lapse to water content maps

With the calibration between resistivity and water content being established and improved, we wanted to validate if ERT alone could be sensitive enough to distinguish local water content variation given such a small observation range of resistivity (0.2 - 2 Ωm). The fitting included inputs of resistivity, temperature, fluid conductivity and initial porosity estimation, while without the direct constraints from CT (Figure 8-26(B)). The ERT and temperature (from the thermocouples) were taken as the radial averaged data. Effluent fluid conductivity was used as the best approximation of fluid conductivity at the moment. Initial porosity was estimated as 0.56 based on 1.2 g/cm^3 dry density. The model would try to stay close to this porosity, which is generally acceptable especially with higher dry density and confined volume. While acknowledging that approximating local pore fluid and porosity with column level measurements would introduce errors in the fitting, it would be a good starting point because these datasets could be the most available if not only ones from the field depending on the sensor types and geochemical measurements routine. The fitting results are displayed in Figure 8-30 and 8-31.

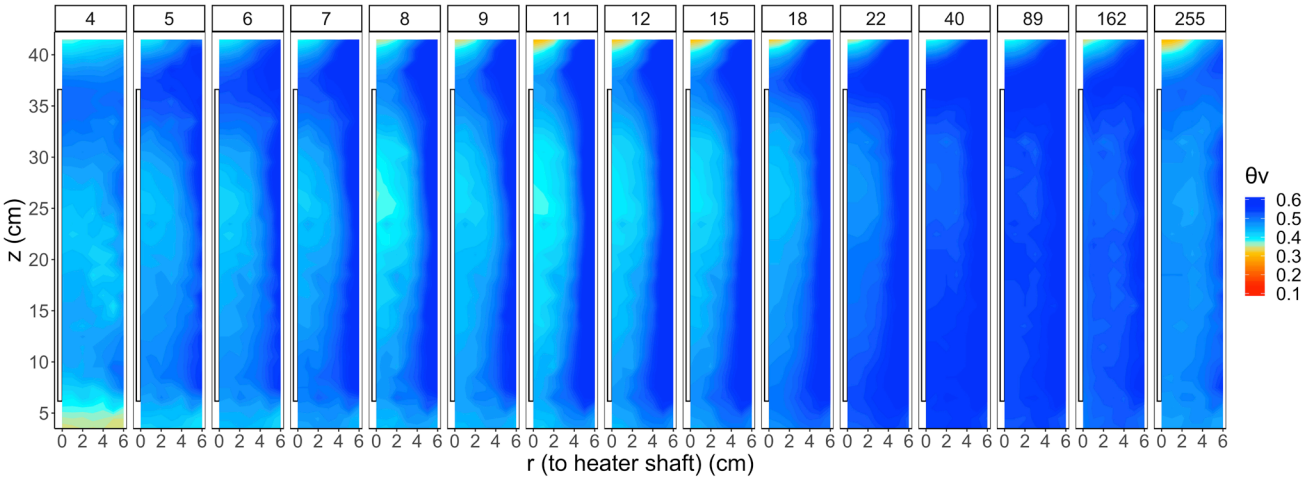

Figure 8-30. Radial water content map of the non-heated column (C2) on selected days (day 4-255). Color bar is volumetric water content (cm^3/cm^3) scaled from 0.1 to 0.6.

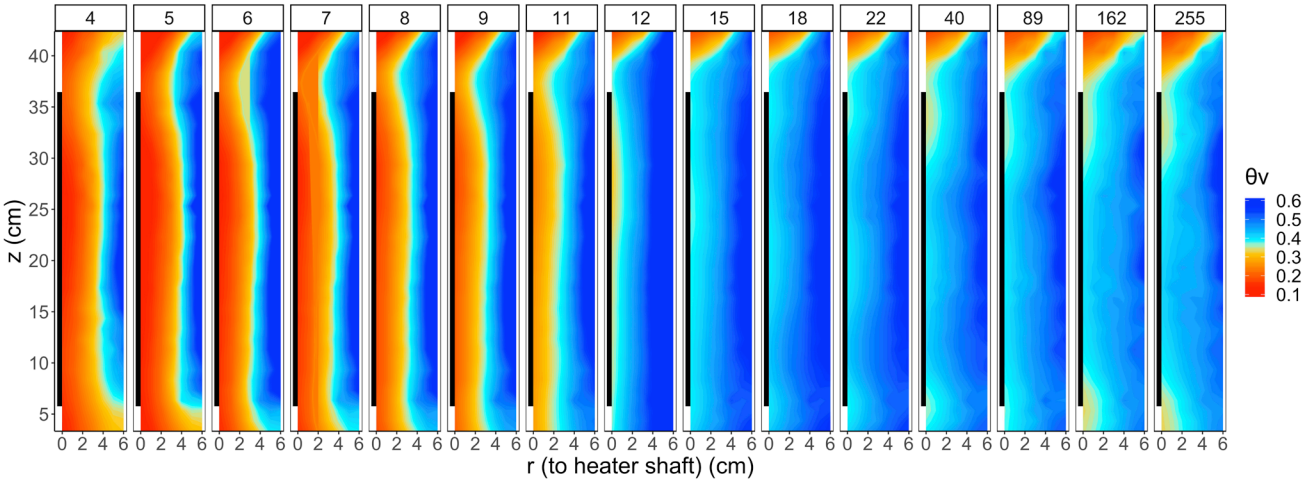

Figure 8-31. Radial water content map of the heated column (C1) on selected days (day 4-255). Color bar is volumetric water content (cm3/cm3) scaled from 0.1 to 0.6.

The movement of the water can generally be matched with the changes in CT images. Note that for the heated column, the temperature input for the ERT-water content fitting was radially interpolated among the readings from the thermocouples, which were located in the heated zone (z ~ 11 cm). Therefore, the temperature near the cold zones (indicated by the white gaps inside the heater shaft, z 0 to 6 cm and z > 36 cm) was overestimated, which would lead to an underestimation of water content in these regions. Also from the thermocouple readings, a small region (few millimeters) around the heater is also expected to have temperature higher than the boiling point at 175 °C (given the columns were pressurized at 120 psi), at which the water is in the vapor form and the calibration wouldn't be applicable. The radial average water content was also calculated across the mid-column depths (z = 11 to 31 cm) (Figure 8-32(A)). THM processes such as (1) initial drying near the heat source, (2) water saturation starting from the sand-clay boundary, and (3) swelling and clay content redistribution were captured.

At the column level, the water content derived from ERT fitting was compared against the water content estimated from mass balance. The ERT-fitted water content was averaged from all the radial values in the mid-column depths (z = 11 to 31 cm, to avoid cold zones), and the mass balance was calculated from how much of the injected fluid was retained inside the column, namely the mass difference between influx and efflux. The influx was continuously tracked with the inlet pump flow rate, and the effluent fluid was collected and measured gravimetrically routinely. Figure 8-32(B) shows that, for non-heated column, the fitting generated pretty similar averaged water content comparing to the mass balance water content, and both of them approached the estimated porosity of 56%. The water content of the heated column derived from the ERT fitting was also found to lower than that of the non-heated column, which was expected due to the heat source at the center. However, the mass balance water content of the heated column still needs to be corrected for potential instrument drift in the pumps.

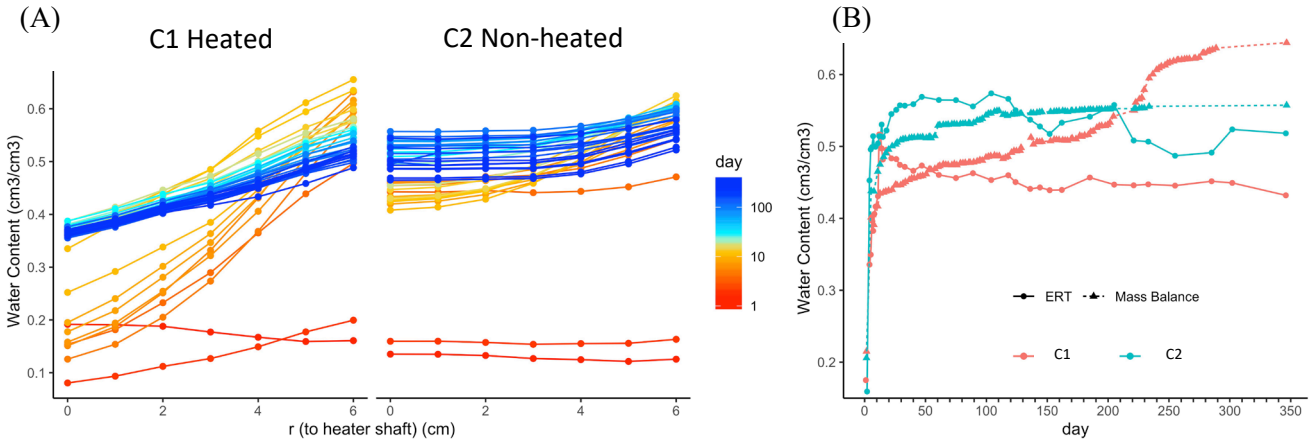

Figure 8-32. (A) Radial averaged water content from the mid-column depths (z = 11 cm to 31 cm). The days are log-scaled for visualization. (B) Mass balance water content versus averaged water content from the mid-column depths derived from ERT.

The fitting results show the capability of ERT in capturing local moisture variation given simple inputs such as temperature, effluent chemistry and porosity estimation. The model applicability will also be tested and improved in the next rounds of experiments. Based on the ERT data we have collected, the data quality could be improved by (1) ensuring good contact between electrodes and the clay, possibly with minimal local wetting and increasing the contact area by varying the sizes and shapes of the electrodes, (2) application of additional electrodes and electrode rods to provide a more detailed spatial coverage. Such

efforts could increase data quality and reduce the needs for data smoothing during the inversion simulation, thereby capturing more of the radial differences in the early days where radial differences have been shown to be more announced from the CT images. For the water content calibration, a temperature distribution model throughout the columns and chemical diffusion analysis would be necessary for more accurate calibration and estimation of water content, and increasing the training datasets could also improve the calibration.

8.5 Summary and Future Work

During FY18-19 pressure columns were designed, built, and instrumented for the HotBENT-lab experiment. Starting in June 2019, hydration was started in both columns, and heating was applied to one column. In FY19-20, columns were monitored continuously for hydration, temperature distribution, effluent chemistry, and density changes. Detailed in this report are results that show steady state hydration for both columns, with some density, hydration and chemistry differences between the heated and non-heated condition.

Major observations shown by the data collected in the column test are:

1. Clay hydration monitored by CT imaging and ERT was able to clearly show the hydration front moving radially inward. Density measurements from CT images were also able to observe clay swelling occurring with hydration, which caused localized compaction, closed fast flow paths created from column packing heterogeneities, and swelling along the clay/sand interface.

2. In the center of the heated column, the clay showed lower hydration but increase in density due to mineral precipitation.

3. Effluent chemistry showed differences between the heated and non-heated columns, specifically with the heated column demonstrating sulfate, calcium, potassium and magnesium reduction and silicon and potassium production.

For the remainder of FY20, we will complete this hydration testing, followed by a detailed dismantling of both heated and non-heated clays. The clays will be carefully removed and measured for water content, mineralogy changes, and chemistry of pore water, following techniques outlined by previous work on heated clays (Cuevas, 1997; Järvinen, 2016). Following the dismantling, we will repack the columns, focusing on the correspondence mineral density and the water chemistry to such characteristics determined the HotBENT field site.

This page is intentionally left blank.

9. SUMMARY

9.1 Investigation of impact of high temperature on EBS bentonite with THMC modeling (Section 2)

In the past few years, we have dedicated our effort to developing a series of coupled THMC models to simulate the chemical alteration and associated mechanical changes in a generic nuclear waste repository, and to better understand the interaction between EBS bentonite and the NS clay formation. In FY20, we tested the BExM using a parametric study, improved the simulator TReactMech, and modified it based on a new coupling strategy. The achievements we have reached are as follows:

- We conducted a parametric study of pre-consolidation pressure for bentonite buffer using the BExM simulations of THMC processes. This study revealed a distinct elasto-plastic behavior of bentonite, and showed that the spatial heterogeneity of the sample may induce uneven interior material changes.
- We have improved the simulator on the Linux platform with the deal.II library, and modified the coupling strategy to a sequential coupling method. A good agreement between numerical simulations and analytical solutions was obtained, but in the THM simulation of high T case, the hydrological calculation failed to converge due to phase changes.

In the remaining time of FY20 and in FY21, we plan to further improve the coupled THMC model on the Windows platform to obtain a better understanding of the coupled processes in EBS bentonites and argillite formations under high temperature, specifically:

- To improve the convergence of hydrological part in the simulator with the deal.II library, and recalculate the high T case. Use this new library to conduct parallel computation and modify the chemical reaction part and link with the THM part. To investigate chemically induced deformation in solid skeleton related to the change of solution compositions, and to derive an improved coupling model for compacted clays following the framework of poromechanics.
- To derive a reduced order model that can be integrated into the performance assessment model in GDSA. The importance of bentonite alteration and its impact on mechanical behavior needs to be integrated into the PA model to assess the relevance to the safety of a repository. Specifically, we will first implement the bentonite swelling models, such as linear swelling, state surface, BBM, and BExM into a parallel THMC simulator, and then a reduced order model will be developed based on a large number of THMC simulations.
- To use a physics-constrained data-driven computational framework to develop a constitutive function with the LSTM method-based strain-stress data search for simulation of the clay behavior under thermal and hydration processes.
- To implement more constitutive models into the new simulator for better representation of different geomaterials, and continue working on coupled THMC modeling of different materials with the new simulator.

9.2 Sorption and diffusion experiments on bentonite (Section 3)

In FY20, diffusion experiments were conducted with 95°C heated- and 20°C cold-zone purified FEBEX bentonite at a bulk density of 1.25 kg/L. The experiments were conducted at a constant ionic strength (0.1 M NaCl) at pH 7 in the presence of 0.1 mM Ca or 2 mM Ca. The average

normalized 3H flux at steady state (≥50-hr) for 3H through-diffusion was not significantly different across samples, with values ranging from 1.38 ± 0.13 x 10-3 m/day to 1.73 ± 0.17 x 10-3 m/day. U(VI) in-diffusion experiments conducted in the presence of 2 mM Ca showed the diffusive loss of U(VI) from the high concentration reservoir was indistinguishable for the heated and cold-zone bentonite, and U(VI) traveled less than 1 mm into the clay over the 30-day diffusion period. While lower U(VI) adsorption was previously measured on the heated-zone FEBEX bentonite compared to the cold-zone bentonite, it is possible that differences in U(VI) diffusion due to differences in adsorption may only become apparent over much longer time periods than can be realistically tested in the laboratory. Reactive transport modeling of these results using CrunchClay is currently underway and will provide further insight into the geochemical conditions and time periods in which differences in U(VI) diffusion as a result of heating may be observed.

In the remaining time of FY20 and FY21 our work will focus on the diffusion and redox transformations of Se through compacted montmorillonite. Experiments will be conducted under a single ionic strength (0.1 M) and three different electrolyte compositions: 0.1 M NaCl, 0.033 M CaCl2, and 0.085 M NaCl + 0.005 M CaCl2, representing pure Na, pure Ca, and a Na-Ca mixture, respectively. We hypothesize that Se(VI) diffusion will be different under these different electrolyte compositions due to both differences in aqueous Se speciation and differences in the clay swelling in the presence of Na and Ca. These experiments will also be modeled using CrunchClay.

9.3 Studying chemical controls on montmorillonite structure and swelling pressure (Section 4)

In FY20 we have conducted a comprehensive set of experiments and simulations, which provided deep insights into the thermodynamics of clay swelling in mixed electrolyte solutions. Accomplishments from the prior funding period include development of molecular simulations approaches (Subramanian et al., 2020) that inform a new thermodynamic model for ion exchange driven clay swelling and collapse (Whittaker et al., 2019). Our FY 2020 efforts focus on transferring this knowledge to compacted clay systems accounting for non-zero effective normal stress. We report on the development of an X-Ray transparent micro-oedometer system for the measurement of montmorillonite swelling pressure as a function of dry bulk density and aqueous solution composition. Initial work focused on pure homoionic NaCl and KCl solutions as well as NaCl+KCl mixtures. Preliminary data are presented from *in-situ* X-Ray scattering experiments conducted at the Advanced Photon Source, Argonne National Laboratory. To develop a theoretical understanding of microstructural evolution, we applied a structural model for cis-vacant smectite clay (Subramanian et al., 2020) to simulate the free energy of mixing crystalline layer states and found that highly unfavorable mixing energetics could drive phase separation in mixed layer state systems. Ongoing simulations of swelling free energy are being conducted using a potential of mean force (PMF) calculation method. Finally, these results are integrated into a thermodynamic model to predict swelling pressure as a function of pore fluid composition in compacted bentonite.

In the future, as soon as laboratory work is resumed in FY20 and extended into FY21, we are going to perform experiments to generate a comprehensive swelling pressure data set in multicomponent electrolyte solutions. The swelling pressure data will be compared against model expectations based on the thermodynamic approach described in Zheng et al. (2019) and Whittaker et al. (2019), with subsequent model refinements based on experimental outcomes. Additional X-ray scattering

beamtime will be sought toward the end of FY20 to obtain additional microstructural data constraints, including the evolution of MMT microstructure, upon ion exchange in mixed electrolyte solutions including calcium. Additional simulations will be completed to determine swelling free energies for mixed electrolytes, but a different simulation technique is required to quantify interlayer ion exchange thermodynamics. These will be investigated further in FY21, using the thermodynamic integration technique described above.

9.4 Microscopic origins of coupled transport processes in bentonite (Section 5)

In this section we present a research plan for a newly added research activity on the development and validation of a microscopic model of coupled transport processes in bentonite and using this model to determine cost effective augmentation strategies to increase the bulk thermal conductivity of hydrated bentonite. Because this activity was added in March 2020, we only report a research plan and some preliminary results, which will serve as a foundation for a larger scale effort in FY20-21 to stably increase the thermal conductivity of bentonite above 2 W/mK at temperature relevant to modern nuclear waste storage design concepts.

Our model predicts two important consequences for the thermal conductivity of bentonite. The first is that a local equilibrium is not possible without macroscopic rearrangement of mineral layers, and therefore microscopic gradients of ions and water are pervasive in bentonite unless or until the mineral is chemically altered to redistribute structural charge. The second is that a 'turbostratic' rearrangement of layers, as is observed in natural bentonites, may minimize the free energy of a given local arrangement, but that any structural fluctuations away from this arrangement will alter the energetic landscape and drive ion and water fluxes. These phenomena represent two important couplings between the chemistry and mechanical deformation of mineral layers in bentonite whose ultimate consequence is to create microscopic fluxes that generate entropy, and therefore, heat. We anticipate that this model can be used to quantify the specific interactions/fluctuations through which heat is transferred and make predictions about deliberate chemical or structural alteration that may augment heat conduction.

With further development in FY20-21, we expect to be able to identify and test bulk chemical modifications to bentonite that enhance the thermal conductivity beyond 2 W/mK. For example, fluorine functionalization of the Mt octahedral sheet reduces hydrophilicity and may significantly alter the dielectric properties of confined water to more effectively screen interlayer charge and sustain dynamic fluctuations that drive thermal transport. Alternatively, mixing bentonite with aromatic hydrocarbons, such as chemical precursors to graphite, may facilitate the in-situ formation of thermally conductive carbon nanomaterials that enhance the thermal conductivity of bentonite.

9.5 Understanding the THMC evolution of bentonite in FEBEX-DP— Coupled THMC modeling (Section 6)

The FEBEX *in-situ* test, which lasted more than 18 years, is extremely valuable for validating the coupled THMC model and improving our understanding of the evolution of the bentonite barrier throughout heating

and hydration. The ultimate goal is to use THMC data from FEBEX-DP to validate the THMC models, and therefore enhance our understanding of coupled THMC processes in bentonite.

From FY16 to FY19, extensive model calibrations were conducted, and finally, in FY19, the THCM model provided a coherent explanation of THMC data collected at the FEBEX *in-situ* test. In FY20, the modeling work included using the THMC model to explore the long-term alteration of bentonite. The first question we are trying to address is the necessity of using the THMC model for studying long-term alteration of bentonite, especially the geochemical alteration. The use of the THMC model is computationally expensive and numerically more unstable than the THC model, while up-gradation of the THMC code, using parallel computing and the better solver, can alleviate this issue. Using the THC model could be beneficial in terms of the computation time and simulation stability, knowing that the performance assessment is most likely based on THC simulations, not THMC simulations. The following results of simulations were obtained:

- In terms of the hydrological behavior, the THMC and THC modeling results are similar for the period of 50 years despite of a remarkable difference for the first 30 years.
- The evolution of conservative chemical species (e.g., chloride) based on the results of THMC and THC modeling is similar.
- The evolution of reactive species (e.g., potassium) based on the results of THMC and THC modeling is different, indicating that the reaction history in THMC and THC models in the early time (<30 years) have a long-term effect.
- Bentonite will become fully saturated in 30-40 years based on the model with a heat decay function, and the bentonite barrier is expected to homogenize in most areas.
- High chemical concentrations in bentonite near the heater, which were observed in the field test, are predicted to disappear after bentonite becomes fully saturated.
- Illitization will continue for 50 years, but won't proceed. However, the THC model shows more illitization in area near the heater compared to the THMC model.

In the remaining time of FY20 and FY21, we will continue improving the stability and numerical efficiency of TOUGHREACT-FLAC and finish the long-term THMC simulations. In addition, a reactive transport model will be developed to study the geochemical changes at the interfacial areas, including the bentonite/concrete interface and the bentonite/steel interface.

9.6 Modeling in Support of HotBENT, an Experiment Studying the Effects of High Temperatures on Clay Buffers/Near-field (Section 7)

We developed a THC model to predict the evolution of Woyming bentonite (MX-80) to be used in the HotBENT field test. Modeling of coupled THC processes affected by high temperature, relatively high permeability and high hydraulic pressure, combined with the effect of artificial hydration, generated the results that have not been observed in FEBEX in-situ test (Zheng et al., 2018). Modeling results can be summarized as follows.

- With a heater temperature of 200 ºC, the temperature at the bentonite/granite interface is expected to reach 87 ºC. In about 3 years, most of bentonite would become fully saturated, but a narrow zone about 3 cm thick in the close vicinity of heater would remain unsaturated with a water saturation degree from 95% to 98% until 20 years.
- The most remarkable chemical changes are expected to occur in a narrow unsaturated zone, because of the continuous strong evaporation (referred as "evaporation zone" in this report). Ion concentrations are expected to increase up to 2-3 mol/kg due to the dissolution of smectite, precipitation of illite, anhydrite, quartz and cristobalite, very high exchange Na and Mg and very low exchange of Ca and K at the cation exchangeable sites. Modeling showed the development a

chemically active area a little further away from the heater and right next to the narrow unsaturated zone. It is referred to as the "condensation zone," in which chemical changes are induced by continuous condensation of vapor that is generated in the "evaporation" zone. In this area, model showed a significant dilution of the bentonite pore water, dissolution of most aluminum-silicate minerals, except muscovite, very high exchange of Ca and K, and very low exchangeable Na and Mg at the cation exchangeable sites.

- It will be a challenging problem of measurements of chemical concentrations in bentonite in a narrow zone close to the heaters, when modules H3 and H4 in HotBENT are dismantled after 5 years operation.

The 1D model sheds light on the potential chemical changes in MX-80 bentonite in HotBENT, but the hydraulic calculation is not entirely faithful to the condition of HotBENT, because of the existence of pedestal underneath the heater. In the remaining time of FY20 and FY21, we will continue making model predictions for the HotBENT, to help design a monitoring protocol and guide the development of a future measurements plan. Specifically, we will

- Develop a 1D THC model for BCV bentonite,
- Extend the 1D axi-symmetrical THC model to the THMC model for the MX-80 bentonite, and
- Develop a 2D THMC model for MX-80 and BCV bentonites.

9.7 High temperature heating and hydration column test on bentonite (Section 8)

During FY18-19, two pressure columns were designed, built, and instrumented for the HotBENT-lab experiment. In June 2019, hydration was started in both columns, and heating was applied to one column. In FY19-20, columns were monitored continuously for hydration, temperature distribution, effluent chemistry, and density changes. Detailed in this report are results that show steady state hydration for both columns, with some density, hydration and chemistry differences between the heated and non-heated conditions. Major results of observations in the column tests are:

- CT imaging and ERT of clay hydration clearly showed the hydration front moving radially inward. Density measurements from CT images indicated that hydration caused clay swelling, which, in turn, caused localized compaction, closed flow paths created from column packing heterogeneities, and swelling along the clay/sand interface.
- In the center of the heated column, the clay hydration was lower, but the density increased due to mineral precipitation.
- Effluent chemistry showed differences between the heated and non-heated columns, specifically, sulfate, calcium, potassium and magnesium reduction and silicon and potassium production occurred in the heated column.

In the remainder of FY20, we will complete the hydration testing, followed by a detailed dismantling of both heated and non-heated columns. The clays will be carefully removed and measured for water content, mineralogy changes, and chemistry of pore water, using the techniques outlined by previous work on heated clays (Cuevas, 1997; Järvinen, 2016). Following the dismantling, we will repack the columns, resembling their mineral density and the water chemistry to such characteristics determined at the HotBENT field site.

This page is intentionally left blank.

10. ACKNOWLEDGEMENTS

Funding for this work was provided by the Spent Fuel and Waste Science and Technology Campaign, Office of Nuclear Energy, of the U.S. Department of Energy under Contract Number DE-AC02-05CH11231 with Lawrence Berkeley National Laboratory.

This page is intentionally left blank.

11. REFERENCES

Altmann, S. (2008) 'Geochemical research: A key building block for nuclear waste disposal safety cases. Journal of Contaminant Hydrology 102, 174-179.

Altmann, S., Tournassat, C., Goutelard, F., Parneix, J.-C., Gimmi, T., and Maes, N. (2012) Diffusion-driven transport in clayrock formations. Applied Geochemistry 27, 463-478.

Arndt, D., Bangerth, W., Clevenger, T.C., Davydov, D., Fehling, M., Garcia-Sanchez, D., Harper, G., Heister, H., Heltai, L., Kronbichler, M., Maguire Kynch, R., Maier, M., Pelteret J.-P., Turcksin, B., and Wells, D. (2019) The deal.II library, Version 9.1. Journal of Numerical Mathematics: 27(4), 203-213.

Balistrieri, L.S., and Chao, T.T. (1987) Selenium Adsorption by Goethite. Soil Science Society of America Journal 51, 1145-1151.

Balistrieri, L.S., and Chao, T.T. (1990) Adsorption of selenium by amorphous iron oxyhydroxide and manganese dioxide. Geochimica et Cosmochimica Acta 54, 739-751.

Balme, S., M. Kharroubi, A. Haouzi, and F. Henn (2010), Non-Arrhenian Ionic dc Conductivity of Homoionic Alkali Exchanged Montmorillonites with Low Water Loadings, Journal of Physical Chemistry C, 114, 9431-9438.

Bangerth, W. (2019) deal.II — an open source finite element library. https://www.dealii.org/.

Bangerth, W., Burstedde, C., Heister, T., and Kronbichler, M. (2012) Algorithms and Data Structures for Massively Parallel Generic Adaptive Finite Element Codes. ACM Transactions on Mathematical Software: 38(2), Article 14.

Bangerth, W., Hartmann, R., and Kanschat, G. (2007) deal.II—A general-purpose object-oriented finite element library. ACM Transactions on Mathematical Software: 33(4), Article 24.

Bárcena, I., Fuentes-Cantillana, J.L. and García-Siñeriz, J.L. (2003). Dismantling of the Heater 1 at the FEBEX "'in situ'" test. Description of operations. Enresa Technical Report 9/2003.

Bar-Yosef, B., and Meek, D. (1987) Selenium Sorption by Kaolinite And Montmorillonite. Soil Science 144, 11-19.

Belarbi, H., A. Haouzi, J. C. Guintini, J. V. Zanchetta, J. Niezette, and J. Vanderschueren (1997) Interpretation of orientation polarization in dry montmorillonite, Clay Minerals, 32, 13-20.

Bérend, I.; Cases, J.-M.; François, M.; Uriot, J.-P.; Michot, L.; Masion, A.; Thomas, F. (1995) Mechanism of Adsorption and Desorption of Water Vapor by Homoionic Montmorillonites: 2. The Li Na , K , Rb and Cs -Exchanged Forms. Clays Clay Miner. 1995, 43 (3), 324–336.

Berendsen H. J. C., Postma J. P., van Gunsteren W. F. and Hermans J. (1981) Interaction models for water in relation to protein hydration. In Intermolecular Forces (ed. B. Pullmann).Reidel, Dordrecht, pp. 331–342.

Booker, J.R. and Savvidou, C. (1985) Consolidation around a point heat source. International Journal for Numerical and Analytical Methods in Geomechanics 9, 173–184.

Bourg, I. C., and J. B. Ajo-Franklin (2017) Clay, Water, and Salt: Controls on the Permeability of Fine-Grained Sedimentary Rocks, Acc Chem Res, 50(9), 2067-2074, doi:10.1021/acs.accounts.7b00261.

Bourg, I.C., Sposito, G., andBourg, A.C.M. (2006) Tracer diffusion in compacted, water-saturated bentonite. Clays and Clay Minerals 54, 363-374.

Bradbury, M. H. and B. Baeyens (2003) "Porewater chemistry in compacted re-saturated MX-80 bentonite." Journal of Contaminant Hydrology 61(1–4): 329-338.

Chamberlin, R. V. (1999) Mesoscopic Mean-Field Theory for Supercooled Liquids and the Glass Transition, PRL, 82(12), 2520.

Charlet, L., Kang, M., Bardelli, F., Kirsch, R., Géhin, A., Grenèche, J.-M., Chen, F. (2012) Nanocomposite Pyrite–Greigite Reactivity toward Se(IV)/Se(VI). Environmental Science & Technology 46, 4869-4876.

Charlet, L., Scheinost, A.C., Tournassat, C., Greneche, J.M., Géhin, A., Fernández-Martı´nez, A., Coudert, S., Tisserand, D., and Brendle, J. (2007) Electron transfer at the mineral/water interface: Selenium reduction by ferrous iron sorbed on clay. Geochimica et Cosmochimica Acta 71, 5731-5749.

Cheshire, M., F.A. Caporuscio, M.S. Rearick, C.F. JovéColón, and M.K. McCarney, Bentonite evolution at elevated pressures and temperatures: An experimental study for generic nuclear repository designs. American Mineralogist, 2014. 99: p. 1662-1675.

Cuadros, J., and Linares, J. (1996) Experimental kinetic study of the smectite-to-illite transformation. Geochimica et Cosmochimica Acta 60, 439-453.

Cuevas, J., Villar, M. V., Fernández, A. M., Gómez, P., and Martín, P. L. (1997) Pore waters extracted from compacted bentonite subjected to simultaneous heating and hydration. Applied Geochemistry, 12(4), 473-481. doi:https://doi.org/10.1016/S0883-2927(97)00024-3

Cui Y.J., Tang A.M., Loiseau C., and Delage P. (2008) Determining the unsaturated hydraulic conductivity of a compacted sand-bentonite mixture under constant-volume and free-swell conditions. Physics and Chemistry of the Earth 33, S462-S471

Cygan, R. T.; Liang, J.-J.; and Kalinichev, A. G. (2004) Molecular Models of Hydroxide, Oxyhydroxide, and Clay Phases and the Development of a General Force Field. J. Phys. Chem. B 2004, 108 (4), 1255–1266. https://doi.org/10.1021/jp0363287.

Dacy, J., & Martin. P. (2006). Practical advances in core-based water saturation analysis of shaly tight gas sands. SCA2006-29.

Delay, J., Vinsot, A., Krieguer, J.-M., Rebours, H., and Armand, G. (2007) Making of the underground scientific experimental programme at the Meuse/Haute-Marne underground research laboratory, North Eastern France. Physics and Chemistry of the Earth, Parts A/B/C 32, 2-18.

Deng, H., Voltolini, M., Molins, S., Steefel, C., DePaolo, D., Ajo-Franklin, J. and Yang, L. (2017) Alteration and erosion of rock matrix bordering a carbonate-rich shale fracture. Environmental science & technology, 51(15), pp.8861-8868.

Detzner K. and Kober F. (2015) FEBEX-DP drilling and sampling report sections 32-34, Internal report, AN15-714, NAGRA.

Dirksen, D. (1969) Thermo-osmosis through compacted saturated clay membranes. Soil Sci. Soc. Am. Proc., 33(6): 821-826.

ENRESA (2000) Full-scale engineered barriers experiment for a deep geological repository in crystalline host rock FEBEX Project, European Commission: 403.

Fernández, A.M., Cuevas, J., and Rivas, P. (2001) Pore water chemistry of the FEBEX bentonite. Mat. Res. Soc. Symp. Proc. 603, 573-588.

Fernández, A., Rivas, P., (2003) Task 141: post-mortem bentonite analysis. geochemical behaviour. CIEMAT/DIAE/54520/05/03, Internal Note 70-IMA-L-0-107 v0.

Fernández, A.M., Baeyens, B., Bradbury, M., and Rivas, P. (2004) Analysis of the porewater chemical composition of a Spanish compacted bentonite used in an engineered barrier. Physics and Chemistry of the Earth, Parts A/B/C 29, 105-118.

Fernández, A. M., & Villar, M. V. (2010) Geochemical behaviour of a bentonite barrier in the laboratory after up to 8years of heating and hydration. Applied Geochemistry, 25(6), 809-824. doi:https://doi.org/10.1016/j.apgeochem.2010.03.001

Fernández, A.M., D.M. Sánchez-Ledesma, A. Melón, L. M. Robredo, J.J. Rey, M. Labajo, M.A. Clavero, S. Carretero, A.E. González. (2017). Thermo-hydro-geochemical behaviour of a Spanish bentonite after dismantling of the FEBEX in situ test at the Grimsel Test SitePore water chemistry of the FEBEX bentonite. CIEMAT report, CIEMAT/DMA/2G216/03/16.

Ferrage, E. (2005) Investigation of Smectite Hydration Properties by Modeling Experimental X-Ray Diffraction Patterns: Part I. Montmorillonite Hydration Properties. Am. Mineral. 2005, 90 (8–9), 1358–1374. https://doi.org/10.2138/am.2005.1776.

Finsterle S., Kowalsky M., Kober F. and Vomvoris, S. (2017) HotBENT – Preliminary Design Study of Phenomenological Aspects, NAB 17-30.

Fiorin, G.; Klein, M. L.; Hénin, J. (2013) Using Collective Variables to Drive Molecular Dynamics Simulations. Mol. Phys. 2013, 111 (22–23), 3345–3362. https://doi.org/10.1080/00268976.2013.813594.

Fox, P.M., Tinnacher, R.M., Cheshire, M.C., Caporuscio, F., Carrero, S., Nico, P.S. (2019) Effects of bentonite heating on U(VI) adsorption. Applied Geochemistry 109, 104392.

García-Gutiérrez, M., Missana, T., Mingarro, M., Samper, J., Dai, Z., Molinero, J. (2001) Solute transport properties of compacted Ca-bentonite used in FEBEX project. Journal of Contaminant Hydrology 47, 127-137.

García-Gutiérrez, M., Cormenzana, J.L., Missana, T., Mingarro, M., and Alonso, U., (2003) Analysis of Uranium Diffusion Coefficients in Compacted FEBEX Bentonite. MRS Proceedings 807, 603.

Garcia-Sineriz, J.L., Abós, H., Martínez, V., De la Rosa, C., Mäder, U. and Kober, F. (2016) FEBEX-DP Dismantling of the heater 2 at the FEBEX "in situ" test. Nagra Arbeitsbericht NAB 16-011. p. 92

Gens, A. (2010) Soil environment interactions in geotechnical engineering. Géotechnique 60, 3-74.

Gens, A., Sánchez, M., Guimarães, L. D. N., Alonso, E. E., Lloret, A., Olivella, S., Villar, M. V., and Huertas, F. (2009) A full-scale in situ heating test for high-level nuclear waste disposal: observations, analysis and interpretation. Géotechnique, 59(4): 377-399.

Ghabezloo S, Sulem J, Guédon S, Martineau F. (2009) Effective stress law for the permeability of a limestone. Int. J. Rock Mech. Min. Sci.;46:297-306.

Ghassemi, A. and Diek, A. (2002) Porothermoelasticity for swelling shales. Journal of Petroleum Science and Engineering, 34: 123-125.

Glaus, M.A., Van Loon, L.R. (2012) Diffusive behavior of charged metal ion complexes in compacted montmorillonite, Clays in natural and engineered barriers for radioactive waste confinement - 5 International meeting Book of abstracts, France, p. 923.

Gómez-Espina, R., & Villar, M. V. (2010). Geochemical and mineralogical changes in compacted MX-80 bentonite submitted to heat and water gradients. Applied Clay Science, 47(3), 400-408. doi:https://doi.org/10.1016/j.clay.2009.12.004

Gregg, B. (2019) Flame Graphs. http://www.brendangregg.com/flamegraphs.html.

Gu, B. X., L. M. Wang, L. D. Minc, and R. C. Ewing (2001) Temperature effects on the radiation stability and ion exchange capacity of smectites, Journal of Nuclear Materials, 297, 345-354.

Guimarães, L.D.N., Gens, A., Sánchez, M., and Olivella, S. (2013) A chemo-mechanical constitutive model accounting for cation exchange in expansive clays. Géotechnique 63, 221–234.

Guyonnet, D., Touze-Foltz, N., Norotte, V., Pothier, C., Didier, G., Gailhanou, H., Blanc, P., and Warmont, F. (2009) Performance-based indicators for controlling geosynthetic clay liners in landfill applications. Geotextiles and Geomembranes 27, 321-331.

Ho, T. A.; Criscenti, L. J.; and Greathouse, J. A. (2019) Revealing Transition States during the Hydration of Clay Minerals. J. Phys. Chem. Lett. 2019, 10 (13), 3704–3709. https://doi.org/10.1021/acs.jpclett.9b01565.

Holmboe, M., and Bourg, I.C. (2013) Molecular dynamics simulations of water and sodium diffusion in smectite interlayer nanopores as a function of pore size and temperature. The Journal of Physical Chemistry C, 118(2), 1001-1013.

Holmboe, M.; Wold, S.; Jonsson, and M. Porosity (2012) Investigation of Compacted Bentonite Using XRD Profile Modeling. J. Contam. Hydrol. 2012, 128 (1–4), 19–32. https://doi.org/10.1016/j.jconhyd.2011.10.005.

Honorio, T., Brochard, L., and Vandamme, M. (2017) Hydration phase diagram of clay particles from molecular simulations. Langmuir, 33(44), 12766-12776.

Horai, K.-I. (1971), Thermal conductivity of rock-forming minerals, Journal of Geophysical Research, 76(5), 1278.

Hsiao, Y., and Hedström, M. (2017) Swelling pressure in systems with na-montmorillonite and neutral surfaces: A molecular dynamics study. The Journal of Physical Chemistry C, 121(47), 26414-26423.

Huertas, F., Fuentes-Cantillana, J., Jullien, F., Rivas, P., Linares, J., Fariña, P., Ghoreychi, M., Jockwer, N., Kickmaier, W., Martínez, M. (2000) Full-scale engineered barriers experiment for a deep geological repository for high-level radioactive waste in crystalline host rock(FEBEX project). EUR(Luxembourg).

Idemitsu, K., Kozaki, H., Yuhara, M., Arima, T., and Inagaki, Y. (2016) Diffusion behavior of selenite in purified bentonite. Progress in Nuclear Energy 92, 279-285.

Idemitsu, K., Tachi, Y., Furuya, H., Inagaki, Y., and Arima, T. (1995) Diffusion of uranium in compacted bentonites in the reducing condition with corrosion products of iron. MRS Online Proceedings Library Archive 412.

Itasca, (2009). FLAC3D, Fast Lagrangian Analysis of Continua in 3 Dimensions, Version 4.0, Minneapolis, Minnesota, Itasca Consulting Group.

Järvinen, J., Matusewicz, M., and Itälä, A. (2016). Methodology for studying the composition of non-interlamellar pore water in compacted bentonite. Clay Minerals, 51, 173-187. doi:10.1180/claymin.2016.051.2.05

Johnson, L., Niemeyer, M., Klubertanz, G., Siegel, P., and Gribi, P. (2002) Calculations of the temperature evolution of a repository for spent fuel, vitrified high-level waste and intermediate level waste in Opalinus Clay. National Cooperative for the Disposal of Radioactive Waste.

Joseph, C., Mibus, J., Trepte, P., Müller, C., Brendler, V., Park, D.M., Jiao, Y., Kersting, A.B., and Zavarin, M. (2017) Long-term diffusion of U(VI) in bentonite: Dependence on density. Science of the Total Environment 575, 207-218.

Joseph, C., Van Loon, L.R., Jakob, A., Steudtner, R., Schmeide, K., Sachs, S., andBernhard, G. (2013) Diffusion of U(VI) in Opalinus Clay: Influence of temperature and humic acid. Geochimica et Cosmochimica Acta 109, 74-89.

Karnland O. (2010) Chemical and mineralogical characterization of the bentonite buffer for the acceptance control procedure in a KBS-3 repository, SKB Technical Report TR-10-60

Kharroubi, M., S. Balme, A. Haouzi, H. Belarbi, D. Sekou, and F. Henn (2012), Interlayer Cation–Water Thermodynamics and Dynamics in Homoionic Alkali and Alkaline-Earth Exchanged Montmorillonites with Low Water Loadings, The Journal of Physical Chemistry C, 116(28), 14970-14978, doi:10.1021/jp303963r.

Kim, J., Sonnenthal, E. L., and Rutqvist, J. (2012), Formulation and sequential numerical algorithms of coupled fluid/heat flow and geomechanics for multiple porosity materials, International Journal for Numerical Methods in Engineering, 92(5), 425–456.

Kim, N. (2020) Uftrace. https://github.com/namhyung/uftrace.

Kiverant, L., Kumpulainen, S., Pintado, X., Karttnen, P., Schatz, T. (2018) Characterization of Bentonite and Clay minerals 2012-2015. POSIVA working report 2016-05

Kober F., Schneeberger, R., Manukyan, E., Stasiek, L., Müller, H., and Vomvoris S., HotBENT : Experiment plan. NAB19-43.

Kronbichler, M., Heister, T., and Bangerth, W. (2012) High accuracy mantle convection simulation through modern numerical methods. Geophysical Journal International, 191, 12-29.

Kuhlman, U., and Gaus, I. (2014) THM Model validation modelling of selected WP2 experiments: Inverse Modelling of the FEBEX in situ test using iTOUGH2. DELIVERABLE-N°: D3.3-1

Kummerow, J., & Raab, S. (2015). Temperature dependence of electrical resistiity - Part I: Experimental investigations of hydrothermal fluids. Energy Procedia, 76, 240-246.

Kwon O., Kronenberg A.K., Gangi A.F., and Johnson B. (2001) Permeability of Wilcox shale and its effective pressure law. J. Geophys. Res.-Sol. Ea.;106:19339-53.

Lammers, L.N., Bourg, I.C., Okumura, M., Kolluri, K., Sposito, G., and Machida, M. (2017) Molecular dynamics simulations of cesium adsorption on illite nanoparticles. Journal of colloid and interface science, 490, 608-620.

Lanyon, G.W., and Gaus, I., 2016. Main outcomes and review of the FEBEX In Situ Test (GTS) and Mock-up after 15 years of operation, Technical Report 15-04, Nagra,

Lee, J. O., H. Choi, and J. Y. Lee (2016), Thermal conductivity of compacted Bentonite as a buffer material for a high level waste repository, Annals of Nuclear Energy, 94, 848-855.

Liu, H.-H. and Birkholzer, J. (2012). On the relationship between water flux and hydraulic gradient for unsaturated and saturated clay. Journal of Hydrology 475: 242-247.

Liu, H.H., Houseworth, J., Rutqvist, J., Zheng, L., Asahina, D., Li, L., Vilarrasa, V., Chen, F., Nakagawa, S., Finsterle, S., Doughty, C., Kneafsey, T. and Birkholzer, J. (2013) Report on THMC modeling of the near field evolution of a generic clay repository: Model validation and demonstration, Lawrence Berkeley National Laboratory, August, 2013, FCRD-UFD-2013-0000244.

Liu, L. (2013) Prediction of swelling pressures of different types of bentonite in dilute solutions. Colloids and Surfaces A: Physicochemical and Engineering Aspects 434, 303-318.

Lloret, A., Villar, M.V., Sánchez, M., Gens, A., Pintado, X., and Alonso, E.E. (2003) Mechanical behaviour of heavily compacted bentonite under high suction changes. Géotechnique: 53(1):27–40.

Ma, B., Charlet, L., Fernandez-Martinez, A., Kang, M., and Madé, B. (2019) A review of the retention mechanisms of redox-sensitive radionuclides in multi-barrier systems. Applied Geochemistry 100, 414-431.

Missana, T., Alonso, U., and García-Gutiérrez, M. (2009) Experimental study and modelling of selenite sorption onto illite and smectite clays. Journal of Colloid and Interface Science 334, 132-138.

Montavon, G., Guo, Z., Lützenkirchen, J., Alhajji, E., Kedziorek, M.A.M., Bourg, A.C.M., Grambow, B. (2009) Interaction of selenite with MX-80 bentonite: Effect of minor phases, pH, selenite loading, solution composition and compaction. Colloids and Surfaces A: Physicochemical and Engineering Aspects 332, 71-77.

Moore, D. M.; Robert C. and Reynolds, J. (1997) Xray diffraction and the identification and analysis of clay minerals. 2 ed.; Oxford University Press: New York, New York, 1997.

Morodome, S., and Kawamura, K. (2009) Swelling behavior of Na-and Ca-montmorillonite up to 150 C by in situ X-ray diffraction experiments. Clays and Clay Minerals, 57(2), 150-160.

Norrish, K. (1954) The swelling of montmorillonite. Discussions of the Faraday Society, 18, 120-134.

Park, S., and Schulten, K. (2004) Calculating Potentials of Mean Force from Steered Molecular Dynamics Simulations. J. Chem. Phys. 2004, 120 (13), 5946–5961. https://doi.org/10.1063/1.1651473.

Pusch, R. (1982) Mineral–water interactions and their influence on the physical behavior of highly compacted Na bentonite. Canadian Geotechnical Journal 19, 381-387.

Ramebäck, H., Skälberg, M., Eklund, U., Kjellberg, L., and Werme, L. (1998) Mobility of U, Np, Pu, Am and Cm from spent nuclear fuel into bentonite clay. Radiochimica Acta 82, 167-172.

Ramírez, S., J. Cuevas, R. Vigil and S. Leguey (2002) Hydrothermal alteration of “La Serrata” bentonite (Almeria, Spain) by alkaline solutions. Applied Clay Science 21(5–6): 257-269.

Rasband, W.S. Image J, U. S. National Institutes of Health, Bethesda, Maryland, USA, https://imagej.nih.gov/ij/, 1997–2020.

Rotenberg, B., Morel, J., Marry, V., Turq, P., and Morel-Desrosiers, N. (2009) On the driving force of cation exchange in clays: Insights from combined microcalorimetry experiments and molecular simulation. Geochimica Et Cosmochimica Acta, 73(14), 4034-4044.

Rutqvist, J., Y. Ijiri and H. Yamamoto (2011) Implementation of the Barcelona Basic Model into TOUGH–FLAC for simulations of the geomechanical behavior of unsaturated soils. Computers & Geosciences 37(6): 751-762.

Rutqvist, J., Zheng, L., Chen, F., Liu, H.-H. and Birkholzer, J. (2014) Modeling of Coupled Thermo-Hydro-Mechanical Processes with Links to Geochemistry Associated with Bentonite-Backfilled Repository Tunnels in Clay Formations. Rock Mechanics and Rock Engineering: 47, 167–186.

Sacchi, E., Michelot, J.L., Pitsch, H., Lalieux, P., Aranyossy, J.F. (2001) Extraction of water and solution from argillaceous rock for geochemical characterisation: methods, processes, and current understanding. Hydrogeology Journal 9, 17–33.

Samper, J., Zheng, L., Fernández, A.M., and Montenegro, L. (2008) Inverse modeling of multicomponent reactive transport through single and dual porosity media. Journal of Contaminant Hydrology 98(3–4): 115-127.

Sánchez, F. G., F. Jurányi, T. Gimmi, L. V. Loon, T. Seydel, and T. Unruh (2008) Dynamics of supercooled water in highly compacted clays studied by neutron scattering, Journal of Physics: Condensed Matter, 20(41), doi:10.1088/0953-8984/20/41/415102.

Sánchez, F. t. G. l., L. R. Van Loon, T. Gimmi, A. Jakob, M. A. Glaus, and L. W. Diamond (2008) Self-diffusion of water and its dependence on temperature and ionic strength in highly compacted montmorillonite, illite and kaolinite, Applied Geochemistry, 23, 3840-3851, doi:10.1016/j.apgeochem.2008.08.008.

Sánchez, M., A. Gens and Guimarães, L. (2012a) Thermal–hydraulic–mechanical (THM) behaviour of a large-scale “in situ” heating experiment during cooling and dismantling. Canadian Geotechnical Journal 49(10): 1169-1195.

Sánchez, M., Gens, A., and Olivella, S. (2012b) THM analysis of a large-scale heating test incorporating material fabric changes. International Journal for Numerical and Analytical Methods in Geomechanics 36(4): 391-421.

Sánchez, M., Gens, A., Guimarães, L. J. D. N., and Olivella, S. (2005) A double structure generalized plasticity model for expansive materials. International Journal for numerical and analytical methods in geomechanics 29: 751-787.

Sánchez, M., Gens, A., Guimarães, L., and Olivella, S. (2008) Implementation algorithm of a generalised plasticity model for swelling clays, Computers and Geotechnics: 35(6), 860-871.

Segad, M., Hanski, S., Olsson, U., Ruokolainen, J., Åkesson, T., and Jönsson, B. (2012) Microstructural and Swelling Properties of Ca and Na Montmorillonite: (In Situ) Observations with Cryo-TEM and SAXS. The Journal of Physical Chemistry C 2012, 116 (13), 7596-7601.

SKB, (2011). Long-term safety for the final repository for spent nuclear fuel at Forsmark. Main report of the SR-Site project. Swedish Nuclear Fuel and Waste Management Co.

Smith, D. E., Wang, Y., Chaturvedi, A., and Whitley, H. D. (2006) Molecular Simulations of the Pressure, Temperature, and Chemical Potential Dependencies of Clay Swelling †. J. Phys. Chem. B 2006, 110 (40), 20046–20054. https://doi.org/10.1021/jp062235o.

Smith, D. W., and Booker, J. R. (1993) Green’s functions for a fully coupled thermoporoelastic material. International Journal for Numerical and Analytical Methods in Geomechanics, 17, 139-163.

Sonnenthal, E. L., Smith, J. T., Cladouhos, T., Kim, J., and Yang L. (2015) Thermal-Hydrological-Mechanical-Chemical Modeling of the 2014 EGS Stimulation Experiment at Newberry Volcano, Oregon. PROCEEDINGS, 40th Workshop on Geothermal Reservoir Engineering. Stanford University, Stanford, California, January 26-28.

Sonnenthal, E., Pettitt, W., Smith T., Riahi, A., Siler D., Kennedy, M., Majer, E., Dobson, P., Ayling, B., Damjanac, B., and Blankenship D. (2018) Continuum Thermal-Hydrological-Mechanical Modeling of the Fallon FORGE Site. GRC Transactions, Vol. 42.

Steefel, C.I., Appelo, C.A.J., Arora, B., Jacques, D., Kalbacher, T., Kolditz, O., Lagneau, V., Lichtner, P.C., Mayer, K.U., Meeussen, J.C.L., Molins, S., Moulton, D., Shao, H., Šimůnek, J., Spycher, N., Yabusaki, S.B., and Yeh, G.T. (2015) Reactive transport codes for subsurface environmental simulation. Computational Geosciences 19, 445-478.

Subramanian, N., Whittaker, M. L., Ophus, C., and Lammers, L. N. (2020) Structural Implications of Interfacial Hydrogen Bonding in Hydrated Wyoming-Montmorillonite Clay. J. Phys. Chem. C 2020, acs.jpcc.9b11339. https://doi.org/10.1021/acs.jpcc.9b11339.

Sun, L., Hirvi, J. T., Schatz, T., Kasa, S., and Pakkanen, T. A. (2015) Estimation of montmorillonite swelling pressure: A molecular dynamics approach. The Journal of Physical Chemistry C, 119(34), 19863-19868.

Svoboda, M., Moučka, F., and Lísal, M. (2018) Saturated Aqueous NaCl Solution and Pure Water in Na-Montmorillonite Clay at Thermodynamic Conditions of Hydraulic Fracturing: Thermodynamics, Structure and Diffusion from Molecular Simulations. J. Mol. Liq. 2018, 271, 490–500. https://doi.org/10.1016/j.molliq.2018.08.144.

Tang, A.-M.; and Cui, Y. (2006) Determining the Thermal Conductivity of Compacted MX80 Clay. (2006) Unsaturated Soil, 1695-1706.

Tang, A.-M., Y.-J. Cui, and T.-T. Le (2007), A study of the thermal conductivity of compacted Bentonites, Applied Clay Science, 41, 181-189.

Teich-McGoldrick, S.L., Greathouse, J.A., Jove-Colon, C.F., and Cygan, R.T. (2015) Swelling properties of montmorillonite and beidellite clay minerals from molecular simulation: Comparison of temperature, interlayer cation, and charge location effects. The Journal of Physical Chemistry C, 119(36), 20880-20891.

Teppen, B. J.; and Miller, D. M. (2006) Hydration Energy Determines Isovalent Cation Exchange Selectivity by Clay Minerals. Soil Sci. Soc. Am. J. 2006, 70 (1), 31–40. https://doi.org/10.2136/sssaj2004.0212.

Tester, C. C., Aloni, S., Gilbert, B., and Banfield, J. F. (2016) Short- and Long-Range Attractive Forces That Influence the Structure of Montmorillonite Osmotic Hydrates. Langmuir 2016, 32 (46), 12039-12046.

Tinnacher, R.M., Holmboe, M., Tournassat, C., Bourg, I.C., and Davis, J.A. (2016a) Ion adsorption and diffusion in smectite: Molecular, pore, and continuum scale views. Geochimica et Cosmochimica Acta 177, 130-149.

Tinnacher, R.M., Tournassat, C., and Davis, J.A. (2016b). Laboratory Experiments on Bentonite Samples: FY16 Progress. U.S. Department of Energy, Used Fuel Disposition Campaign.

Torstenfelt, B., and Allard, B. (1986) Migration of fission products and actinides in compacted bentonite. KBS Report 86, 14.

Tournassat, C., and Appelo, C.A.J. (2011) Modelling approaches for anion-exclusion in compacted Na-bentonite. Geochimica et Cosmochimica Acta 75, 3698-3710.

Tournassat, C., Steefel, C.I., Bourg, I.C., and Bergaya, F. (2015) Natural and engineered clay barriers. Elsevier.

Tournassat, C., Bourg, I.C., Holmboe, M., Sposito, G., and Steefel, C.I. (2016) Molecular dynamics simulations of anion exclusion in clay interlayer nanopores. Clays and Clay Minerals, 64(4), 374-388.

Tournassat, C., Tinnacher, R.M., Grangeon, S., and Davis, J.A. (2018) Modeling uranium(VI) adsorption onto montmorillonite under varying carbonate concentrations: A surface complexation model accounting for the spillover effect on surface potential. Geochimica et Cosmochimica Acta 220, 291-308.

Tournassat, C., and Steefel, C.I. (2019a) Modeling diffusion processes in the presence of a diffuse layer at charged mineral surfaces: a benchmark exercise. Computational Geosciences.

Tournassat, C., and Steefel, C.I. (2019b) Reactive Transport Modeling of Coupled Processes in Nanoporous Media. Reviews in Mineralogy and Geochemistry 85, 75-109.

Underwood, T. R., and Bourg, I. C. (2020) Large-Scale Molecular Dynamics Simulation of the Dehydration of a Suspension of Smectite Clay Nanoparticles. J. Phys. Chem. C 2020, 124 (6), 3702–3714. https://doi.org/10.1021/acs.jpcc.9b11197.

Van Loon, L.R., Soler, J.M., and Bradbury, M.H. (2003) Diffusion of HTO, 36Cl− and 125I− in Opalinus Clay samples from Mont Terri: Effect of confining pressure. Journal of Contaminant Hydrology 61, 73-83.

Villar M.V.(2005) MX-80 Bentonite Thermo-Hydro-Mechanical Characterisation Performed at CIEMAT in the Context of the Prototype Project, Informes Técnicos Ciemat 1053 Febrero, 2005

Villar, M. V., Fernandez, A. M., Martin, P. L., Barcala, J. M., Gomez-Espina, R., and Rivas, P. (2008). Effect of Heating/hydration on Compacted Bentonite: tests in 60-cm Long Cells. Spain: Editorial CIEMAT.

Villar, M.V., Iglesias, R.J., and García-Siñeriz, J.L. (2018a) State of the in situ Febex test (GTS, Switzerland) after 18 years: a heterogeneous bentonite barrier. Environmental Geotechnics, 1-13.

Villar, M.V., Iglesias, R.J., Gutiérrez-Álvarez, C., and Carbonell, B. (2018b) Hydraulic and mechanical properties of compacted bentonite after 18years in barrier conditions. Applied Clay Science 160, 49-57.

Villar, M.V., Iglesias, R.J., Gutiérrez-Álvarez, C., and Carbonell, B. (2018) Hydraulic and mechanical properties of compacted bentonite after 18 years in barrier conditions. Applied Clay Science 160, 49-57.

Vomvoris, S., Birkholzer, J., Zheng, L., Gaus, I., and Blechschmidt, I. (2015) THMC behavior of clay-based barriers under high temperature- from laboratory to URL scale. 2015, 678-687.

Voltolini, M., Kwon, T.H. and Ajo-Franklin, J. (2017a) Visualization and prediction of supercritical CO2 distribution in sandstones during drainage: An in situ synchrotron X-ray micro-computed tomography

Voltolini, M., Haboub, A., Dou, S., Kwon, T.H., MacDowell, A.A., Parkinson, D.Y. and Ajo-Franklin, J. (2017b) The emerging role of 4D synchrotron X-ray micro-tomography for climate and fossil energy studies: five experiments showing the present capabilities at beamline 8.3. 2 at the Advanced Light Source. Journal of synchrotron radiation, 24(6), pp.1237-1249.

Voltolini, M. and Ajo-Franklin, J. (2019) The effect of CO2-induced dissolution on flow properties in Indiana Limestone: An insitu synchrotron X-ray micro-tomography study. International Journal of Greenhouse Gas Control, 82, pp.38-47.

Voltolini, M., Barnard, H., Creux, P. and Ajo-Franklin, J. (2019) A new mini-triaxial cell for combined high-pressure and high-temperature in situ synchrotron X-ray microtomography experiments up to 400° C and 24 MPa. Journal of synchrotron radiation, 26(1).

Wang, X., Chen, C., Zhou, X., Tan, X., and Hu, W. (2005) Diffusion and sorption of U (VI) in compacted bentonite studied by a capillary method. Radiochimica Acta 93, 273-278.

Wang, Z., Wang, H., Li, Q., Xu, M., Guo, Y., Li, J., and Wu, T. (2016) pH effect on Re(VII) and Se(IV) diffusion in compacted GMZ bentonite. Applied Geochemistry 73, 1-7.

Waxman, M. H., and Smits, L. J. (1968) Electrical conductivities in oil-bearing shaly sands. Soc. Pet. Eng. J., 8, 107–122.

Wersin, P., Johnson, L.H., and McKinley, I.G. (2007) Performance of the bentonite barrier at temperatures beyond 100°C: A critical review. Physics and Chemistry of the Earth, Parts A/B/C 32, 780-788.

Whitley, H. D., and Smith, D. E. (2004) Free Energy, Energy, and Entropy of Swelling in Cs–, Na–, and Sr–Montmorillonite Clays. J. Chem. Phys. 2004, 120 (11), 5387–5395. https://doi.org/10.1063/1.1648013.

Whittaker, M. L., L. N. Lammers, S. Carrero, B. Gilbert, and J. F. Banfield (2019) Ion exchange selectivity in clay is controlled by nanoscale chemical–mechanical coupling, Proceedings of the National Academy of Sciences, doi:10.1073/pnas.1908086116.

Whittaker, M. L., L. R. Comolli, B. Gilbert, and J. F. Banfield (2020) Layer size polydispersity in hydrated montmorillonite creates multiscale porosity networks, Applied Clay Science, 1.

Wu, T., Wang, Z., Wang, H., Zhang, Z., and Van Loon, L.R. (2017) Salt effects on Re(VII) and Se(IV) diffusion in bentonite. Applied Clay Science 141, 104-110.

Xu, H. Rutqvist, J., Plua, C., Armand, G., and Birkholzer, J. (2020) Modeling of Thermal Pressurization in Tight Claystone using Sequential THM Coupling: Benchmarking and Validation against In-situ Heating Experiments in COx Claystone. Tunnelling and Underground Space Technology, http://doi.org/10.1016/j.tust.2020.103428.

Xu, T., Sonnenthal, E., Spycher, N., and Zheng, L. (2014) TOUGHREACT V3. 0-OMP reference manual: a parallel simulation program for non-isothermal multiphase geochemical reactive transport. University of California, Berkeley.

Xu, T., Spycher, N., Sonnenthal, E., Zhang, G., Zheng, L. and Pruess, K. (2011) TOUGHREACT Version 2.0: A simulator for subsurface reactive transport under non-isothermal multiphase flow conditions. Computers & Geosciences 37(6): 763-774.

Zarzycki, P., and B. Gilbert (2016) Long-Range Interactions Restrict Water Transport in Pyrophyllite Interlayers, Sci Rep, 6, 25278, doi:10.1038/srep25278.

Zheng, L., Samper, J., and Montenegro, L. (2011) A coupled THC model of the FEBEX "in situ" test with bentonite swelling and chemical and thermal osmosis. Journal of Contaminant Hydrology 126(1–2): 45-60.

Zheng, L., Li, L., Rutqvist, J., Liu, H. and Birkholzer, J.T. (2012) Modeling Radionuclide Transport in Clays. Lawrence Berkeley National Laboratory. FCRD-URD-2012-000128.

Zheng, L. Rutqvist, J., Steefel, C., Kim, K., Chen, F., Vilarrasa, V., Nakagawa, S., Zheng, J., Houseworth, J., and Birkholzer, J. (2014) Investigation of Coupled Processes and Impact of High Temperature Limits in Argillite Rock. FCRD-UFD-2014-000493, LBNL-6719E.

Zheng L., Rutqvist J. Kim, K. and Houseworth J. (2015a) Investigation of Coupled Processes and Impact of High Temperature Limits in Argillite Rock. FCRD-UFD-2015-000362, LBNL-187644.

Zheng, L., J. Rutqvist, J. T. Birkholzer and H.-H. Liu (2015b) On the impact of temperatures up to 200 °C in clay repositories with bentonite engineer barrier systems: A study with coupled thermal, hydrological, chemical, and mechanical modeling. Engineering Geology 197: 278-295.

Zheng, L., Kim, K., Xu, H., and Rutqvist, J. (2016) DR Argillite Disposal R&D at LBNL. FCRD-UFD-2016-000437, LBNL-1006013, Lawrence Berkeley National Laboratory.

Zheng, L., Rutqvist, J., Xu, H., Kim, K., Voltolini, M., and Cao, X. (2017) Investigation of Coupled Processes and Impact of High Temperature Limits in Argillite Rock. SFWD-SFWST-2017-000040, LBNL-2001014. Lawrence Berkeley National Laboratory.

Zheng, L., Xu, H., Fox, P., Nico, P., and Birkholzer, J. (2018) Engineered Barrier System Research Activities at LBNL: FY18 Progress Report. SFWD-SFWST-2018-000040, LBNL-200117. Lawrence Berkeley National Laboratory.

Zheng, L., P. Fox, P. Zarzycki, E. Sonnenthal, S. Borglin, C. Chang, C. Chou, Y. Wu, H. Xu, P. Nico, B. Gilbert, T. Kneafsey, Y. Cheng and J. Birkholzer (2019a) Engineered Barrier System Research Activities at LBNL Via International Collaboration: FY19 Progress Report, Lawrence Berkeley National Laboratory, LBNL-2001210.

Zheng, L., H. Xu, J. Rutqvist, M. Reagan, J. Birkholzer, M. V. Villar, and A. M. Fernández (2019b) The hydration of bentonite buffer material revealed by modeling analysis of a long-term in situ test. Applied Clay Science, 105360.

Zhou, Y., Rajapakse, R.K.N.D., and Graham, J. (1999) Coupled Field in a deformable unsaturated medium. International Journal of Solid and Structures, 36: 4841-4868.